



HAL
open science

Design, synthesis and characterization of new organic semi-conductors for photovoltaics

Chunxiang Chen

► **To cite this version:**

Chunxiang Chen. Design, synthesis and characterization of new organic semi-conductors for photovoltaics. Materials. Université Paul Sabatier - Toulouse III, 2016. English. NNT : 2016TOU30108 . tel-01483841

HAL Id: tel-01483841

<https://theses.hal.science/tel-01483841>

Submitted on 6 Mar 2017

HAL is a multi-disciplinary open access archive for the deposit and dissemination of scientific research documents, whether they are published or not. The documents may come from teaching and research institutions in France or abroad, or from public or private research centers.

L'archive ouverte pluridisciplinaire **HAL**, est destinée au dépôt et à la diffusion de documents scientifiques de niveau recherche, publiés ou non, émanant des établissements d'enseignement et de recherche français ou étrangers, des laboratoires publics ou privés.

Université Fédérale



Toulouse Midi-Pyrénées

THÈSE

En vue de l'obtention du

DOCTORAT DE L'UNIVERSITE DE TOULOUSE

Délivré par :

Université Toulouse 3 Paul Sabatier (UT3 Paul Sabatier)

Présentée et soutenue par **Chunxiang CHEN**

Le 19 Juillet 2016

Design, synthesis and characterization of new organic semi-conductors for photovoltaics

Ecole doctorale et discipline ou spécialité :

ED SDM : Sciences et Génie des Matériaux

Unité de recherche :

CNRS-UPR 8241 Laboratoire de Chimie de Coordination

Directrice de thèse :

Dr. Kathleen MOINEAU CHANE-CHING

Jury :

Philippe LAINE	Directeur de Recherche – ITODYS	Rapporteur
Arnaud MARTEL	Professeur – I.U.T Le Mans	Rapporteur
Fabienne ALARY	Professeure– LCPQ-IRSAMC	Examinatrice
Zéphirin MOULOUNGUI	Directeur de Recherche, INP-ENSIACET	Examineur
Kathleen MOINEAU CHANE-CHING	Directeur de Recherche – LCC, Invitée	Directrice de thèse

Acknowledgment

Acknowledgment

First of all, I would like to express my deepest gratitude to my thesis advisor Dr. Kathleen I. Moineau-Chane Ching for providing me all the opportunity to do this research, her enthusiastic and patient guidance, continuous and unconditional support, and good advice throughout the project greatly encouraged and helped me, which has profound impact on me. I was sincerely honored to meet and work with her, because she is so knowledgeable, hard-working, rigorous and prudent attitude towards science, kind and warm-hearted, and so on. I highly appreciate and never forget the time spent with her.

I would like to extend warm thanks to the whole team "Molecules and Composites for Optics" which is directed by Prof. Isabelle Malfant, for their attention and expert advice for my work which contribute to the success of this thesis. Their knowledge, guidance, skills and confidence were the driving forces for my work. It's my great pleasure to work with them throughout these 3 years. Thanks to the team, my stay in LCC was an unforgettable memory in many aspects of my life. I'm also grateful to all group mates and collaborators in LCC who have helped and inspired me in many aspects during the period of my study in France, in particular Dr. Daniel Hernandez Maldonado, Damien Le Borgne with whom I had many helpful and encouraging discussions.

I'm also much thankful to Dr. Fabienne Alary and Dr. Jean-Louis Heully from Laboratoire de Chimie et Physique Quantiques (LCPQ) in Toulouse, for their involvement in the project. I learned a lot about theoretical calculation from them, their enthusiasm, help and guidance are highly appreciated.

Apparently, it's impossible to achieve all the goals without the help of all the technical and administrative services of Laboratoire de Chimie de Coordination, because they are fundamental parts of daily work in LCC. Thanks to them for providing good work conditions and environment.

I give special thanks to my committee members: Dr. Philippe Lainé (ITODYS), Prof. Arnaud Martel (IMMM), Dr. Zéphirin Mouloungui (INRA) and Dr. Fabienne Alary (LCPQ) for their time, helpful comments and interest in my work.

I would never come to pursue the PhD project without the enormous contribution, guidance and help of Dr. Wei Shen and Dr. Rongxing He, who are my previous Master supervisors from the Southwest University in China.

Many thanks to all my friends (here and elsewhere), the friendship were previous wealth of my life, which made my stay in Toulouse (and in China) an unforgettable memory.

I would like to acknowledge the financial support from the China Scholar Council (CSC) for offering me the abroad study opportunity and supporting my research in France.

For the last but not least, my sincere gratitude goes to my families in China and in France, for their love and never-ending support. Thanks to them, my life in France is wonderful and impressive. Like a motto in French: *la vie est belle*. Specifically, many thanks to my husband Dr. Yohan Dall'Agnese not only for his endless and deep love, but also for his thoughtfulness, generous help, support and encouragement in all aspects of my life, especially during the hard time of my thesis writing.

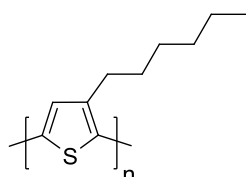
Abbreviations

Abbreviations

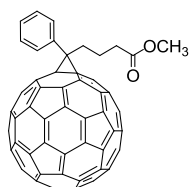
AM	Air Mass means the proportion of atmosphere that the sunlight must travel through before radiating at the Earth's surface (or sea level) relative to its overhead path length, and $AM=1/\cos(\theta)$ (zenith angle, namely where θ is the angle from the vertical)
AM0	the standard spectrum outside the Earth's atmosphere that is typically used for power applications of solar cells in space
AM1	refers to the spectrum after passing through the atmosphere (perfectly clear and cloudless sky) at the Earth's surface when the sun is directly overhead ($\theta=0^\circ$)
AM1.5	corresponds to a solar zenith angle of $\theta=48.2^\circ$, 1.5 atmosphere thickness that is useful to represent the overall yearly average for temperate latitudes
AM1.5G	stands for the standard spectrum at the Earth's surface where the G represents global and involves both direct and diffuse radiation
AM2	corresponds to a solar zenith angle of $\theta=60^\circ$ which is useful to predict wintertime performance of cells in temperate latitudes
HOMO	highest occupied molecular orbital
LUMO	lowest unoccupied molecular orbital
SOMO	a singly occupied molecular orbital
Eg	energy gap, refers to the difference (in electron volts) of energy between the bottom of the conduction band and the top of the valence band of the electrons in solids, related to energy difference between the HOMO and LUMO in chemistry
Isc	the short-circuit current, corresponds to the maximum current from a solar cell and happens when the voltage across the device is zero
Jsc	the short-circuit current density (mA/cm^2)
Voc	the open circuit voltage, represents the maximum voltage obtainable from a solar cell that occurs at zero current
FF	Fill factor, a parameter which, in relevance with V_{oc} and J_{sc} , evaluates the maximum power from a solar cell. The FF is equal to the ratio of the highest power from a solar cell to the product of V_{oc} and J_{sc}
PCE	Power conversion efficiency, represents the percentage of input power that is

converted to electricity; the most commonly used parameter to determine the performance of a solar cell and compare the performance of one solar cell to another

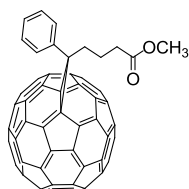
OFET	Organic Field Effect Transistors
OLED	Organic Light Emitting Diodes
OPVs	Organic Photovoltaics
ITO	Indium tin oxide
NBS	N-bromosuccinimide
THF	Tetrahydrofuran
DCM	Dichloromethane
DCB	Dichlorobenzene
DMA	<i>N,N</i> -Dimethylacetamide
P3HT	Poly(3-hexyl thiophene) (C ₁₀ H ₁₄ S) _n , N° CAS : 108568-44-1



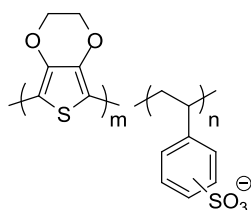
PC₆₁BM	or PCBM, or PC ₆₀ BM, [6,6]-phenyl-C ₆₁ -butyric acid methyl ester N° CAS : 160848-22-6
--------------------------	--



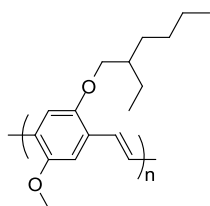
PC₇₁BM	or PC ₇₀ BM, [6,6]-phenyl-C ₇₁ -butyric acid methyl ester N° CAS : 609771-63-3
--------------------------	--



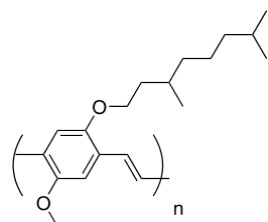
PEDOT-PSS	Poly(3,4-ethylenedioxythiophene):poly(styrene sulfonate)
------------------	--



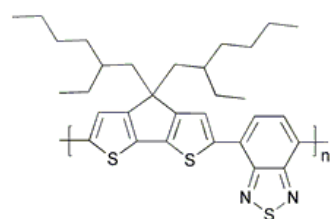
MEH-PPV Poly[2-methoxy-5-(2-ethylhexyloxy)-1,4-phenylenevinylene]
(C₁₇H₂₄O₂)_n, N° CAS : 138184-36-8



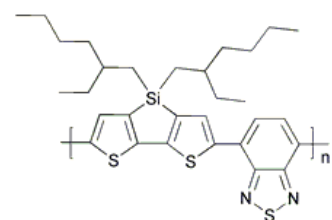
MDMO-PPV Poly [2-methoxy-5-(3,7-dimethyloctyloxy)]-1,4-phenylenevinylene



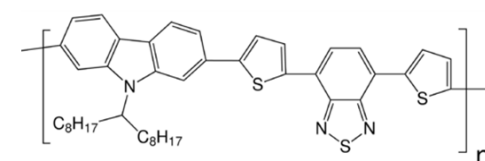
PCPDTBT Poly[2,1,3-benzothiadiazole-4,7-diyl[4,4-bis(2-ethylhexyl)-4*H*-cyclopenta[2,1-*b*:3,4-*b'*]dithiophene-2,6-diyl]] (C₃₁H₃₈N₂S₃)_n, N°CAS: 920515-34-0



PSBTBT Poly[(4,4'-bis(2-ethylhexyl)dithieno[3,2-*b*:2',3'-*d*]silole)-2,6-diyl-alt-(2,1,3-benzothiadiazole)-4,7-diyl]

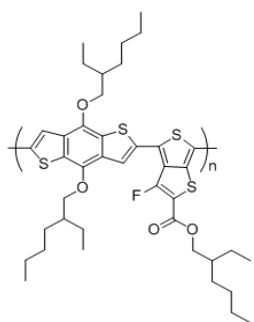


PCDTBT Poly[[9-(1-octylnonyl)-9*H*-carbazole-2,7-diyl]-2,5-thiophenediyl-2,1,3-benzothiadiazole-4,7-diyl-2,5-thiophenediyl] (C₄₃H₄₇N₃S₃)_n, N°CAS: 958261-50-2



PTB7 Poly[(4,8-bis[(2-ethylhexyl)oxy]benzo[1,2-*b*:4,5-*b'*]dithiophene-2,6-diyl)(3-

fluoro-2-[(2-ethylhexyl)carbonyl]thieno[3,4-*b*]thiophenediyl]



Contents

Table of Contents

General introduction	1
Chapter I : Bibliography	5
I Renewable solar energy	5
II Organic photovoltaics	6
II. 2 Functional principle of organic photovoltaic cells.....	9
II. 2-1 Photon absorption and excitons generation	11
II. 2-2 Diffusion and dissociation of excitons	12
II. 2-3 Transport of charge carriers and charge collection	13
II. 3 Characterization of OPV performance.....	14
II. 3-1 Test conditions for OPV - standard solar spectra	14
II. 3-2 Important parameters for OPV efficiency	15
II. 3-3 Power conversion efficiency (PCE)	19
II. 4 Types of OPV and their architectures	20
II. 4-1 Bilayer heterojunction	20
II. 4-2 Bulk heterojunction	21
II. 4-3 Tandem OPV cells.....	23
II. 5 Organic semiconducting materials for OPVs.....	24
II. 5-1 Introduction of semi-conductor property and π -conjugation.....	24
II. 5-2 Optical properties of semiconducting polymers.....	26
II. 5-3 Charge transport mechanism in conjugated polymers.....	27

II. 5-4	Polymer-based and small molecule-based materials for OPV	28
II. 6	Outlook	38
III	PhD objectives	40
Chapter II	: Molecular design	45
I	Introduction	45
I. 1	Theoretical work on molecular design	45
I. 2	Theoretical work on active-layer interface	47
II	Small molecules design	48
II. 1	Small molecules based on benzothiadiazole (Bz) core	49
II. 2	Small molecules based on dithienosilole (DTS) core	51
II. 3	Small molecules based on subphthalocyanines (SubPcs)	56
III	Theoretical calculation	60
III. 1	Bz-based small molecules	60
III. 1-1	Electronic and optical properties	60
III. 1-2	Effect of fluorine substitution	67
III. 2	DTS-based small molecules	70
III. 3	SubPcs-based small molecules	72
IV	Conclusion	75
Chapter III	: Green chemistry approach for materials synthesis	79
I	Introduction	79
II	Synthesis of benzothiadiazole (Bz) based small molecules	80

II. 1	Synthesis and environmental evaluation of di-substituted compounds Bz(T ₁ CHO) ₂ , Bz(T ₂ CHO) ₂ and target molecules	82
II. 1-1	Synthesis of compounds Bz(T ₁ CHO) ₂ and Bz(T ₂ CHO) ₂	82
II. 1-2	Environmental and economic aspects.....	85
III	Synthesis of molecules based on dithienosilole (DTS) core	89
III. 1	Synthesis of mono-substituted compounds and related BzT ₂ CAO molecule	89
III. 1-1	Synthesis of fragment BrBzT ₁ CHO	89
III. 1-2	Synthesis of fragment BrBzT ₂ CHO	93
III. 1-3	Synthesis of another Bz-based unsymmetrical molecule (BzT ₂ CAO)	93
III. 2	Synthesis of DTS cores and DTS-based target molecules	94
IV	Subphthalocyanine (SubPc) derivatives: synthesis and axial substitution	97
IV. 1	Synthesis of chloroboron subphthalocyanine (SubPcBCl)	97
IV. 2	Axial substitution of SubPcBCl	98
V	Conclusion	99
Chapter IV : Materials characterization		103
I	Optical properties	103
II	Electrochemical properties.....	109
III	Thermal properties.....	114
IV	Structural properties	115
V	Conclusion	118
Chapter V : Experimental section		121

I Materials, equipment and methods.....	121
II Computational details	122
III Films elaboration	123
IV Synthetic procedure	123
General conclusion	143
Future work	144
Annexes	149
Figure list	171
Scheme list.....	179
Table list.....	183
Résumé de thèse.....	187
References	209

General introduction

General introduction

Energy is nowadays the most important and urgent problem facing humans, and the global demand for renewable energy is growing ever faster. Fossil fuels such as oil, gas, coal and other non-renewable energy are the main energy sources human consumed in the last century, their production and combustion have become a serious issue of our ecological environment, because of the large amount of carbon dioxide (CO₂) emission, a key driver of global warming. The fossil fuels are not able to meet the future need due to their limited resources and sky-rocketing price, leading to ever urgent need for clean, renewable and sustainable energy sources. To achieve this goal is one of humanity's greatest challenges. The sun can provide our planet an inexhaustible and endless source of energy, and the Earth receives sufficient solar energy per hour to satisfy humans' annual demand. The energy irradiated on the Earth's surface from the sun each year is twice as the energy of all fossil and nuclear energy stores. Solar energy is therefore a promising alternative to these non-renewable energy sources and will play a significant role in meeting increasing energy demands.

The organic photovoltaic cells (OPV cells) promise to provide solar-to-electric energy conversion. It is one of the most important and promising long-term strategies for providing clean and renewable energy to our planet. It have attracted widespread attention as promising candidates to meet the increasing demand for renewable energy, due to their outstanding properties, such as ease of fabrication, mechanical flexibility, potential for renewable and green energy source low-cost potential, etc.(1-5) Currently, a record power conversion efficiency (PCE) of 13.2% for an OPV multi-junction cell was reached by Heliatek.(6) The development and synthesis of new organic semiconductors, that can be electron donor or acceptor for their use in the active layer is of great importance, together with technical progress in the device fabrication to reach OPV cells with high performance. Small molecules for OPVs have emerged as attractive candidates over their polymer counterparts, because of the well-defined but versatile chemical structures which allow easier energy level control, together with higher purity.

The work reported herein is focused on the development and synthesis of small molecules. The motivation is to obtain new small molecules for use as active materials *via* green synthesis within as simple as possible procedures. In this work, we investigated few new materials from initial design to synthesis and to characterization.

The first chapter is a bibliographic review. We explain the functional principle, important characterizations, and different types of organic photovoltaic devices before focusing on the state-of-the-art electronic materials for OPV devices. A summary of the performance of various organic π -conjugated materials used as donors or acceptors for OPV cells is given. The outlook on organic photovoltaics is summarized as the closing remark.

The second chapter focuses on theoretical calculations used for molecular design. In particular, a series of small molecules based on benzothiadiazole (Bz) core, 4,4'-di-n-octyl-dithieno[3,2-b:2',3'-d] silole (or dithienosilole, DTS) core, and subphthalocyanines (SubPcs) unit are theoretically investigated. Their electronic properties are predicted *via* theoretical calculations using density functional theory (DFT). The synthetic strategies for obtaining these molecules are also described.

The third chapter describes the experimental synthetic methods used for the molecules previously designed. In particular, direct arylation methods used as a green synthetic approach are presented, as well as traditional Suzuki cross-coupling. The E-Factor (kg waste / kg product) for assessing the environmental impact of the two manufacturing processes is also given.

In the fourth chapter, four obtained Bz-based small molecules are investigated in terms of optical, electrochemical, thermal properties and structural properties. We identify these molecules as promising materials for applications in OPV cells.

The fifth chapter presents the experimental procedures related to the synthesized molecules throughout this work.

Finally, the general conclusion and perspective of this work are presented.

Chapter I: Bibliography

Chapter I : Bibliography

I Renewable solar energy

Currently, more than 80% (as shown in the following two figures) of the worldwide energy supply is from carbon-based fossil fuels like oil, coal, gas, and other non-renewable sources.(7) Their production and combustion have become nowadays a major problem of our environment due to the emission of huge amount of carbon dioxide (CO₂), a dominant greenhouse gas and a key driver of global climate change. Use of fossil fuels has led to serious ecological problems (global warming, pollution, planet degradation) and economic concerns (limited resources while sky-rocketing price). Therefore, renewable energies are one of the hot topics of the global energy strategy. The demand to explore and develop renewable energy sources has become increasingly urgent.

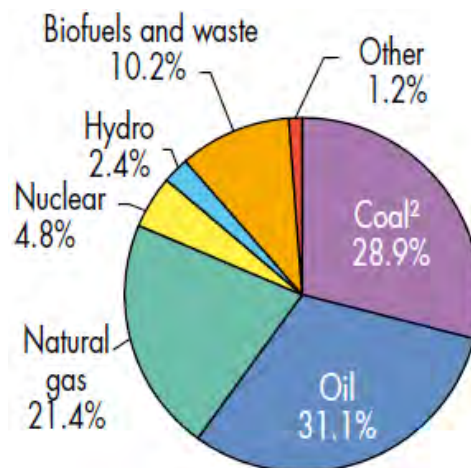


Figure I-1: World total primary energy supply in 2013, provided by International Energy Agency. Coal: peat and oil shale are aggregated with coal, other: geothermal, solar, wind, heat, etc., are included.(7)

Among the renewable energy resources: biomass, hydropower, geothermal, wind and solar, the inexhaustible solar energy appears as one of the most promising energies.(8) The sun represents the most powerful energy source available on earth. The energy received from sunlight striking the earth surface in 1 hour (120 000 TW, consisting of 5% ultraviolet, 43% visible and 52% infrared, as plotted in Figure I-3) is far more than all of the energy consumed on our planet in an entire year.(9, 10) Consequently, the use of solar energy is one of the most significant challenges nowadays in scientific community.

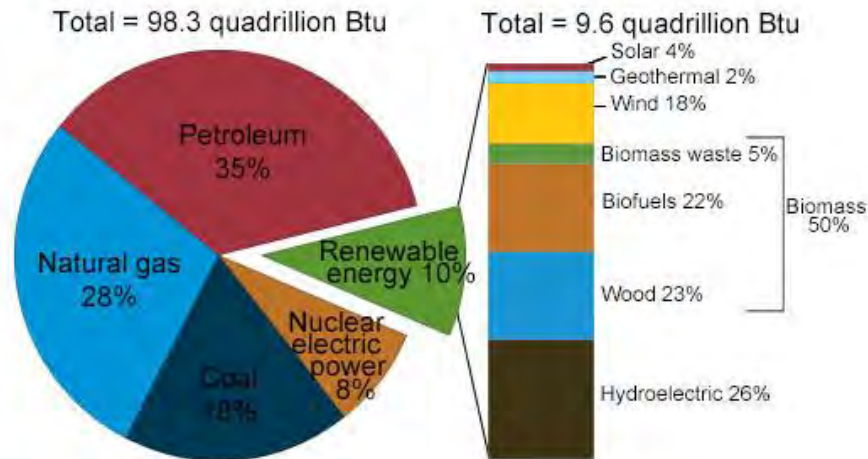


Figure I-2: U.S. energy consumption by energy source in 2014. Source: U.S. Energy Information Administration.(11)

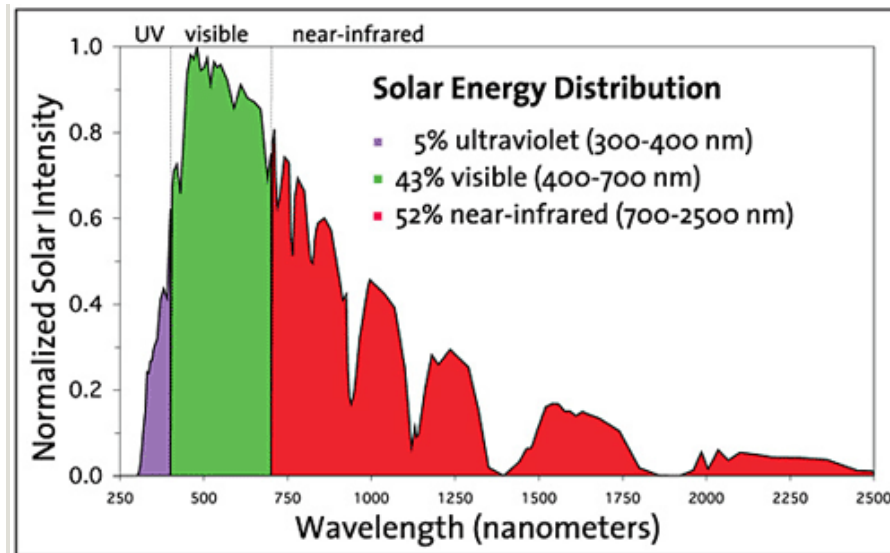


Figure I-3: The spectrum of solar radiation.(12)

II Organic photovoltaics

II. 1 Introduction

Organic photovoltaic cells (OPVs) which convert directly solar energy into electrical energy are considered as one of the most promising long-term and cost-effective solutions to meet the demand of clean and renewable energy source for our planet. OPVs therefore have attracted great concern in both science and industry.(3, 13-31) The common building block of an organic photovoltaic system consists of one or several photoactive organic materials sandwiched between an anode and a cathode. A randomized network of active materials

blending is often used as the organic photovoltaic system. It is named as a bulk heterojunction (BHJ). Figure I-4 depicts a BHJ-based organic photovoltaic device (OPV). The often used anode is indium tin oxide (ITO) coated on a glass substrate modified with an interfacial layer based on poly(ethylenedioxythiophene):poly(styrene sulfonic acid)(PEDOT:PSS) which offers good charge transport. The cathode is typically a low work function metal. The most frequently used cathode according to the literature is aluminum. Poly-(3-hexylthiophene) (P3HT) and [6,6]-phenyl-C61-butyric acid methyl ester (PCBM) blend is one of the most commonly used photoactive layer.(32) P3HT and PCBM are the most common electron donor and electron acceptor, respectively. The detailed photovoltaic process in organic photovoltaic cells will be given below (section II.2). There are mainly two kinds of organic materials for photovoltaic cells: polymers and small molecules. A common feature of both polymers and small molecules is that both of them are constituted of large π -conjugated systems.

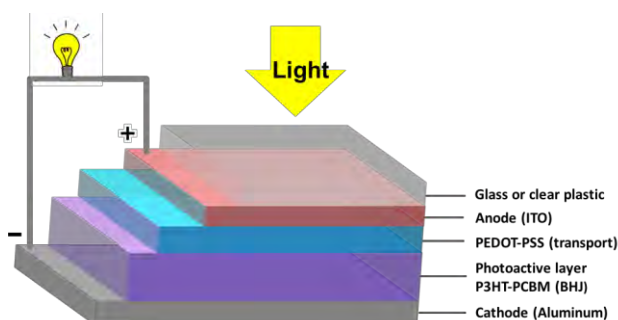


Figure I-4: Device architecture of a bulk heterojunction photovoltaic cell.

OPV cells have drawn more and more attention from both academic and industrial researchers, as evidenced by the evaluation of the numbers of articles concerning organic solar cells and published in international journals over the last three decades (see Figure I-5).

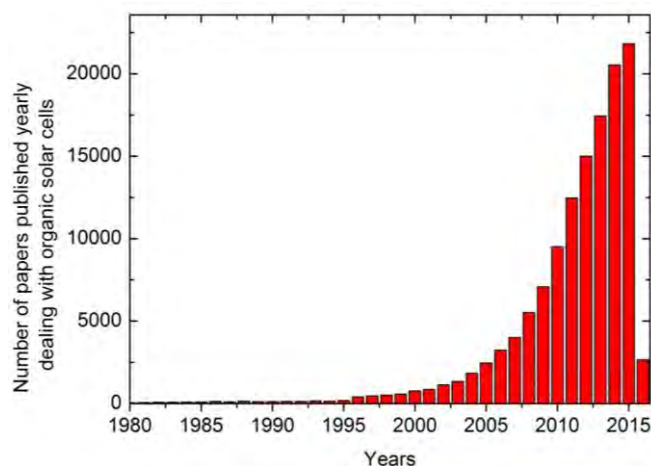


Figure I-5: Number of publications dealing with organic solar cells during the period of 1980-2016 (Source Scopus).

As shown in Figure I-5, a big rise occurred in the very beginning of the last ten years, and the interest in organic solar cells is steadily continuing and increasing. Figure I-6 shows the best research-cell efficiencies for a variety of photovoltaic technologies, with leading efficiencies for inorganic multijunction cells up to 46%, and with efficiencies of single crystalline and multicrystalline Si cells surpassing 27% and 25%, respectively. Although these high efficiencies are appealing and promising, they are not the only standard for evaluating the potential of these technologies. The overwhelming drawbacks of these inorganic photovoltaic technologies are their high production costs owing to the amount of materials needed for these devices and vacuum processing demanded for production, as well their high fabrication costs.(32) Besides, inorganic silicon solar cells are expensive, rigid, heavy, and complicated to produce. Organic photovoltaic cells based on π -conjugated small molecules and polymers

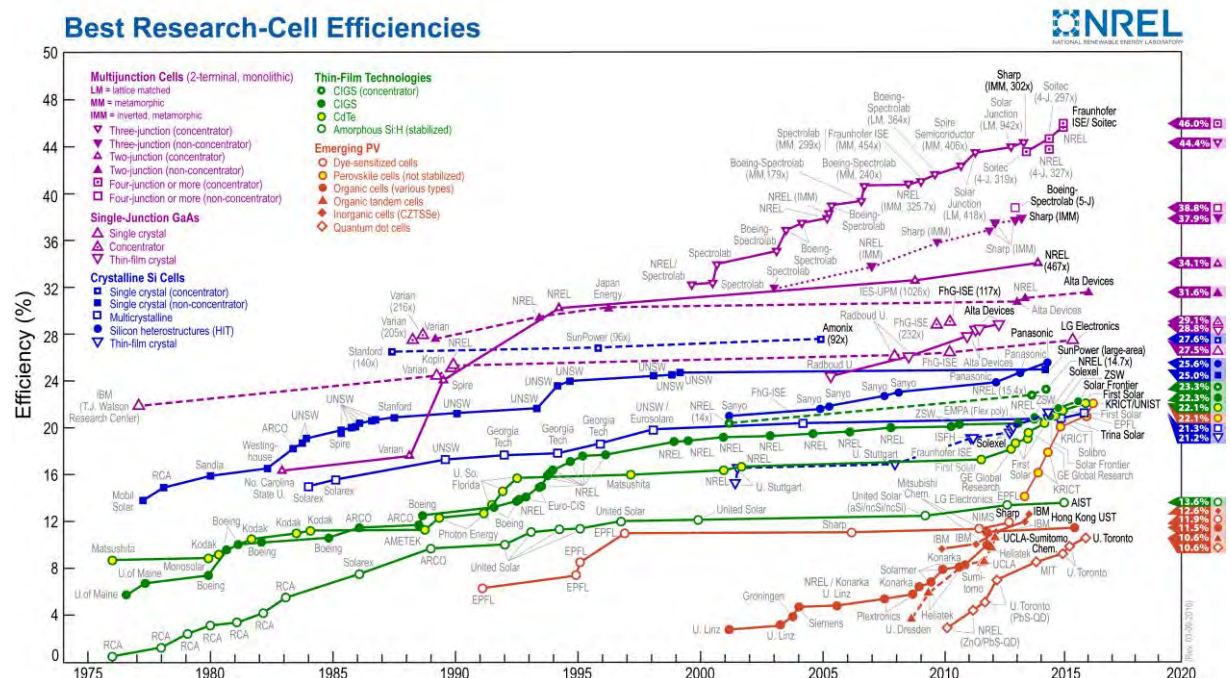


Figure I-6: The latest chart on record cell efficiencies, provided by The National Center for Photovoltaics (NCPV) at National Renewable Energy Laboratory (NREL).(33) Progress in photovoltaic power conversion efficiencies is tracked six monthly by Green et al.(34)

are part of an emerging photovoltaic technology with best power conversion efficiencies (PCEs) for both triple-junction (25) and single-junction achieving 11.5% (21), with appealing properties such as low cost, light weight, flexibility, transparency, solution processability, printability, portability and large-area fabrication compatibility.(4, 14, 19, 20, 24, 26-28, 35-50) The photovoltaic effect, namely, the transform of light into electricity, can be tracked to the pioneering studies of Becquerel in liquid electrolytes in 1839 (51) and has been investigated for a wide range of materials. It took quite a long time before the first report by

Chapin *et al.* in 1954 (52) on a silicon-based single p-n junction device with an efficiency of 6%. Almost 30 years after, Tang *et al.*(1) developed a two-layer organic photovoltaic cell and reported the first thin-film OPV cell affording a power conversion efficiency of about 1% in 1986. Hereafter, organic photovoltaics have become one of the state-of-the-art issues in science, as illustrated by the blooming and fruitful publication numbers shown in Figure I-5. The OPV performances have been improved steadily to power conversion efficiencies over 11% (see Figure I-6).(21, 25) In addition, the considerable contribution from world-wide industries such as Solarmer (USA), Heliatek (Germany) and so on, has so far leaded OPV to a new record power conversion efficiency of 13.2% set by Heliatek R&D teams (6) on 8 February, 2016.

Organic photovoltaic cells belong to a significant emerging technology in the modern era. It could facilitate the ever broader use of solar energy in coming years, wherever clean, renewable energy is needed, not only for industries such as building and construction materials, but also automotive, light architectural structures and flexible devices.

II. 2 Functional principle of organic photovoltaic cells

Contemporary organic photovoltaic cells are often based on a heterojunction made of two materials: an electron donor (D) and an electron acceptor (A). In the molecular case, the basic energy level diagram used to describe the operating principle of an OPV cell is shown in Figure I-7. The molecular energy levels involved in the light conversion into electricity are the highest occupied molecular orbital (HOMO) and the lowest unoccupied molecular orbital (LUMO), respectively. The ionization potential (IP) is the energy needed to remove an electron from a neutral molecule, and is related to the HOMO energy level. The fundamental gap, E_{fund} or HOMO-LUMO energy gap is defined as the difference between IP and the electron affinity (EA).(53) The EA is the amount of energy released when an electron is added to a neutral molecule. EA is used to estimate the electron-withdrawing ability of a molecule to act as an electron-acceptor in an OPV device, and is thus linked to the LUMO energy level relative to vacuum.

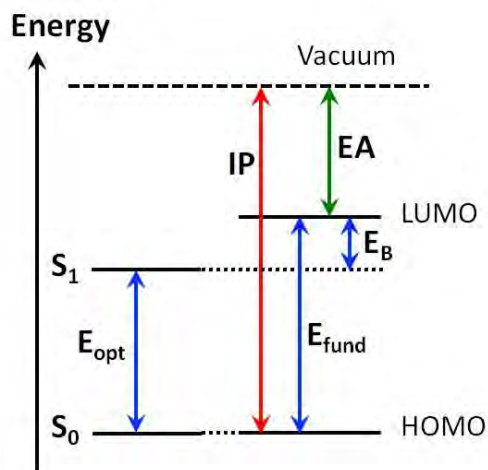


Figure I-7: Basic energy level diagram and illustration of energy gap in molecular case of an organic semiconductor.(53)

S_0 indicates the (singlet) electronic ground state and S_1 denotes the lowest (singlet) excited state (here considered to be available *via* one-photon absorption). The energy difference between S_1 and S_0 is called the optical gap (E_{opt} (eV)), given by the equation:(54)

$$E = hc / \lambda \quad (1)$$

Where h is Planck's constant (6.626×10^{-34} J·s) and c is the speed of light (2.998×10^8 m·s⁻¹), and $hc = 1240$ eV·nm, thus

$$E \text{ (eV)} = 1240 / \lambda \text{ (nm)} \quad (2)$$

E_{opt} is generally lower than the E_{fund} , which is ascribed to the electrostatic bound between electron and hole in the excited state contrary to the ionized state. The exciton (or electron-hole pair) binding energy E_B is the difference between fundamental gap and the optical gap, given by Figure I-7:

$$E_B = E_{fund} - E_{opt} \quad (3)$$

In the material case, the molecular energy levels are broadened into electronic bands. The upper occupied band is referred to as the valence band and the lower unoccupied band is referred to as the conduction band. The material band gap is defined as the energy difference between the top of the valence band and the bottom of the conduction band.

As simply described in Figure I-8, the photovoltaic effect of converting sunlight into electricity in an organic photovoltaic cell can be summarized as the following four steps:(27, 55) (i) Photon absorption and excitons generation; (ii) excitons diffusion to the D/A interface; (iii) excitons dissociation into free charge carriers (electrons and holes), and (iv) charge transport and charge collection at the electrodes, which produces current in the external circuit.

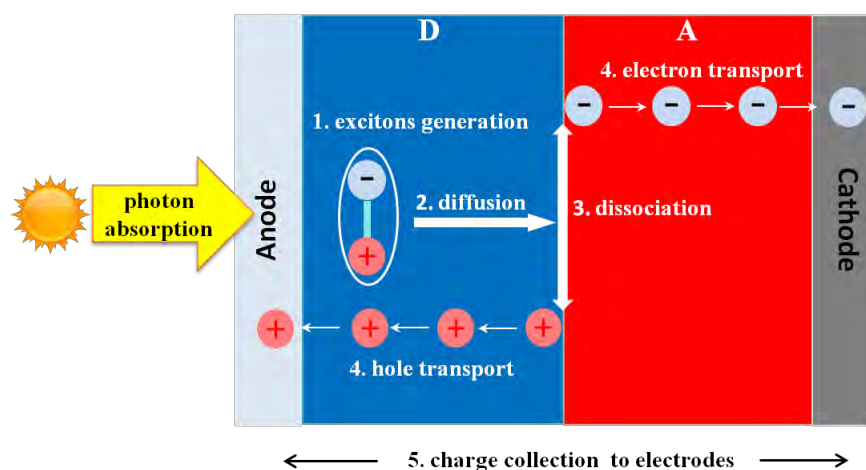


Figure I-8: Functional principle of a D/A solar cell.

II. 2-1 Photon absorption and excitons generation

For efficient photon absorption, the absorption spectrum of the photoactive layer should match the solar spectrum and the layer should be adequately thick to absorb the maximum of the incident solar light. Due to the relatively large band gap in organic materials, only a small portion of the sunlight is absorbed (see Figure I-9(up)). For example, the conjugated polymers MDMO-PPV and P3HT (two of the most commonly used donor polymers) show poor absorption in the red and NIR part of the solar spectrum, and PCBM (the most widely used acceptor polymer) shows a low extinction coefficient at visible and near-IR wavelengths, thus, the polymer donor is the dominant light-absorbing component in a photovoltaic blend. The chemical structures of these commonly used materials are provided in Figure I-9(down). The band gap, evaluated from the onset of the absorption band, are of 580 nm and 660 nm (*i.e.* 2.13 eV and 1.88 eV) for MDMO-PPV and P3HT, respectively.(37) A material presenting a band gap of 1.1 eV (1100 nm, $E_{\text{opt}} \text{ (eV)} = 1240 / \lambda \text{ (nm)}$) is able to absorb 77% of the solar emission on the Earth surface, while the band gap of most of the semiconducting polymers is larger than 2 eV (620 nm) which restricts the possible harvest of solar photons to around 30%.(14, 37, 55) Thus, it is possible to harvest more sunlight and as a result, an increase in the photocurrent can be prospected by lowering the band gap of organic semiconductors. In addition, since the absorption coefficients of organic materials are as high as 10^5 cm^{-1} (see Figure I-9(up)), a thickness of active layer of only 100 nm is sufficient to absorb most of the incident photons.(55) Increasing the layer thickness might hamper charge transport and therefore lower the fill factor (see II-3.2), though it is often favorable to light absorption.

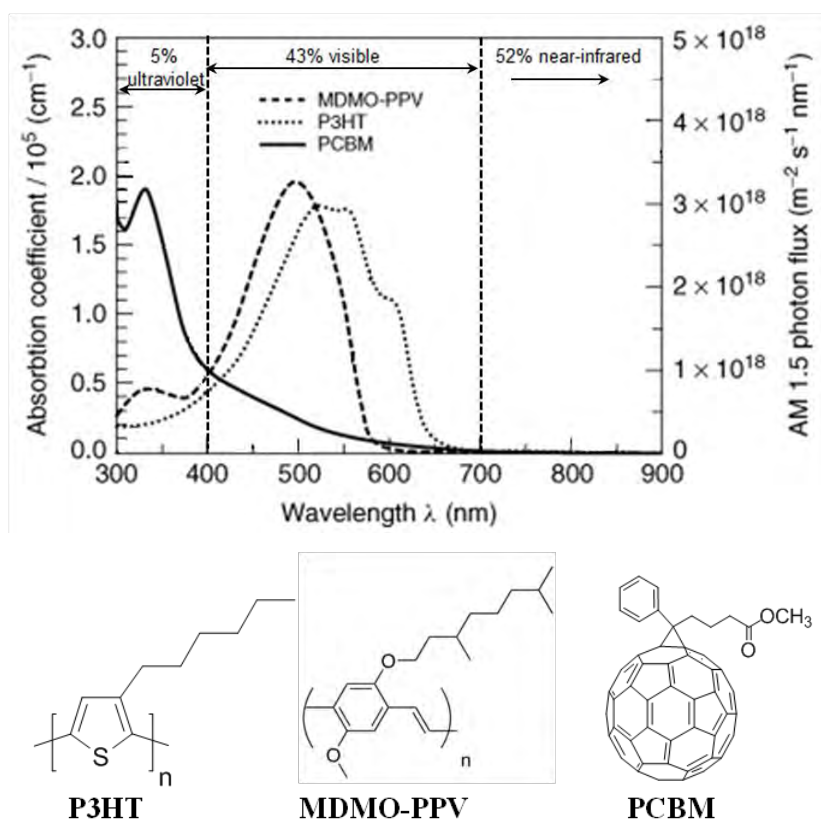


Figure I-9: Absorption coefficients of films of commonly used materials are depicted in comparison with the standard AM 1.5 terrestrial solar spectrum (up)(according to Ref.(56)), and the structures of the materials (down).

Unlike what happens in inorganic semiconductors, and owing to the low dielectric constant of organic materials, the photon absorption at room temperature in organic materials results in coulombically bound neutral electron-hole pairs (excitons), rather than free charge carriers. The exciton binding energy is in the range of 0.35 - 0.5 eV.(57) That is the reason why an electron donor/electron acceptor interface is needed in OPV devices to provide a driving force for the dissociations of excitons and the generation of free charge carriers.

II. 2-2 Diffusion and dissociation of excitons

For achievement of high power conversion in OPV, the maximum of excitons generated due to light absorption should give rise to the formation of free charge carriers (electron and hole). It is shown that only 10% of the incident photons result in free charge carriers generation in conjugated polymers.(58) One of the reasons for this low percentage is the low exciton lifetime (10 to 400 ps).(59) As a consequence, the order of magnitude of exciton diffusion length should be the same as the size of the photoactive domain, which limits the component thickness.(60) Otherwise, excitons decay via luminescence or non-radiative recombination to

the ground state, which is in competition with exciton diffusion before reaching the interface. Generally, exciton diffusion lengths in organic semiconductors are of about 10-20 nm.(55)

Charge dissociation is one of the subsequent key steps for sunlight conversion into electricity. In this step, the exciton is split in free charge carriers, the electron is transferred to the electron acceptor material and the hole to the electron donor material. Blending conjugated electron-donor polymers with electron-withdrawing materials such as the commonly used fullerene derivatives is a quite effective method for forming a charge transfer state (CTS). The CTS can be regarded as a state in which charge carriers are coulombically bound across the D/A interface. It is possible to promote charge dissociation from CTS when the energy offset (ΔE) between the LUMO of donor and the LUMO of acceptor is larger than the exciton binding energy. The minimum offset required for charge separation is approximately 0.3 eV.(61-63) Then the photoinduced charges can migrate to their corresponding electrodes. Therefore, the effect of charge recombination processes should be reduced or avoided as much as possible.

II. 2-3 Transport of charge carriers and charge collection

For efficient photovoltaic cells, the separated charges are required to be transported to the suitable electrodes within their lifetime which is estimated to be the order of magnitude of a few μs at 295 K.(64) The dominant driving force is the internal electric field created by the equalization of the Fermi energy levels of the two electrodes. Under the influence of the electric field, the charges remain separated (and thus no recombination after exciton dissociation) and migrate to the organic layers.(62) Thus, the work functions of the electrodes (or of the charge transport layers) are determinant and require a careful choice of the electrode metals (and the interface layers). In addition, transport of charge carriers is strongly affected by charge recombination during the charge transport to the electrodes, especially if the transport medium for both holes and electrons is the same material.(60) Therefore, charge carries recombination process should adequately slow down to let charge carriers reach the electrodes. Thus, the charge carrier mobilities (strongly dependent on the molecular organization of the material) through the active layer are determinant and require careful control on the active layer morphology. An important objective for OPV cells is to minimize the energy and charge loss processes for the purpose of improving the device efficiencies.

As the last step, charge carriers are collected from the device *via* two selective contacts (see Figure I-4). Usually, an indium tin oxide (ITO) due to its large optical transparency and high

conductivity serves as the anode on one side, matching the HOMO levels of donor.(65) A low work function metal serves as the cathode on the other side of the device. The most often used cathode is evaporated aluminum which possesses a work function of around 4.3 eV,(66) matching the LUMO of acceptor PCBM.

II. 3 Characterization of OPV performance

II. 3-1 Test conditions for OPV - standard solar spectra

Various solar spectra conditions based on different spectral distributions are used for photovoltaic characterization, thus it is important to have a standard reference spectra in order to allow the reproducibility of characterization and comparison of photovoltaic devices from different research laboratories and manufacturers. The standard spectrum outside the Earth's atmosphere that is typically used for power applications of solar cells in space is **AM0** (in red on Figure I-10), which has an overall power of 1366.1 W/m². Herein Air Mass (**AM**) means the proportion of atmosphere that the sunlight must travel through before striking at the Earth's surface (or sea level) relative to its overhead path length, as shown in Figure I-11, and **AM** is equal to Y/X, namely, $AM = 1/\cos(\theta)$ (where θ is the angle from the vertical, zenith angle). **AM1** refers to the spectrum after passing through the atmosphere (perfectly clear and cloudless sky) at the Earth's surface when the sun is directly overhead ($\theta = 0^\circ$). **AM2** corresponds to a solar zenith angle of $\theta = 60^\circ$ which is useful to predict wintertime performance of cells in temperate latitudes.

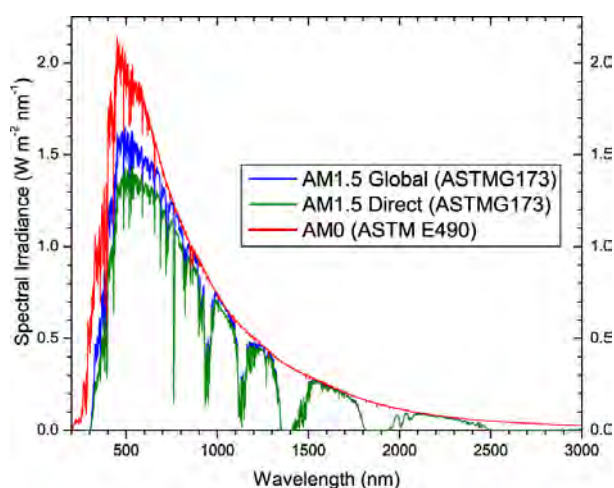


Figure I-10: Standard Solar Spectra for space and terrestrial use. (Source: pveducation)

The standard solar spectrum at the Earth's surface is named **AM1.5G** (67)(the G represents global and includes both direct and diffuse radiation, in blue on Figure I-10) or **AM1.5D** (the D means direct and which involves direct radiation only, in green on Figure I-10), where Air mass 1.5 (**AM1.5**, 1.5 times thickness of Earth's atmosphere normal to Earth's surface)

corresponds to a solar zenith angle of $\theta = 48.2^\circ$ (see Figure I-10). Photovoltaic cells are usually tested at a temperature of 298K (25°C) under **AM1.5G** condition, simulating the 48.2°C irradiation from the sunlight to the ground. Under this condition, the incident power per unit area of the incident light is 1000 W/m² (100 mW/cm²).

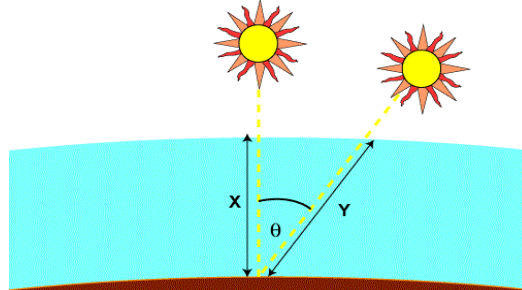


Figure I-11: Scheme of the sunlight path length, in units of Air Mass and dependent on the angle from the vertical (zenith angle θ). (Source: pveducation)

II. 3-2 Important parameters for OPV efficiency

The performance of OPVs is principally characterized by the power conversion efficiency.⁽¹³⁾ There are three important photovoltaic parameters for evaluating photovoltaic performance: the open-circuit voltage (V_{oc}), the short-circuit (photo) current density (J_{sc}), and the fill factor (FF). A typical current density *versus* voltage curve for a typical bulk heterojunction OPV device (see architecture provided in Figure I-4) in the dark and under illumination is illustrated in Figure I-12. All photovoltaic cells are photo diodes, which are able to create current or voltage from incident light when processing in reverse bias (where the voltage at the cathode is lower than at the anode). In the dark, as the orange dashed line showed in the current density *versus* voltage (J-V) curve, there is nearly no current flow until forward bias larger than the open circuit voltage are injected. When under illumination, as evidenced by the shift (blue solid line) in J-V curve, power is generated by the device.

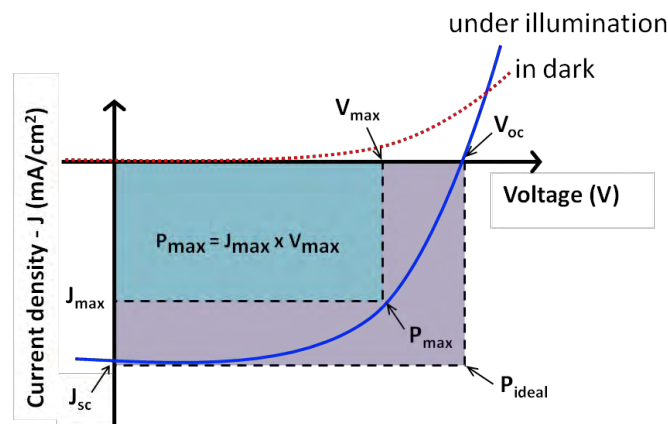


Figure I-12: Current density *versus* voltage schematic diagram of organic solar cells in the dark and under illumination.

(a) Short-circuit (photo) current density (J_{sc})

The short-circuit current density, J_{sc} , corresponds to the maximum current delivered under lighting by a solar cell and is measured when no voltage is applied to the device. J_{sc} is mainly determined by factors associated with each of the four steps described above. A broad absorption spectrum is favorable to harvest as much as possible of the photons from the solar light and would increase the J_{sc} value. For a given absorption outline of a given material, the bottleneck of charge carriers is the charge mobility which is sensitive to the nanoscale morphology of the organic semiconducting-material thin film.(68-72)

(b) Open-circuit voltage (V_{oc})

The open circuit voltage, V_{oc} , represents the maximum voltage obtainable from a solar cell, and is measured when the current equals to zero. Experimentally, the HOMO and LUMO energy levels can be evaluated from the oxidation potential of the donor and reduction potential of the acceptor *via* electrochemical characterization. In organic photovoltaic cells, it has been reported that the V_{oc} value is not exactly determined by the energy difference between the HOMO of the donor material and the LUMO of the acceptor at the interface.(73, 74) Its value also depends on that of the binding energy of the excitons.

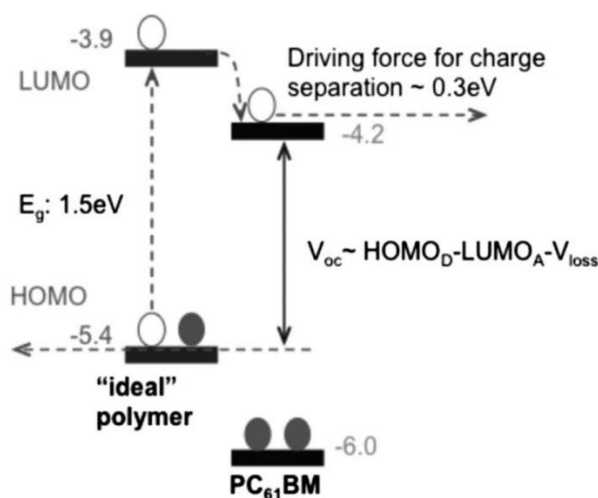


Figure I-13: Schematic energy level diagram between an ideal polymer and a PC₆₁BM acceptor.(63)

The V_{oc} of a conjugated polymer-PCBM photovoltaic cell (see Figure I-13) can be estimated by the Scharber model given the empirical equation:(61)

$$V_{oc} = 1/e (| E^{\text{D}_{\text{HOMO}}} - E^{\text{A}_{\text{LUMO}}} |) - 0.3 \text{ V} \quad (4)$$

Where e is the elementary charge, and the value of 0.3 V is an empirical factor. 0.3 V is found to be the deviations between the theoretical biggest built-in potential (V_{BI}) and the V_{oc} .(61) It is necessary that the electron acceptor material has a conduction band edge that is lower than

that of the electron donor material.(56, 75-77) A minimum energy offset between the LUMO level of the polymer donor and the PCBM acceptor of approximately 0.3 eV has been demonstrated necessary to achieve efficient electron transfer from the LUMO of polymer donor to the LUMO of PCBM acceptor.(61, 62, 78)

According to equation (4), to offer a high V_{oc} , HOMO energy level of the donor can be decreased or LUMO energy level of the acceptor can be increased. However, such changes could simultaneously result in wider band gap and narrower absorption width, which means lower efficiency of photon absorption from the solar spectrum. Meanwhile, the LUMOs offset shown in Figure I-13 in BHJ should be larger than 0.3 eV.

In the Scharber model, the only inputs required are the HOMO and LUMO energy levels. The generated PCE values in the Scharber model should be understood as the potential performance that may be reached, if the assumptions can be met. These assumptions combine various additional conditions that have to be met to achieve a high-performance candidate, especially requirements associated with complicated optimization and control of BHJ active-layer morphology, interface behavior, and the dynamics of exciton and charge carriers. The standard parameters that reflect the assumptions in the Scharber model include a uniform external quantum efficiency of 65%, a fill factor (FF) of 0.65, a required LUMO offset of 0.3 eV between donor and acceptor for efficient charge separation, and an empirical loss parameter of 0.3 eV. However, there is no certainty that the top candidates will truly perform as well as expected, because their performances may be affected by various factors, such as morphology control, interface layer and device fabrication. It is indicated that the theoretical efficiency limit in the standard Scharber model is 11.1%, which requires energy levels of LUMO and HOMO of the ideal donor have to be -3.9 eV and -5.4 eV ($E_g = 1.5$ eV) respectively as the optimal parameter combination.

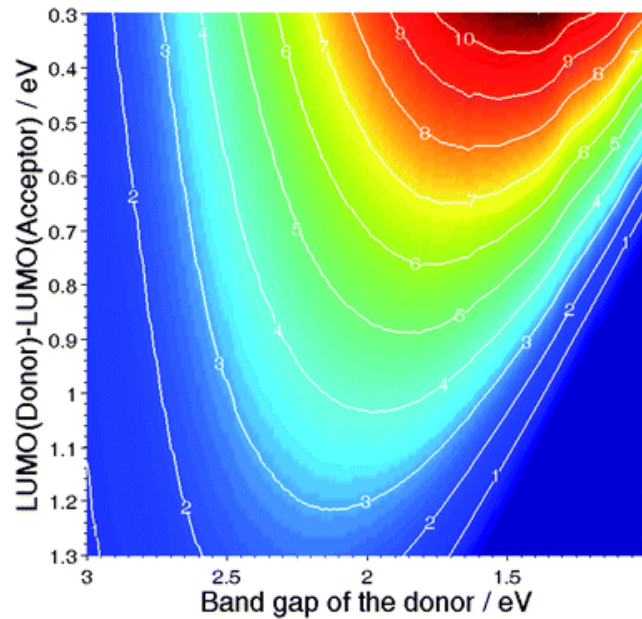


Figure I-14: Efficiency of a D/A OPV cell vs the band gap energy of the donor, and the LUMO offset between the two materials.(79)

Figure I-14 provides the efficiency of a D/A OPV cell *versus* the band gap energy of the donor and the offset between the LUMO of the donor and the LUMO of the acceptor, with the assumption that V_{oc} obeys equation (4).(61) It is of great interest that the efficiency of the device keeps consistent with the LUMO offset (ΔE), precisely, the lower the offset, the higher the efficiency. Figure I-14 suggests that the photovoltaic efficiency of a BHJ solar cell should be more sensitive to variations of the LUMO offset compared to changes of the band gap of the donor. As a result, we can conclude that the choice of the D/A couple is as significant as the band gap of the donor material.

(c) Fill factor (FF)

The Fill factor (FF) is a parameter that is associated with V_{oc} and J_{sc} , and evaluates the maximum portion of electric power that can be extracted from a photovoltaic cell. The FF can be given by the ratio of the electric power between the blue and purple areas the J-V curve (see Figure I-12), and defined by equation:

$$FF = P_{max} / (J_{sc} \times V_{oc}) = (J_{max} \times V_{max}) / (J_{sc} \times V_{oc}) \quad (5)$$

Where J_{max} is the current density and the voltage at the maximum or ideal power point, and V_{max} is the voltage at the maximum or ideal power point. The FF provides a sign of how possibly charges can be extracted from a cell and is usually described as the “squareness” of the J-V curve, and will have a value of unity in an ideal case that corresponds to output power of P_{ideal} . Alan J. Heeger (27) suggested that the FF in BHJ solar cells is affected by the

competition between charge carriers sweep-out by the internal voltage (built in electric field) and the loss of charge carriers by recombination. It is also indicated that the series and shunt resistances are two essential factors that affect the fill factor of a solar cell.(32, 56, 80) Besides, morphology is also of high influence on FF.(81)

II. 3-3 Power conversion efficiency (PCE)

As mentioned previously, the performances of terrestrial solar cells are measured under AM1.5G conditions with incident power of 100 mW/cm² and at a temperature of 25°C. Power conversion efficiency (*PCE*) suggests the percentage of incident optical power that converts into electricity, and is defined as the ratio of output energy from a PV device to input energy from the solar spectrum. It is the most important and commonly used metric to determine the performance of a solar cell and compare it to the others. As sketched in the J-V curve, the maximum power point (P_{max}) is localized on the J-V curve where the product of the current density and voltage is the highest.(56) To determine the efficiency of a solar cell, the output power requires to be compared to the input power, as indicated below:

$$PCE = P_{max} / P_{in} = (J_{max} \times V_{max}) / P_{in} \quad (6)$$

According to equation (6), the maximum power created in the external circuit is the product of the fill factor, open circuit voltage and short-circuit current density. Consequently, the power conversion efficiency can be described as:(4)

$$PCE = (FF \times J_{sc} \times V_{oc}) / P_{in} \quad (7)$$

Where P_{in} represents the total power density of the incident light source. Therefore, the power conversion efficiency is mainly dependent on the three parameters: the open circuit voltage (V_{oc}), the fill factor (FF), and the short-circuit current density (J_{sc}).

Furthermore, it is worth mentioning that external quantum efficiency (EQE) is a means for estimating the portion of current that can be generated by a special wavelength of light. It is defined as the number of charge carriers divided by the total number of incident photons. It shows the potential that one absorbed photon will lead to the generation of one electron that can flow through an external field. EQE indicates the overall efficiency of the four principle steps in the photovoltaic process, as given by equation (8):

$$EQE(\lambda) = \eta_A(\lambda) \times \eta_{ED}(\lambda) \times \eta_{CT}(\lambda) \times \eta_{CC}(\lambda) \quad (8)$$

Here, η_A is the photon absorption efficiency, the exciton diffusion efficiency η_{ED} is the portion of photoinduced excitons that reaches the D/A interface prior to recombination. η_{CT} is the charge transfer efficiency, and the charge collection efficiency η_{CC} is the potential that a free

charge carrier originated from excitons dissociation at the D/A interface reaches its respective electrodes, and λ is the wavelength of interest.(32, 82) It shows the closer of the EQE value to 1, the more efficient of current generation at a certain wavelength, with limited recombination loss. Clearly, decreasing recombination loss will offer higher EQE values.

II. 4 Types of OPV and their architectures

D/A heterojunction devices can be divided into two principal types of architectures: bilayer (or planar) heterojunction (1) and bulk heterojunction (BHJ) that was first reported in 1995(29, 35, 83).

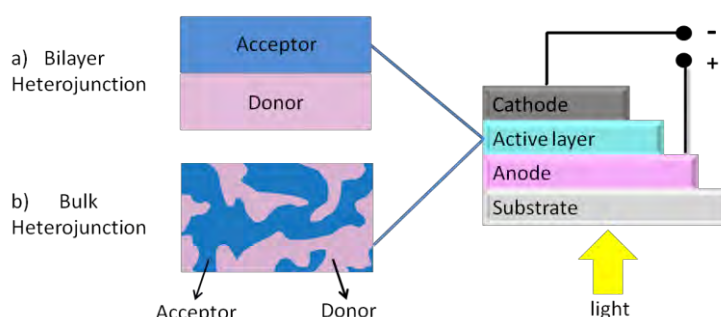


Figure I-15: The architecture structure of (a) bilayer heterojunction and (b) BHJ OPV devices.(84)

II. 4-1 Bilayer heterojunction

In a bilayer heterojunction device, donor and acceptor materials are stacked sequentially with a planar interface as displayed in Figure I-15a. The photoactive layer is sandwiched between a high work function anode matching the HOMO of donor and a relatively low work function metal cathode matching the LUMO of acceptor, for efficient collection of the corresponding charge carriers. Figure I-16 shows the schematic energy level diagram of an OPV, revealing the anode and cathode work functions. Generally, a transparent indium tin oxide (ITO) (presenting a work function of -4.7 eV) and aluminum (presenting a work function of -4.3 eV) are the most commonly used anode and cathode, respectively.(85) Generally, bilayer heterojunction devices are achieved by vacuum deposition due to the difficulty to find proper solvents for donor and acceptor layers without damaging the D/A interface.(84)

The first reported thin-film organic photovoltaic cells was a donor/acceptor (D/A) heterojunction cell, which gave a power conversion efficiency of approaching 1%.(1) This first report paved the way towards higher power conversion efficiencies reached thanks to the development of enhanced active materials. The performance of bilayer based organic

photovoltaics is hampered by the short exciton diffusion length (5-20 nm) in organic materials,(55, 86) because the optimal thickness of the photoactive layer in planar architecture is related to the exciton diffusion length. Therefore the optimal percentage of the incident light that the device can absorb and transform into electrical power is limited.

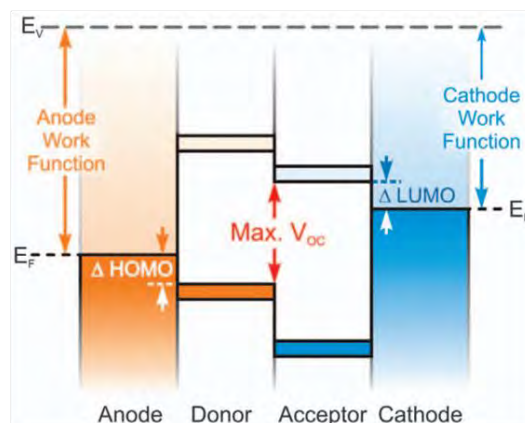


Figure I-16: Schematic energy level diagram of an OPV, revealing the anode and cathode work functions, the HOMO and LUMO offsets (ΔHOMO and ΔLUMO , respectively) and the maximum open-circuit voltage (V_{oc}).(87)

The bilayer architecture is one of the most common types of OPV, but it causes efficiency loss not only due to excitons created too far away from the D/A interface, but also because of the low D/A interfacial area. One big advantage of bilayer heterojunction over single layer(56) is that holes and electrons can be effectively separated to reduce efficiency loss due to charge recombination after the excitons dissociation. But, it also constitutes a limit for high conversion efficiency, because the bilayer structures are primarily limited by the exciton diffusion length.(32)

II. 4-2 Bulk heterojunction

Due to the limitation of bilayer heterojunction, further evolution was achieved in polymer devices by means of blends of the electron-rich and electron-deficient materials (2, 35). Different from bilayer heterojunction device, the active layer is blend of bicontinuous and interpenetrating donor and acceptor materials in a bulk heterojunction (BHJ) device. The BHJ concept was created by Yu *et al.*(35) and Halls *et al.*(5) in 1995, which is one of the state-of-the-art device architectures for OPV so far. BHJ is resulted from phase separation in a 5-20 nm length scale of the donor and acceptor materials during spin-coating and solvent evaporation. It overcomes the exciton diffusion bottleneck (55, 86) by producing an intricate interpenetrating network (Figure I-15b), and also provides charge transport paths to facilitate the charge collection at electrodes for achieving photoelectric conversion. A typical BHJ solar cell,(28) as the architecture outlined in Figure I-15b. As for the bilayer case, the active layer is

sandwiched between anode and cathode. Holes and electrons are transported to anode and cathode respectively in a standard architecture. As indicated in the schematic energy level diagram of an OPV (see Figure I-16), the anode typically includes a high work function transparent conducting electrode that is coated with a conducting substrate, and adjusted with an interfacial layer favorable to hole selection and/or electron blocking. The most commonly selected materials used as anode are indium tin oxide (ITO) (presenting a work function of ~ 4.7 eV) on glass substrates adjusted with a interfacial layer about 40nm thick based on poly(ethylenedioxythiophene):poly(styrene sulfonic acid)(PEDOT:PSS).(88) These materials are preferable because of their great optical transparency and good charge transport. A low work function metal with an electron selective layer is often selected as the cathode (as revealed in the schematic energy level diagram). The most commonly encountered cathode is aluminum not only due to its low work function value but also high reflectivity.

Bulk heterojunction can be fabricated *via* vacuum deposition or solution processing techniques. Soluble materials can be deposited from solution *via* spin coating. Some of small molecules can be deposited under vacuum *via* thermal evaporation, for instance, thin films of DCV5T-Me: C₆₀ reported by Bäuerle *et al.*(89) was vacuum deposited in BHJ single layer. Active layers of metal phthalocyanine: C₆₀ and DCV6T: C₆₀ were vacuum processed in a tandem cell. Because vacuum deposition allows for good control of the layer thickness which is necessary for the optimization of the device stack with regard to optical interference effects.(90) Vacuum deposition for OPV devices in an efficient roll-to-roll-process developed by Heliatek is an innovative technology that meets pioneer spirit.(6) In addition, thermal annealing, as another method for the fabrication of bulk heterojunction device completed with a metal cathode, was used to improve the efficiency of polymer solar cells.(91) This effect was ascribed to polymer chain alignment, leading to an increase in the formation of an interfacial layer at the organic/cathode interface or the charge carrier mobility. Another effect of efficiency enhancement in BHJ cells was attributed to a confined geometry by using a metal contact during annealing, preventing the formation of a rough surface morphology while allowing for the formation of an interpenetrating donor–acceptor network.(82) Whereas solution-processed BHJ type architecture with a fullerene acceptor was first reported in 1995 by Yu *et al.*(35) and Halls *et al.*(5). Over the last decade, the solution-processed BHJ OPVs has shown dramatic improvement in power conversion efficiency from less than 1% in the earliest publications to 11.7% (21) in the very recent literature. The power conversion efficiency of OPV cells based on small molecules and polymers have improved steadily over

the past decade. Moreover, bulk-heterojunction OPVs based on small molecules (SM-BHJ) have become a competitive alternative to the more widely investigated counterparts based on conjugated polymers.(92) So far, the performance of both polymer-based BHJ (23, 25, 40, 93-100) and SM-BHJ (19, 85) are comparable, with power conversion efficiency over 10%.

BHJ is regarded as the state of the art active layer morphology so far, because the interfacial area between donor and acceptor phases in a bulk heterojunction is greatly improved. Therefore, compared to bilayer heterojunction, the bicontinuous, nanoscale and interpenetrating network formed in BHJ architecture leads to higher performance of the OPV devices.(56, 84, 101) The progress is mainly ascribed to the improvement of the D/A heterojunction (1, 102) that acts as a dissociation position for the coulombically bound photon generated excitons. However, due to the complicated nanomorphology, a D/A blend is hard to control and optimize the active layer morphology.(68)

II. 4-3 Tandem OPV cells

A class of OPV technology is “tandem cell” architecture (as shown in Figure I-17(left)),(47) which is based on a multilayer structure that comprises two or even more independent active layers in series. It reveals numerous advantages for further improvement, as reviewed by Christoph J. Brabec *et al.* in 2009(79) and by Yang Yang *et al.* in 2013(103). It is sufficient to realize the practical application of plastic photovoltaics in rooftop solar panel.

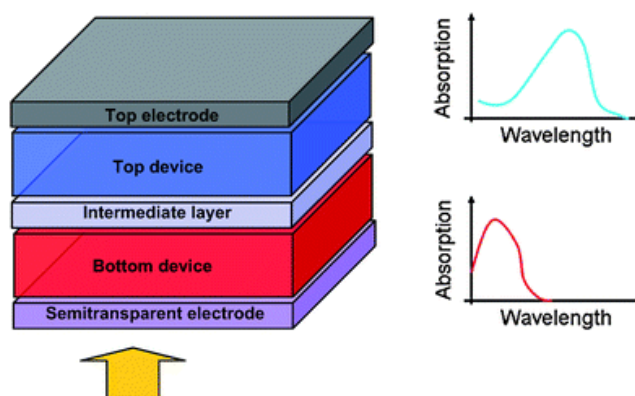


Figure I-17: Schematic architecture of an organic tandem solar cell including two sub-cells with different and complementary absorption spectra.(79)

A wide band-gap material for the first cell and a relatively lower band-gap semiconductor for the second charge-separation layer with are typically used in the tandem cells.(32, 47, 104) The tandem architecture allows to address two particular weakness originated from the inherent properties of π -conjugated organic materials.(105-109) To begin with, the

combination of two semiconductors with different band gaps enables a wide absorption over a wide range of solar emission spectrum due to the complementary absorption spectra from each layer (see Figure I-17(right)). The power conversion efficiency of the tandem cell is inherently higher than that of a single cell made from the narrower band-gap material, resulting from the higher energy of electron-hole pair generated by photons compared to that of the energy gap that rapidly relax to the band edges respectively. Moreover, owing to the low mobility of the charge carriers, an addition in the thickness of the active layer enhances the internal resistance of the device, as a consequence, both the V_{oc} and fill factor (FF) are improved.(110) Hence, the tandem cells are able to give a higher optical density over a broader fraction of the solar spectrum. In other words, the tandem cell structure is beneficial to the efficiency of light harvest. The organic tandem photovoltaic cells have showed the highest performance of a bulk heterojunction solar cell to date, achieving over 11%.(23, 25, 111) Specifically, a new record power conversion efficiency of 13.2% for a multi-junction device had been set by Heliatek on February 8, 2016.(6)

However, one major issue with tandem cells is that the total current of the cell is limited by the current generated in the front or back cell which is lowest. Therefore, to make full use of a tandem cell, the current generated in each sub-cell should match each other. Determining by the specific absorption and charge carrier mobilities of semiconducting materials, tandem cells generally use thicker back cell than the front cell so that the photocurrent created in each sub-cell are balanced.(47, 112) Due to the number of sub-cells and required precision of various processing steps, the scale up to roll-to-roll production in tandem cells is even a greater challenge.

II. 5 Organic semiconducting materials for OPVs

Generally, organic semiconductors have a wide band gap above 1.4 eV but less than 3 eV, materials with a band gap above 3 eV are considered as insulators. Organic semiconductors have been the focus of considerable research due to their intrinsic properties.(13, 113) The explored applications of organic semiconductors include organic light emitting diodes (OLED)(114-116), organic field effect transistors (OFET)(117-119), and organic photovoltaics (OPV)(13, 14, 36, 40, 60).

II. 5-1 Introduction of semi-conductor property and π -conjugation

The molecular structure of organic semiconductors consistently contains a π -conjugated backbone, along which the carbon or hetero atoms (nitrogen, oxygen and sulfur) are sp^2p_z -

hybridized. The first classic example of a semiconducting polymer is polyacetylene (containing alternating single and double bonds, the structure and π orbital are showed in Figure I-18), which was studied in 1977 (120) by Hideko Shirakawa, Alan Heeger and Alan MacDiarmid who has been honored with the Nobel Prize in 2000 for their discovery and development of conductive polymers (121, 122). The π conjugation (overlap) along the backbone leads to the formation of π orbital delocalization, relating to the molecular frontier orbitals (HOMO and LUMO) and determining the electronic and optical properties of the molecules or polymers.

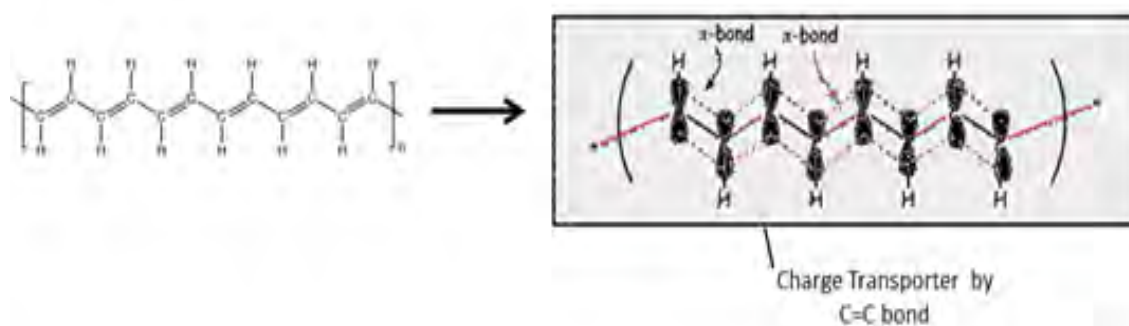


Figure I-18: *trans*-polyacetylene and its schematic π orbital.

As sketched in Figure I-19, the frontier energy levels changes with the increase in the conjugation length in polyacetylene, which results in narrowing the band gap. The overlap of frontier π molecular orbitals between neighboring molecules or polymer main chains represents the strength of the intermolecular interactions (electronic coupling), which plays a key role in governing charge carrier mobilities. Different from crystalline inorganic semiconductors, which have a large charge carrier mobility owing to their three dimensional feature and rigid lattice, organic semiconductors generate more modest charge carrier mobilities because of formation of polarons (hole and electron) and localization of charge carrier. For organic semiconductors, the charge carrier mobilities strongly rely on the morphology, for instance, the charge carrier mobilities of highly disordered amorphous films (normally 10^{-6} to 10^{-3} $\text{cm}^2 \text{V}^{-1} \text{S}^{-1}$) can be enhanced over several orders of magnitude when making them highly ordered crystalline (over $1 \text{cm}^2 \text{V}^{-1} \text{S}^{-1}$). (123)

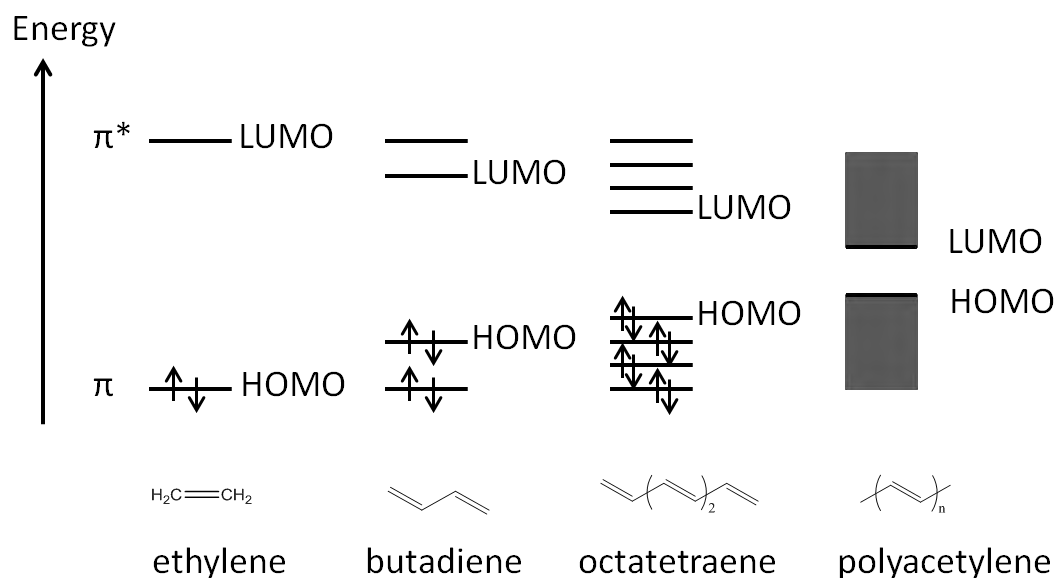


Figure I-19: Illustration of energy banding mechanism with increase in the conjugation length of the ethylene in polyacetylene.

II. 5-2 Optical properties of semiconducting polymers

Normally, the sp^2p_z hybridized wave functions of the carbon atoms in repeat unit causes the π -conjugated electronic structure of polymers.^(26, 121, 122, 124) As a schematic band diagram shown in Figure I-20(left), semiconducting polymers are depicted in aspects of the energy bands including the orthogonal π -bands that generated by the p_z wave functions and the bonding and anti-bonding σ -bands between neighboring carbon atoms. As provided in Figure I-20(right), the absorption of photons results in the migration of electrons from the valence band (π -band) to the conduction band (π^* -band). As a result, mobile electrons and holes, which are responsible for the photoelectric conversion, are generated. The electrons and holes generated on a single chain relax fast to the respective band edges and, accordingly, either form neutral intrachain excitons or recombine when at energy $h\nu > E_g$. If the electrons and holes are on isolated chains, polarons will be formed due to their self-localization.^(121, 122, 124) The π - π^* interchain stacking is a key parameter for the wave function of excitons spread onto the adjacent chains (interchain transfer of excitons). The intrachain excitons can migrate, separate to produce polaron pairs on adjacent chains, go through intersystem crossing to the triplet state, or radiatively and non-radiatively decay to ground state.

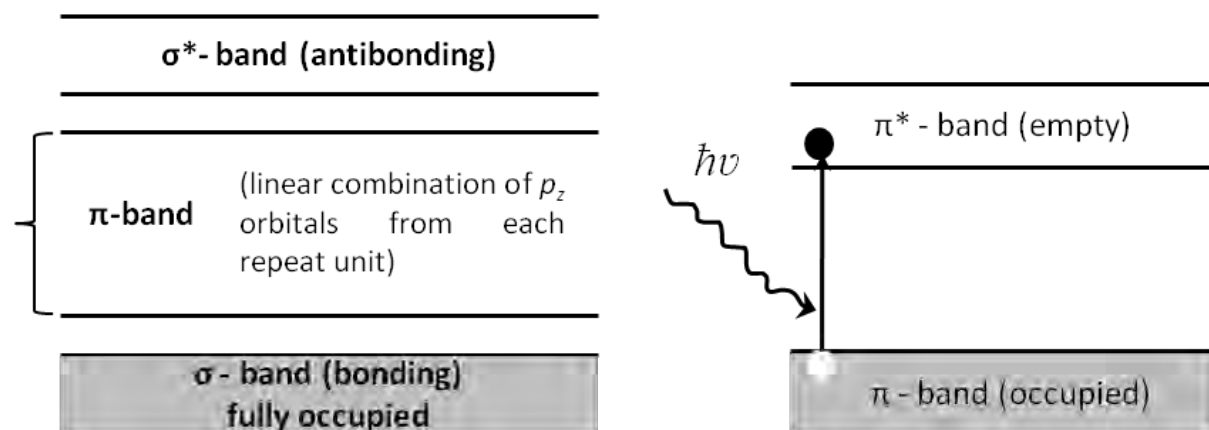


Figure I-20: Schematic band diagram for π -conjugated polymers (left) and π - π^* interband transition associated with generation of a mobile electron and a mobile hole in the π^* -band and π -band respectively (right).(26)

II. 5-3 Charge transport mechanism in conjugated polymers

The morphology of polymeric materials plays a significant role in charge transport. It is worth noting that the mechanism of charge transport process in polymers is quite complex. Band transport and hopping are the main mechanisms of charge transport in conjugated polymers.(125) Band transport, often called intrachain transport, can be considered as exclusively for intrachain motion, which is the mechanism that should be conceived when considering conjugation. Hopping can be considered for both intrachain and interchain transport.(125) Here, hopping is a process by which charge carriers jump from one monomer or chain to another instead of transport coherently, which is considered to be very important in devoting to the charge carrier mobility. It is possible that a mix of band transport and hopping occurs in conjugated polymers (see Figure I-21b). It should also be noted that hopping can exhibit intrachain transport, as sketched in Figure I-21a. A defect or kink in a conjugated polymer will create the chance for charge to travel from one part of a chain to another without moving along the chain. Similarly, some non-conjugated materials show good semiconducting behavior with charge transport being exclusively owing to hopping.(125) Poly (vinyl carbazole) may be the simplest case of a polymer of which the charge transport mechanism is exclusively hopping (Figure I-21c).

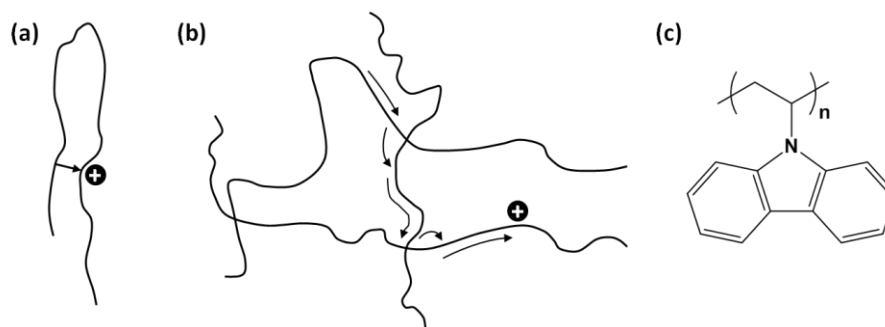


Figure I-21: One difference of hopping transport from coherent (band) transport is that there is no need for charge carrier to move from one unit to the next. (a) This involves intrachain transport that may occur by a hopping mechanism, particularly when defects are existed in the chain. (b) It is possible that both coherent transport and hopping can occur in conjugated polymers, with the charge carrier hopping from one chain to another. (c) Only hopping transport exhibits in some polymers like poly(vinyl carbazole), due to lack of conjugated backbone.(125)

II. 5-4 Polymer-based and small molecule-based materials for OPV

Currently, organic photovoltaic donors are principally based on two types of electron-donating materials: polymers(14, 26, 29, 126-128) and small molecules (19, 20, 30, 45, 46, 84, 85, 92, 129-133), and OPV acceptors are mainly based on either fullerene or their derivatives (3, 29, 35, 45, 127, 131) and fullerene-free materials including both polymer and small molecules) (22, 31, 128, 134-136).

(a) Polymer donors

Polymer-based BHJ solar cells have attracted great attention and been extensively investigated in science and industry because of their advantages such as solution processability, low cost, light weight, flexibility. Conjugated polymers are often built from blocks of electron-donating and electron-withdrawing units. As shown in Figure I-22, various central electron donor cores (thiophene, benzodithiophene (BDT), dithienosilole (DTS), dithienocyclopenta (DTC), dithienopyrrole (DTP), silafluorene (SFL), fluorene (FL), carbazole (CZ), etc.), electron acceptor cores (2,1,3-benzothiadiazole (Bz), fluorinated benzothiadiazole (ffBz), triazole, thieno[3,4-b]thiophene, diketopyrrolopyrrole (DPP), thieno[3,4-c]pyrrole-4,6-dione (TPD), thieno[3,4-b] thiophene (TT) etc.), together with terminal units (dicyanovinyl, alkyl cyanoacetate, rhodanine, and 1,3-indanedione), as well as π -conjugated bridges made of thiophene rings with different conjugation lengths have been used for the molecular design.(81, 137)

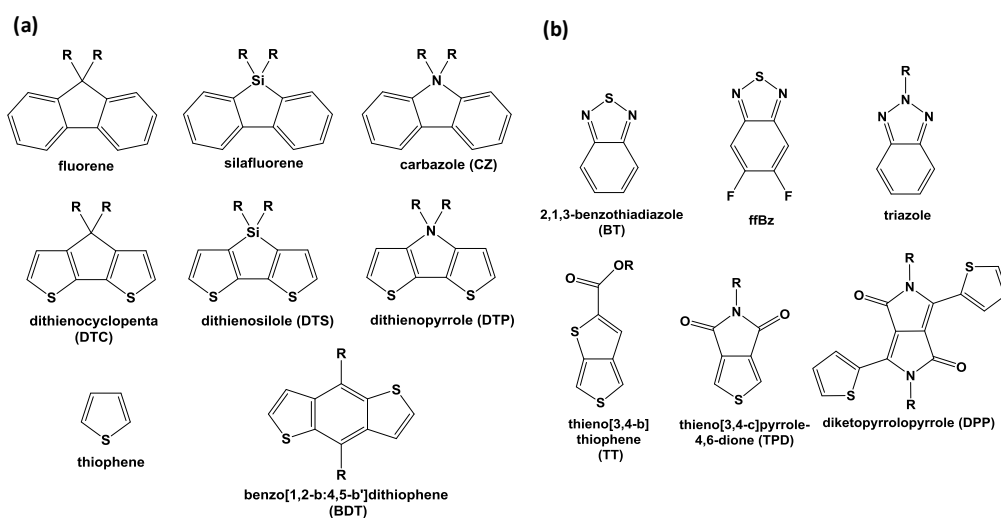


Figure I-22: Structures of some (a) electron donor and (b) electron acceptor units.

Polymer solar cells (PSCs) have been the leading candidates in OPV cells in the last decade. The chemical structures of some representative electron-donating materials based on donor and acceptor building blocks with high performance are illustrated in Figure I-23.

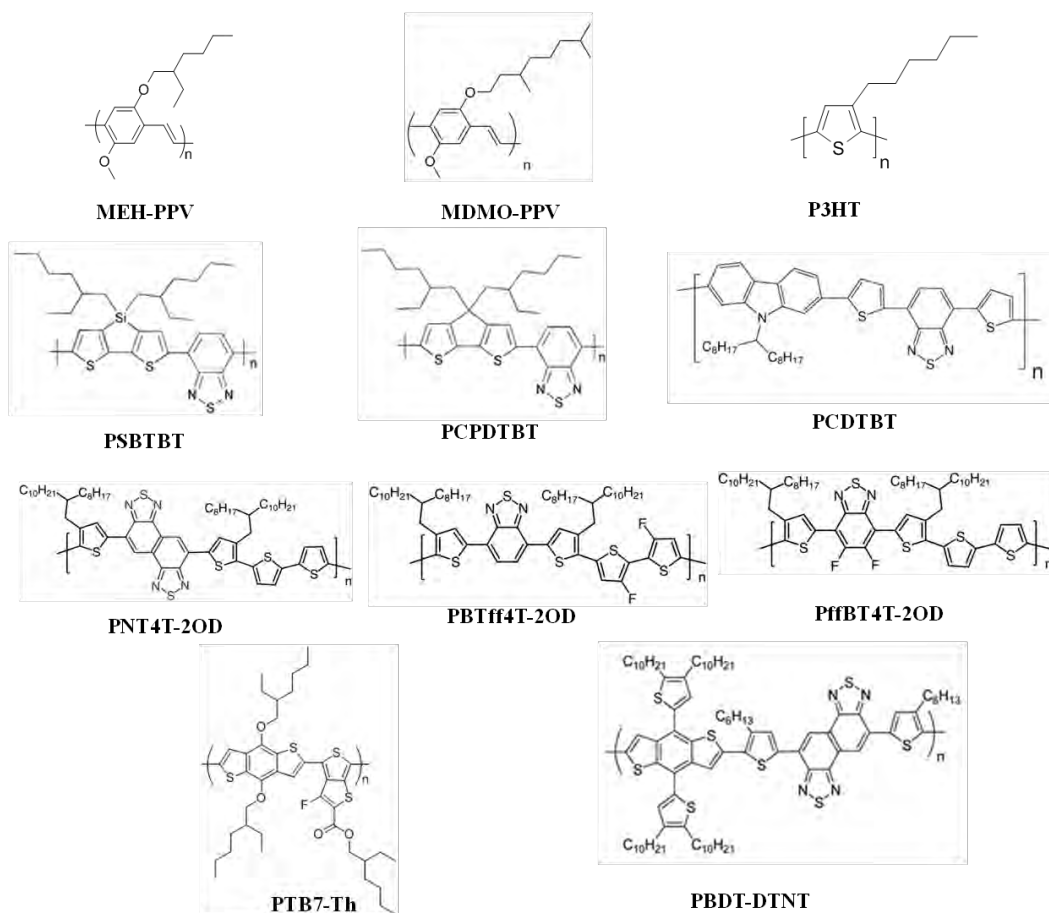


Figure I-23: Chemical structures of representative polymers acting as donors in OPV devices.

By far, poly[2-methoxy-5-(2-ethylhexyloxy)-1,4-phenylenevinylene] (MEH-PPV), poly[2-methoxy-5-(3,7-dimethyloctyloxy)]-1,4-phenylenevinylene (MDMO-PPV), and poly(3-hexyl thiophene) (P3HT) have been the most studied π -conjugated polymers for use as donor components in BHJ devices. From the efficiencies in Table I-1, it is clear that PPV-based BHJ devices exhibit relatively poor performance, such as 2.3% and 2.5%. PCE as high as 3.3% was achieved in BHJ device based on MDMO-PPV which was blended with PC₆₀BM as acceptor, attributed to active layer morphologies tune.^(138, 139) Hereafter, P3HT-based BHJ devices have been thoroughly studied due to its lower band gap (1.9 eV) (as shown in Table I-1) which leads to a remarkably higher current density of more than 10 mA/cm², as well as its enhanced π -stacking and crystallinity which results in a higher hole mobility.⁽¹⁴⁰⁻¹⁴²⁾ An impressive efficiency of 5% in BHJ device based on P3HT:PCBM blend was achieved by Kim *et al.* in 2006 by optimizing active layer morphology.⁽¹⁴¹⁾

Table I-1: Electronic properties and OPV performance of some typical polymer-based donors.

Donor	HOMO/LUMO ^a (eV)	E _g (eV)	Acceptor ^b	J _{sc} (mA cm ⁻²)	V _{oc} (V)	FF	PCE (%)	Ref.
MEH-PPV	-5.0/-2.8	2.2	PCBM	3	0.67	0.36	2.3	(143)
MDMO-PPV	-5.3/-3.0	2.3	PC ₇₁ BM	5.25	0.82	0.61	2.5	(138)
P3HT	-5.2/-3.3	1.9	PCBM	11.1	0.61	0.66	5.0	(141)
PSBTBT	-5.05/-3.27	1.78	PC ₇₁ BM	12.7	0.68	0.55	4.75	(144)
PCPDTBT	-4.9/-3.5	1.4	PC ₇₁ BM	16.2	0.62	0.55	5.5	(48)
PCDTBT	-5.5/-3.6	1.9	PC ₇₁ BM	12.40	0.88	0.68	7.5	(28, 145)
PBDT-DTNT	-5.19/-3.26	1.93	PC ₇₁ BM	17.4	0.75	0.61	8.4	(146)
PNT4T-2OD	-5.24/-3.71	1.53	PC ₇₁ BM	19.8	0.76	0.68	10.1	(94)
PBTff4T-2OD	-5.20/-3.57	1.63	PC ₇₁ BM	18.2	0.77	0.74	10.4	(94)
PTB7-Th	-5.22/-3.63	1.59	PC ₇₁ BM	17.43	0.825	0.74	10.6	(96)
PffBT4T-2OD	-5.34/-3.69	1.65	TC ₇₁ BM	18.8	0.77	0.75	10.8	(94)

^afrom electrochemistry, ^bfor the detailed donor/acceptor weight ratio in device, see the relevant references.

However, the V_{oc} has limited to about 0.6 V in the related P3HT-based BHJ devices with PCBM as the acceptor due to the high HOMO level (-5.2 eV) of P3HT, which consequently

restricts the device performance. Thus, presently, numerous novel conjugated polymers built from donor and acceptor building blocks have been emerged and have promoted a rapid development of high performance BHJ devices, such as poly[(4,4'-bis(2-ethylhexyl)dithieno[3,2-*b*:2',3'-*d*]silole)-2,6-diyl-*alt*-(2,1,3-benzothiadiazole)-4,7-diyl] (PSBTBT), poly[2,6-(4,4-bis(2-ethylhexyl)-4H-cyclopenta[2,1-*b*;3,4-*b'*]dithiophene)-*alt*-4,7-(2,1,3-benzothiadiazole)] (PCPDTBT), poly[N-9'-heptadecanyl-2,7-carbazole-*alt*-5,5-(4',7'-di-2-thienyl-2',1',3'-benzothiadiazole)](PCDTBT), poly[(4,8-bis-(2-ethylhexyloxy)-benzo(1,2-*b*:4,5-*b'*)dithiophene)-2,6-diyl-*alt*-(4-(2-ethylhexyl)-3-fluorothieno[3,4-*b*]thiophene)-2-carboxylate-2,6-diyl] (PTB7-Th), Poly[(5,6-difluoro-2,1,3-benzothiadiazol-4,7-diyl)-*alt*-(3,3''-di(2-octyldodecyl)-2,2';5',2'';5'',2'''-quaterthiophen-5,5'''-diyl)] (PffBT4T-2OD). The power conversion efficiencies of BHJ architecture fabricated by blends of conjugated polymers and soluble fullerene derivatives have seen a dramatic rise from around 1% in 1992(39) to over 10% in 2013 - 2015(23, 25, 40, 93-99), as evidenced by the performance shown in Table I-1. High J_{sc} over $17.3 \text{ mA} \cdot \text{cm}^{-2}$ (94, 96, 146), high V_{oc} over 1 V (147-149), and fill factor (FF) over 0.70 (94, 96) have been reported in different polymer-based BHJ devices. The combination of all these striking values should ultimately drive the efficiency to 12% and beyond in the near future in single junction PSCs. Particularly, so far the best PCE for single junction (BHJ) has reached 11.7%.(21) Typically, for tandem device, efficiencies over 11% have also been achieved, such as 11.3% for double junction (23), 11.5% for triple junction(25), and a new record of 13.2% set by Heliatek for multijunction (6).

(b) Small-molecules based donors

As succinctly illustrated in Figure I-24, solution-processed π -conjugated small molecules with narrow band gap have recently gained more attention for use as the donor component in BHJ solar cells with fullerene derivatives as electron acceptor materials. In regard to the performance in BHJ-OPVs, small molecules have almost caught up with their polymer counterparts.(19-21, 24, 29, 45, 84, 129, 130, 132, 137, 150)

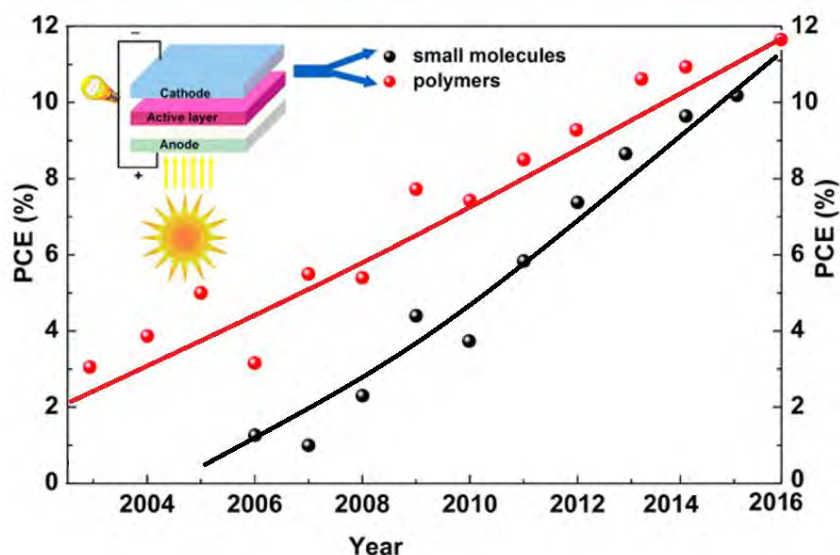


Figure I-24: The development of heterojunction solar cells based on polymers and small molecules.(30)

Small molecules-based OPV cells (SM-OPVs) are an attractive and comparable alternative to polymer-based OPV cells. Small molecules offer several advantages compared to their polymer counterparts, including well-defined but versatile chemical structures which allow easier energy level control, higher material purity, better ordered, generally higher V_{oc} (92), reduced even no batch-to-batch variation, and good solubility *via* employment of the appropriate type, number and length of side chains.(29, 130, 133, 151-153) Furthermore, small molecule processed through solution deposition affords the possibility of cost-effective roll-to-roll (R2R) manufacture. Similarly, small molecules are also based on electron donor and electron acceptor cores. Figure I-22 provides several representative small molecular-based donors that show good performance in BHJ devices, their chemical structures are given in Figure I-25.

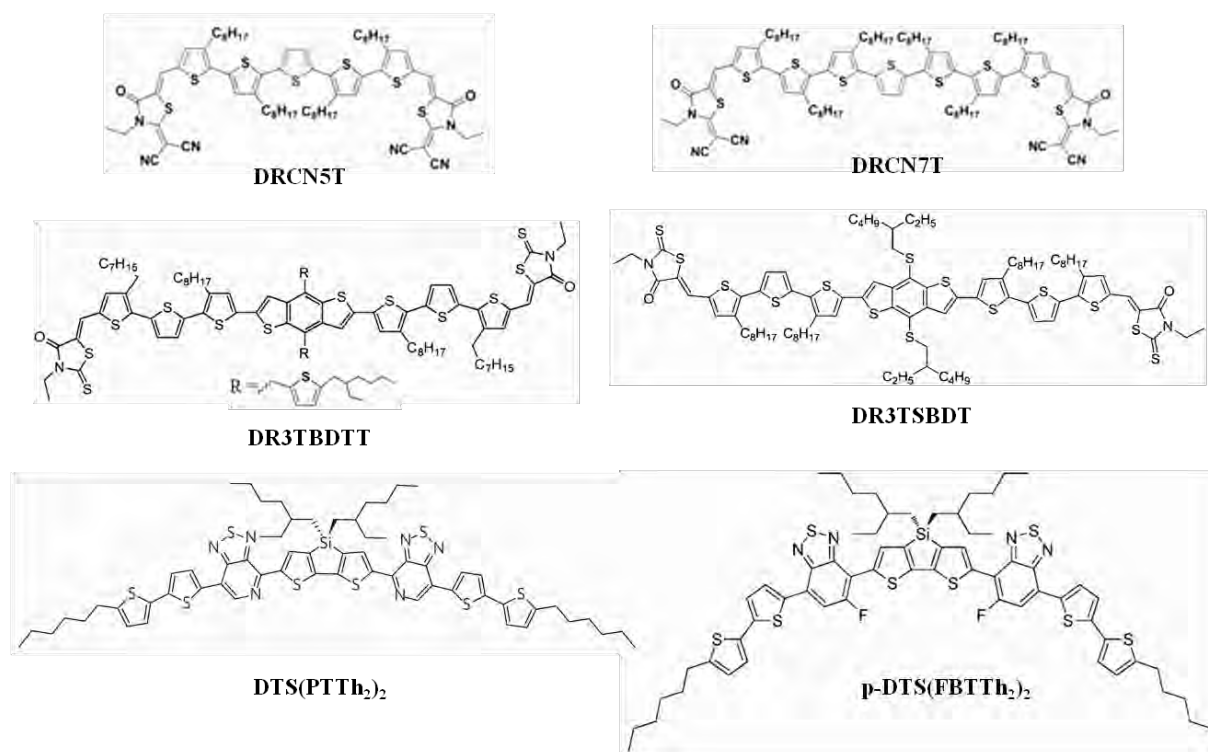


Figure I-25: Chemical structures of representative small molecular-based donors.

Table I-2 provides the electronic properties and OPV performance of the small molecules displayed in Figure I-25. It is clear that all of these high performance small molecule-based donors are endowed with good molecular design. For instance, 5,5'-bis((4-(7-hexylthiophen-2-yl)thiophen-2-yl)-[1,2,5]thiadiazolo[3,4-c]pyridine)-3,3'-di-2-ethylhexylsilylene-2,2'-bithiophene (DTS(PTTh₂)₂), the design of which is based on a core acceptor/donor/acceptor (A/D/A) framework incorporated with donor end-capping units. The electron-rich core dithienosilole (DTS) unit linked with two electron-deficient units [1,2,5]thiadiazole[3,4-c]pyridine (PT) leads to strong intramolecular charge transfer feature, and the 4-coordinate silicon atom allows for incorporation of alkyl chains to enable good solubility in organic solvent.⁽²⁹⁾ DTS(PTTh₂)₂ and p-DTS(FBTTh₂)₂ have been well investigated by Alan J. Heeger and co-workers, giving PCEs of 6.7% and 8.24% respectively.^(29, 154) A series of small molecules-based donor materials blended with PC₇₁BM reported by Y. Chen *et al.* exhibit higher efficiencies above 9%, such as DRCN7T, DR3TSBDT, DRCN5T listed here.

Table I-2: Electronic properties and OPV performance of some typical small molecular donors.

Donor	HOMO/LUMO ^a (eV)	E _g (eV)	Acceptor	J _{sc} (mA cm ⁻²)	V _{oc} (V)	FF	PCE ^b (%)	Ref.
DTS(PTTh ₂) ₂	-5.2/-3.6	1.6	PC ₇₁ BM	14.4	0.78	0.593	6.7	(29)
DR3TBDDT	-5.02/-3.27	1.75	PC ₇₁ BM	13.17	0.93	0.663	8.12	(155)
p-DTS(FBTTh ₂) ₂	-5.12/-3.34	1.78	PC ₇₁ BM	14.74	0.773	0.724	8.24	(154)
DRCN7T	-5.08/-3.44	1.64	PC ₇₁ BM	14.87	0.91	0.69	9.3	(19)
DR3TSBDT	-5.07/-3.30	1.77	PC ₇₁ BM	14.61	0.92	0.74	9.95	(156)
DRCN5T	-5.22/-3.41	1.81	PC ₇₁ BM	15.88	0.92	0.69	10.08	(19)

^afrom electrochemistry, ^bfor the detailed donor/acceptor weight ratio in device, see the relevant references.

Small molecules are good candidates for OPVs not only due to their advantages but also their high performances.(19, 129) So far, the performance of small molecules-based BHJ device (19, 85) is comparable to that of polymer-based OPV devices (23, 25, 40, 93-100), both showing power conversion efficiency over 10%. The highest PCE for single-junction OPVs based on small molecule reported to date has reached to 10.10%.(19) Via careful and interdisciplinary efforts in the design and synthesis of new small molecules based on D/A building blocks, together with morphology control and device optimization, it is believed that the performance of a single junction OPV based on small molecule will achieve 12% in the near future.

(c) Fullerene and fullerene derivative acceptors

As the rapid development of electron-donating materials including polymers and small molecules, efficiencies of BHJ devices based on donor/fullerene derivatives blends have achieved over 11%.(21, 23) Taking into account of the wide spread in the reported good performances in OPVs, so far, fullerene derivatives (see Figure I-26) are no doubt considered as the more successful candidates for acceptor in OPVs, which can be ascribed to their advantages, such as good electron mobility and large electron affinity, adequate band gaps,

and good interaction with donor materials to form nanoscale morphological network in organic photovoltaic devices.(134, 157, 158)

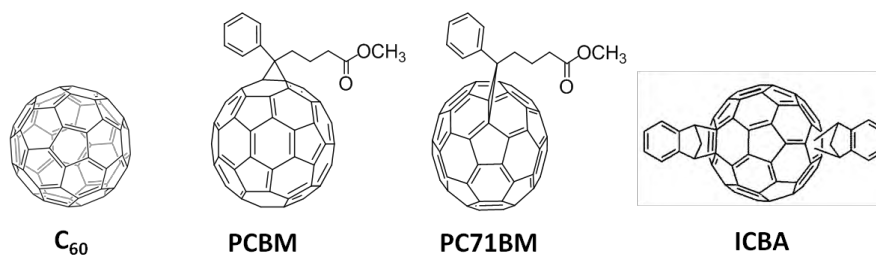


Figure I-26: Common fullerene and its derivatives acceptor materials.

Buckminsterfullerene (C_{60}) has first proven to be an ideal acceptor with conjugated polymer MEH-PPV donor by Sariciftci and co-workers in 1992.(39) Later, Yu *et al.* introduced the BHJ architecture and replaced C_{60} with its derivative [6,6]-phenyl- C_{61} -butyric acid methyl ester ($PC_{61}BM$) as acceptor.(35) The efficiency of BHJ cells are able to be further improved by replacing $PC_{60}BM$ with [6,6]-phenyl- C_{71} -butyric acid methyl ester ($PC_{71}BM$) due to its stronger light absorption in the visible spectrum region than that of C_{60} . Indene- C_{60} bisadduct (ICBA) is easier to synthesis in comparison to that of PCBM and shows better solubility than PCBM. Table I-3 gives relevant examples about the efficiencies of OPVs based on fullerene derivatives acceptors, which indicates the development of electron acceptors based on fullerene derivatives. For instance, the device made from P3HT and ICBA presented a V_{oc} of 0.84V, a J_{sc} of 10.61(mA cm^{-2}), a FF of 0.727, and a PCE of 6.48% (158), which is higher than that of P3HT/PCBM (5.0%) (141).

Table I-3: Electronic properties and OPV performance of typical fullerene and its derivatives as acceptors.

Acceptor	HOMO/LUMO ^a (eV)	E_g (eV)	Donor	J_{sc} (mA cm^{-2})	V_{oc} (V)	FF	PCE ^b (%)	Ref.
C_{60}	-6.1/-3.7	2.4	SubPcBCl	3.36	0.97	0.57	2.1	(74)
PCBM	-6.1/-4.3	1.8	P3HT	11.1	0.61	0.66	5.0	(141)
$PC_{71}BM$	-5.8/-4.0	1.8	DRCN5T	15.88	0.92	0.69	10.08	(19)
ICBA	-5.7/-3.74	1.96	P3HT	10.61	0.84	0.73	6.48	(158)

^afrom electrochemistry, ^bfor the detailed donor/acceptor weight ratio in device, see the relevant references.

(d) Non-fullerene acceptors

While fullerene derivatives are the most commonly representative electron acceptors used in OPVs, they also have a few distinct disadvantages, such as weak absorption in the visible region, difficulty in modifying the energy levels, high cost of synthesis and purification.(159-162) Therefore, the design and synthesis of fullerene-free (n-type) materials including polymers and small molecules have recently drawn more and more attention.(22, 43, 84, 130, 134-136, 163)

Different from fullerene derivatives, the energy levels of polymer and small molecular acceptors can be tuned more efficiently by chemistry engineering. Moreover, by combining matched donor and acceptor building blocks, non-fullerene semiconductors can show wide and strong absorption in the visible region owing to intramolecular charge transfer. Generally, polymer non-fullerene acceptors include amide/imide-functionalized polymers and benzothiadiazole-based copolymers. Small molecule non-fullerene acceptors consist of rylene diimides and their analogues, other amide/imide-functionalized small molecules, benzothiadiazole-based small molecules and electron-deficient aromatic fused rings, as reviewed by Y. Lin *et al.*(134) Figure I-27 presents the chemical structures of some polymers and small molecules that are used as electron acceptors in OPV with relatively high efficiencies. Herein the electronic properties and performances of these non-fullerene materials in OPVs are listed in Table I-4.

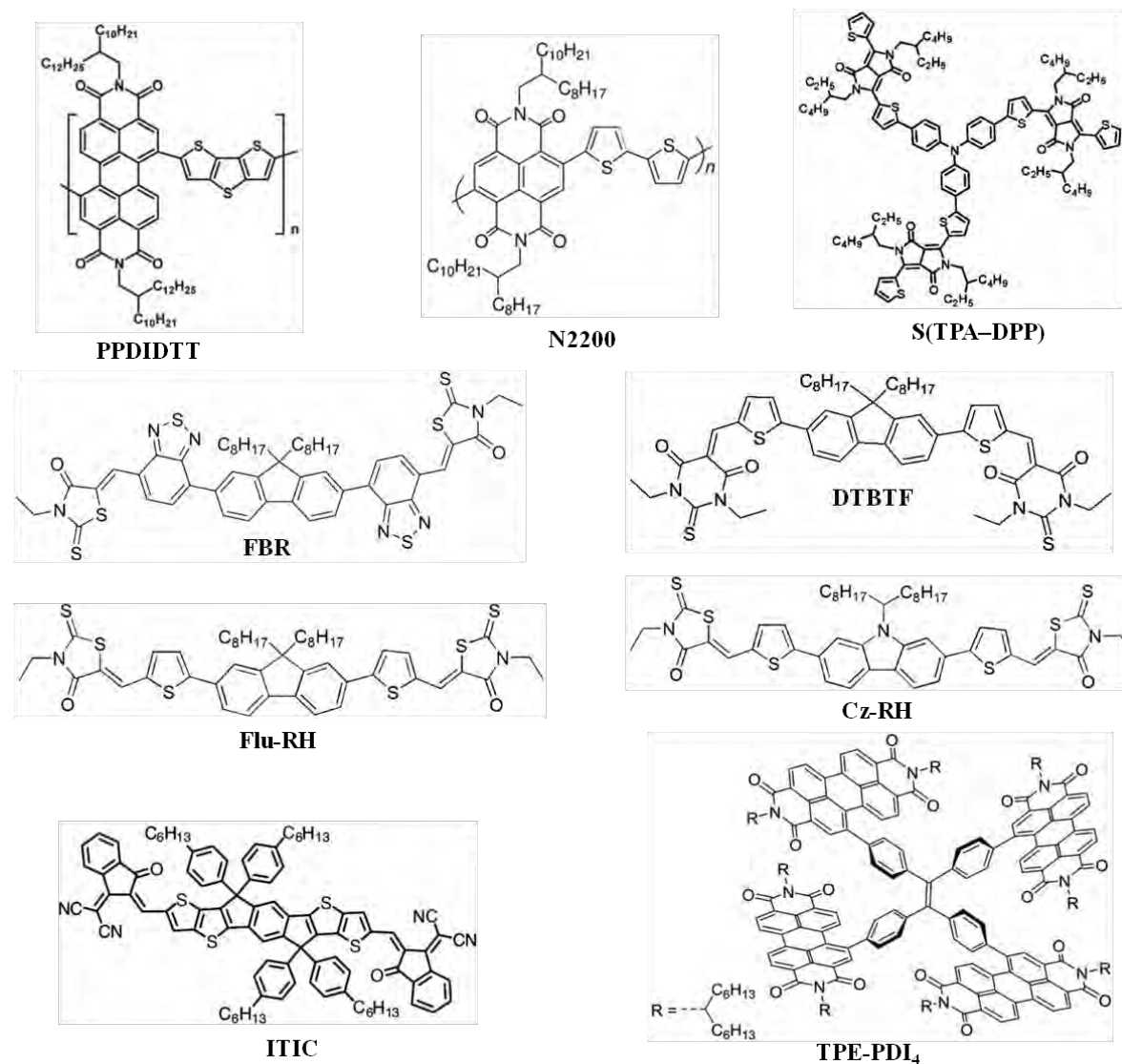


Figure I-27: Chemical structures of fullerene-free acceptors for OPVs.

It is worth noting that more and more research efforts are devoted to non-fullerene acceptors, although the efficiency of devices based on these materials are lower than that of fullerene systems. Efficiency reaching 6.8% has been achieved for the device based on polymer and small molecular blend by Y. Lin *et al.* in 2015.(164) A new record efficiency of 9.6% has been reached for OPV device based on fullerene-free acceptors by Y. Lin *et al.* in 2016.(165) Therefore, developing fullerene-free acceptors would be a promising approach for cost-effective and high performance devices.

Table I-4: Electronic properties and OPV performance of some typical non-fullerene acceptors.

Acceptor	HOMO/LUMO ^a (eV)	E _g (eV)	Donor	J _{sc} (mA cm ⁻²)	V _{oc} (V)	FF	PCE ^b (%)	Ref.
S(TPA-DPP)	-5.26/-3.26	2.0	P3HT	2.68	1.18	0.379	1.20	(166)
Cz-RH	-5.53/-3.50	2.03	P3HT	4.69	1.03	0.53	2.56	(43)
Flu-RH	-5.58/-3.53	2.05	P3HT	5.70	1.03	0.52	3.08	(43)
PPDIDTT	-5.5/-3.6	1.9	PBDTTT-C-T	8.55	0.752	0.515	3.45	(167)
DTBTF	-5.68/-3.62	2.06	DR3TSBDT	7.42	1.15	0.45	3.84	(136)
FBR	-5.70/-3.57	2.14	P3HT	7.95	0.82	0.63	4.11	(22)
TPE-PDI4	-5.77/-3.72	2.05	PBDTT-F-TT	11.7	0.91	0.52	5.53	(168)
N2200	-5.9/-4.3	1.6	PBDTTT-EF-T	13.0	0.794	0.556	5.73	(169)
ITIC	-5.48/-3.83	1.65	PTB7-TH	14.21	0.81	0.591	6.80	(164)

^afrom electrochemistry, ^bfor the detailed donor/acceptor weight ratio in device, see the relevant references.

II. 6 Outlook

Many novel and excellent polymers and small molecules have been designed and synthesized for organic photovoltaics, and an attractive efficiency of over 10% PCE has been achieved. Concerning chemical design, the D/A (also named push-pull) framework has confirmed to be a smart strategy to obtain good light absorption. Apart from the absorption, energy levels, morphologies, solubility and mobility *etc.* could also be well controlled *via* careful efforts in molecule design. Various electron donor cores, electron acceptor units, terminal units, as well as bridges with different conjugation lengths have been employed in the initial design. Attributed to the complicated and multi-step photoelectric conversion processes, it is necessary and important to obtain a delicate balance among molecular design,(30, 81, 84, 129, 130, 137, 153, 170, 171) morphology,(172, 173) interfacial layer,(174-176) and device fabrication (17, 177, 178) to optimize the efficiencies of OPV devices (179).

For these prospects, the following issues need to be paid attention and solved:

(1) *Molecular engineering to obtain low-band gap polymers or small molecules, as well as a delicate balance between V_{oc}, J_{sc} and FF.* New materials developed in various research teams focus on improving three key parameters that define the power conversion efficiency of a

solar cell, such as the short-circuit current density (J_{sc}), the open-circuit voltage (V_{oc}), and the fill factor (FF). First, molecules with broad absorption allow maximum photocurrent and thus have potential for high J_{sc} devices. To increase the absorption range, especially to red and near infrared (IR) region and thus to improve solar photon harvesting, the only approach is to design and synthesis low-band gap materials.^(129, 180) Second, because the V_{oc} is governed by the HOMO of the donor and the LUMO of the acceptor, increasing the LUMO energy level of the acceptor or decreasing the HOMO energy level of the donor or both seems to be the most promising approach. A delicate balance should be found to provide donor (or acceptor) materials with appropriate absorption properties and low-lying enough HOMO (or high-lying enough LUMO) levels that enable a high V_{oc} , and a downshift offset for efficient exciton dissociation and a lowest energy loss. Third, the fill factor is determined by the series and the shunt resistance of the devices. Due to the low charge carrier mobilities and the disordered feature of numerous BHJ films, they often have a relatively low shunt resistance and a relatively high series resistance, which should lead to low FF values. Despite this, FF values over 0.70 have been achieved. In brief, it is worth noting that design and synthesis of molecules with strong and extended absorption band are just the initial and relatively easy steps. High charge carrier mobility, proper donor-acceptor energy levels matching, and morphology control in the device optimization are all huge problems as well.

(2) Optimization of nanoscale morphology for BHJ and nanomorphology control. Since an ideal morphology (see Figure A.1 in Annexes section) with appropriate domain size and phase separation is one of the determining factors for improving device performance, a full study and well understand of the morphology is of high importance. The phase separation of D/A blend film can be determined by the chemical properties and tuned by device fabrication. Besides, morphology could be controlled and optimized by different process methods, such as vacuum deposition and thermal annealing. In the phase separation of active layer, the sweep-out time is confined to the charge mobility and thus by the blend morphology of the phase separation in BHJ materials. Therefore, improvement in the morphology with better structural order could obviously enhance the mobility and thus result in a reduction of the sweep-out time, which could facilitate the charge carriers to sweep out to the external circuit prior to their recombination to ground state, giving rise to higher FF.⁽²⁷⁾ However, to finely control the phase separation of different D/A blend films and thus to optimize and achieve ideal morphology which can lead to the highest theoretical efficiency is still a big challenge.

(3) *Green chemistry for material synthesis.* Organic materials for OPV have been studied intensively in recent years. However, as the technologies become commercialized, these materials will be required in large scale. Thus, efficient syntheses of these materials are of great significance. State of the art syntheses often rely on traditional cross-coupling methods (Suzuki, Stille, Heck, etc.) for the formation of new C-C bonds. However, these traditional coupling methods exhibit drawbacks including the usage of an organometallic reagent that yields a stoichiometric amount of metal waste and is often toxic, expensive, difficult to handle, and require extra synthetic steps. Owing to disadvantages of typical coupling methods, direct arylation (the coupling of transition-metal (palladium, Rhodium, Ruthenium) catalyzed aryl C-H bonds with aryl halides) proceeds *via* C-H bond activation without need of the preparation of organometallic. It has emerged as a feasible alternative, allowing for promising and atom-economical method to classical cross coupling reactions for the formation of new C-C bonds.^(181, 182) Therefore, direct arylation can be added to chemists' toolbox. It would be quite attractive to give rise to organic materials for OPV devices by using this strategy.

We should also bear in mind that tandem-architecture technology is advantageous for efficient and complementary absorption. It has been demonstrated experimentally that realizing tandem structure can be highly favorable to improve the performance of devices based on materials unable to fully realize their potential.⁽⁷⁹⁾ Besides, the lifetime of organic solar cells is still an important challenge to realize commercialization.

To conclude, organic photovoltaics have gone through enormous progress in the last decade. The device performance was greatly improved from below 3% to the present 13.2% power conversion efficiency. If OPVs holds its promise, we believe that it can soon become a widespread, clean and renewable energy source to meet the increasing energy demand in our planet and to benefit future generations.

III PhD objectives

As a clean and sustainable energy source, organic photovoltaic cells seem to have the potential of replacing the often used fossil fuels and satisfying the increasingly energy demand in our planet. The striking progress in organic photovoltaics encourages chemists to design and synthesis new conjugated materials for OPVs, which also have drawn our

attention. Therefore, to design and synthesize novel organic small molecules for application in OPV devices is the aim of our team, attributed to the advantages of small molecules (see section II.5-4(b)). According to numerous experimental and theoretical reports about molecules design, the push-pull structures offer a facile way to tune the physical and optoelectronic properties of electron-donating or electron-accepting materials in organic photovoltaic cells. Thus, to fulfil this aim, we first designed new molecules composed of strong electron-donating unit and strong electron-accepting units from theoretical point of view by collaboration with Laboratoire de Chimie et Physique Quantiques (LCPQ). The theoretical calculations are carried out by OCRA program (183) with density functional theory (DFT) (184). Due to the strong electron-donating ability of thiophene and dithienosilole (DTS), and the strong electron-accepting ability of benzothiadiazole (Bz), they were chosen as building blocks for the backbone of π -conjugated small molecules.(81, 137) Attributed to the feature of fluorine (will be discussed in detail in chapter II), fluorinated benzothiadiazole (ffBz) were also chosen as an acceptor building block. To ensure sufficient solubility of small molecules, alkyl (linear octyl- and branched 2-ethylhexyl-) cyanoacetate were selected as the terminal group. Linear side groups may lead to a relatively coplanar backbone structure thus allows for closer π - π stacking distance and consequently increased charge mobility, whereas branched side chains may result in steric hindrance if molecular chains undergo packing.(63) Therefore, the difference in the nature of the alkyl chains would provide us interesting results leading to different morphologies in a blend.(81)

Once a molecule was designed, the following aim was to synthesize them within as less as possible steps. The synthesis of these materials originated from appropriate precursors was conducted with co-workers *via* different methods in parallel. Interestingly, our designed Bz-based small molecules were able to be obtained in a considerable yield through eco-friendly synthetic approach (direct arylation) within only two steps. With regard to synthesized molecules, material characterizations were performed in terms of electrochemistry, UV-Vis absorption, fluorescence, thermal characteristics. Atomic Force Microscopy (AFM) was also envisaged to study the morphology of thin films. As the final target, the synthesized materials should be subjected to the measurement in OPV device *via* collaboration with Laboratoire d'analyse et d'architecture des systèmes (LAAS-CNRS) and the Centro de Investigaciones en Óptica (CIO-León) in Mexico.

To be mentioned, subphthalocyanines (SubPcs)-based small molecules were also envisaged as an extension of molecular design, due to their unique optical and electronic properties and thus great potential in the field of photonic devices.^(185, 186)

Herein, in brief, the following three aspects are the primary objectives of this PhD thesis and will be further discussed in the following successive chapters.

- (1) Molecular design
- (2) Green chemistry approach for materials synthesis
- (3) Materials characterization

Chapter II: Molecular design

Chapter II : Molecular design

I Introduction

As mentioned in Chapter I, novel appropriate materials need to be designed and synthesized to develop the OPV technology for the future demand. One design method is the conventional experimental development of novel materials that is mainly based on experience or empirical intuition with a certain series of molecules. Employing this method, one obvious drawback is that only a few materials per year can be studied by an experimental team owing to the lengthy and complicated synthesis and characterization procedures. The other design method is based on the virtual large-scale screening framework conducted by theoretical research and assessment using first-principles quantum chemistry. Here, it is worth mentioning that the Harvard Clean Energy Project has made great effort to molecules design; more details will be addressed below.

I. 1 Theoretical work on molecular design

The Harvard Clean Energy Project (CEP) initiated in 2008, is a theory-driven and high-throughput screening framework for the aim of identifying promising high-performance material candidates for organic electronics, in particular organic photovoltaics.⁽¹⁸⁷⁻¹⁸⁹⁾ It is administered by the Alán Aspuru-Guzik Research Group at Harvard University and supported by many external contributors and collaborators.^(190, 191) The CEP currently focuses on the characterization of millions of molecular motifs by means of first-principles quantum chemistry. In this project, millions of molecular structures were studied to propose proper compounds particularly for the harvesting and conversion of solar energy and for other organic electronic applications. To our knowledge, the CEP is the most extensive quantum chemical study ever conducted. The computational exploration of compounds merging the level of theory and scope established in the CEP is unprecedented. So far, 2.3 million molecular motifs derived from 150 million density functional theory (DFT) simulations and comprised 400TB of data have been assessed. These massive data are stored and freely accessible in the Clean Energy Project Database (CEPDB) which is a massive reference database for organic semiconducting materials with a special emphasis on organic photovoltaic applications.⁽¹⁹²⁾ The 2.3 million molecular motifs are based on 26 building

blocks and bonding rules (see Figure II-1), which were chosen with potential and feasibility following the advice from Zhenan Bao group at Stanford University.

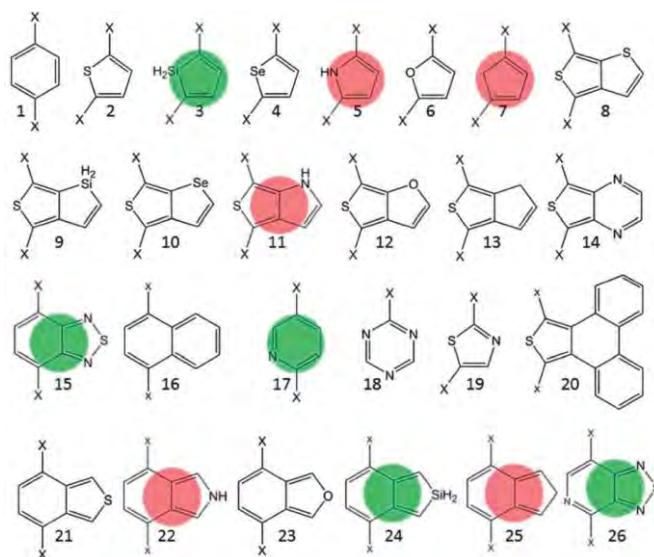


Figure II-1: The 26 building blocks (including chemical connections indicated by ‘X’) of the resulting CEP molecular candidate library. Five most efficient moieties in the top PCE are highlighted in green, and red indicates the five less efficient moieties.(188)

The performance of the top virtual candidates built from the building blocks marked in red and green in Figure II-1 with predicted PCE $\geq 10\%$ are given in Figure II-2. It reveals that these top candidates comprised of the five most efficient fragments have the highest efficiencies compared to those of most other fragments, while those comprised of the five less efficient moieties lead the lowest performances.

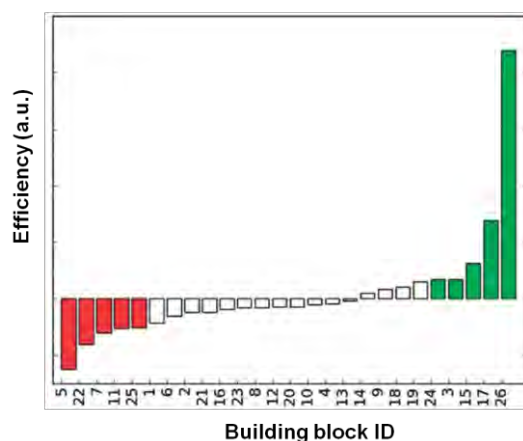


Figure II-2: Ranking of building blocks related to calculated PCE $\geq 10\%$.(188)

It is worth mentioning that the candidates in the CEP were assessed and ranked by means of the Scharber model (61), a specialized version of the Shockley-Queisser model (193) for OPV donor material performance prediction. Top candidates are in a list of candidates with efficiencies beyond 10% in the CEPDB. According Scharber model, the power conversion

efficiency values of systems based on the molecules of the CEPDB correspond to a standard PCBM acceptor counterpart with LUMO level at -4.3 eV. Among the 2.3 million molecules explored, about 1000 lead to a Scharber PCE of over 11%, 35000 have a value above 10%, and most of them are predicted to show a PCE less than 4%.⁽¹⁸⁸⁾

The computations conducted in the CEP provide insights into novel and promising molecular patterns that can be further studied by more detailed simulations, which facilitate the reasonable design of new materials. However, it should be pointed out that most of promising candidates would be difficult to synthesize due to their structural complexity (see Figure II-3), notwithstanding these massive design choices. Actually, these predicted molecules probably won't be soluble and adding alkyl chain is a supplementary difficulty.

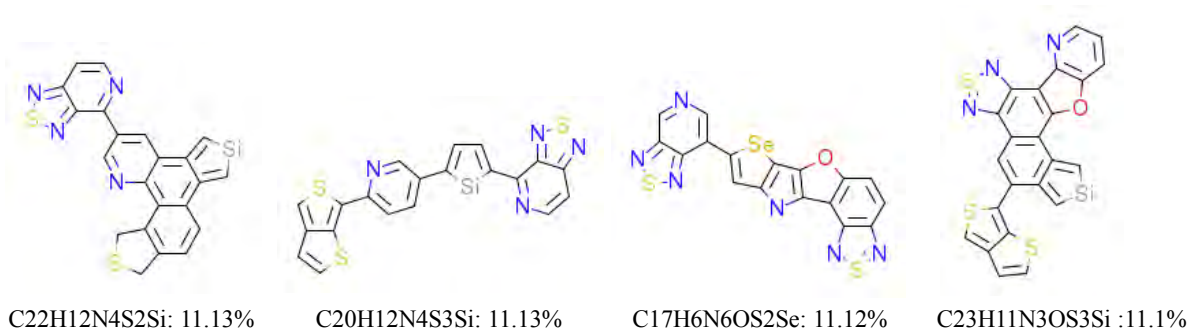


Figure II-3: Chemical structures of some top candidates gathered in the CEPDB.

In general, the top candidates in the CEPDB are comprised of fused rings which would offer rigid structure, but their non-symmetrical structures will make the synthesis difficult. Of the 26 building blocks shown in Figure II-1, the building block 15 (4,7-dibromobenzo-2,1,3-thiadiazole, diBrBz) is among the best fragments that lead to the highest efficiencies and proved to be stable, which could be a guiding for us to design molecules built from diBrBz.

I. 2 Theoretical work on active-layer interface

In addition to the high-throughput design effort to organic photovoltaics from the Harvard Clean Energy Project, other advanced theoretical investigations on the complicated bilayer interfacial interaction were reported. The aim is to provide visual view to help researchers achieve deep understanding. For instance, the theoretical research performed in Brédas group provides deep insight into the interfacial packing configuration between fullerene (C_{60}) and pentacene (see Figure II-4a) by atomistic molecular dynamics (MD) modeling,⁽¹⁹⁴⁾ as well as the study of interface interaction between C_{60} and pentacene conducted in Cantrell group (see Figure II-4b) using MD simulation.⁽¹⁹⁵⁻¹⁹⁷⁾ These simulated results reveal the

morphological complexity at the active layer interface which will affect the electronic processes taking place during the photovoltaic effect. On the other hand, calculations and morphology simulation work using dynamical Monte Carlo model have indicated that the ideal morphology of a donor-acceptor blend in bulk heterojunction cells should give rise to ideal performance.(198)

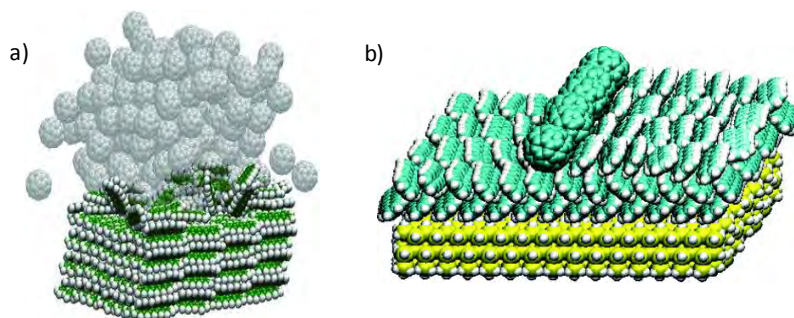


Figure II-4: Pentacene-C₆₀ bilayer interface simulated by molecular dynamics.

Therefore, designing new candidates for organic solar cells with the modern advanced computational technology has been a widely recognized approach, and these theoretical simulations provide us useful tools for the optimization of molecular design and for the understanding of interface morphology.

II Small molecules design

From the previous description, we need to bear in mind that the design of new materials for organic photovoltaics involves not only careful balances between J_{sc} , V_{oc} and FF, but also a comprehensive understanding of all of the optical and electronic processes that occur in a solid-state OPV. Many efforts have been recently devoted to the design and synthesis of low-band gap copolymers combining alternating donor and acceptor (D-A) fragments, used as electron-donating components to harvest the low-energy photon portion of the solar spectrum, in the other words, to achieve wide spectrum in the Infrared and near-Infrared region.(199-201) Power conversion efficiencies beyond 10% have been achieved in organic BHJ devices using D-A units.(40) However, due to the disadvantages of polymer synthesis and purification, increasingly attention nowadays has turned to small molecules. Thus, we aimed to develop a new series of organic small molecules for photovoltaic applications. To achieve our objectives, the design of such materials needs to be first conducted. It is most of time accomplished by an exhaustive bibliographic work that is evidenced by the II.5-4 part of Chapter I. Moreover, we have used theoretical calculations to anticipate the energy levels of the frontier orbitals (HOMO and LUMO) of target molecules.

In the search for new and efficient materials for organic photovoltaics, many small molecules have been designed and synthesized in the past few years.⁽⁸⁴⁾ Nowadays, their efficiency in term of photo conversion (DRCN5T: 10.08%)⁽¹⁹⁾ has become equivalent to that of polymers (PffBT4T-2OD: 10.8%)^(94, 202) for single junction BHJ devices. Besides, their synthetic reproducibility and the numerous attainable structures make them very attractive for generating materials with easy energy level control, mobility, solid packing mode and solubility.^(84, 153) To our knowledge, alternating electron-rich and electron-deficient (D–A) fragments in a conjugated polymer backbone is one of the most commonly employed approaches for tuning the material band gap. In the same manner, this strategy has also been proven to be a good strategy for reaching efficient narrow band-gap small molecules. Various central electron acceptor cores like Bz, DPP, etc. and electron donor cores such as DTS, BDT, FL and so on, (see Figure I-22), terminal units (dicyanovinyl, alkyl cyanoacetate, rhodanine, and 1,3-indanedione), as well as π -conjugated bridges made of thiophene rings with different conjugation lengths have been used for the design of small functional molecules.^(81, 137) Here we will focus on symmetrical structures for simplicity, using the D-A strategy. In consequence, an A or D fragment will be in the center of the molecule. In our work, a series of small molecules comprised of the building block Bz and those of DTS as the central core were designed.

II. 1 Small molecules based on benzothiadiazole (Bz) core

Since Bz has been explored as a common acceptor unit in many high performance materials^(15, 28, 48, 127, 203, 204), which is also in good agreement with the five most enriched moieties of the Harvard Clean Energy Project, it was chosen in our molecular design. Adequate lengths of alkyl chains can ensure the material solubility. Octyl (linear chain) cyanoacetate and 2-ethylhexyl (branched chain) cyanoacetate as the terminal groups were proved to confer a good solubility of small molecules and thus promote self-organization in nanoaggregate structures which contribute to enhanced photovoltaic performances.⁽²⁰⁵⁾ Besides, linear side groups may lead to a relatively coplanar backbone structure thus allows for closer π - π stacking distance and consequently increased charge mobility, whereas branched side chains may result in steric hindrance prohibiting molecular packing.⁽⁶³⁾ Therefore, the difference in the nature of the alkyl chains would provide us interesting results leading to different morphologies in blend.⁽⁸¹⁾ Thus, the combination of the Bz, thiophene or bithiophene and alkyl (octyl- and 2-ethylhexyl) cyanoacetate fragments leads to one kind of non-sophisticated designed molecules: A-D-A-D-A-type symmetric molecules (as provided in

Figure II-5). The differences between these molecules are the number of thiophene rings forming the π -conjugation bridges and the nature of the alkyl chains.

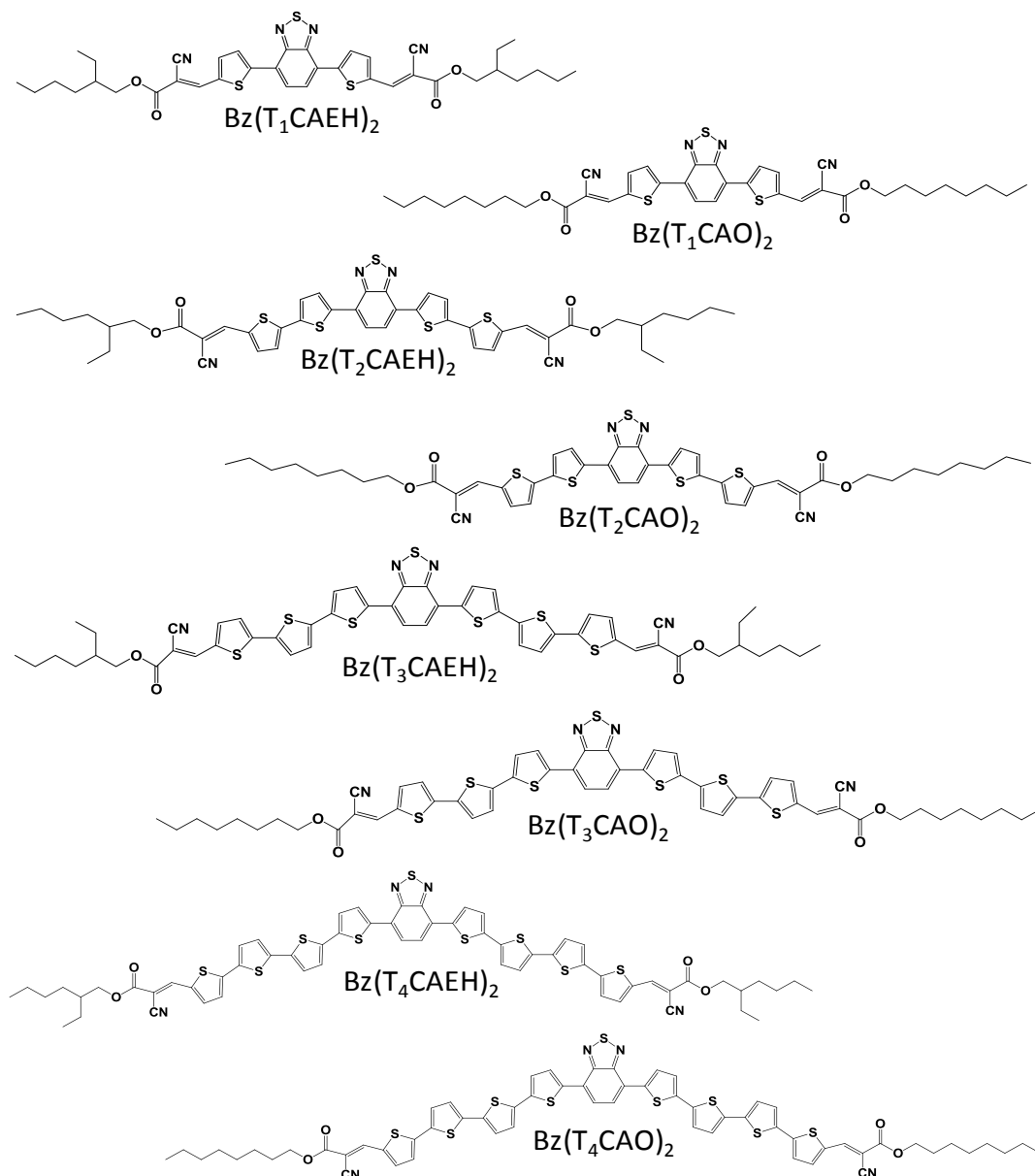
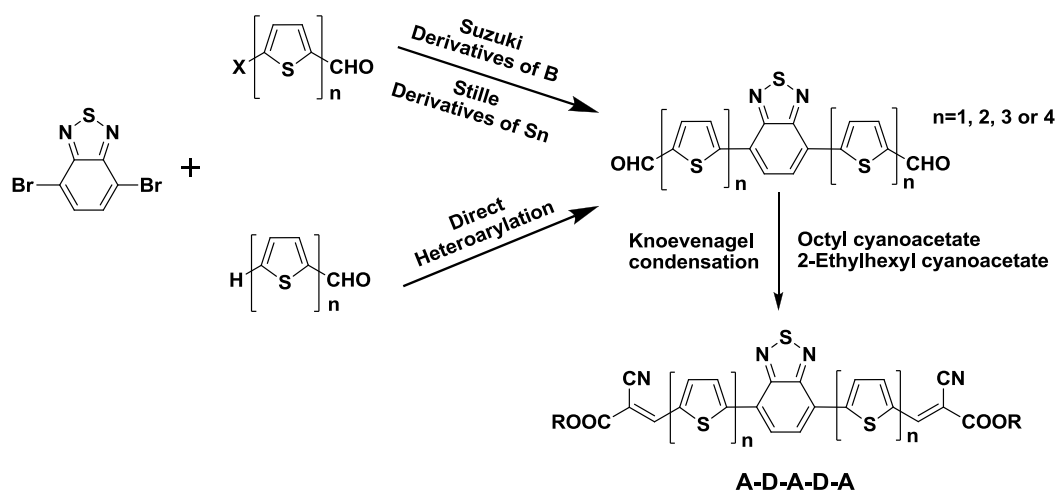


Figure II-5: Chemical structures of designed small molecules based on Bz core.

As illustrated in Scheme II-1, to obtain the target molecules, the first step consists of coupling 4,7-dibromobenzo-2,1,3-thiadiazole with thienyl carboxaldehyde *via* a chosen coupling method, leading to a D-A-D intermediate. In that purpose, synthesis methods *via* eco-friendly synthetic approaches are of paramount importance. Thus, we intend to investigate this first coupling by comparing the classical Suzuki or Stille coupling with direct arylation, which could be a method of choice for the present work. The chosen synthetic approach will be further discussed in the next chapter.



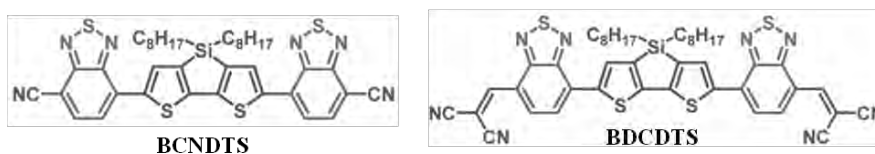
Scheme II-1: Synthesis strategies designed for obtaining Bz-based small molecules (R= octyl cyanoacetate and 2-ethylhexyl cyanoacetate).

Then, the D-A-D intermediate backbone will be further elongated by double Knoevenagel condensation, leading finally in only two steps to an A-D-A-D-A structure, with the benzothiadiazole as the central core.

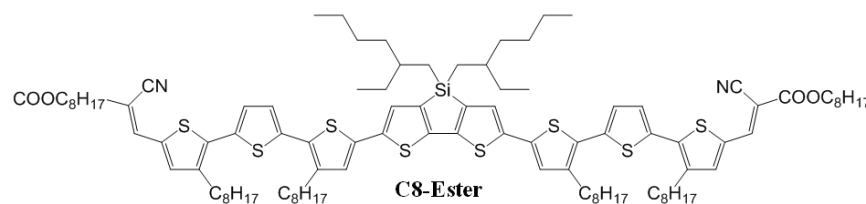
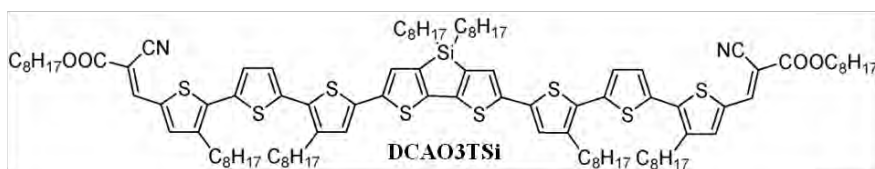
II. 2 Small molecules based on dithienosilole (DTS) core

The 4,4'-di-n-octyl-dithieno[3,2-b:2',3'-d]silole (dithienosilole, DTS) is a well-known electron-rich unit used for developing efficient organic photovoltaic cells, attributed to its highly planar geometry and good electron-donating ability.⁽²⁰⁶⁻²⁰⁹⁾ Yang *et al.* demonstrated that the 4-coordinate Si atom allows for incorporation of aliphatic side chains to guarantee the solubility of small molecules in organic solvents.⁽¹⁴⁴⁾ Figure II-6 shows chemical structures of some small-molecule donors based on DTS unit, their corresponding electronic properties and OPV performance are given in Table II-1.

A-A-D-A-A



A-D-D-D-A



D-A-D-A-D

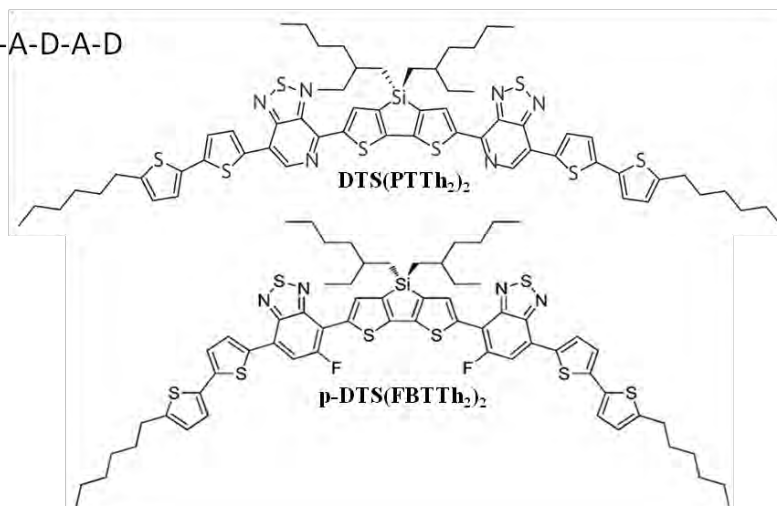


Figure II-6: Chemical structures of some donor materials based on DTS core (C8 = octyl).

L.-Y. Lin *et al.* reported two A-A-D-A-A structure molecules (BCNDTS and BDCDTS), where two different terminal electron-accepting moieties (cyano and dicyanovinylene, respectively) are connected to the central DTS block unit through another electron-withdrawing block (2,1,3-benzothiadiazole, Bz) have been used as electron donors for small-molecule based OPV. By changing cyano group to dicyanovinylene group, the efficiency decreased from 2.3% to 0.07%, which suggests that the cyano is better than dicyanovinylene group in this case (see Table II-1).⁽²¹⁰⁾ But these molecules with such terminal groups are not very soluble, thus their applications in OPV device are limited. Another two A-D-D-D-A structure small molecules, DCAO3TSi and C8-Ester, with the DTS unit as the central building

block, terthiophene as the π -bridge and octyl cyanoacetate as the terminal acceptor group, also showed moderate performance, offering efficiencies of 4.35% and 5.84%, respectively.(205, 211) Here the alkyl cyanoacetate group is a good compromise between dicyanovinyl for electron withdrawing and terminal alkyl chains for the solubility. For molecules DTS(PTTh₂)₂ and p-DTS(FBTTh₂)₂, the two electron acceptor units ([1,2,5] thiadiazolo [3,4-c] pyridine (PT) unit and fluorinated Bz unit) are linked through the DTS central block, and hexyl-substituted bithiophene are incorporated as the end-capping units, formatting a framework of D-A-D-A-D structure. This D-A-D-A-D structure contributes to strong intramolecular charge transfer characteristics and thus broad optical spectrum. From DTS(PTTh₂)₂ and p-DTS(FBTTh₂)₂, the fluorination simultaneously raises the HOMO and LUMO energy levels and increases the band gap (see Table II-1).

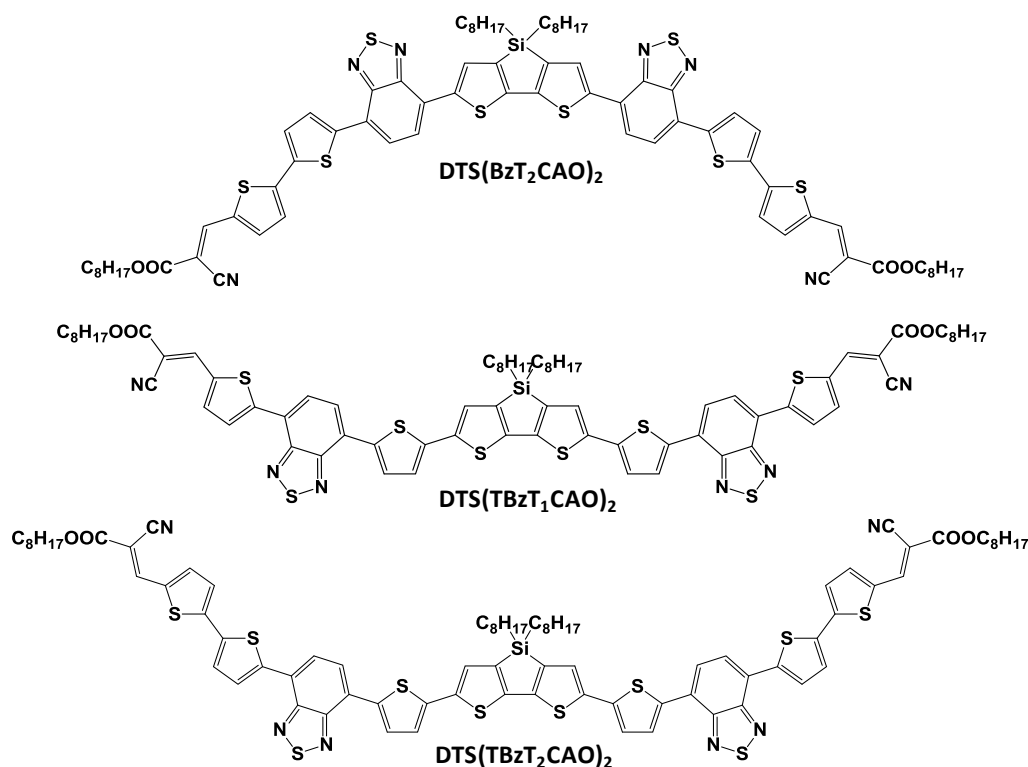
Table II-1: Electronic properties and OPV performance of some typical donors based on dithienosilole core.

Donor	HOMO/LUMO ^a (eV)	E _g (eV)	Acceptor	J _{sc} (mA cm ⁻²)	V _{oc} (V)	FF	PCE ^b (%)	Ref.
BDCDTS	-5.80/-3.92	1.88	C ₆₀	0.73	0.43	0.24	0.07	(210)
BCNDTS	-5.40/-3.23	2.17	C ₆₀	4.17	1.02	0.54	2.3	(210)
C8-Ester	-5.28/-3.52	1.76	PCBM	9.79	0.82	0.54	4.35	(205)
DCAO3TSi	-4.95/-3.26	1.69	PCBM	11.51	0.80	0.64	5.84	(211)
DTS(PTTh ₂) ₂	-5.2/-3.6	1.6	PC ₇₁ BM	14.4	0.78	0.593	6.7	(29)
p-DTS(FBTTh ₂) ₂	-5.12/-3.34	1.78	PC ₇₁ BM	14.74	0.773	0.724	8.24	(154)

^afrom electrochemistry, ^bfor the detailed donor/acceptor weight ratio in device, see the relevant references.

Among all the small molecules listed in Table II-1, DTS(PTTh₂)₂ and p-DTS(FBTTh₂)₂ show the highest performance, with PCEs of 6.7% and 8.24%, respectively.(29, 154) The improvement of performance is not only due to the role of molecular structure but also to the role of additives and annealing technique. Heeger *et al.* described that hexyl-substituted bithiophene end-capping units are advantageous for extending the π -conjugated structure and equally importantly for improving film-forming properties.(29) These studies reveal that different strategies such as changing the length of alkyl side chain and choosing different

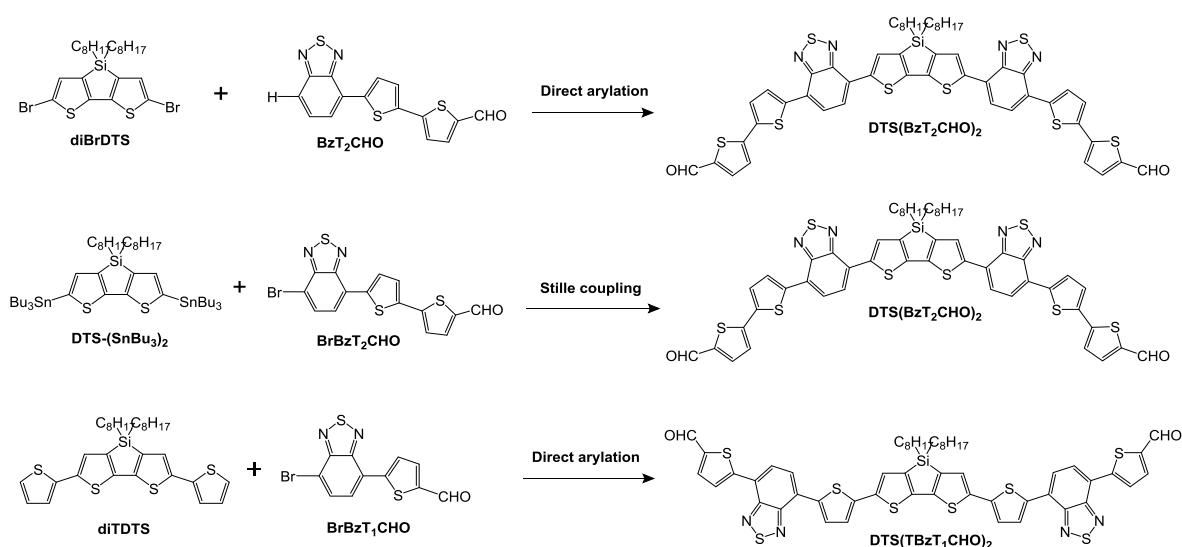
terminal acceptor moieties could be used to finely tune the molecular structures and thus tune the optoelectronic properties, solubility and intermolecular interactions of DTS-based small molecules. Inspired by these small molecules, as a result, we designed a set of A-D-A-D-A-D-A-type small molecules, with the DTS unit as the central block linked with high electron-affinity Bz units, thiophene or bithiophene as the π -conjugated bridge, and octyl cyanoacetate or 2-ethylhexyl cyanoacetate as two different terminal electron-accepting moieties. The chemical structures of these DTS-based target molecules are given in Scheme II-2.



Scheme II-2: Chemical structures of designed target molecules based on DTS core.

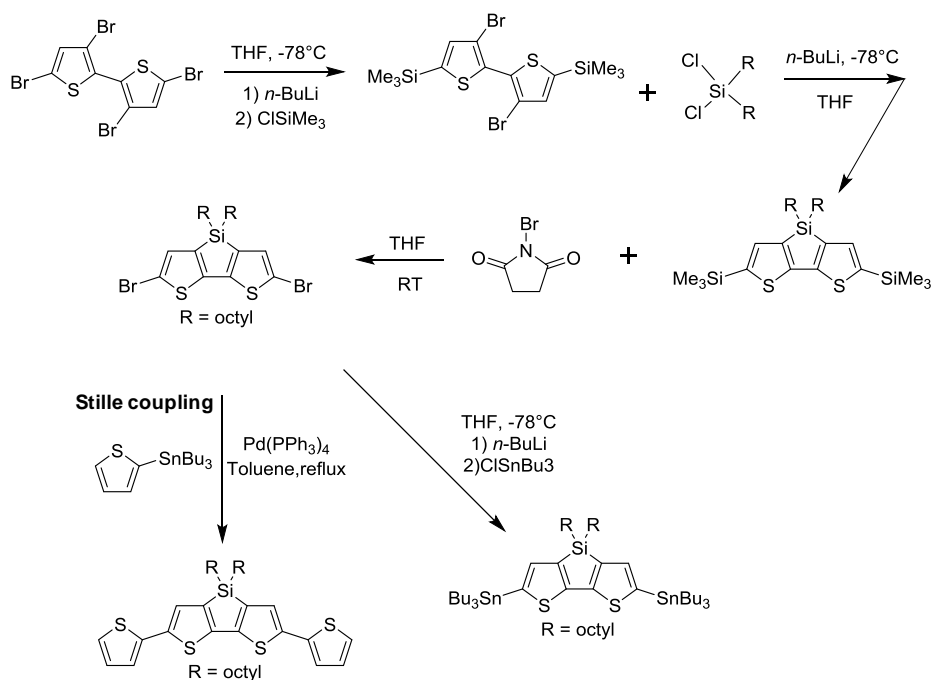
To obtain these DTS-based target molecules, first we need to find appropriate intermediates. As evidenced by Scheme II-3, different precursors, such as $\text{DTS}(\text{BzT}_2\text{CHO})_2$ and $\text{DTS}(\text{TBzT}_1\text{CHO})_2$ are necessary to be obtained. The reactant 4,4'-dioctyl-5,5'-dibromodithieno[3,2-b:2',3'-d]-silole (diBrDTS) is commercial. The $\text{DTS}(\text{BzT}_2\text{CHO})_2$ precursor could be obtained within two steps and *via* direct arylation: the first step consists of the coupling between 4-bromo-2,1,3-benzothiadiazole (BrBz) and 2,2'-bithiophene-5-carboxaldehyde (T_2CHO), which are both commercial, leading to fragment BrBzT_2CHO ; the second step consists of the coupling of the diBrDTS core with the previously obtained BzT_2CHO fragment (see Scheme II-3 top). $\text{DTS}(\text{BzT}_2\text{CHO})_2$ could be also obtained within three steps, the two last belonging to Stille coupling: the first step is the direct arylation leading to fragment BrBzT_2CHO ; the second step is the reaction between diBrDTS and tri-n-

butyltin chloride (ClSnBu_3), leading to fragment $\text{DTS}-(\text{SnBu}_3)_2$; the third step is the Stille coupling between fragments $\text{DTS}-(\text{SnBu}_3)_2$ and BrBzT_2CHO . After double Knoevenagel condensation, therefore, the target molecule $\text{DTS}(\text{BzT}_2\text{CAO})_2$ could be obtained in three (*via* direct arylation) or four steps (*via* Stille coupling). Similarly, precursor $\text{DTS}(\text{TBzT}_1\text{CHO})_2$ could be obtained within three steps: the first step is the coupling between 4,7-dibromobenzo-2,1,3-thiadiazole (diBrBz) and 2-thiophenecarboxaldehyde (TCHO), leading to fragment BrBzT_1CHO ; the second step is the Stille coupling between diBrDTS and 2-(tributylstannyl) thiophene (TSnBu_3), leading to fragment diTDTS; the third step is the coupling between fragments diTDTS and BrBzT_1CHO . Thus, after double Knoevenagel condensation, the target molecule $\text{DTS}(\text{TBzT}_1\text{CAO})_2$ could be obtained in four steps *via* direct arylation. The synthesis strategy for obtaining the target molecule $\text{DTS}(\text{TBzT}_2\text{CAO})_2$ is very similar to that for $\text{DTS}(\text{TBzT}_1\text{CAO})_2$, the third step will be the coupling between fragments diTDTS and BrBzT_2CHO , and the last step will be double Knoevenagel condensation.

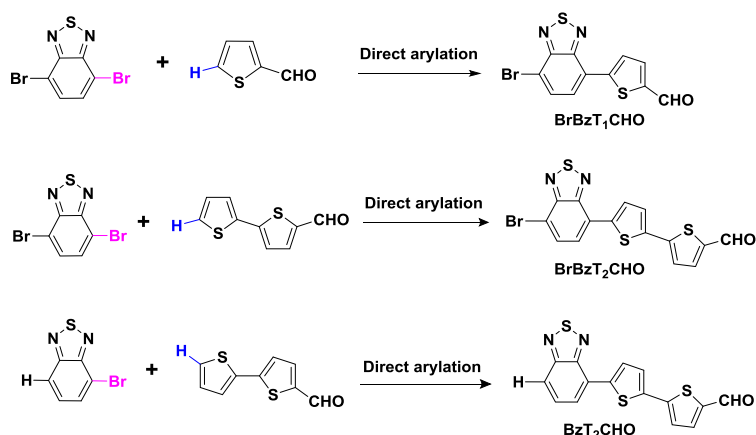


Scheme II-3: Synthesis routes to obtain precursors for DTS-based target molecules.

Prior to the synthesis of precursors, various fragments displayed in Scheme II-3 need to be synthesized, such as different DTS cores and fragments originated from 2,1,3-benzothiadiazole and thiophene (or bithiophene) carboxaldehyde. Due to the high cost of fragment diBrDTS, we planned to synthesize it in our lab although it is commercially available. The proposed synthetic strategies for obtaining DTS cores and Bz-based fragments are presented in Scheme II-4 and Scheme II-5, respectively.



Scheme II-4: General procedure to synthesize the DTS cores for the target molecules.



Scheme II-5: Envisaged synthesis routes for Bz-based fragments *via* direct arylation.

Fragment diBrDTS can be obtained in three steps, while DTS-(SnBu₃)₂ and diTDTS can be obtained in one more step. Bz-based fragments (BrBzT₁CHO, BrBzT₂CHO and BzT₂CHO) can be obtained in one step by direct arylation. Then DTS-based cores need to be coupled with these non-symmetrical Bz-based fragments that are not easy to be isolated to achieve target molecules. The details about these syntheses will be given in Chapter III.

II. 3 Small molecules based on subphthalocyanines (SubPcs)

Subphthalocyanines (SubPcs) were discovered coincidentally in 1972 by Meller and Ossko (212) when they were attempting to synthesize boron phthalocyanines (BPCs). SubPcs (185, 186, 213) as the best known contracted porphyrinoid species, are a novel class of Pcs (214) related compounds, comprising three instead of four N-fused diiminoisoindoline units

centered around a boron core. They possess a 14 π -electron aromatic core but nonplanar cone-shaped geometry (see Figure II-7) with the tetrahedral boron center out of plane with the three aromatic ligands as confirmed by X-ray crystallography.(215) The 14- π -electron system feature of SubPcs endows them attractive research topic due to their unique optical (strong absorption in the visible 550-600 nm) that have been demonstrated great potential in the fields of nonlinear optics, photonic devices, and dyes.(185, 186) In addition, their electrical properties could be fine-tuned as the peripheral and axial positions in SubPcs can be easily functionalized or derived.(185, 186) SubPcs and their derivatives have attracted great concern of numerous of chemists, physicists and materials scientists, attributed to the promising and profound influence in many cutting-edge fields, such as the applications in organic photovoltaic cells,(31, 74, 216-231) as novel and efficient light-harvesting units for artificial photosynthetic systems,(232) organic light-emitting diodes,(233-236) organic field effect transistors (OFETs),(237-240) optical information recording media.(241-245) Moreover, the unique electronic and optical properties displayed in SubPcs have been demonstrated to exhibit a significant extinction coefficient (k , associated with complex refractive index $\tilde{n} = n - ik$) up to 1.6 at 590 nm in sublimated films, and promising power conversion efficiency of 3.0% have been proved in OPVs.(74, 218)



Figure II-7: 3D structure of SubPcBCl illustrating its unique bowl-shaped structure: a top view (left) and side view (right). (white sticks: H; grey sticks: C; blue sticks: N; yellow sticks: B; green stick: Cl).(221)

In particular, SubPcs exhibit two absorption bands, a Soret (B) band (in the UV) and a Q-band (in the visible) at $\lambda_{\max} = 307$ and 565 nm, respectively. Axial (see Figure II-8) substituents have only a quite weak influence on the location of the bands.(185, 246, 247) Conversely, peripheral (see Figure II-8) electron donor or acceptor substituents are capable to slightly elongate the π -conjugation of the aromatic ring to shift the Q band of SubPcs toward longer wavelengths.(232, 248, 249) Particular attention has been paid to enhance light-harvesting and adjust the kinetics, as well as the yield of photo-induced energy and electron transfer

processes in SubPc-based donor-acceptor systems. The singular structures of SubPc-based chromophores show intense Q-band transitions in the 550-650 nm range.

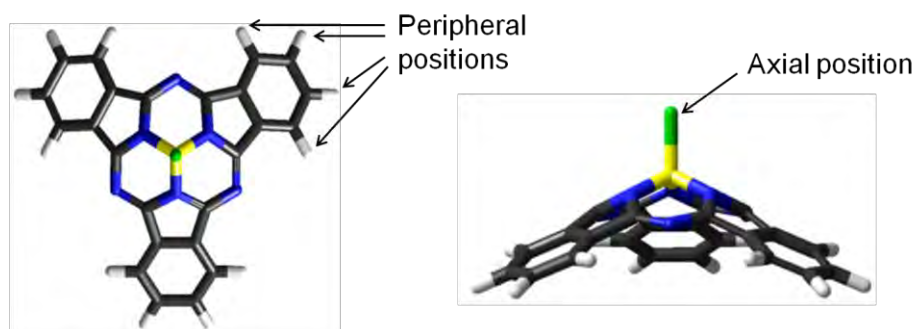


Figure II-8: The axial and peripheral positions on SubPcBCl. (white sticks: H; grey sticks: C; blue sticks: N; yellow sticks: B; green sticks: Cl).(221)

Apart from the outstanding electronic properties, SubPcs display multiple options for functionalization at the axial (219, 234, 247, 250) or peripheral positions (185, 186, 216, 234, 248) (see Figure II-8). As a consequence, peripheral substituted SubPcs have significant influence on the electronic characteristics of macrocycle, and it is worth mentioning that their nature, with respect to that of axial groups, induces the most relevant impact on the stability of the SubPcs materials exposed to sunlight.(186) The presence of π -conjugated functional groups or electron-rich or electron-deficient groups on the isoindole rings significantly affects the location of the frontier orbital levels (HOMO-LUMO), thus as a consequence, the Q-band absorption and emission maxima, and the redox potentials.(234, 251) On one hand, it has been demonstrated that SubPcs can function as energy donors (252-255) or energy acceptors(256), or function as electron donors or acceptors in D-A systems (249, 257). On the other hand, SubPcs show low tendency to aggregate in solution because of their non-planar structure. Nonetheless, it is easy to tailor the redox and excited states of these molecules, so that SubPcs can play various roles in electron/energy donors or acceptors in artificial photosynthetic systems.(232, 249, 252, 255, 257-265)

Recently, an extraordinary development of organic photovoltaic cells has taken place. Now, SubPcs can be regarded as both donor and acceptor materials in OPV cells due to their special electronic and optical properties.(216, 218) Figure II-9 provides the chemical structures of some materials associated with SubPcs in OPV application. The corresponding performances are presented in Table II-2.

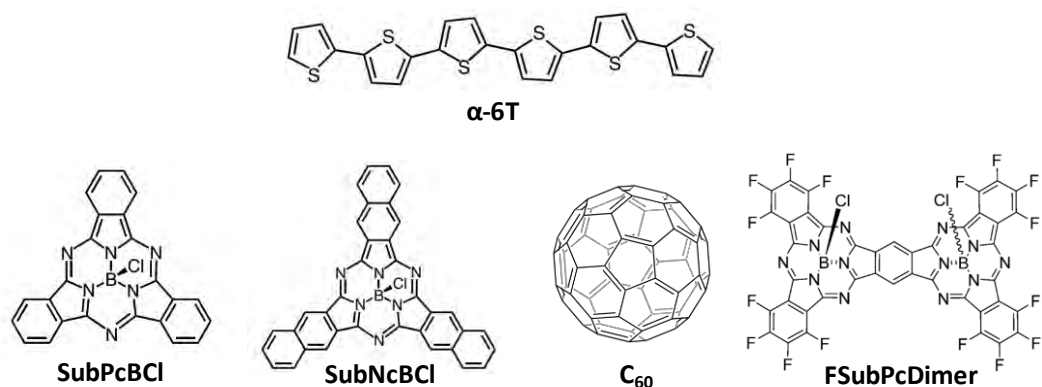


Figure II-9: Chemical structures of some materials associated with SubPcs in OPV application.

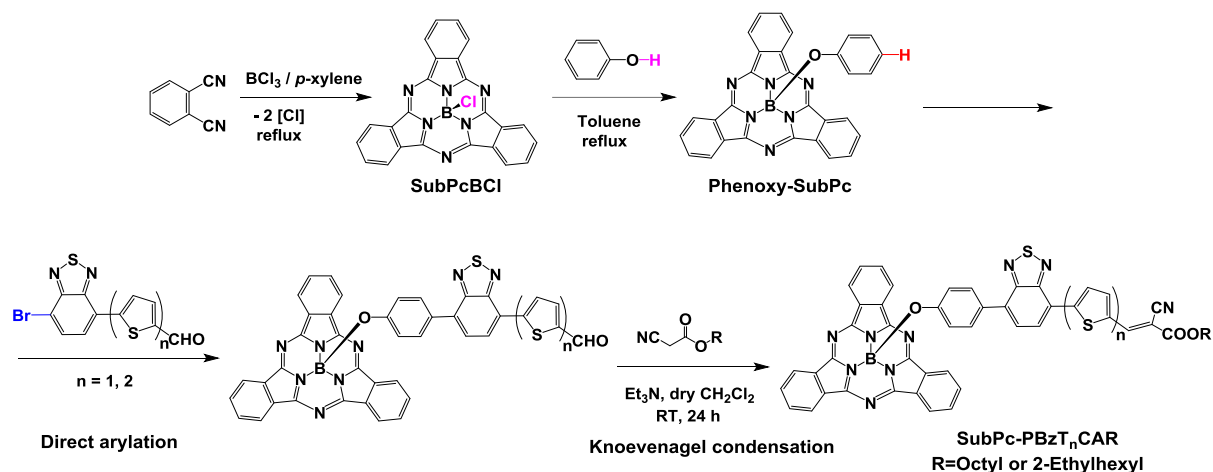
From Table II-2, we can see that SubPcs can function as electron donor with a good efficiency of 3.0% and 4.0% when using C₆₀ and fused fluorinated SubPc dimer (FSubPcDimer, see Figure II-9) as electron acceptors, respectively. SubPcs can also act as electron acceptor with a higher efficiency of 4.69%. When combining SubPcBcl and SubNcBcl as acceptors in a three-layer device, this leads to a remarkable PCE of 8.4%. This is the best non-fullerene-based OPV cell reported up to now, consisting of a SubPcBcl acceptor.

Table II-2: Performance of some OPV devices based on SubPcs.

Donor	Acceptor	J _{sc} (mA cm ⁻²)	V _{oc} (V)	FF	PCE ^a (%)	Ref.
SubPcBcl	C ₆₀	5.4	0.92	0.61	3.0	(216)
SubPcBcl	FSubPcDimer	7.8	0.95	0.54	4.0	(226)
α -6T	SubPcBcl	4.17	1.02	0.54	4.69	(31)
α -6T	SubNcBcl/SubPcBcl	9.79	0.82	0.54	8.40	(31)

^afor the detailed donor/acceptor weight ratio in device, see the relevant references.

In summary, inspired by the unique optical and electrical properties of SubPcs and their potential in OPV device, we envisaged to combine fragments BrBzT₁CHO and BrBzT₂CHO with phenol-substituted SubPcs (see Scheme II-6). This would lead to a set of novel SubPcs derivatives. The chemical structures and synthesis strategies proposed for SubPcs-based novel molecules are shown in Scheme II-6. More details about the synthesis will be described in the next chapter.



Scheme II-6: Designed SubPcs derivatives and synthesis strategies *via* axial substitution.

Once molecules were designed, theoretical calculations were carried out to predict their electronic properties and thus to evaluate their potential in OPV applications.

III Theoretical calculation

Nowadays, molecular modeling techniques and particularly quantum chemistry provide a competitive alternative for interpretation of experimental results, as well as for molecular design through the prediction of optoelectronic properties. The density functional theory (DFT) (184) method and time-dependent DFT (TD-DFT)(266-268) can offer a good treatment of the electron correlation effects, therefore, compare very well with the experimental results.(269, 270) Thus, to further predict the electronic properties of all designed molecules aforementioned, we conducted all the calculations using DFT method at the B3LYP/Def2-TZVP(-f) level. To facilitate the computation, the terminal octyl or 2-ethylhexyl chains were replaced by methyl groups.

III. 1 Bz-based small molecules

III. 1-1 Electronic and optical properties

To ensure that optimized geometries of Bz-based small molecules will be the most stable conformation, the core fragment (4,7-dithieno-2,1,3-benzothiadiazole, diTBz) was first optimized with different configuration (see Figure II-10). From the energy listed in Table II-3, one can observe that the *trans-trans* conformation offers the lowest energy among the three confirmations, suggesting it is the most stable confirmation. It shows good agreement with the work of Nielsen and co-worker which declared that calculations using Gaussian at the

B3LYP/6-31G* level of theory predicted the *trans-trans* conformation to be the most stable for diTBz.(271)

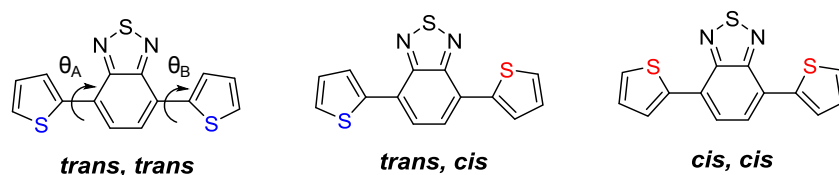


Figure II-10: Conformations of diTBz characterized by dihedral angles (θ_A and θ_B).

Orbital energy levels and dihedral angles of diTBz in different conformation are also listed in Table II-3. Their energy levels are very close to each other, with slightly deviation in the range of 0.03-0.05 eV. *Trans-trans* conformation shows the lowest energy gap and smallest dihedral angles, revealing that *trans-trans* conformation is theoretically easier for electron transfer along the backbone chain compared to *trans-cis* and *cis-cis* conformations. It reveals that the *trans-trans* conformation is the good choice in our related calculations.

Table II-3: Total energy, orbital energy levels and dihedral angles of diTBz.

conformation	Total energy (Eh)	HOMO/LUMO (eV)	E_g (eV)	θ_A/θ_B ($^\circ$)
<i>trans-trans</i>	-1842.65750205	-5.60/-2.85	2.75	2.17 / 5.21
<i>trans-cis</i>	-1842.65638543	-5.64/-2.80	2.84	20.85 / 23.28
<i>cis-cis</i>	-1842.65547381	-5.60/-2.80	2.80	22.18 / 18.89

Figure II-11 displays the frontier orbitals of diTBz in different conformations. It shows no difference in the electron density distribution among the three conformations. The HOMO is delocalized over the whole molecule, while the LUMO is localized on the electron-accepting Bz unit.

Conformation	HOMO	LUMO
<i>trans-trans</i>		
<i>trans-cis</i>		
<i>cis-cis</i>		

Figure II-11: Frontier molecular orbitals of diTBz in different conformations at the B3LYP/Def2-TZVP(-f) level.

For the Bz-based small molecules, named as Bz(T₁CAEH)₂, Bz(T₁CAO)₂, Bz(T₂CAEH)₂, Bz(T₂CAO)₂, Bz(T₃CAEH)₂, Bz(T₃CAO)₂, Bz(T₄CAEH)₂ and Bz(T₄CAO)₂ (see Figure II-5), replacing terminal octyl or 2-ethylhexyl chains by methyl groups leads to the newly named Bz(T₁CAMe)₂, Bz(T₂CAMe)₂, Bz(T₃CAMe)₂ and Bz(T₄CAMe)₂ (see Figure II-12).

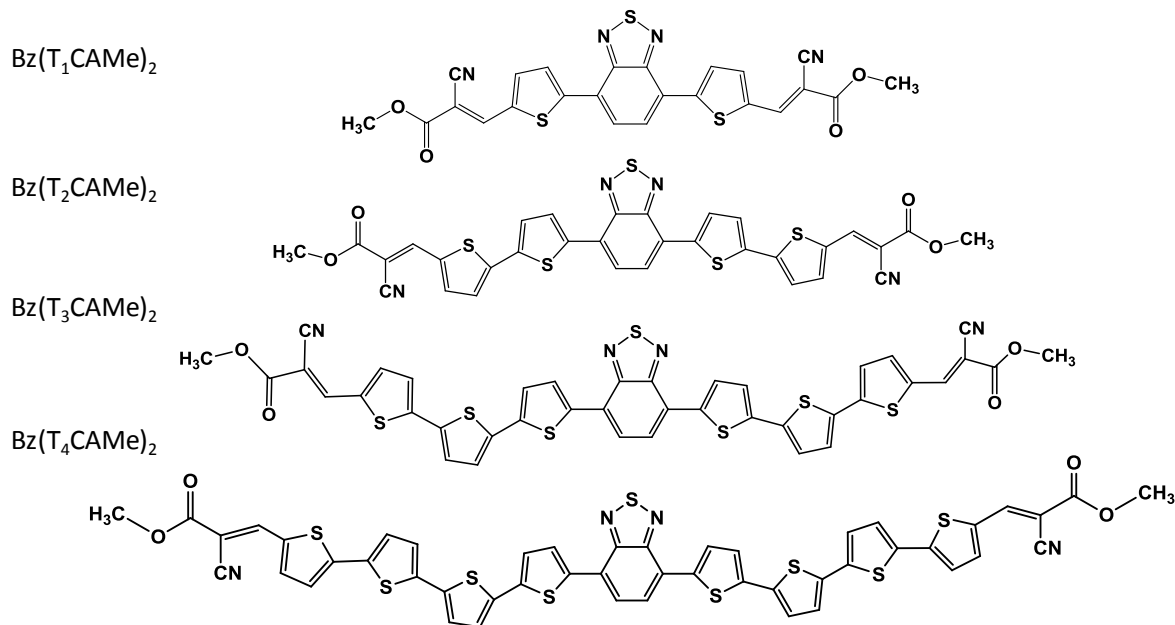


Figure II-12: Structures of designed molecules with different conjugation lengths.

Generally, the molecular structure is a critical factor to determine the performance of SM-OPVs. Especially a planar molecular conformation is benefit for favouring the intermolecular π - π packing over other conformations.⁽²¹¹⁾ Therefore, the geometries at the ground state of these molecules was optimized by using B3LYP functional with Def₂-TZVP(-f) basis set. The structural analysis for optimized geometries of Bz(T₁CAMe)₂, Bz(T₂CAMe)₂, Bz(T₃CAMe)₂ and Bz(T₄CAMe)₂ were investigated by examining calculated dihedral angles (defined as the dihedral angle for adjacent rings) indicated in Figure II-13. These results are collected in Table II-4.

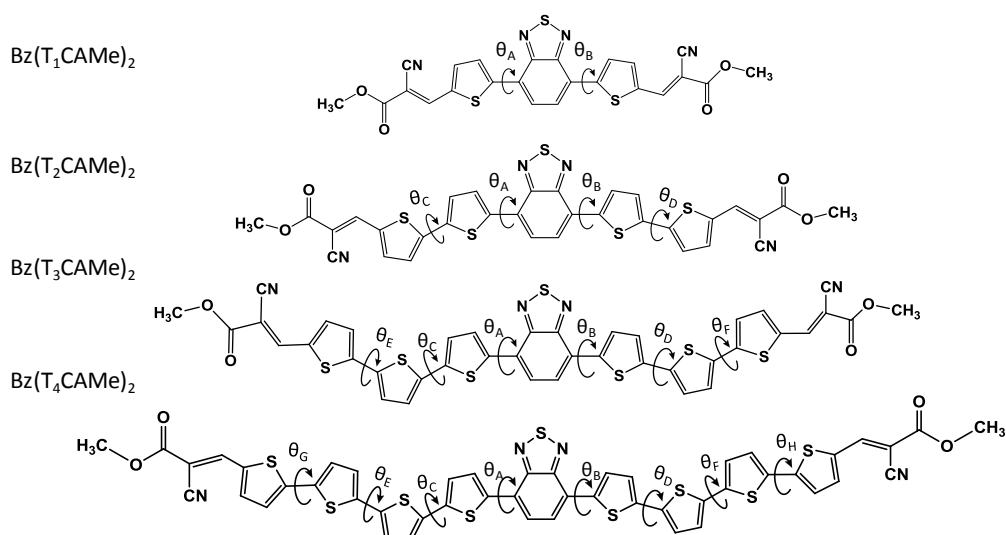


Figure II-13: The scheme of dihedral angles for structural analysis.

The dihedral angles (θ_A , θ_B , θ_C , θ_D) are defined as the dihedral angle for adjacent rings. The dihedral angles for $\text{Bz}(\text{T}_1\text{CAME})_2$, $\text{Bz}(\text{T}_2\text{CAME})_2$ and $\text{Bz}(\text{T}_3\text{CAME})_2$ are in the range of 1-6°, suggesting their good coplanarity. It indicates such nearly planar geometry is favorable to the π electron transfer from the electron-donating unit to electron-withdrawing moiety. Note that here the dihedral angle values (italic) for $\text{Bz}(\text{T}_4\text{CAME})_2$ are not strictly accurate because here the geometry optimization of $\text{Bz}(\text{T}_4\text{CAME})_2$ is not totally achieved (as there is one imaginary frequency), although it shows good coplanarity. Due to the large molecular system of $\text{Bz}(\text{T}_4\text{CAME})_2$, the computation is time-consuming, thus the further optimization is so far not finished yet. In addition, to synthesis ter-thiophene and quater-thiophene fragments, at least one or two more steps will be needed from the commercial reagent, which will cause difficulty in the synthesis. Thus we do not envisage to synthesize $\text{Bz}(\text{T}_3\text{CAME})_2$ and $\text{Bz}(\text{T}_4\text{CAME})_2$.

Table II-4: Dihedral angles (°) in $\text{Bz}(\text{T}_1\text{CAME})_2$, $\text{Bz}(\text{T}_2\text{CAME})_2$, $\text{Bz}(\text{T}_3\text{CAME})_2$ and $\text{Bz}(\text{T}_4\text{CAME})_2$.

	θ_A	θ_B	θ_C	θ_D	θ_E	θ_F	θ_G	θ_H
$\text{Bz}(\text{T}_1\text{CAME})_2$	1.25	1.24						
$\text{Bz}(\text{T}_2\text{CAME})_2$	2.68	2.05	3.01	1.29				
$\text{Bz}(\text{T}_3\text{CAME})_2$	0.85	3.25	1.07	0.29	6.22	4.63		
$\text{Bz}(\text{T}_4\text{CAME})_2$	<i>0.12</i>	<i>4.93</i>	<i>0.20</i>	<i>1.93</i>	<i>1.59</i>	<i>2.27</i>	<i>1.00</i>	<i>0.75</i>

Frontier molecular orbitals of $\text{Bz}(\text{T}_1\text{CAME})_2$, $\text{Bz}(\text{T}_2\text{CAME})_2$, $\text{Bz}(\text{T}_3\text{CAME})_2$ and $\text{Bz}(\text{T}_4\text{CAME})_2$ are presented in Figure II-14. It illustrates that the HOMOs of $\text{Bz}(\text{T}_1\text{CAME})_2$ and $\text{Bz}(\text{T}_2\text{CAME})_2$ are distributed almost entirely over the conjugated molecule that adopts an aromatic character, which is beneficial for obtaining high charge mobility. The LUMO of $\text{Bz}(\text{T}_1\text{CAME})_2$ and $\text{Bz}(\text{T}_2\text{CAME})_2$ are slightly concentrated on benzothiadiazole unit in the two species with a quinoid character. However, for $\text{Bz}(\text{T}_3\text{CAME})_2$ and $\text{Bz}(\text{T}_4\text{CAME})_2$, their HOMO orbitals are more concentrated in the central part of the backbone, while their LUMOs are more localized on the benzothiadiazole and cyano groups. This phenomenon could be interpreted as the effect of the torsion in their geometries. Besides, we can observe that from $\text{Bz}(\text{T}_1\text{CAME})_2$ to $\text{Bz}(\text{T}_4\text{CAME})_2$, with the increase in the conjugation length, the HOMO and LUMO energy levels are increased simultaneously. The increased degree of HOMO energy levels is larger than that of LUMO, which leads to lowering trend in the band gap. Note that although the nature of the optimized $\text{Bz}(\text{T}_4\text{CAME})_2$ was not checked, it is expected that the electron density distribution of its frontier molecular orbitals and the general trend in energy levels and energy gaps from $\text{Bz}(\text{T}_1\text{CAME})_2$ to $\text{Bz}(\text{T}_4\text{CAME})_2$ will not be affected.


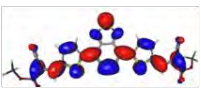
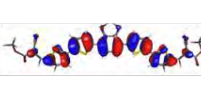
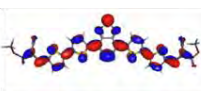

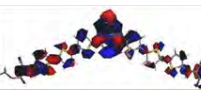

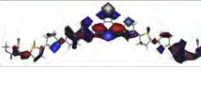
	HOMO	LUMO	HOMO (eV)	LUMO (eV)	Eg (eV)
$\text{Bz}(\text{T}_1\text{CAME})_2$			-6.29	-3.89	2.4
$\text{Bz}(\text{T}_2\text{CAME})_2$			-5.79	-3.64	2.15
$\text{Bz}(\text{T}_3\text{CAME})_2$			-5.56	-3.51	2.05
$\text{Bz}(\text{T}_4\text{CAME})_2$			-5.37	-3.39	1.98

Figure II-14: Frontier molecular orbitals of $\text{Bz}(\text{T}_1\text{CAME})_2$, $\text{Bz}(\text{T}_2\text{CAME})_2$, $\text{Bz}(\text{T}_3\text{CAME})_2$ and $\text{Bz}(\text{T}_4\text{CAME})_2$ in their optimized geometries at B3LYP/Def2-TZVP(-f) level.

To obtain further insights into the effect of molecular structure and electron distribution on the electronic characteristics, calculations of the electronic structure of molecules $\text{Bz}(\text{T}_1\text{CAME})_2$ and $\text{Bz}(\text{T}_2\text{CAME})_2$ in excited states were performed with the help of Prof. Fabienne Alary. Because molecules $\text{Bz}(\text{T}_3\text{CAME})_2$ and $\text{Bz}(\text{T}_4\text{CAME})_2$ are much larger, to perform TD-DFT calculations on them will be very time-consuming, and it is not necessary to synthesize them, therefore, they were not further studied by TD-DFT. The Natural Transition

Orbitals (NTOs) can provide a qualitative description of an electronic excitation. One can obtain a nicely pictorial view of the transition process from the NTOs.(272) In order to get qualitative insights on the nature of the electronic transitions responsible for the absorption spectrum of Bz(T₁CAMe)₂ and Bz(T₂CAMe)₂, the NTOs have been calculated and the strongest transition of each molecule is indicated in Figure II-15. A more extensive list of computed transitions and the simulated TD-DFT spectra are provided in the Annexes 7. It appears from the NTO analysis that for the two species, the highest transition is dominated by a HOMO-LUMO transition leading to an excitation slightly localized on the acceptor part. To complete this analysis, calculations on the redox species definitely confirm that electron abstraction and electron addition take place on the HOMO and LUMO, respectively, of the ground state neutral species.


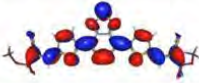

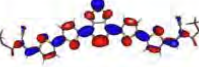
	λ_{\max} (nm)	Hole	Electron
Bz(T ₁ CAMe) ₂	471		
Bz(T ₂ CAMe) ₂	528		

Figure II-15: NTOs isodensity surface for the strongest transition are represented and the associated wavelengths are indicated for Bz(T₁CAMe)₂ and Bz(T₂CAMe)₂ in CH₂Cl₂ at B3LYP/Def2-TZVP(-f) level.

Different functionals were tested to predict the absorption spectra, including PBE0, B3LYP, CAM-B3LYP and BHandHLYP. The simulated absorption spectra with various functionals for Bz(T₁CAMe)₂ and Bz(T₂CAMe)₂ in the CH₂Cl₂ environment are shown in Figure II-16. It shows that both molecules have the similar spectrum shape and the latter exhibits a red shift of around 50 nm relative to Bz(T₁CAMe)₂ due to its stronger π conjugation. The spectra shape shows no change with different functionals, only red or blue shift of the maximum absorption peaks occurs. The excitations and absorption maxima in energies are of 2.63 and 2.35 eV for Bz(T₁CAMe)₂ and Bz(T₂CAMe)₂, respectively. From these computed data, addition of one thiophene unit determines a sizable red shift of the spectra. The BHandHLYP simulated absorption spectrum of Bz(T₁CAMe)₂ and Bz(T₂CAMe)₂ in CH₂Cl₂ and NTO isodensity surface for main transitions ($f > 0.05$, f is oscillator strengths) are given in Annexes 7.

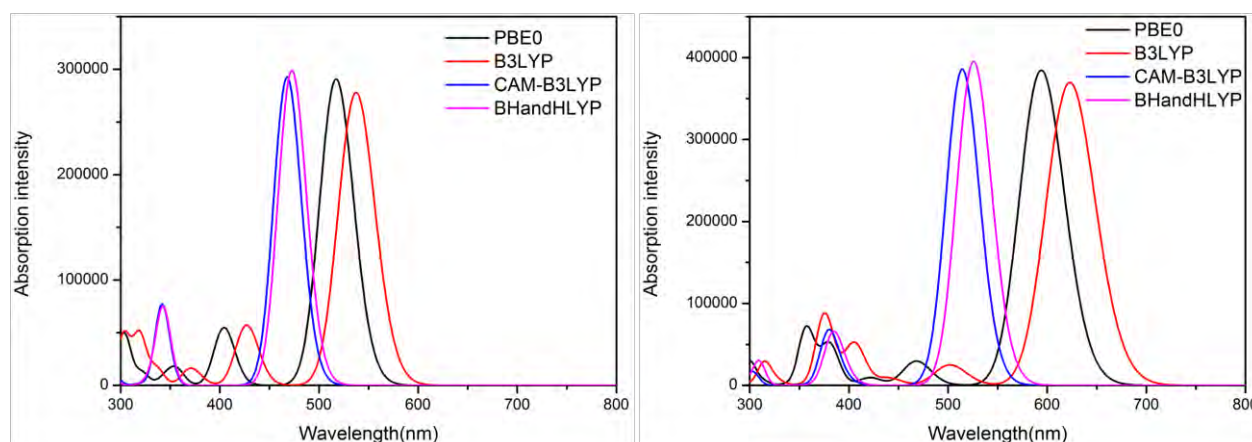


Figure II-16: Simulated absorption spectra of Bz(T₁CAMe)₂ (left) and Bz(T₂CAMe)₂ (right) with different functionals with Def2-TZVP(-f) basis set.

As already discussed in chapter I, for OPVs, the energy level of donor HOMO and the energy level of acceptor LUMO should match the anode/cathode to achieve a higher/lower work function, respectively. Meanwhile, the energy difference or offset (ΔE), between the donor LUMO energy and the acceptor LUMO energy should be larger than 0.3 eV, which is the determining driving force required to guarantee efficient charge separation at the D/A interface. The V_{oc} value can be theoretically obtained from the LUMO of PCBM (-4.3 eV)(141), according to the empirical Scharber model.(61) Table II-5 lists evaluated V_{oc} and ΔE predicted with Bz(T₁CAMe)₂, Bz(T₂CAMe)₂, Bz(T₃CAMe)₂ and Bz(T₄CAMe)₂ as donors associated with PCBM as the acceptor. The calculated V_{oc} values of OPV systems based on these molecules are from 0.77 to 1.7 V. Such large values are of great importance for OPV performance. In particular, V_{oc} predicted with molecules Bz(T₁CAMe)₂ and Bz(T₂CAMe)₂ exhibit significantly large values (beyond 1.0 V), suggesting that active layers consisting of these components associated with PCBM can be expected to have a potential in OPV devices. The ΔE values for the four molecules are all larger than 0.3 eV, which is an encouraging parameter for charge separation upon electron transfer from donor to acceptor.

Table II-5: Theoretical open-circuit voltage and energy offset in blends of Bz(T₁CAMe)₂, Bz(T₂CAMe)₂, Bz(T₃CAMe)₂ and Bz(T₄CAMe)₂ with PCBM.

	V_{oc} (V)	ΔE (eV)
Bz(T ₁ CAMe) ₂	1.7	0.4
Bz(T ₂ CAMe) ₂	1.2	0.66
Bz(T ₃ CAMe) ₂	0.96	0.8
Bz(T ₄ CAMe) ₂	0.77	0.9

III. 1-2 Effect of fluorine substitution

Substitution of carbon or hydrogen atoms with fluorine in D-A based organic molecules has been shown to tune the molecular orbital levels and thus impact on the photovoltaic performance of an OPV device.(63, 81, 127) The introduction of F atom into the conjugated backbone can simultaneously lower the HOMO and LUMO levels, giving only minor changes to the optical band gap.(49) Thus, enhanced stability against photo-oxidation by lowering the HOMO energy level can be achieved. Fluorination of conjugated molecules offers a series of unique features such as great thermal and oxidative stability, elevated resistance to degradation,(273) enhanced hydrophobicity,(274) and high lipophobicity in perfluorinated substances.(275) These features are related to the unique properties of the fluorine atom: first, fluorine atom is the smallest electron-withdrawing group with a Van der Waals radius of 1.35 Å, only slightly larger than that of hydrogen (1.2 Å); second, fluorine atom is the most electronegative element, presenting a Pauling electronegativity of 4.0, which is much larger than that of hydrogen (2.2).(127) In addition, fluorine atoms often have a great effect on inter- and intramolecular interactions *via* C-F \cdots H, F \cdots S, and C-F \cdots π_F interactions.(274, 276) Such interactions can improve molecular organization leading to shorter π - π stacking distances that improve charge carrier mobility.(277) Fluorination may be therefore a promising strategy to improve the PCE of OPV devices.

To theoretically study the effect of fluorine substitution, we started from the simple case: the fluorinated diTBz derivative, 5,6-difluoro-4,7-dithieno-2,1,3-benzothiadiazole (diTffBz), deriving from Figure II-10. To compare the calculated results on diTBz and diTffBz, their corresponding frontier orbitals and electronic properties with different conformations are provided in Figure II-17. Like it was the case for diTBz, it shows no difference in the electron density distribution among the three conformations of diTffBz. The HOMO is distributed over the whole molecule, while the LUMO is concentrated on the electron-accepting Bz unit. It shows that the theoretically most stable conformation, for diTffBz, is *trans-trans*, like for the previously studied diTBz. One can also observe that the di-fluorination of diTBz unit reduces both HOMO and LUMO energy levels but widens the energy gap, which is in good agreement with the experimental results reported by Son *et al.*(278).

	Total Energy (Eh)	HOMO	LUMO	HOMO/LUMO (eV)	E_g (eV)
diTBz (<i>trans-trans</i>)	-1842.65750205			-5.60/-2.85	2.75
diTBz (<i>trans-cis</i>)	-1842.65638543			-5.64/-2.80	2.84
diTBz (<i>cis-cis</i>)	-1842.65547381			-5.60/-2.80	2.80
diTffBz (<i>trans-trans</i>)	-2041.20436988			-5.81/-2.95	2.86
diTffBz (<i>trans-cis</i>)	-2041.20388083			-5.79/-2.94	2.85
diTffBz (<i>cis-cis</i>)	-2041.20321912			-5.82/-2.91	2.91

Figure II-17: Frontier molecular orbitals and electronic properties of diTBz and diTffBz with different conformations calculated by DFT. (Eh = Hartree energy, 1 hartree = 27.2107 eV)

Following calculation results on diTffBz, the fluorinated Bz(T₁CAMe)₂, Bz(T₂CAMe)₂, Bz(T₃CAMe)₂ and Bz(T₄CAMe)₂ are named as ffBz(T₁CAMe)₂, ffBz(T₂CAMe)₂, ffBz(T₃CAMe)₂ and ffBz(T₄CAMe)₂ with the diTffBz core. Their geometries at the ground state were optimized using DFT method with the B3LYP/Def₂-TZVP(-f) level. Similarly, the structural analysis for optimized geometries of these fluorinated derivatives were investigated by examining calculated dihedral angles (as indicated in Figure II-13). These results are presented in Table II-6.

Table II-6: Dihedral angles (°) in ffBz(T₁CAMe)₂, ffBz(T₂CAMe)₂, ffBz(T₃CAMe)₂ and ffBz(T₄CAMe)₂.

	θ_A	θ_B	θ_C	θ_D	θ_E	θ_F	θ_G	θ_H
ffBz(T ₁ CAMe) ₂	3.81	0.95						
ffBz(T ₂ CAMe) ₂	0.69	0.19	4.16	0.17				
ffBz(T ₃ CAMe) ₂	3.65	8.85	1.70	1.90	4.63	3.07		
ffBz(T ₄ CAMe) ₂	21.78	14.90	4.55	1.43	3.36	2.54	4.90	10.10

Like it is the case for Bz(T₁CAMe)₂, Bz(T₂CAMe)₂, and Bz(T₃CAMe)₂, the dihedral angles for ffBz(T₁CAMe)₂, ffBz(T₂CAMe)₂ and ffBz(T₃CAMe)₂ are in a reasonable range of 1-8°, suggesting good coplanarity. It indicates that such good coplanarity is benefit for the π electron transfer from the electron-donating unit to the electron-withdrawing moiety. On the contrary, the large dihedral angles observed for ffBz(T₄CAMe)₂ reveal obvious torsion in the geometry due to the elongated chain. Similarly, like it is the case for Bz(T₃CAMe)₂ and Bz(T₄CAMe)₂, we do not envisage to synthesize ffBz(T₃CAMe)₂ and ffBz(T₄CAMe)₂ due to the difficulty in their synthesis.

Figure II-18 presents their frontier orbitals and electronic properties. The comparison of these results with those obtained with Bz(T₁CAMe)₂, Bz(T₂CAMe)₂, Bz(T₃CAMe)₂ and Bz(T₄CAMe)₂ (Figure II-14) shows that the fluorination reduces HOMO and LUMO energy levels simultaneously but widens the energy gap of about 0.1 eV. In addition, from Bz(T₁CAMe)₂ to Bz(T₄CAMe)₂, the HOMO and LUMO energy levels are increased simultaneously with the increase in the conjugation length, and the increasement in the degree of HOMO energy level is larger than that of LUMO energy level, leading to lowering tendency in the band gap. It also shows similar electron density distribution of the frontier orbitals: the HOMOs of ffBz(T₁CAMe)₂, ffBz(T₂CAMe)₂ and ffBz(T₃CAMe)₂ are distributed entirely over the conjugated backbone that adopts an aromatic character, and their LUMOs are rather localized on benzothiadiazole unit with a quinoid character; for ffBz(T₄CAMe)₂, its HOMO orbitals is more localized in the central part of the backbone, while its LUMO is more localized on the benzothiadiazole and cyano groups, which is related to its elongated chain.


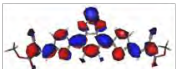

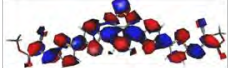

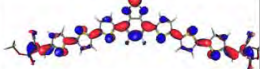
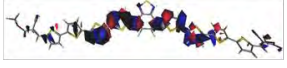

Molecules	HOMO orbital	LUMO orbital	HOMO/LUMO (eV)	E _g (eV)
ffBz(T ₁ CAMe) ₂			-6.44/-3.94	2.5
ffBz(T ₂ CAMe) ₂			-5.92/-3.69	2.23
ffBz(T ₃ CAMe) ₂			-5.32/-3.21	2.11
ffBz(T ₄ CAMe) ₂			-5.18/-3.13	2.05

Figure II-18: Frontier molecular orbitals and electronic properties of ffBz(T₁CAMe)₂, ffBz(T₂CAMe)₂, ffBz(T₃CAMe)₂ and ffBz(T₄CAMe)₂ at B3LYP/Def2-TZVP(-f) level.

The previous results showed that the most appropriate absorption spectra were simulated by BHandHLYP functional with Def2-TZVP(-f) basis set. Thus, based on the optimized geometries, the absorption spectra of ffBz(T₁CAMe)₂ and ffBz(T₂CAMe)₂ were simulated at the same level, as presented in Figure II-19. Note that ffBz(T₃CAMe)₂ and ffBz(T₄CAMe)₂ were not further studied by TD-DFT like it was the case for Bz(T₃CAMe)₂ and Bz(T₄CAMe)₂. The simulated maximum absorptions for Bz(T₁CAMe)₂, ffBz(T₁CAMe)₂, Bz(T₂CAMe)₂ and ffBz(T₂CAMe)₂ peak at 472, 444, 525 and 505nm, respectively. These results show on one hand fluorine substitution leads to a blue shift of 28 nm and 20 nm for Bz(T₁CAMe)₂ and Bz(T₂CAMe)₂, respectively. On the other hand it causes a slightly stronger absorption, suggesting that the molar extinction coefficient should increase when F atoms are introduced on the benzothiadiazole core.

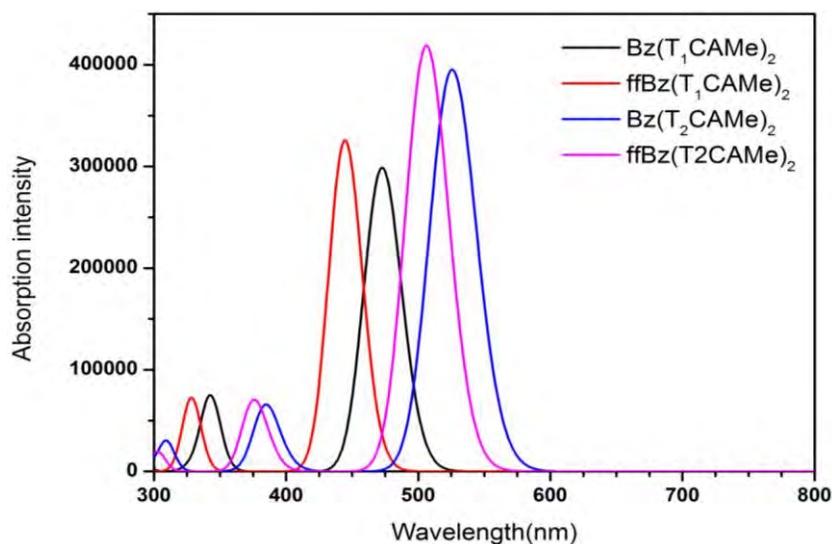


Figure II-19: Simulated absorption spectra of Bz(T₁CAMe)₂, ffBz(T₁CAMe)₂, Bz(T₂CAMe)₂, ffBz(T₂CAMe)₂ at BHandHLYP/ Def2-TZVP(-f) level.

III. 2 DTS-based small molecules

A set of A-D-A-D-A-D-A-type molecules (DTS(BzT₂CAO)₂, DTS(TBzT₁CAO)₂ and DTS(TBzT₂CAO)₂) based on DTS core have been envisaged (see Scheme II-2). In order to facilitate the computation, all the octyl chains were replaced with methyl group, leading to molecules DTS(BzT₂CAMe)₂, DTS(TBzT₁CAMe)₂ and DTS(TBzT₂CAMe)₂, as displayed in Figure II-20. Similar calculations were conducted on molecules containing DTS. These molecules are much more complex than Bz-based molecules and thus the necessary calculations require long time to optimize the geometry. Whereas the vibration frequency calculations have not performed currently, we may estimate that the calculated structures are very close to those of the ground state. This allows us to have a clear vision of the influence of the conjugation length on the molecular structure.

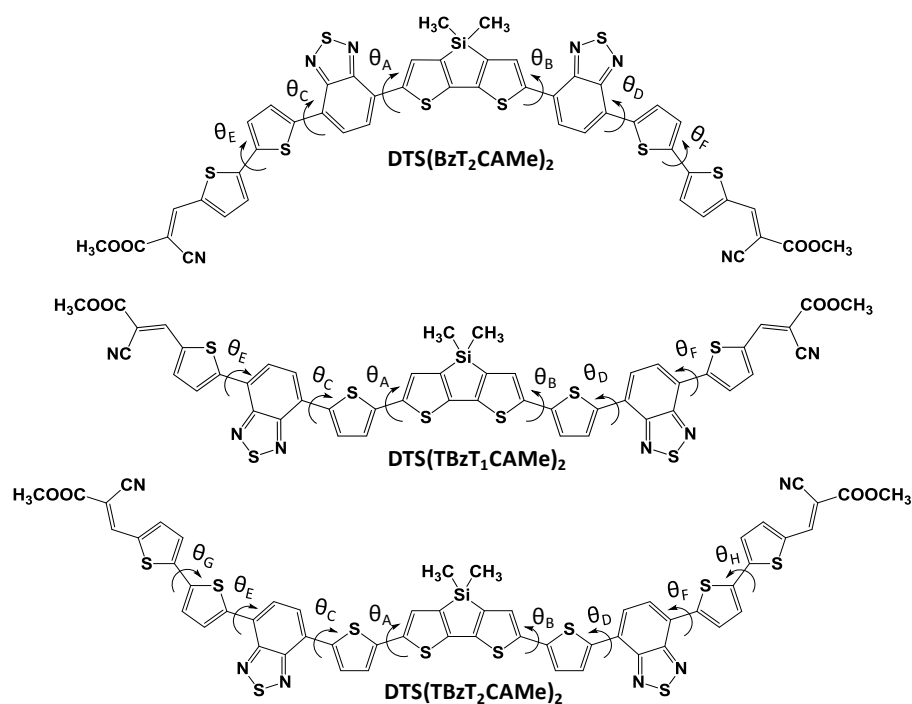


Figure II-20: The scheme of dihedral angles for structural analysis.

The structural analysis for optimized geometries of $\text{DTS}(\text{BzT}_2\text{CAME})_2$ and $\text{DTS}(\text{TBzT}_1\text{CAME})_2$ (Note that the geometry optimization of $\text{DTS}(\text{TBzT}_2\text{CAME})_2$ has not accomplished yet) were studied by examining calculated dihedral angles (defined as the dihedral angle for adjacent rings) indicated in Figure II-20. These results are summarized in Table II-7. From these results, it is apparent that the modeled structures of DTS molecules are relatively planar, the dihedral angles between the constituent rings is generally low. This is certainly related to the π -conjugated A-D structure of these compounds.

Table II-7: Dihedral angles ($^\circ$) in $\text{DTS}(\text{BzT}_2\text{CAME})_2$ and $\text{DTS}(\text{TBzT}_1\text{CAME})_2$.

	θ_A	θ_B	θ_C	θ_D	θ_E	θ_F	θ_G	θ_H
$\text{DTS}(\text{BzT}_2\text{CAME})_2$	0.48	0.56	1.02	1.01	0.27	0.37		
$\text{DTS}(\text{TBzT}_1\text{CAME})_2$	4.43	4.36	0.26	0.60	7.00	1.42		
$\text{DTS}(\text{TBzT}_2\text{CAME})_2$	*	*	*	*	*	*	*	*

*Non-available data due to the time-consuming calculations.

The frontier molecular orbitals and electronic properties of molecules $\text{DTS}(\text{BzT}_2\text{CAME})_2$ and $\text{DTS}(\text{TBzT}_1\text{CAME})_2$ are presented in Figure II-21. One can observe that the electron spatial distributions of their HOMOs are more localized on the central part of the backbone, and their LUMOs are slightly localized on the benzothiadiazole core and the cyano group. Besides, the

electronic parameters of these compounds were also evaluated. It turns out that the energies of their frontier orbitals are very close, in the order of -5.35 eV for the energy of the HOMO and -3.6 eV for the energy of the LUMO. These values are very close to those of an ideal donor, according to the Scharber model, which indicates that the optimized energy values of HOMO and LUMO are -5.4 eV and -3.9 eV, respectively.(37, 81) In addition, the calculation shows that these molecules have a narrow gap in the order of 1.8 eV. Such low energy gap means they may exhibit wide absorption extended to Infrared - Near Infrared region, which is of great significance for the photovoltaic effect. Our DTS-based target molecules may act as electron donors with PCBM as acceptor and may guarantee good performances for OPV cells. These results encourage us therefore to continue this work by carrying out the synthesis of these molecules.

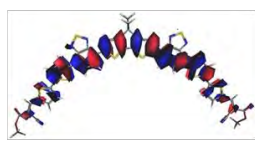
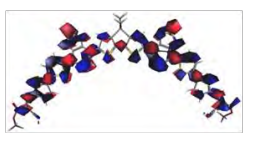


	HOMO	LUMO	HOMO/LUMO (eV)	E_g (eV)
DTS(BzT ₂ CAMe) ₂			-5.39/-3.55	1.84
DTS(TBzT ₁ CAMe) ₂			-5.34/-3.58	1.76

Figure II-21: Frontier molecular orbitals and electronic properties of DTS-based small molecules calculated by DFT at B3LYP/Def2-TZVP(-f) level.

III. 3 SubPcs-based small molecules

Boron subphthalocyanines have been successfully used in organic solar cells. In order to take advantage of the knowledge previously acquired during the first part of calculations, we envisaged the axial substitution on phenoxy-subphthalocyanines with fragments BrBzT₁CHO or BrBzT₂CHO, leading to a series of SubPcs-based small molecules. Their chemical structures are presented in Figure II-22.

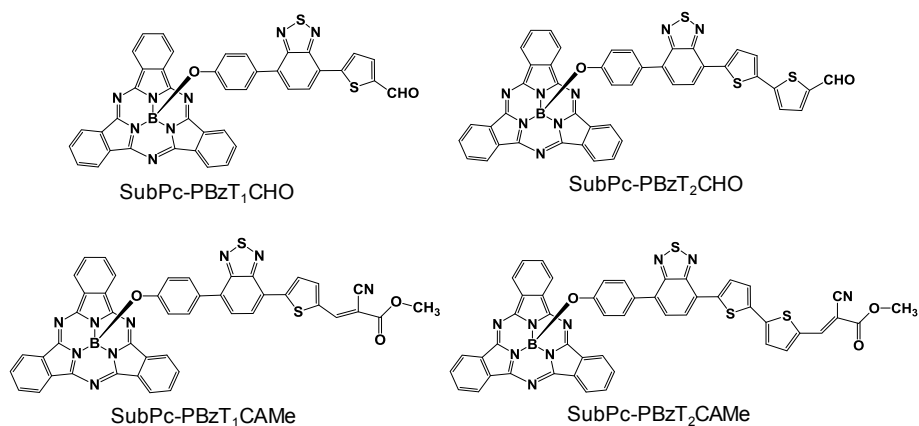


Figure II-22: Chemical structures of calculated SubPcs-based small molecules.

A purely theoretical work has been completed on molecules derived from boron SubPcs. The frontier orbital and electronic properties of SubPcs-based small molecules are shown in Figure II-23. In general, one can observe that the designed axial substitution leads to reduction in energy levels of both frontier orbitals and results in lowering the energy gap of phenoxy-SubPcs. Substituent PBzT₁CAME shows greater effect on the LUMO energy level and band gap of phenoxy-SubPc than PBzT₁CHO does. Similarly, PBzT₂CAME shows greater effect on the LUMO energy level and band gap of the phenoxy-SubPc than PBzT₂CHO does. The slight energy difference between energy gaps of similar compounds, like SubPc-PBrBzT₁CHO and SubPc-PBrBzT₂CHO, SubPc-PBrBzT₁CAME and SubPc-PBrBzT₂CAME), are of 0.06 eV and 0.07 eV, respectively, which can be ignored. For phenoxy-SubPc, it shows that the electron density distribution of both HOMO and LUMO are only localized on the macrocycle of SubPcs, which is in accordance with the prediction of HOMO and LUMO energy levels of boron subphthalocyanines reported by Bender *et al.*(251) Interestingly, with regard to axial substituted SubPc derivatives, the electron density distribution of the HOMO is localized on the macrocycle of SubPcs for most of the derivatives, excluding SubPc-PBzT₂CHO for which the HOMO is localized on the axial substituent. This unusual distribution of HOMO of SubPc-PBzT₂CHO could be ascribed to the more electron-rich bithiophene fragment relative to macrocycle. This phenomenon is in accordance with the axial thiophene-BSubPcs reported by Mauldin *et al.* (219) For SubPc-PBrBzT₁CHO and SubPc-PBrBzT₂CHO, their electron density distribution of the LUMO is greatly located on the axial substituents and slightly distributed on the macrocycle of SubPcs. This may due to the electron-rich nature of the thiophene or bithiophene fragments. It is worth to note that for SubPc-PBrBzT₁CAME and SubPc-PBrBzT₂CAME, the LUMOs are localized only on the axial substituents, which could be attributed to the electron-withdrawing nature of

the cyano group.(262) This suggests that the SubPc core may act as an electron donor and the axial substituent as an electron acceptor. Upon photoexcitation, these molecules may undergo electron transfer through the oxygen atom that acts as an electronically active linker between the two parts of the molecule, and may generate charge-separated species that could take an active part to the photovoltaic effect.

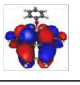
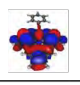
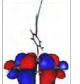
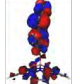

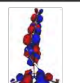

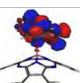
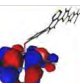
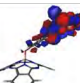
	HOMO	LUMO	HOMO/LUMO (eV)	E_g (eV)
Phenoxy-SubPc			-5.44/-2.72	2.72
SubPc-PBzT ₁ CHO			-5.59/-2.93	2.67
SubPc-PBzT ₂ CHO			-5.51/-2.90	2.61
SubPc-PBzT ₁ CAMe			-5.56/-3.23	2.33
SubPc-PBzT ₂ CAMe			-5.59/-3.19	2.40

Figure II-23: Frontier molecular orbitals and electronic properties of SubPcs-based small molecules calculated by DFT at B3LYP/Def2-TZVP(-f) level.

To understand the interaction between the macrocycle of SubPcs and axial substituents, these lasts (see Figure II-24) were also studied by DFT.

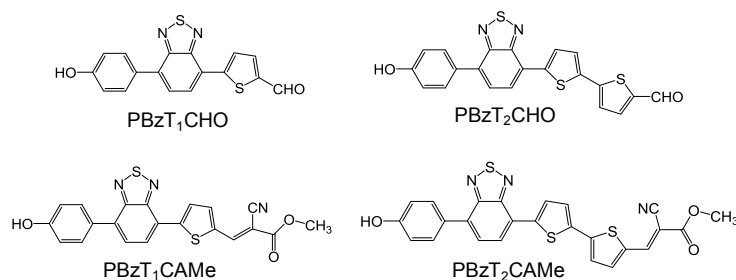


Figure II-24: Structure of axial substituents.

The frontier molecular orbitals and electronic properties of the four substituents are provided in Figure II-25. One can observe that for similar fragments, like PBrBzT₁CHO and PBrBzT₂CHO, PBrBzT₁CAMe and PBrBzT₂CAMe, increasing thiophene rings lead to increasing the energy levels (especially the HOMO levels) of both frontier orbitals, and results in reducing the energy gap of around 0.2 eV. This is due to the enhanced conjugation length. Comparing PBrBzT₁CHO with PBrBzT₁CAMe, we can see that both HOMO and LUMO energy levels are reduced (especially the LUMO energy levels) when introducing

alkyl cyanoacetate group, lowering energy gap of approximately 0.2 eV. This is owing to the spatial electron delocalization that helps to stabilize the molecule. In addition, combining these substituents to phenoxy-SubPc and their respective SubPcs derivatives, for instance, PBrBzT₁CHO, phenoxy-SubPc and SubPc-PBrBzT₁CHO, the energy levels of SubPc-PBrBzT₁CHO are higher than those of substituents but lower than those of phenoxy-SubPc, and the energy gap of SubPc-PBrBzT₁CHO (2.67 eV) is lower than both the substituent (2.82 eV) and phenoxy-SubPc (2.72 eV). It again reveals that there may be intramolecular interaction between the axial substituent and the macrocycle of SubPcs, which contributes to stabilize both of them.

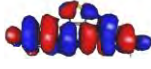
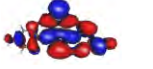
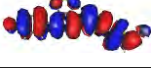
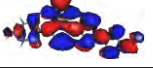
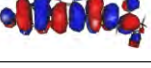
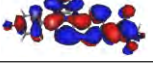

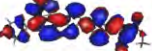
	HOMO	LUMO	HOMO/LUMO ^e (eV)	E _g (eV)
PBzT ₁ CHO			-5.90/-3.08	2.82
PBzT ₂ CHO			-5.64/-3.04	2.60
PBzT ₁ CAMe			-5.95/-3.34	2.61
PBzT ₂ CAMe			-5.70/-3.27	2.43

Figure II-25: Frontier molecular orbitals and electronic properties of axial substituents calculated by DFT at B3LYP/Def2-TZVP(-f) level.

Generally, peripheral substitution on SubPcs has influence on the electronic characteristics of macrocycle in SubPcs, and it is rarely seen that axial substitution exhibits effect on the electronic properties of SubPcs.^(185, 186) Based on our theoretical studies, it reveals that our designed SubPc-based molecules exhibit different and original electronic properties, which will be interesting for further study in the field of SubPcs.

IV Conclusion

To summary, three different series of small molecules were designed and theoretically studied *via* DFT computations at B3LYP/Def₂-TZVP(-f) level. Their geometries and electronic properties were investigated. For Bz-based molecules, the lower the conjugation length is, the flatter the structure is. The optical and electronic band gaps decrease when the conjugation length increases. For DTS-based molecules, they show quite low band gaps of about 1.8 eV. Our proposed axial substituents make the target SubPcs-based molecules innovative components with original behavior for organic electronics.

To provide a visual comparison, the HOMO and LUMO energy levels of molecules designed by DFT are presented in Figure II-26. The HOMO and LUMO levels of P3HT and PCBM were evaluated by cyclic voltammetry (CV) measurements in CH_2Cl_2 solution in our lab. Given the resultant energy level diagram of these new designed molecules, it implies that they all may be promising candidates for use as active materials for organic photovoltaics applications. We should keep in mind that the LUMO offset should be larger than 0.3 eV in the Scharber model. Theoretically, on one hand, all of the Bz-, DTS-, and SubPcs-based molecules could be used as electron donor when using PCBM as acceptor. In particular, with regard to DTS-based target molecules, their HOMO and LUMO energy levels are very close to those of ideal donor materials, making them promising donors for OPV cells. On the other hand, only molecules $\text{Bz}(\text{T}_1\text{CAME})_2$ and $\text{ffBz}(\text{T}_1\text{CAME})_2$ could act as electron acceptors when using P3HT as the donor.

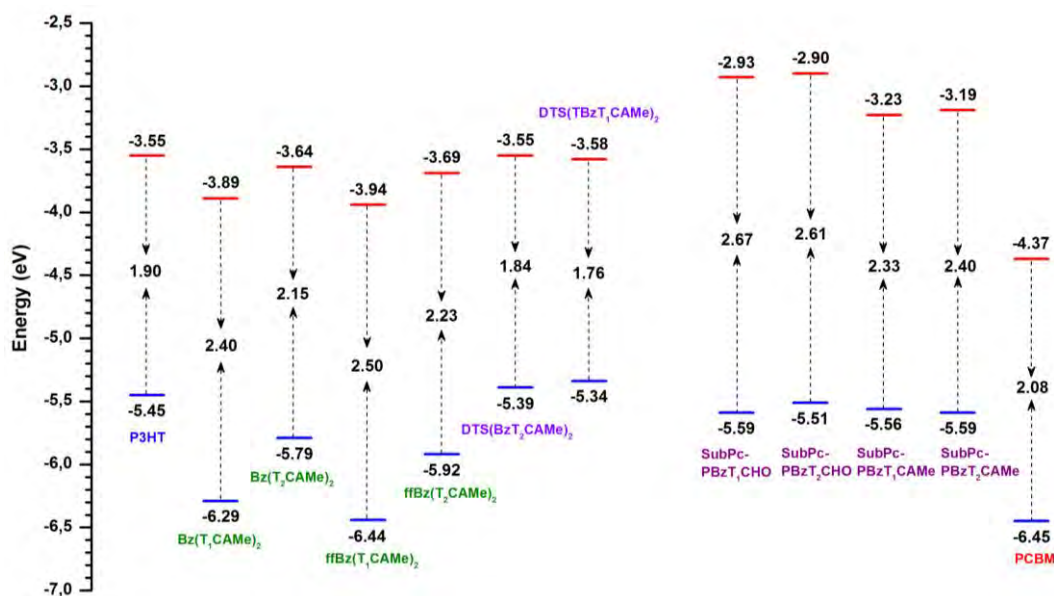


Figure II-26: Energy level diagram of molecules calculated by DFT at B3LYP/Def2-TZVP(-f) level.

From synthesis point of view, Bz-based molecules could be obtained in two steps, DTS-based molecules could be obtained in at least three steps in the case of using the commercial fragment diBrDTS, and SubPc-based molecules could be obtained in more than four steps. Both DTS- and SubPcs-based molecules need non-symmetrical intermediates to be synthesized, which make their syntheses more difficult. Thus, we planned to synthesize Bz-based molecules first, then DTS-based molecules, finally SubPcs-based molecules. The details about their syntheses will be presented in the following chapter.

Chapter III: Green chemistry approach for materials synthesis

Chapter III : Green chemistry approach for materials synthesis

I Introduction

Organic molecules for photovoltaics are often based on alternating electron donor and electron acceptor (D-A) moieties that result in materials with a strong absorption. From the synthetic point of view, the drawback of this D-A strategy is related to the coupling methods required for connecting these cores, bridges, and terminal units. On the one hand, D-A molecules are often obtained by units coupling *via* polluting synthetic procedures using stannylated derivatives (279) or *via* reactions involving diboronic acid pinacol esters which belong to a class of expensive and low yield isolated intermediates.(280, 281) On the other hand, direct arylation (the coupling of transition-metal (palladium, Rhodium, Ruthenium) catalyzed aryl C-H bonds with aryl halides) proceeds *via* C-H bond activation without need of the preparation of organometallic compounds, allowing for promising and atom-economical alternative to traditional cross-coupling reactions for the formation of new C-C bonds.(181) This method becomes very commonly used nowadays for polymers synthesis and is identified as an eco-friendly synthetic procedure offering new opportunities for the production of green energy from more environmentally friendly materials.(282, 283) It has recently emerged as a simple and feasible method to synthesize conjugated materials from simple building blocks for use in organic electronics.(182, 284-287) It was proposed two decades ago in pioneering works of Ohta *et al.* on direct arylation of thiophenes with aryl halides *via* C-H bond functionalization using palladium catalysis which gave moderate yields at 150°C.(288) Doucet and co-workers demonstrated that direct arylation can be considered as an environmentally and economically attractive approach to yield highly selective 2 or 5-arylated thiophenes employing low loading catalyst at 150°C.(289-295) Moreover, the direct arylation through ligand-free catalysis offers advantages: properly used, the catalysis may be faster (296) and due to reduced numbers of additives and reactants, the work-up is easier and thus costs are reduced. The proposed mechanism of this procedure involves the decomposition at 100°C of Pd(OAc)₂ with formation of solvent-stabilized Pd(0)-colloids in a polar solvent.(297) This is very close to what happens in the Heck reaction where Pd(OAc)₂ can be used as catalyst on aryl iodides without additional ligand.(298) However, if the solvent

is concentrated (296) or if the catalyst/substrate ratio is too high, the solvent-stabilized Pd(0)-colloids show a tendency to agglomerate and form non active black palladium powder. To our knowledge, the direct arylation without ligand at low catalyst loading has been used only once for π -conjugated polymers synthesis, in particular the polycondensation reaction of 3,3',4,4'-tetramethylbithiophene with 2,7-dibromo-9,9-dioctylfluorene in the presence of 2 mol % of Pd(OAc)₂.(299) In this case however, 30 mol % of PivOH was used. This method offers simpler, shorter and cheaper reaction pathways for intermediates and final materials synthesis, and generates less toxic waste in comparison to classic cross-coupling techniques. The motivation of the present work is to demonstrate an unsophisticated and easy preparation of organic semi-conducting small molecules with a structure based on alternating D-A fragments, in accordance to the theoretical study presented in Chapter II. As demonstrated in Chapter I, among D and A fragments, thiophene (D), benzothiadiazole (A) and cyanoacetate (A) are simple units usually associated with good conversion yields.(15, 28, 48, 127, 203, 204, 300-302) These fragments are aimed at being connected together by coupling reactions. In this context, we propose here to use an environmentally attractive coupling procedure without polluting wastes in a cost-effective way in comparison to the other existing procedures.

II Synthesis of benzothiadiazole (Bz) based small molecules

The basic idea of this study is to provide small, as simple as possible molecules obtained after as few synthetic steps as possible, from commercially available raw materials. The need of two steps is believed to be the minimum reachable path, leading to the fewest waste production and lowest cost. 4,7-dibromobenzo-2,1,3-thiadiazole (diBrBz) acts here as the electrophile on both sides, in reaction with thiophene carboxaldehyde which is found here to be exclusively 5-arylated, thus providing an interesting D-A-D core for building semi conducting small molecules. The presence of two aldehyde functions at both extremities of the D-A-D core renders possible to elongate the molecule by a double Knoevenagel condensation leading to an A-D-A-D-A molecule, which is suitable for presenting semiconducting character associated with low band gap properties. Among the available terminal electron-withdrawing groups, alkyl cyanoacetate,(43, 211, 303) 3-alkylrhodanine,(155, 156, 304) and 1,3-indandione (305, 306) are easily introduced by Knoevenagel condensation. Both octyl cyanoacetate and 2-ethylhexyl cyanoacetate were chosen as the terminal groups because they confer a good solubility of the final molecule,

promote self-organization in nanoaggregate structures, and contribute to enhanced photovoltaic performances. (205) Among the Bz-based molecules presented before, we chose to synthesize Bz(T₁CAO)₂, Bz(T₁CAEH)₂, Bz(T₂CAO)₂ and Bz(T₂CAEH)₂ because they are achievable in two steps. Their precursors Bz(T₁CHO)₂ and Bz(T₂CHO)₂ can be obtained from commercially available reagents, such as diBrBz, TCHO and T₂CHO.

Three synthetic protocols for obtaining the intermediate molecule have been compared: i) the classical Suzuki coupling (thereafter referred to as **Route a**) using a boronylated intermediate which is rather expensive and generates polluting wastes, ii) a direct heteroarylation procedure (**Route b**) without organometallic nor boronylated intermediate but using palladium catalyst, phosphine ligands, and pivalic acid (PivOH) in combination with potassium carbonate (K₂CO₃), and finally, iii) the direct heteroarylation procedure (**Route c**) without ligand nor PivOH, but only with palladium acetate (Pd(OAc)₂) as the catalyst and potassium acetate (KOAc) as the base.

Figure III-1 shows the structures of molecules that have been achieved in only two steps. The first step consists in synthesis of intermediates 5,5'-(2,1,3-benzothiadiazole-4,7-diyl)bis-(2-thiophenecarboxaldehyde) (molecule Bz(T₁CHO)₂), or 5',5'''-(2,1,3-benzothiadiazole-4,7-diyl)bis-[(2,2'-bithiophene)-5-carboxaldehyde] (Bz(T₁CHO)₂) by coupling a benzothiadiazole ring with a thiophene or bithiophene carboxaldehyde unit, respectively. The second step consists in the Knoevenagel condensation of Bz(T₁CHO)₂ or Bz(T₂CHO)₂, respectively, with 2-ethylhexyl- or octyl-cyanoacetate. It is showed here that the coupling method may have a dramatic impact on environmental and economical parameters of the synthetic method.

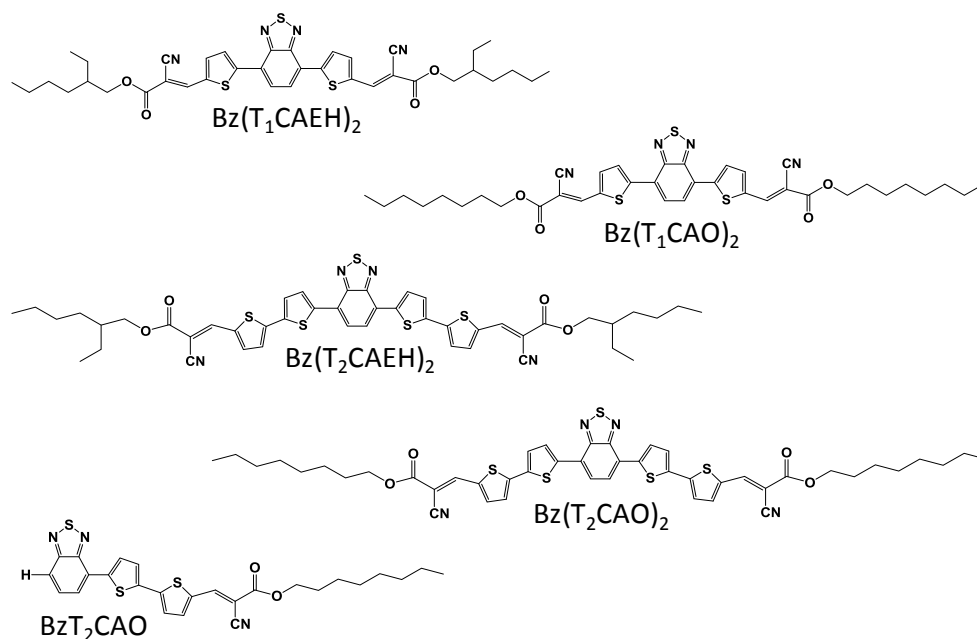


Figure III-1: Chemical structures of the synthesized molecules.

II. 1 Synthesis and environmental evaluation of di-substituted compounds

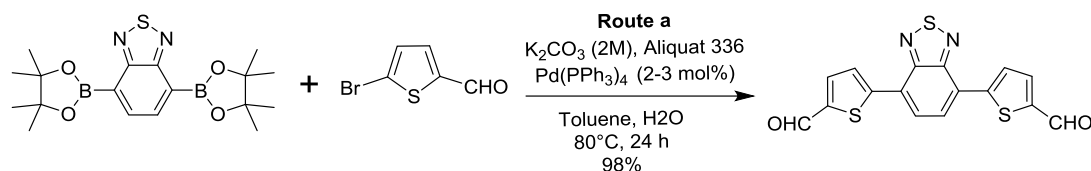
Bz(T₁CHO)₂, Bz(T₂CHO)₂ and target molecules

II. 1-1 Synthesis of compounds Bz(T₁CHO)₂ and Bz(T₂CHO)₂

The detailed synthetic routes used for obtaining molecules Bz(T₁CHO)₂ and Bz(T₂CHO)₂ are documented in the Experimental section, and summarized in Scheme III-1 (**Route a**), Scheme III-2 (**Route b**), Scheme III-3 (**Route c**), and Scheme III-4 (**Routes a and c**), respectively. Their structures were confirmed by ¹H NMR spectroscopy in CDCl₃ and DMSO-D₆ (see experimental section).

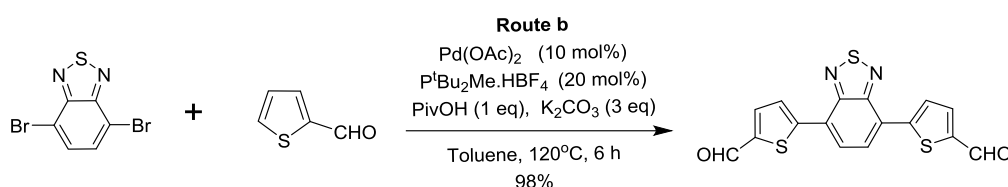
The key intermediate compounds Bz(T₁CHO)₂ and Bz(T₂CHO)₂ were first obtained *via* **Route a** (see Scheme III-1), *i.e.* the usual Pd-catalyzed Suzuki coupling, using 2,1,3-benzothiadiazole-4,7-bis(boronic acid pinacol ester) (BzB-ester) and 5-bromo-2-thiophene carboxaldehyde (BrTCHO). The used procedure was adapted from published protocols of synthesis of alkylated thiophene derivatives. According to these protocols, either three equivalents of thiophene reactant were required (307) or a reaction time of 3 days at 80°C was recommended.(308) We found that 2.5 equivalents of molecule BrTCHO and a reaction time of 24 h were adequate to yield the desired molecule in quantitative yields and we did not investigate this reaction further to improve the yield. This method offers the advantage to be highly efficient and regioselective. However, it involves reactants that are either expensive

(BzB-ester) (244) or very reactive (BrTCHO). Because of the high reactivity of molecule BrTCHO, we used it in excess to reach quantitative yield, since it also leads to non-desired homocoupling by-products (although easily eliminated during the work up by simply washing with ethyl acetate).



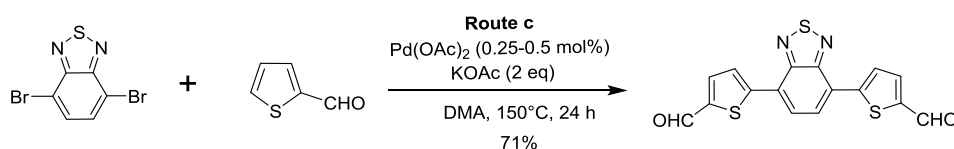
Scheme III-1: Classical coupling (Route a) to molecule Bz(T₁CHO)₂.

Then **Route b** was explored (see Scheme III-2), a greener and low-cost method based on the direct arylation reaction offering the advantage to avoid metallated intermediates. Marder and co-workers(309) demonstrated that the C-H bond of the benzothiadiazole ring can be functionalized by aryl bromides under palladium acetate (10 mol%) catalysis in presence of trialkyl phosphines, such as $\text{P}^t\text{Bu}_2\text{Me}\cdot\text{HBF}_4$ as the ligand, pivalic acid as the proton shuttle and potassium carbonate as the base in toluene at reflux. Inspired by this work, we adapted the reaction conditions in using 4,7-dibromobenzo-2,1,3-thiadiazole (diBrBz, 1 eq) as the arylating reagent and 2-thiophene carboxaldehyde (TCHO, 2.2 eq) as the C-H active component. Without any optimization study, the desired product was directly isolated in 98% yield. This reaction proved to be regio-selective since only the 5-position of thiophene reacted in the coupling process.



Scheme III-2: Direct arylation Route b to molecule Bz(T₁CHO)₂.

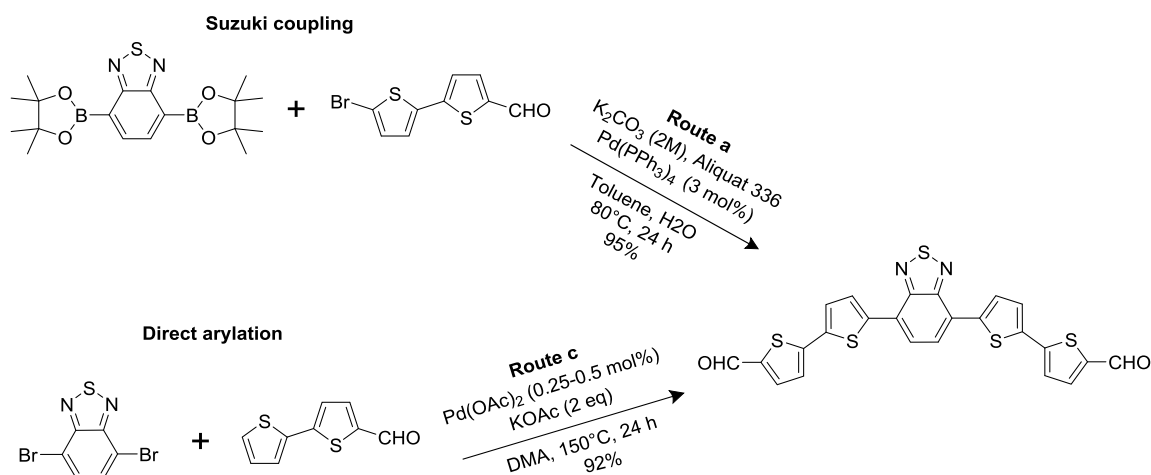
To further extend the synthetic utility of direct arylation, we finally tested *via* **Route c** (see Scheme III-3), a one-pot unprecedented synthesis of molecule Bz(T₁CHO)₂ starting from the same reactants and using the same ratio of TCHO/diBrBz 2.2:1 as for **Route b**, but in *N,N*-dimethylacetamide (DMA) as the solvent, at lower palladium concentration, and without neither ligand nor pivalic acid.



Scheme III-3: Direct arylation Route c to molecule Bz(T₁CHO)₂.

This “ligand-free” strategy was first proposed by Doucet and co-workers (289) who obtained high yields using only 0.1-0.001 mol% catalyst. Such low quantities of catalyst are impossible to weigh accurately in our conditions due to the too low quantities of reactants, so we employed slightly higher relative amounts of palladium acetate. In presence of 0.25 and 0.5 mol% catalyst and of 2 equivalents of potassium acetate relative to diBrBz, the desired product was synthesized in 73% and 71% yield, respectively. Note that once again, the work-up of the reaction is extremely easy, as it consists only of filtration, then washing with water, ethyl acetate, and petroleum ether. It is worth noting that only the desirable coupling product resulting from C-H cleavage on the 5-position of 2-thiophene carboxaldehyde was found. Moreover, no arylation of the acetyl function was observed as this was the case for the reaction of TCHO with other aryl bromides.(305, 306) Only monoarylated product (see experimental section) and homocoupling product of thiophene carboxaldehyde (¹H NMR spectrum shown in Figure A.5 in Annexes) were detected as side products. In order to check the stability of the reactants under the reaction conditions, both starting materials diBrBz and TCHO were engaged separately in the direct arylation conditions *via* **Route c** without any other reactant. After 24h at 150°C, each batch was treated as previously described. Analyses of the batch conducted with diBrBz revealed the absence of homocoupling by-products and any other degradation processes, and the total recovery of diBrBz. It demonstrates the outstanding stability of di-bromobenzothiadiazole that does not undergo undesirable reaction. In contrast, the batch with molecule TCHO resulted only in black degradation products: thiophene carboxaldehyde is indeed unstable under direct arylation conditions and must be employed in such conditions that it reacts quickly and completely. This is the reason why we tested the reaction of direct arylation of diBrBz with TCHO in default in **Route c** (see experimental section). When TCHO is used in 0.9 eq and even down to 0.5 eq with regard to diBrBz, then the yield (calculated with respect to the limiting reactant) is quantitative, and no degradation product is produced. It is worth noting that the purification of the molecule is very easy, driven by simple washing with water to eliminate KOAc and KBr, ethyl acetate to eliminate Pd(OAc)₂, and finally petroleum ether to help in eliminating AcOEt and remaining DMA. The ease of purification is undoubtedly linked to the cleanliness of the reaction that does not generate side products.

The two routes used for obtaining the elongated intermediate Bz(T₂CHO)₂, documented in the experimental section are summarized in Scheme III-4.



Scheme III-4: Classical (top) and new (bottom) routes to molecule Bz(T₂CHO)₂.

As described above for the synthesis of Bz(T₁CHO)₂, Bz(T₂CHO)₂ was obtained in quantitative yield by Suzuki coupling (**Route a**), using the same synthetic procedure. **Route c** was then directly tested by reacting T₂CHO and diBrBz in the ratio of 2.2:1 as for molecule Bz(T₁CHO)₂. In this case, molecule Bz(T₂CHO)₂ was obtained with an excellent yield of 92% which was not further investigated. The improved yield is attributed to the greater reactivity of molecule T₂CHO towards the coupling compared to that of molecule TCHO and to the lower solubility of Bz(T₂CHO)₂ with respect to that of Bz(T₁CHO)₂.

The Knoevenagel condensation is driven in a classical manner. Most of organic molecules for organic electronics are purified by means of column chromatography. Here, it is noteworthy that the target molecules are purified by simple recrystallization in ethyl acetate, reducing the waste problem originated from the synthesis procedure. All the target molecules were fully characterized and their structures are confirmed by different analytic tools (elemental analysis, NMR, MS) which are summarized in experimental section.

II. 1-2 Environmental and economic aspects

Among the aspects of importance for OPV (efficiency, stability, printability), materials for large-scale production should be as inexpensive as possible. The cost trends of 20 €/g for the upscaling scenario and 10 €/g for the industrial scenario have been recently suggested.⁽³¹⁰⁾ The materials synthesis must be realized from commercially available chemicals in few steps and with straightforward purification procedures.⁽¹³³⁾ Overall yields and E-factor (defined by the ratio of the mass of waste per unit mass of product) are quantifiable green metrics used for evaluating the environmental impact associated with the production of organic materials for

sustainable applications.(311, 312) These metrics for the molecules elaborated in this work have been evaluated (see Table III-1 and Annexes 6 for details).

(a) Molecule Bz(T₁CHO)₂ obtained *via* **Routes a, b, and c**

The three synthesis protocols described above (Scheme III-1, Scheme III-2 and Scheme III-3) have been compared for the synthesis of molecule Bz(T₁CHO)₂. As can be seen in Table III-1, the calculated E-factor and price of Bz(T₁CHO)₂ (see Annexes 6) show dramatic change from one route to another. The atom economy is calculated as the ratio of the mass of the desired product to the mass of the reactants. Surprisingly, the E-factor calculation for **Route b** affords a value very close to that calculated for **Route a**. This is due to the consequent amount of catalyst (10 mol% Pd(OAc)₂) and ligand (20 mol% P^tBu₂Me.HBF₄) used for the direct arylation which is revealed here to be less eco-friendly than the Suzuki coupling. On the other hand, Suzuki coupling involves expensive raw materials which increase the cost of Bz(T₁CHO)₂. A consequent improvement of the green metrics is obtained when direct arylation without ligand (**Route c**) is carried out. This process involves a low amount of catalyst (0.5 mol% palladium acetate) and the absence of any additive, resulting in a very simple protocol with an E-factor of 143g/g, which is approximately one third of that obtained from the two other routes. Moreover, the cost of Bz(T₁CHO)₂ becomes nearly one twelfth and one third of that resulted from **Route a** and **Route b**, respectively. This represents a great improvement in term of waste production and cost for the synthesis of the same intermediate.

Table III-1: Reaction yields, E-factors and costs calculated for Bz(T₁CHO)₂ obtained *via* the three investigated routes.

	Route a	Route b	Route c
Yield (%)	100%	98%	71%
E-factor (g/g)	441	495	143
Cost (€/g)	176	38.5	14
Atom economy	41%	65%	47%

In addition, the atom economy of **Route b** and **c** are higher than that of **Route a**, suggesting that the direct arylation is greener than the traditional Suzuki coupling. The difference in atom economy between **Route b** and **Route c** is attributed to the yield.

(b) Molecule $\text{Bz}(\text{T}_1\text{CHO})_2$ obtained via **Route c** and different ratios (r)

We then examined if it was possible to improve the **Route c** metrics by increasing the yield of the reaction. For achieving better yields and decreasing the amount of degradation products associated with side reactions experienced by TCHO, the molecular ratio between TCHO and diBrBz was lowered to 0.9, then 0.5 (instead of 2.2). The obtained values are gathered in Table III-2. The reaction yield is improved, but with much worse green metrics. This is due to the fact that the non-reacted molecule diBrBz (when used in excess) is accounted as a waste, thus substantially contributes to the increase of the calculated value of the E-factor. Due to the fact that molecule diBrBz does not react by homocoupling reaction nor decomposes through any other degradation processes under these reaction conditions as demonstrated earlier, it may be possible to recycle it. Thus, with optimized synthesis conditions, including the recycling of diBrBz, it is feasible to synthesize $\text{Bz}(\text{T}_1\text{CHO})_2$ in 71% yield and more with an E-factor approaching 143 g/g and a cost of around 14 €/g as reported in first column of Table III-2.

Table III-2: Reaction yields, E-factors and costs calculated for the synthesis of $\text{Bz}(\text{T}_1\text{CHO})_2$ obtained via Route c with decreasing the TCHO/diBrBz ratios (r).

	r = 2.2	r = 0.9	r = 0.5
Yield (%)	71%	100%	100%
E-factor (g/g)	143	226	408
Cost (€/g)	14	22	39

(c) Molecule $\text{Bz}(\text{T}_2\text{CHO})_2$ obtained via **Routes a** and **c**

For the synthesis of $\text{Bz}(\text{T}_2\text{CHO})_2$, the calculated green metrics for **Route a** and **Route c** confirmed the previous trends (see Table III-3): the E-factor calculation for **Route c** returned a value of 76 g/g, which was around one-sixth of that found for **Route a**, and the cost was reduced by a factor 5 between **Route a** and **Route c**. It is worth noting here that for **Route c**, the molecular ratio $\text{T}_2\text{CHO}/\text{diBrBz}$ ratio (r) was 2.2.

Table III-3: Reaction yields, E-factors and costs calculated for $\text{Bz}(\text{T}_2\text{CHO})_2$ obtained via Route a and Route c.

	Route a	Route c
Yield (%)	100%	91%
E-factor (g/g)	497	76
Cost (€/g)	201	40
Atom economy	48%	66%

From the aspect of atom economy, it is obvious that the Route c is greener than Route a, which is also consistent with the E-factor. It confirms that ligand-less direct arylation is a greener procedure.

(d) Target molecules obtained by Knoevenagel condensation

Finally, the four target molecules, $\text{Bz}(\text{T}_1\text{CAEH})_2$, $\text{Bz}(\text{T}_1\text{CAO})_2$, $\text{Bz}(\text{T}_2\text{CAEH})_2$ and $\text{Bz}(\text{T}_2\text{CAO})_2$, were obtained *via* **Route c** followed by Knoevenagel condensation. The overall green metrics are presented in Table III-4. In a general manner, the E-factor is twice higher for molecules bearing one thiophene ring at each side of benzothiadiazole, than for those bearing bithiophene units. This is directly linked to the E-factors for intermediate synthesis, of 143 and 76 g/g for compounds $\text{Bz}(\text{T}_1\text{CHO})_2$ and $\text{Bz}(\text{T}_2\text{CHO})_2$, respectively, and to the best Knoevenagel reaction yields obtained with molecule $\text{Bz}(\text{T}_2\text{CHO})_2$.

Table III-4: Reaction yields for Knoevenagel condensation, and total E-factors and costs calculated for the target molecules obtained *via* Route c followed by Knoevenagel condensation.

	$\text{Bz}(\text{T}_1\text{CAO})_2$	$\text{Bz}(\text{T}_1\text{CAEH})_2$	$\text{Bz}(\text{T}_2\text{CAO})_2$	$\text{Bz}(\text{T}_2\text{CAEH})_2$
Knoevenagel condensation yield	51%	47%	76%	68%
Total E-factor (g/g)	230	380	144	162
Total cost (€/g)	45	37	50	47

The estimated cost per gram is constant from one molecule to another, of around 45 €/g, which is acceptable for a fine chemical with a potential large scale application. It is worth noting that these numbers are maximum values deduced from (non-negotiated) prices of commercial raw materials, always more expensive at laboratory scale than for upscaling or industrial purpose.

The good figures of merit obtained for total E-factors as well as for the costs are undoubtedly linked to the fact that the target molecules are unsophisticated, obtained in only two steps, and which do not require column chromatography technics for their purification. The simple purification techniques used in this work, *i.e.* washing or recrystallization, are useful tools for green methods.

III Synthesis of molecules based on dithienosilole (DTS) core

In chapter II, we have already discussed the molecular design based on DTS cores, and the synthetic routes to obtain precursors for DTS-based target molecules were also given (see Scheme II-2 in Chapter II). To obtain such precursors, it is now necessary to synthesize relevant DTS fragments. Their chemical structures are presented in Figure III-2.

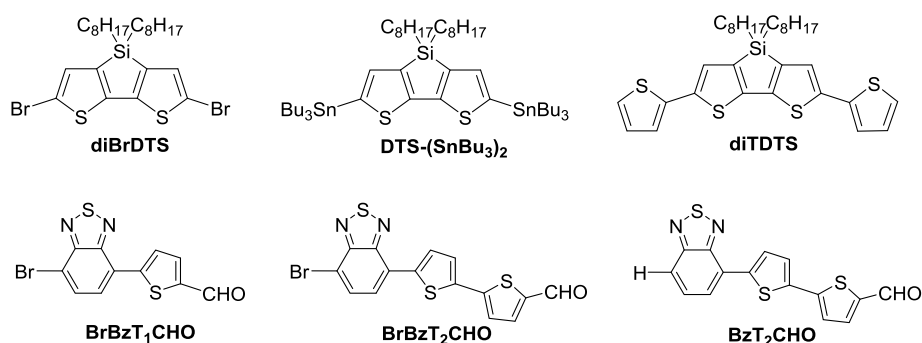


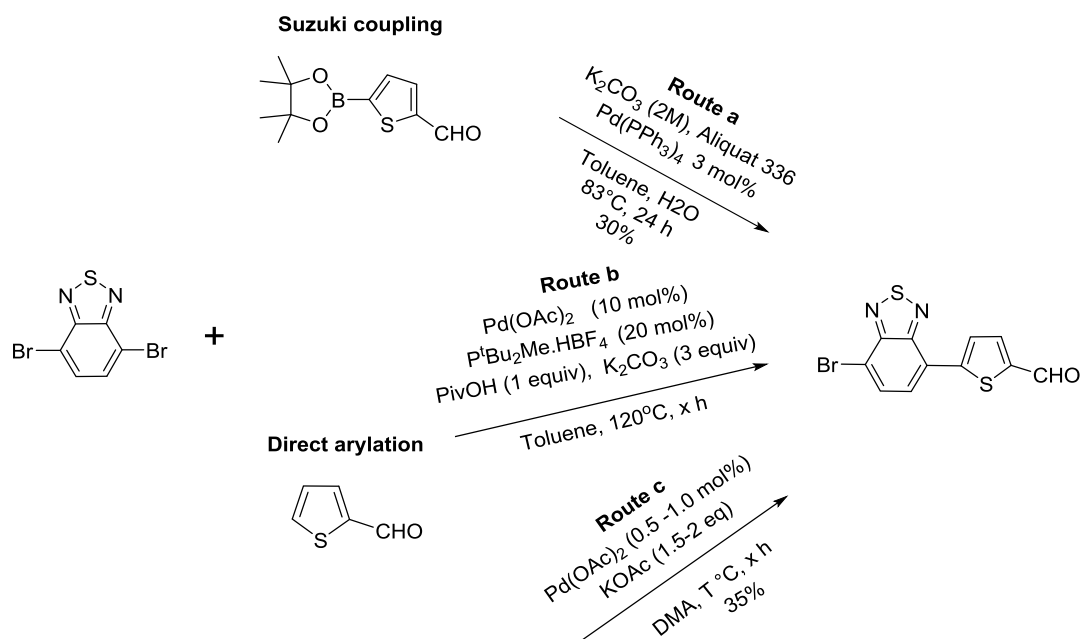
Figure III-2: Chemical structures of various fragments for DTS-based target molecules.

III. 1 Synthesis of mono-substituted compounds and related BzT₂CAO molecule

According to the designed target molecules mentioned in Chapter II, small molecules based on DTS core are aimed to be synthesized. In contrary to Bz-based molecules originated from the symmetric di-arylated products: molecules Bz(T₁CHO)₂ and Bz(T₂CHO)₂ which have been discussed above, syntheses of DTS-based target molecules need an intermediate step which consists of the synthesis of mono-substituted compounds, as previously specified (see Scheme II-5 in Chapter II). Here, we are going to discuss the synthesis of mono-arylated product *via* Suzuki coupling or direct arylation. These mono-substituted compounds are 5-(7-bromo-2,1,3-benzothiadiazol-4-yl)-2-thiophenecarboxaldehyde (BrBzT₁CHO) and 5'-(7-bromo-2,1,3-benzothiadiazol-4-yl)-[2,2'-bithiophene]-5-carboxaldehyde (BrBzT₂CHO).

III. 1-1 Synthesis of fragment BrBzT₁CHO

Based on our experience in the syntheses of di-arylated compounds Bz(T₁CHO)₂ and Bz(T₂CHO)₂, same strategies were applied to obtain fragment 5-(7-bromo-2,1,3-benzothiadiazol-4-yl)-2-thiophenecarboxaldehyde (BrBzT₁CHO) as those used for synthesizing compounds Bz(T₁CHO)₂ and Bz(T₂CHO)₂. The different routes to obtain fragment BrBzT₁CHO, including Suzuki coupling (**Route a**) (308) and direct arylation (**Route b** (309) and **c** (289)), are provided in Scheme III-5.



Scheme III-5: Different strategies to synthesize fragment BrBzT₁CHO.

These reactions were conducted in classical laboratory conditions (reaction carried out in a three-necked flask under inert atmosphere), even microwave method inspired by the work of Y. Geng *et al.*(313) was also attempted. For Suzuki reactions followed by TLC (thin layer chromatography), principally four products were found to be included in the crude product (see Figure III-3): diBrBz (it was in excess, so this was considered as normal), di-substituted molecule Bz(T₁CHO)₂, mono-substituted BrBzT₁CHO and TCHO.

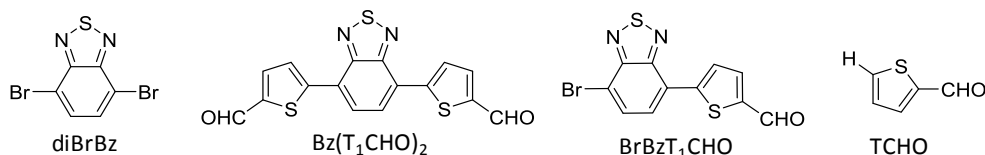


Figure III-3: Products found in the crude product of Suzuki reaction for fragment BrBzT₁CHO.

Among the four products identified in the crude sample, there was always an excess of diBrBz making the isolation of the mono-substituted product very difficult. It seems that diBrBz is poorly reactive. We even tested synthesis at room temperature, to reduce or avoid the formation of di-substituted molecule Bz(T₁CHO)₂, but it was still found in the crude product, as proved by ¹H NMR analysis. Another issue was the large quantity of TCHO also identified by ¹H NMR spectroscopy in the crude product. We can infer that diBrBz is very stable under Suzuki reaction and undergoes very slow additive oxidation during the catalytic cycle, while the transmetalation of the borate of the thiophene moiety takes place more rapidly (the catalytic cycle of Suzuki cross-coupling reaction is given in Annexes, on Figure

A.2). Finally, the thiophene moiety was protonated instead of reacting with Bz, forming TCHO and killing the catalytic cycle.

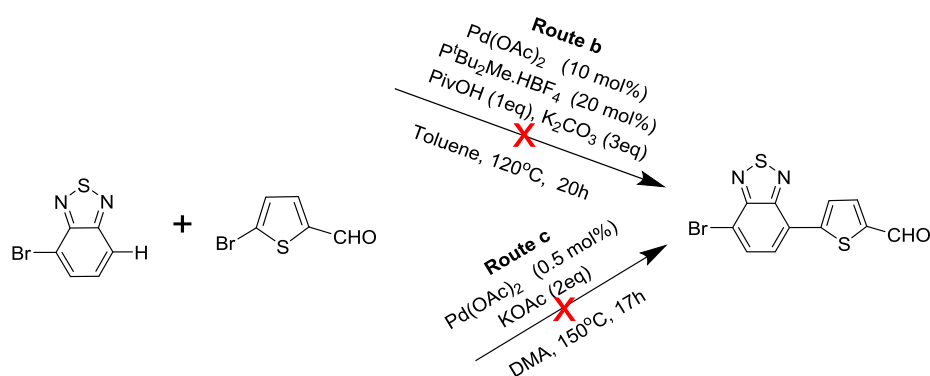
In order to optimize the reaction yield in decreasing risks of degradation of the 5-formyl-2-thiopheneboronic acid pinacol ester before it reacts, we tried to add it drop wisely under heating at 83 °C and vigorous stirring. Whereas the obtained yield was poorly reproducible, we reached at best 30% yield. This result may support the hypothesis of different reaction kinetics of diBrBz and thiophene carboxaldehyde boronic derivatives, which renders the coupling conditions tricky.

Direct arylation methods were thus implemented to synthesis BrBzT₁CHO *via* **Routes b** and **c**, as illustrated in Scheme III-5. **Route b** was conducted in toluene for four times under different conditions with fixed amount of catalyst and base. We tried to change the ratio between diBrBz and TCHO, the loading of ligand, the amount of additive, and length of reaction time. More details about synthesis are presented in the experimental section (see Table V-2). The same by-products as previously were found in the crude sample: diBrBz, molecule Bz(T₁CHO)₂, BrBzT₁CHO and TCHO. The reaction yield was evaluated from ¹H NMR analysis of the crude product. At the best, a 22% yield in non-isolated product was reached by using the following conditions: the molar ratio of 2-thiophenecarboxaldehyde (500 mg, 1.7 mmol, 1eq)/4,7-dibromobenzo-2,1,3-thiadiazole is 0.7, the amount of ligand (P^tBu₂Me.HBF₄) and additive (pivalic acid) is 10 mol% and 30 mol% (relative to diBrBz), respectively; fixed amount of potassium carbonate (K₂CO₃, 705 mg, 3eq) and palladium acetate (Pd(OAc)₂, 38 mg, 10% mol) (relative to diBrBz), 7.5 mL dry toluene under an argon atmosphere in a three-necked flask and refluxed for 18h.

In order to improve the yield of this mono-coupling reaction, lots of efforts were made to optimize reaction conditions, such as playing with the TCHO/diBrBz ratio, the amount of catalyst and base, various temperatures and time of reaction. The relevant details in synthesis of fragment BrBzT₁CHO *via* various conditions are summarized in the experimental section (Table V-3 and V-4). Like it was the case for Suzuki reactions, mainly four products were identified in the crude mixture: diBrBz, molecule Bz(T₁CHO)₂, BrBzT₁CHO and TCHO. It is worth to note that the non-reacted starting materials can be recovered. First, **Route c** was carried out at temperature of 105°C, 115°C, 125°C and 140°C (oil bath, the temperature of the reaction mixture is at around 10°C below) (see Table V-3). Note that when the temperature of

the oil bath reached 140°C, only di-substituted product was formed. We reached a 20% of non-isolated product at best at 115°C. Thus, various procedures were carried out at a maximum temperature of 115°C (oil bath) (see Table V-4). The best obtained result was 35% yield of isolated product, which was obtained *via* **Route c** under the following condition: molar TCHO/diBrBz ratio of 0.5, 1.5 equivalent of potassium acetate (KOAc) and 1 mol% catalyst palladium acetate (Pd(OAc)₂) (relative to diBrBz), 6 mL DMA and stirring at 105 °C for 21 h under an argon atmosphere in a three-necked flask. As a 30% yield of isolated product was obtained *via* **Route a** as mentioned above, thus, direct arylation is comparable to the traditional Suzuki coupling method. Taking into account the environmental factors, direct arylation (especially **Route c**) is preferable in that case, and this fully validates our efforts in optimizing the direct arylation method.

In order to increase more the yield in mono-substituted compounds *via* **Routes b** and **c**, another protocol was designed and carried out, as displayed in Scheme III-6. But this time, the reactants were changed into 4-bromobenzo-2,1,3-thiadiazole (BrBz) and 5-bromo-2-thiophenecarboxaldehyde (BrTCHO). The reaction conditions were based on the optimal conditions found for syntheses of molecules Bz(T₁CHO)₂ and Bz(T₂CHO)₂. The protocol was tested with a molar ratio of 1:1 between BrBz and BrTCHO under **Routes b** and **c** given in Scheme III-6. Unfortunately, the ¹H NMR analysis showed only reactants in the crude samples.

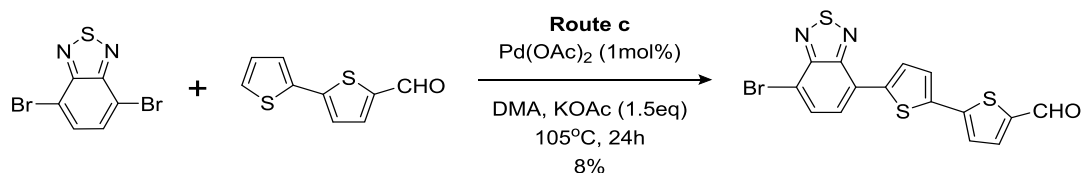


Scheme III-6: Other protocols to obtain fragment BrBzT₁CHO.

In conclusion, we have tested Suzuki and direct arylation coupling procedures with many different operating conditions. The best yield in isolated product is 35% by using **Route c**. Therefore, the **Route c** is best coupling protocol for the formation of new C-C bond throughout our work.

III. 1-2 Synthesis of fragment BrBzT₂CHO

Inspired by previous work, we also tried to synthesize 5'-(7-bromo-2,1,3-benzothiadiazol-4-yl)-[2,2'-bithiophene]-5-carboxaldehyde (BrBzT₂CHO) *via* **Route c**. The best way for obtaining BrBzT₁CHO was directly applied to the present case, as presented in Scheme III-7. The only difference was the T₂CHO/diBrBz molar ratio which was fixed at 1 instead of 0.5.

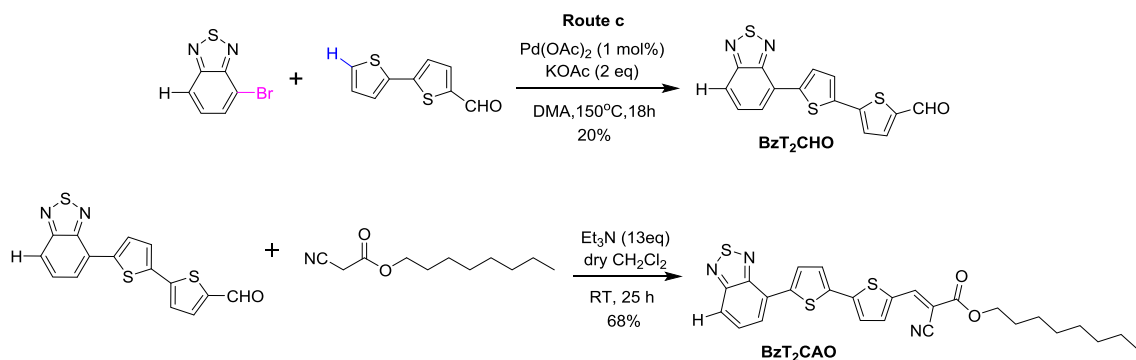


Scheme III-7: Synthetic route to obtain fragment BrBzT₂CHO.

Similar to the case of BrBzT₁CHO, mainly four products were identified in the crude mixture, consisting of diBrBz, T₂CHO, BrBzT₂CHO and di-substituted molecule Bz(T₂CHO)₂. They were detected by TLC under UV lamp and their ratio was able to be analysed by ¹H NMR spectroscopy. Based on the experience for purifying fragment BrBzT₁CHO, the crude product was subjected to flash chromatography to isolate very pure mono-arylated BrBzT₂CHO in 8% yield. This result was reproducible. In spite of the fact that the yield was not optimistic, the isolated mono-substituted product was very pure. This very pure fragment BrBzT₂CHO would be very advantageous for the further synthesis of DTS-based target molecules.

III. 1-3 Synthesis of another Bz-based unsymmetrical molecule (BzT₂CAO)

Symmetric target molecules have been successfully obtained by Knoevenagel condensation using the symmetric intermediates (molecules Bz(T₁CHO)₂ and Bz(T₂CHO)₂). Inspired by this previous work, we also planned to synthesize non-symmetric molecules, which could be of interest for understanding structure-property correlation. Guided by the prior experience, the unsymmetrical molecule BzT₂CAO was isolated through the unsymmetrical intermediate BzT₂CHO obtained *via* **Route c**, as shown in Scheme III-8.

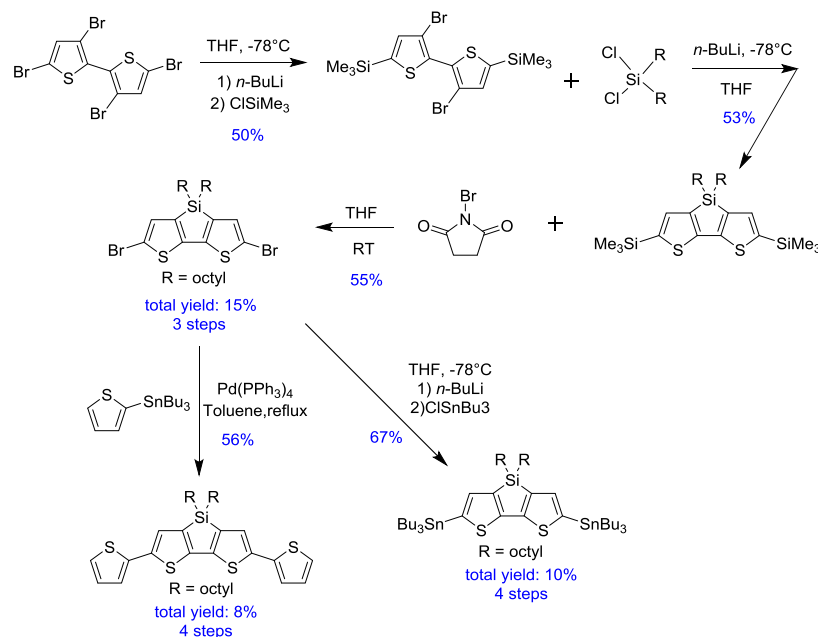


Scheme III-8: Strategy to obtain non-symmetric molecule BzT₂CAO.

The first step consists of obtaining the intermediate BzT_2CHO . Similar to the case for molecule $Bz(T_2CHO)_2$, 4-bromobenzo-2,1,3-thiadiazole (BrBz) and 2,2-bithiophene-5-carboxaldehyde (T_2CHO) with a molar ratio of 1:1, were dissolved in DMA under elevated temperature overnight. Flash chromatography was used to give very pure BzT_2CHO (orange colour) in 20% yield. Then BzT_2CHO was engaged in Knoevenagel condensation to give rise to the final molecule BzT_2CAO (orange solid) in 68% yield.

III. 2 Synthesis of DTS cores and DTS-based target molecules

As the syntheses of fragments $BrBzT_1CHO$, $BrBzT_2CHO$ and BzT_2CHO have been discussed previously, herein, the syntheses of fragments 4,4'-dioctyl-5,5'-dibromodithieno[3,2-b:2',3'-d]-silole (diBrDTS), 4,4'-dioctyl-2,6-bis(tributylstannyl)dithieno[3,2-b:2',3'-d]silole ($(SnBu_3)_2$) and 4,4'-dioctyl-2,6-di-2-thienyl-4H-silolo[3,2-b:2',3'-d]dithiophene (diTDTS) will be discussed. Scheme III-9 reminds the general procedures to obtain these DTS cores.



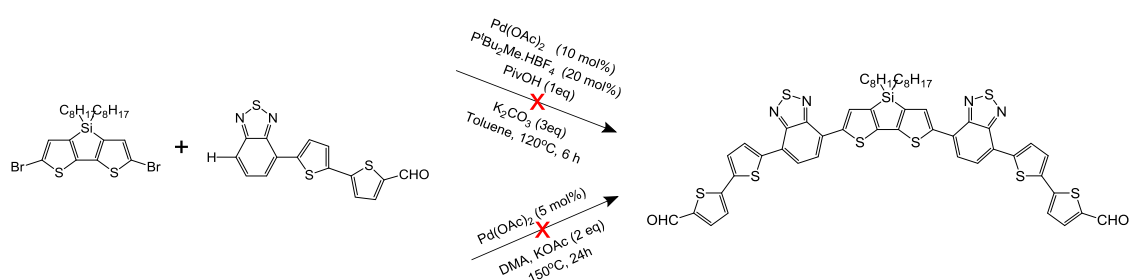
Scheme III-9: General procedures to synthesize the DTS cores for the target molecules.

The starting compound 3,3',5,5'-tetrabromo-2,2'-bithiophene was synthesized in quantitative yield *via* procedure described by Huang *et al.*(314) Then the following syntheses were carried out based on the synthetic routes shown in Scheme III-9. The 3,3'-Dibromo-5,5'-bis(trimethylsilyl)-2,2'-bithiophene was obtained by adding $n-BuLi$ (in hexanes) drop wisely into a solution of 3,3',5,5'-tetrabromo-2,2'-bithiophene in tetrahydrofuran (THF) under $-78^\circ C$ followed by chlorotrimethylsilane.(144) To continue with the synthesis of DTS with octyl chains, to a solution of 3,3'-dibromo-5,5'-bis(trimethylsilyl)-2,2'-bithiophene, $n-BuLi$ (in hexanes) was added at $-78^\circ C$ drop by drop and then followed by dichlorodiuoctylsilane. The

residue was purified by flash chromatography to yield a yellow oil named 4,4'-dioctyl-2,6-bis(trimethylsilyl)dithieno[3,2-b:2',3'-d]silole (DTS-(SiMe₃)₂) in 53% yield.^(144, 314) To achieve the finale fragment 4,4'-dioctyl-5,5'-dibromodithieno[3,2-b:2',3'-d]-silole (diBrDTS), *N*-bromosuccinimide (NBS) was used to brominate 4,4'-Dioctyl-2,6-bis(trimethylsilyl)dithieno[3,2-b:2',3'-d]-silole in THF at room temperature.⁽¹⁴⁴⁾

To get fragment 4,4'-dioctyl-2,6-di-2-thienyl- 4H-Silolo[3,2b:2',3'-d] dithiophene (diTDTS), to a solution of diBrDTS in toluene was added 2-(tributylstannyl)thiophene, and then tetrakis(triphenylphosphine) (Pd(PPh₃)₄), and the mixture was refluxed for overnight. The residue was purified by column chromatography using hexane as the eluent to give a red oil in 56% yield. To obtain 4,4'-dioctyl-2,6-bis(tributylstannyl)dithieno[3,2-b:2',3'-d]silole (DTS-(SnBu₃)₂), *n*-Buli (in hexanes) was added drop by drop to a solution of diBrDTS in THF at -78°C, then Tri-*n*-butyltin chloride was added in one portion. The resulting yellow oil (¹H NMR yield: 65%) was stored in fridge for further work without additional purification.

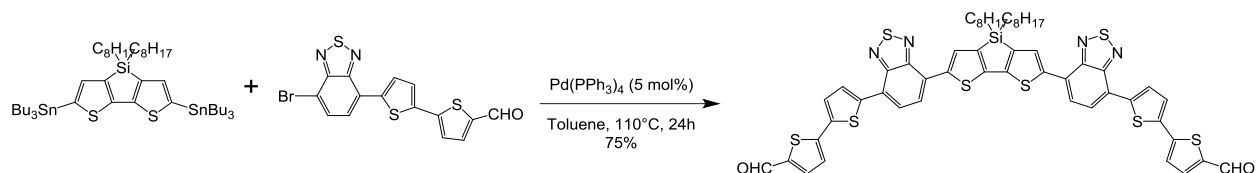
Once these fragments were obtained, they could be coupled *via* either direct arylation or Stille coupling, forming DTS-based precursors (see Scheme II-3 in Chapter II). Synthesis *via* direct arylation is a preferable approach throughout this project. Then these precursors will be engaged in Knoevenagel condensations to yield a series of the target DTS-based molecules (see Scheme II-2 in Chapter II). To fulfil these aims, the first strategy was to couple fragment diBrDTS with BzT₂CHO under different direct arylation conditions that are proven to be very effective, for obtaining the di-substituted molecules Bz(T₁CHO)₂ and Bz(T₂CHO)₂. Two tested reactions are given in Scheme III-10.



Scheme III-10: One strategy supposed to obtain DTS(BzT₂CHO)₂.

However, neither of the reactions worked, only both of the starting materials were found in the crude mixture as proved by ¹H NMR analysis. Since the strategy *via* direct arylation failed, the fragment BzT₂CHO was recovered and used for the synthesis of BzT₂CAO previously described. It infers that the C-H bond activation is harder to reach on the

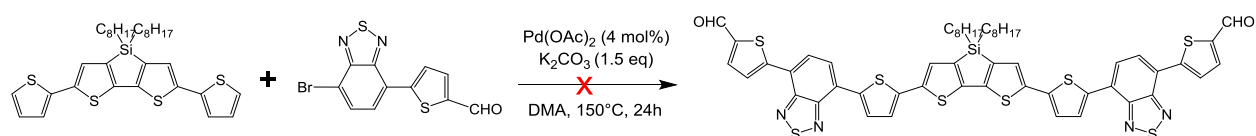
benzothiadiazole ring than that on the thiophene ring. Thus, we turned to another strategy using Stille coupling (see Scheme III-11), which has been demonstrated to be a traditional procedure for synthesis of D-A based small molecules or polymers. Stannylated derivatives (DTS-(SnBu₃)₂) was coupled with aryl halides (BrBzT₂CHO), giving the corresponding product DTS(BzT₂CHO)₂.



Scheme III-11: Second strategy for obtaining DTS(BzT₂CHO)₂.

The next step (or final step) will carry out the Knoevenagel condensation on DTS(BzT₂CHO)₂, which will form another A-D-A-D-A-D-A small molecule (This last step has not been conducted due to the limited time and graduation schedule).

To obtain another DTS-based small molecule, direct arylation procedure was carried out on fragments diTDTS and BrBzT₁CHO, as provided in Scheme III-12. This direct arylation procedure was inspired by Scherf and co-workers' work that uses 4,4-dialkyl-cyclopenta[2,1-*b*:3,4-*b'*]dithiophene (CPDT) and 4,7-dibromobenzo-2,1,3-thiadiazole (diBrBz) as monomers to get polymer PCPDTBT efficiently without additional phosphine ligands.⁽³¹⁵⁾ Unfortunately, this reaction did not work in our case.



Scheme III-12: The strategy for obtaining DTS(TBzT₁CHO)₂.

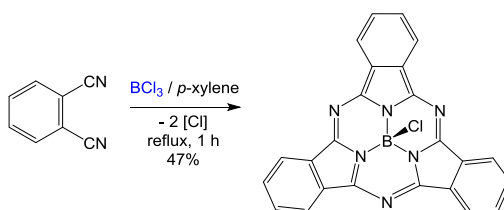
Due to the limited time, further work on DTS(TBzT₁CHO)₂ was also suspended. More efforts should be devoted to find the optimal direct arylation procedure for obtaining it. Once it will be obtained, followed by Knoevenagel condensation, the target molecule DTS(TBzT₁CAO)₂ (see Scheme II-2 in Chapter II) will be achieved. Besides, if the strategy for obtaining DTS(TBzT₁CHO)₂ would be realized, the coupling between fragments diTDTS and BrBzT₂CHO would also be achieved and thus similar target molecule DTS(TBzT₂CAO)₂ (see Scheme II-2 in Chapter II) would be obtained afterwards.

IV Subphthalocyanine (SubPc) derivatives: synthesis and axial substitution

IV. 1 Synthesis of chloroboron subphthalocyanine (SubPcBCl)

SubPcs have become molecular materials in areas of energy and electron transfer, particularly ascribe to their unique optical properties. The chemistry of SubPcs has been well explored over the last two decades because of the great contribution from the teams of Torres (185, 186, 247, 316), Bender (234, 250), Hanack (317) *etc.*. So far SubPcs are only known as boron complex (BSubPcs). The boron atom performed perfectly as the central cavity and efficiently directs the phthalonitrile cyclotrimerization reaction that causes these macrocycles. The general synthesis procedure is typically carried out in the presence of a boron trihalide (BCl_3 or BBr_3) at high temperature (185, 186, 234, 316, 318). As a consequence, a halide atom (Cl or Br) consequently occupies the axial position of the SubPc, forming chloroboron SubPcs (SubPcBCl) or bromine boron SubPcs.

Dedicated efforts have been devoted to the preparation of SubPcBCl. One of major breakthroughs is the Torres group's discovery of a high efficient method for the preparation of SubPcs in high yields.(316) They reported that the experimentally determined optimal stoichiometry between phthalonitrile and BCl_3 is 1:1. Another major breakthrough is the development of general methodology for axial substitution in BSubPcs species.(316) Herein, we carried out the following reactions (see Scheme III-13) several times to reproduce the work of Claessens *et al.*(316) From the results summarized in the experimental section (see Table V-5), a maximum of 47% yield was achieved.



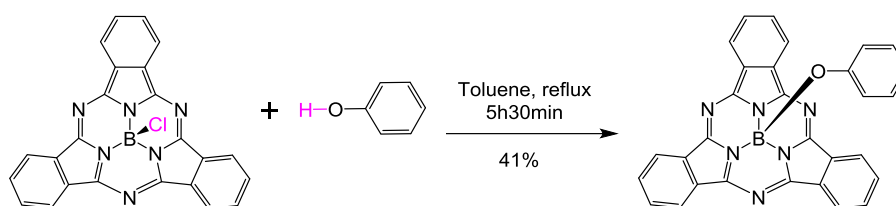
Scheme III-13: Synthesis route to SubPcBCl.

In our work, we did exactly the same treatment as described by Claessens *et al.*,(316) but the yield (12%) was quite lower than that claimed in their article (82%). Then a little different treatment was tried. We skipped directly to the washing step in place of washing after extraction, and washing, and a moderate yield (47%) was finally obtained using this modified treatment (see experimental section).

IV. 2 Axial substitution of SubPcBCl

SubPcs are synthetically diverse molecules, and their reactivity is presumably classified in mainly three groups: axial reactivity, peripheral reactivity, and ring expansion reactivity.⁽¹⁸⁶⁾ The electronic and physical properties of SubPcs are rather attractive, and they may be well-tuned by alternating their axial ligands with certain nucleophiles ⁽²⁴⁷⁾ or by modifying the peripheral substituents at the isoindole rings.

The reactivity at the axial position in SubPcs has been exhaustively investigated for the substitution of these molecules for different aims. To begin with, axial functionalization can help these molecules soluble in water⁽³¹⁹⁾ or organic ⁽³²⁰⁾ media, which is important for the device processing and biological applications. Furthermore, it has been proved that substitution with some ligands enhances their optical, thermal, and chemical stability ^(320, 321). Moreover, this axial substitution tolerates for straightforwardly merging these singular chromophores into larger multicomponent and more complex systems without influencing the electronic characteristics of the macrocycles, which are principally evaluated by the feature of the peripheral substituents.^(232, 251) Besides, the variation of axial substitution is of great interest for SubPcs chemistry. Among the many possible substituting compounds, phenol derivatives are to date the most widely used reagent for the axial substitution reactions. From the point of experiment, we found that phenol derivatives provide many advantages: (i) phenol derivatives are available in considerable quantities; (ii) the reaction is carried out in a simple and straightforward way and it generally affords moderate to favorable yield.^(185, 186, 316) A recent study showed that over 90% of the research published in chemistry journals on SubPcs involve the synthesis of phenoxy-SubPcs during the last decade.⁽¹⁸⁶⁾ Therefore, our study commenced with the axial substitution using phenol, as schemed in Scheme III-14. This work was inspired by the work of Torres *et al.*^(247, 316). It was found that the phenol in fivefold excess can give good yields of phenoxy- perfluoroSubPc. Thus the same condition and procedure were applied to our work. The corresponding phenoxy-SubPc was able to be monitored by TLC and ¹H NMR. It was purified by column chromatography in 41% yield.



Scheme III-14: Synthesis route to phenoxy-SubPc.

With regard to synthesized SubPcBCl and phenoxy-SubPc, they were also characterized in term of UV-Vis absorption as well as ^1H NMR analysis. Their normalized absorption spectra in dichloromethane are shown in Figure III-4. Our spectrum of SubPcBCl (red) is in very good accordance with that of Bender.(221) Both BSubPc derivatives share very similar absorption curve that is characteristic of BSubPc derivatives in general.(234) The main absorption bands for SubPcBCl and phenoxy-SubPc are observed at λ_{max} 565 and 563 nm with distinct shoulders at 549 and 547 nm, respectively.

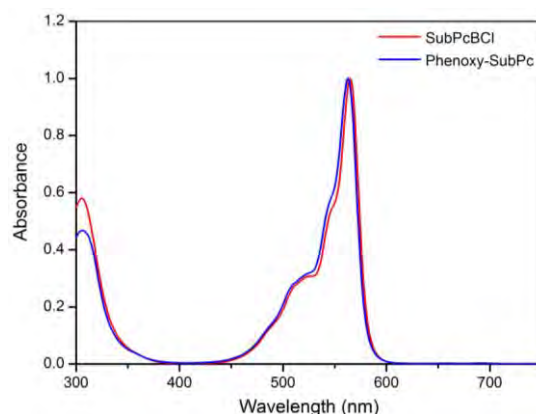


Figure III-4: Normalized absorption spectra of SubPcBCl and phenoxy-SubPc in CH_2Cl_2 solution.

According to the designed SubPcs derivatives and synthetic strategy *via* axial substitution (see Scheme II-6 in chapter II), the next step will be carried out on phenoxy-SubPc with fragment BrBzT_1CHO or BrBzT_2CHO (see Figure III-2) *via* direct arylation procedure to achieve the axial substituted target molecules. Although both phenoxy-SubPc and BrBzT_1CHO (or BrBzT_2CHO) were obtained at the moment, the following interesting work hasn't been conducted due to lack of time. Besides, we may encounter difficulties in the following synthesis due to reactivity of the hydrogen on the benzene ring. However, based on our theoretical calculations, once SubPcs-based target molecules were achieved, their interesting electronic properties would make them promising candidates for electron donors or acceptors.

V Conclusion

To conclude, the present study provides chemical synthetic protocols for the synthesis of regioselective D-A based materials in addition to give a general guideline towards the design of benzothiadiazole and thiophene-based materials for the applications in OPVs. As synthetic chemists, our aim is to contribute to develop clean energy using materials that are obtained according to green practices. Five new Bz-based molecules have been synthesized according

to green practices. The proposed molecules are unsophisticated and obtained *via* a synthetic approach that may significantly impact the environmental factors, in term of non-reacted raw materials or waste generation. The ligand-less direct arylation reaction has proved to be a powerful green tool for obtaining dithienylbenzothiadiazole blocks, which are very often used as a building block for more expanded materials used in organic electronics. E-factor values below 400 g/g associated with molecules prices in the order of 45 €/g are promising numbers for potential large-scale applications. Their full characterization will be described in Chapter IV.

Direct arylation method in our work on di-substituted molecules $\text{Bz}(\text{T}_1\text{CHO})_2$ and $\text{Bz}(\text{T}_2\text{CHO})_2$ has exhibited the following advantages over traditional cross-coupling techniques: fewer synthetic steps, higher yields, lower catalyst loadings, no use of organometallic intermediate, and does not require chromatographic purification. The advantages of direct arylation make it an ideal and green strategy for the synthesis of organic electronic materials. It is quite an attractive method that can be added to chemists' toolbox, enabling more effective designation and preparation of highly efficient polymers or small molecules and providing a new vision into promising and novel electrical materials.

Many efforts and energy were devoted to the syntheses of DTS-based target molecules, from syntheses of various DTS-based fragments to syntheses of mono-substituted fragments. The final coupling between these fragments were first attempted *via* direct arylation procedure, and then conducted *via* traditional Stille coupling. One more step needs to be done on compound $\text{DTS}(\text{BzT}_2\text{CHO})_2$ using Knoevenagel condensation, to get one DTS-based target molecule $\text{DTS}(\text{BzT}_2\text{CAO})_2$ (A-D-A-D-A-D-A). Although direct arylation procedure did not succeed for the syntheses of DTS-based target molecules so far, it is without any doubt a green approach.

Syntheses of SubPcBCl and its axial substitution using phenol were studied. Axial substitution using mono-substituted fragments (BrBzT_1CHO or BrBzT_2CHO) *via* direct arylation were also envisaged. Due to lack of time, this idea has not yet been explored. Based on theoretical calculations presented in the previous chapter, it is predicted that original electronic properties are awaited for these SubPcs-based new materials that may lead to promising performances in organic photovoltaics, paving the way for innovative materials.

Chapter IV: Materials characterization

Chapter IV : Materials characterization

In this section, the obtained and well characterized compounds including $\text{Bz}(\text{T}_1\text{CAO})_2$, $\text{Bz}(\text{T}_1\text{CAEH})_2$, $\text{Bz}(\text{T}_2\text{CAO})_2$ and $\text{Bz}(\text{T}_2\text{CAEH})_2$ are going to be described and discussed in terms of optical and electrochemical properties, thermal properties, structural properties and their potential in organic photovoltaic application. The influence of the different alkyl chains (linear and branched) on these characteristics will also be investigated. For convenience, $\text{Bz}(\text{T}_1\text{CAR})_2$ represents both $\text{Bz}(\text{T}_1\text{CAO})_2$ and $\text{Bz}(\text{T}_1\text{CAEH})_2$, and $\text{Bz}(\text{T}_2\text{CAR})_2$ represents both $\text{Bz}(\text{T}_2\text{CAO})_2$ and $\text{Bz}(\text{T}_2\text{CAEH})_2$. Besides, molecule BzT_2CAO was obtained very recently, thus it is not well studied, and here we will just simply discuss its electronic properties in solution.

I Optical properties

The UV-vis absorption of the four molecules in dichloromethane (DCM) solution was recorded at room temperature, as given in Figure IV-1. It is noticeable that the nature of the alkyl chain ($\text{R} = \text{octyl}$ or 2-ethylhexyl) does not affect the absorption spectrum. The large absorption band that peaks at 497 nm and 525 nm for $\text{Bz}(\text{T}_1\text{CAR})_2$ and $\text{Bz}(\text{T}_2\text{CAR})_2$, respectively, can be attributed to the intramolecular charge transfer (ICT) transition.⁽³²²⁾ A higher energy transition occurs at 385 nm and 450 nm for $\text{Bz}(\text{T}_1\text{CAR})_2$ and $\text{Bz}(\text{T}_2\text{CAR})_2$, respectively. It should be noted that the increase of the number of thiophene units from one to two at both sides of the benzothiadiazole core induces a red shift of 28 nm, as a result of the extension of the conjugation.

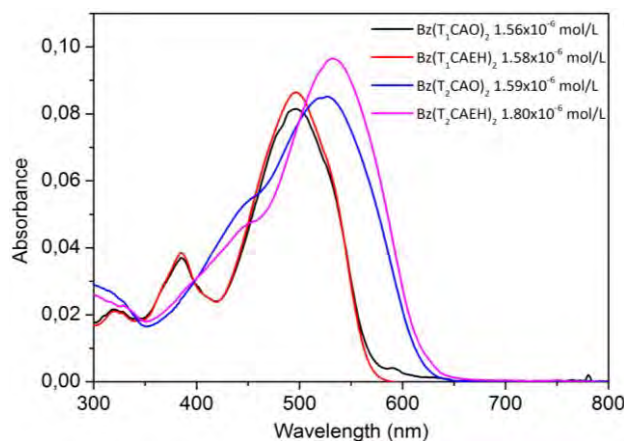


Figure IV-1: Absorption spectra of the four molecules under study in DCM solution with concentrations as indicated.

Absorption spectra in solution were simulated using the `orca_mapspc` program that applies Gaussian-type lineshape function to the calculated transition with a defined full-width-half-maximum of 1200cm^{-1} . Different functionals have been tested to predict the absorption spectra that may help us to further understand optical properties of $\text{Bz}(\text{T}_1\text{CAME})_2$ and $\text{Bz}(\text{T}_2\text{CAME})_2$. It suggests that BHandHLYP method offers good agreement with experimental results in our case, as evidenced by Figure IV-2. The large absorption band that peaks at 525 nm for simulated $\text{Bz}(\text{T}_2\text{CAME})_2$ is observed at the same energy than that experimentally recorded. The maximum absorption wavelength of the large band simulated for $\text{Bz}(\text{T}_1\text{CAME})_2$ is 476 nm, which slightly blue shifted of 21 nm compared to that of experimental result. The most important contribution to this principal absorbance band originates from the HOMO to LUMO transition (as discussed in chapter II).

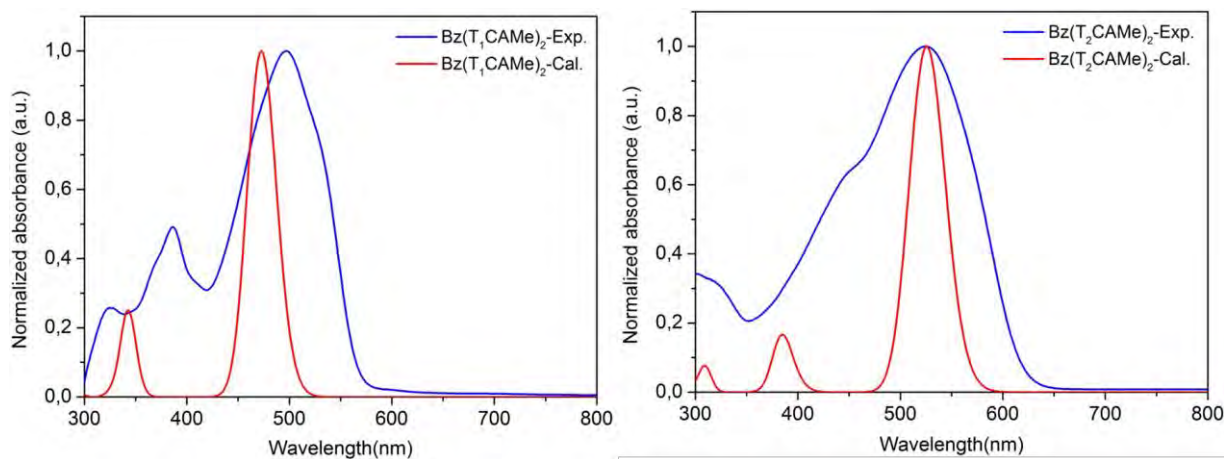


Figure IV-2: Experimental and simulated absorption spectra of $\text{Bz}(\text{T}_1\text{CAME})_2$ and $\text{Bz}(\text{T}_2\text{CAME})_2$ in DCM solution (simulation performed at BHandHLYP/Def2-TZVP level).

The effect of fluorination has already been theoretically discussed in chapter II (see Figure II-19). To study the fluorination from the experimental point of view, the absorption spectra of both $\text{Bz}(\text{T}_1\text{CAME})_2$ and $\text{ffBz}(\text{T}_1\text{CAME})_2$ in dichloromethane solution are provided in Figure IV-3(left). Note that the fluorinated target molecules ($\text{ffBz}(\text{T}_1\text{CAO})_2$ and $\text{ffBz}(\text{T}_1\text{CAEH})_2$) were synthesized by my co-worker, Damien Le Borgne. The experimental maximum absorptions for $\text{Bz}(\text{T}_1\text{CAME})_2$ and $\text{ffBz}(\text{T}_1\text{CAME})_2$ peak at 497 and 474 nm, respectively, revealing a 23 nm blue shift due to the fluorination. This confirms the theoretical simulations previously presented in Chapter II. Both experimental and simulated spectra of $\text{ffBz}(\text{T}_1\text{CAME})_2$ are presented here to allow clear comparison (Figure IV-3(right)). The simulated maximum absorption for $\text{ffBz}(\text{T}_1\text{CAME})_2$ peaks at 444 nm, which is 30 nm blue shifted relative to its experimental spectrum. Therefore, the reliability of the simulation at

BHandHLYP/Def2-TZVP level is demonstrated by the very subtle deviation between experimental and computational results.

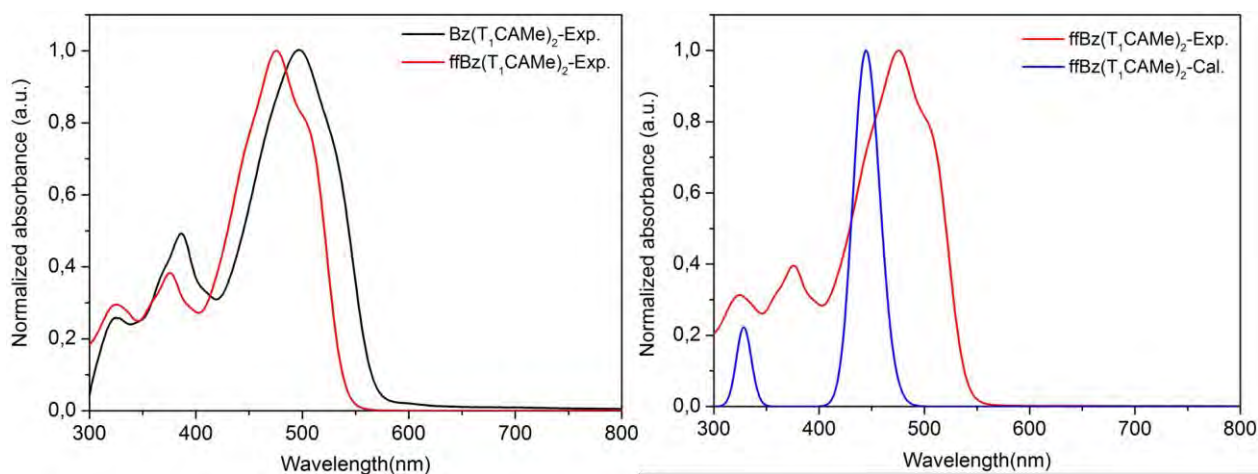


Figure IV-3: UV-vis absorption spectra of molecules $Bz(T_1CAME)_2$ and $ffBz(T_1CAME)_2$ under study in DCM solution and by DFT at BHandHLYP/Def2-TZVP level. (Exp. indicates experimental absorption; Cal. means calculated absorption)

The fluorescence in dichloromethane solution was also measured to analyse the emission due to excitation at a wavelength corresponding to the principal absorption, as shown in Figure IV-4. One can observe that Stokes shifts for compounds $Bz(T_1CAR)_2$ and $Bz(T_2CAR)_2$ are of 70 nm (0.32 eV) and 80 nm (0.30 eV), respectively. The fluorescence spectra of $Bz(T_1CAR)_2$ present two principal peaks: a maximum at 567 nm and a large shoulder at 606 nm. The energy between this two neighbouring peaks is about 0.14 eV (1129 cm^{-1}), which could correspond to the vibration energy of the C=C ring stretching.⁽³²³⁾ This phenomenon indicates a fine (or rigid) structure of $Bz(T_1CAR)_2$. The fluorescence spectra of $Bz(T_2CAR)_2$ show only one dominant wide peak at 625 nm.

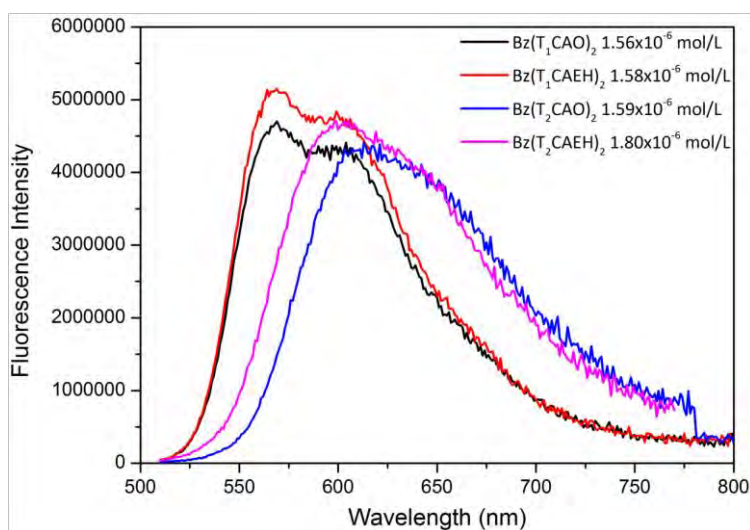


Figure IV-4: Emission spectra of the four molecules under study in DCM solution with concentrations as indicated.

The excitation spectra have been measured as well (Figure IV-5). The excitation wavelengths were scanned at a constant emission wavelength as indicated in the figure. This analysis may generate the absorbance characteristics of a single fluorescent compound when emitting at the detected emission wavelength. The shape of excitation spectrum should be the same as that of the absorption spectrum. On contrary, if the two spectra are different, it reveals the presence of more than one light-absorbing species. For both $\text{Bz}(\text{T}_1\text{CAR})_2$ and $\text{Bz}(\text{T}_2\text{CAR})_2$, their excitation spectra reproduce the absorption spectra very well, which confirm that the observed optical phenomena belong to one-single molecule properties.

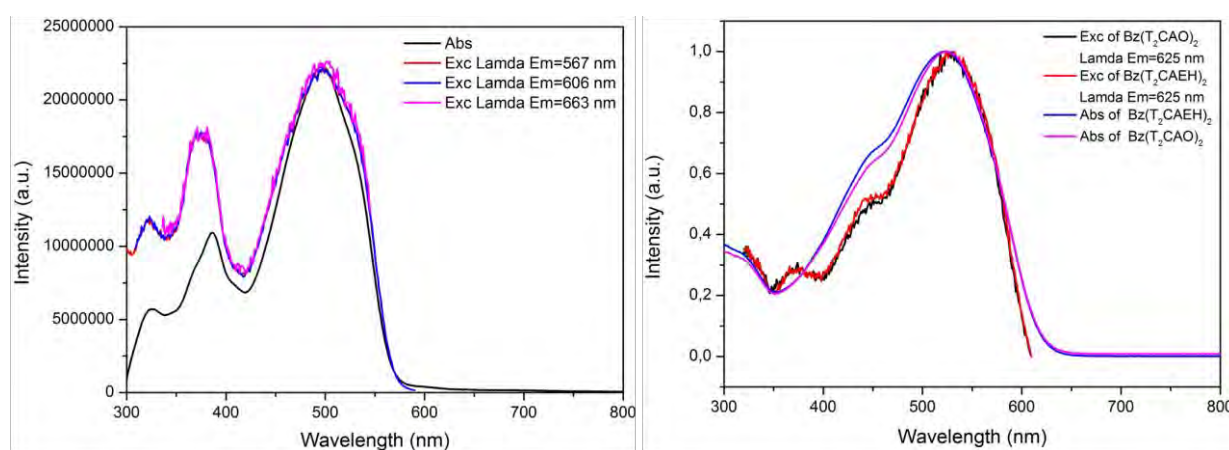


Figure IV-5: Normalized absorption and excitation spectra of $\text{Bz}(\text{T}_1\text{CAO})_2$ in dichloromethane (left) and of $\text{Bz}(\text{T}_2\text{CAR})_2$ in DCM (right).

Transitioning from solution to the solid state (thin films were prepared by spin coating from dichlorobenzene solutions in collaboration with Dr. Isabelle Séguy from LAAS), as shown in Figure IV-6. We observe that the absorption band of both $\text{Bz}(\text{T}_1\text{CAO})_2$ and $\text{Bz}(\text{T}_1\text{CAEH})_2$ exhibit two maxima of equivalent intensity centred at about 540 and 580 nm, respectively. The energy between this two adjacent peaks is about 0.16 eV (1290 cm^{-1}) that corresponds to the vibration energy of the C=C ring stretching. We can also observe a shoulder at about 504 nm for both molecules. Both molecules in solid state exhibit broad and red-shifted optical absorption maxima ($\Delta\lambda = 40\text{-}110\text{ nm}$), along with the emergence of fine structure within the low energy band. Such features are ascribed to a more rigid and ordered structure in the solid state, which result in greater π -electron delocalization across the molecular backbone and increased intermolecular interactions.⁽¹³²⁾

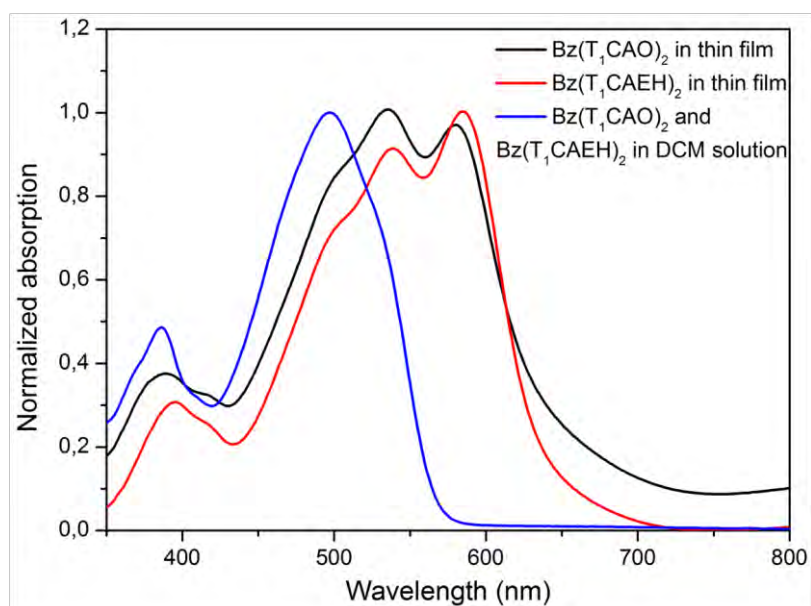


Figure IV-6: Normalized absorption spectra of $Bz(T_1CAO)_2$ and $Bz(T_1CAEH)_2$ in thin film in DCM solution.

The effect of thermal annealing on thin films of $Bz(T_1CAEH)_2$ deposited on ITO/glass was also examined. This work was done by my co-worker in LCC with thin films fabricated in LAAS. The film was sequentially annealed at increasing temperature for 20 minutes. Temperature-dependent absorption of pure $Bz(T_1CAEH)_2$ film is presented in Figure IV-7, showing obvious changes due to heating process. It reveals a disaggregation behavior towards elevated temperature. The optical density of lowest energy absorption peak (centred at around 590 nm) is progressively decreased upon thermal annealing at and above 100°C. It indicates aggregation effect of $Bz(T_1CAEH)_2$ film at room temperature for forming fine structure and.(94, 324, 325) It also suggests annealing weakens the aggregation effect greatly at elevated temperature due to weaker π - π packing, resulting in less-ordered structure. In particular, annealing at 160°C for 20 min results in almost no aggregation, and the absorption shape is like the one observed from solution. We can conclude that annealing makes morphology of $Bz(T_1CAEH)_2$ film less ordered. Thus, annealing is not suitable for our molecules even they are chemically stable until 300°C, although it has been proven to be effective for controlling film morphology to improve the performance of OPV devices.(326) This may explain the poor performance of $Bz(T_1CAO)_2$ and $Bz(T_1CAEH)_2$ in OPV devices recently fabricated *via* annealing by my colleague.(327) One possible solution to develop organic nanostructures and thus improve the device performances could consist of using crystalline diindenoperylene (DIP) film as a nanostructured template.(328)

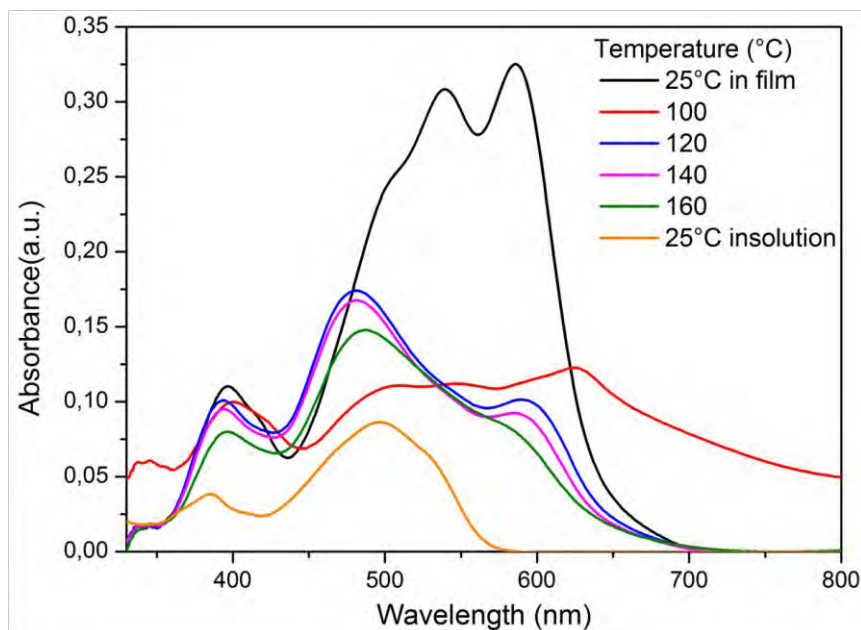


Figure IV-7: UV-vis absorption spectra of Bz(T₁CAEH)₂ film spin coated from chlorobenzene solution at room temperatures and annealed as indicated. The film was sequentially annealed at increasing temperature for 20 minutes.

Blends of both Bz(T₁CAO)₂ and Bz(T₁CAEH)₂ with P3HT in thin film (1:1 wt. ratio) were prepared by spin coating *via* collaboration with Dr. Isabelle Séguy from LAAS laboratory. The absorption analysis on pristine thin films and blend are presented in Figure IV-8. Pure P3HT in thin film shows a typical π - π^* absorption band centred at approximately 550 nm with well-resolved shoulders at 523, 555, and 605 nm, respectively. For blend P3HT:Bz(T₁CAO)₂ (1:1 wt.), a maximum absorption peaks at 533 nm with a shoulder at 582 nm. The spectrum of the P3HT:Bz(T₁CAO)₂ blend shows the behavior of pristine Bz(T₁CAO)₂ film with the shoulder at around 580 nm, while the shoulder of P3HT at 605 nm collapsed. Similarly, P3HT:Bz(T₁CAEH)₂ blend shows the behavior of pristine Bz(T₁CAEH)₂ film with the shoulder at around 584 nm, while the shoulder of P3HT at 605 nm also collapsed. For both blends, their spectra are very close to that of pristine Bz(T₁CAO)₂ and Bz(T₁CAEH)₂ thin films but with less-resolved shoulders. It suggests that there is almost no change on the structure of Bz(T₁CAO)₂ and Bz(T₁CAEH)₂ but on the structure of P3HT in the blends. We can infer the existence of the interaction between the two compounds (Bz(T₁CAO)₂ and Bz(T₁CAEH)₂) and P3HT, and the interaction has much influence on the structure of P3HT but weak influence on the structure of these two compounds.

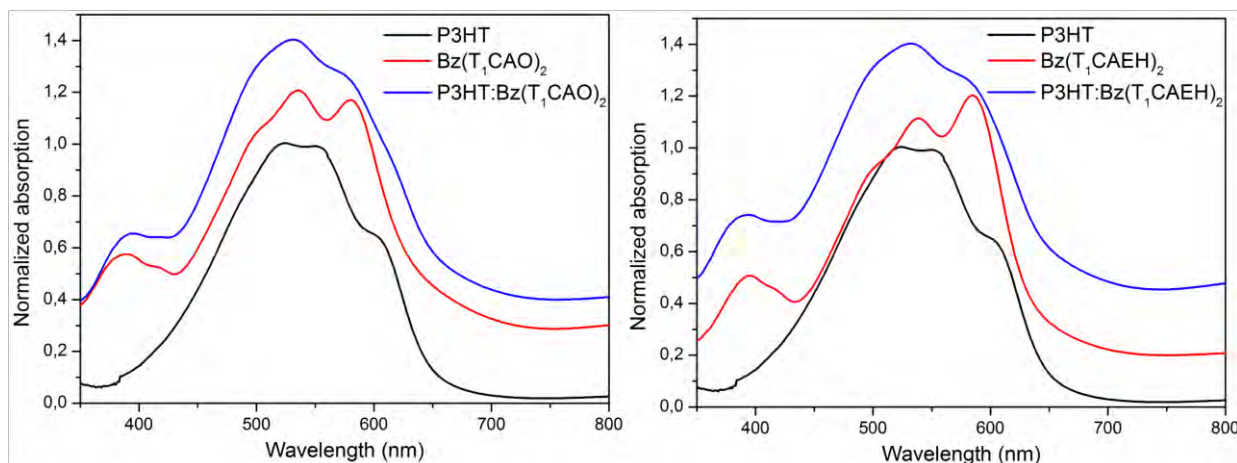


Figure IV-8: Normalized absorption spectra of pure P3HT, $Bz(T_1CAO)_2$ and $Bz(T_1CAEH)_2$ and 1:1 wt. blends in thin films.

II Electrochemical properties

Cyclic voltammetry (CV) measurements of molecules in CH_2Cl_2 solution were used to evaluate electrochemical characteristics. The electrochemical behaviors of $Bz(T_1CAO)_2$ and $Bz(T_1CAEH)_2$ are almost the same. In the same manner, $Bz(T_2CAO)_2$ and $Bz(T_2CAEH)_2$ show quite similar behaviors, thus here we show typical cyclic voltammograms of $Bz(T_1CAO)_2$ (Figure IV-9) and $Bz(T_2CAEH)_2$ (Figure IV-10). Relevant data are provided in Table IV-1.

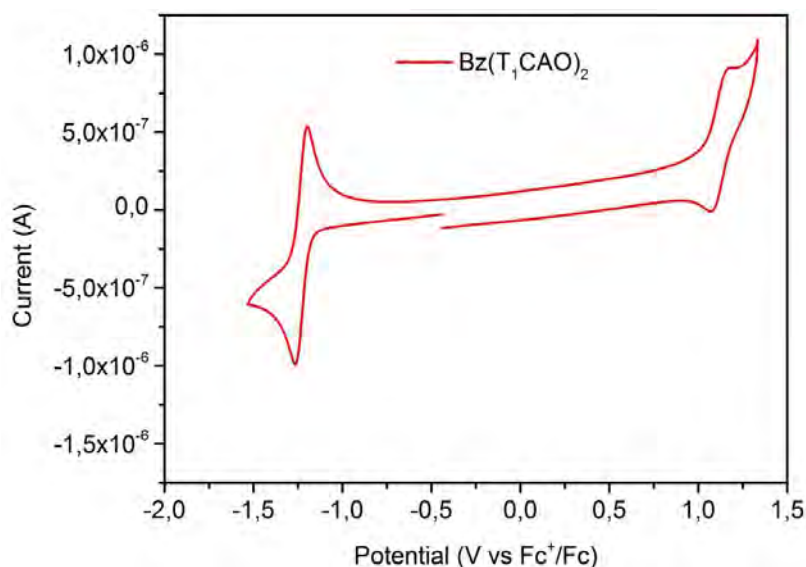


Figure IV-9: Cyclic voltammetry of $Bz(T_1CAO)_2$ in 0.1 M PF_6TBA dichloromethane solution; Pt electrode; scan rate = $200 \text{ mV}\cdot\text{s}^{-1}$.

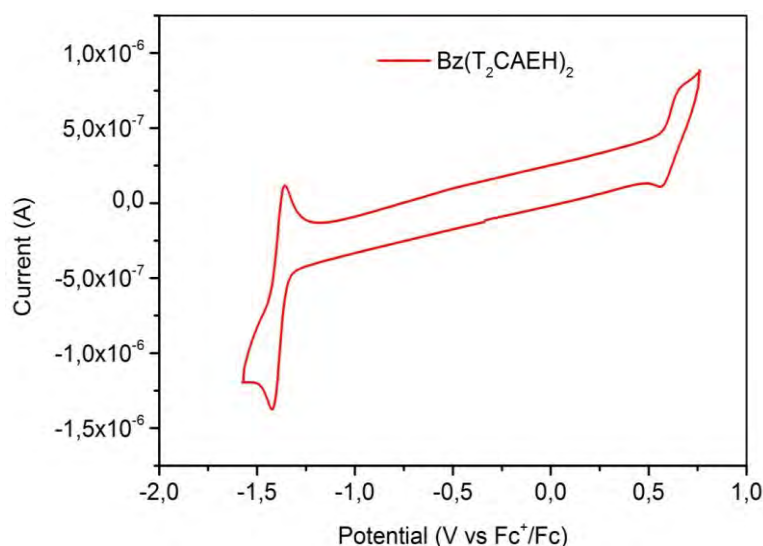


Figure IV-10: Cyclic voltammetry of Bz(T₂CAEH)₂ in 0.1 M PF₆TBA dichloromethane solution; Pt electrode; scan rate = 200 mV.s⁻¹.

The correlation of electrochemical potentials with orbital energies is according to the equations as follows:(329)

$$E_{\text{HOMO}} = - (E_{[\text{onset, ox vs. Fc}^+/\text{Fc}]} + 5.39) \text{ (eV)}$$

$$E_{\text{LUMO}} = - (E_{[\text{onset, red vs. Fc}^+/\text{Fc}]} + 5.39) \text{ (eV)}$$

The four molecules undergo reversible reduction and oxidation events. This demonstrates that the reduction and oxidation species are electrochemically stable, a positive feature for their potential operational stability in OPV devices. The highest occupied molecular orbital (HOMO) and the lowest unoccupied molecular orbital (LUMO) values were estimated from the onset voltages of the oxidation and reduction waves, respectively.

As indicated in Table IV-1, their electrochemical gaps are in good agreement with the optical gaps. The high molar extinction coefficient (beyond $5.1 \times 10^4 \text{ M}^{-1}\text{cm}^{-1}$) at the maximum absorption wavelength is attributed to the strong conjugation of the alternating D-A structure. The five molecules exhibit deep LUMO energies values: -4.20 eV, -4.05 eV and -3.94 eV for the symmetrical thiophene, bithiophene derivatives and non-symmetrical bithiophene derivative, respectively. They also show deep HOMO energies values: -6.4 eV, -6.0 eV and -6.24 eV for the symmetrical thiophene, bithiophene derivatives and non-symmetrical bithiophene derivative, respectively. To make the parallel with well-known materials for OPV, we may point out that these LUMO and HOMO energy values are of 0.6 eV, 0.7 eV and 0.4 eV, respectively, lower than those of P3HT (-3.55 eV and -5.45 eV, respectively), and very close to those of PC₆₀BM (-4.37 eV and -6.45 eV, respectively), as depicted in Figure

IV-11 that offers visual comparison. Thus, if thin films made of these molecules exhibit good electron mobility, then they would be good acceptors candidates according to the energy levels of their frontier orbitals. Besides, we can observe the trends in decreasing optical and electrochemical band gap in solution from Bz(T₁CAR)₂ to Bz(T₂CAR)₂. These trends are supported by DFT calculations, as indicated in Figure IV-11. The calculated HOMO and LUMO energy levels are higher than those obtained from experimental condition, and the band gap is 0.2 eV larger than experimental result. This trivial difference reveals that our calculations are of good accuracy. In addition, one can see the trends in decreasing optical and electrochemical band gap in solution from non-symmetrical structure to symmetrical structures.

Table IV-1: Optoelectronic properties of the target molecules.

	λ_{\max} (nm) ^a	ϵ (M ⁻¹ cm ⁻¹)	E_g^{opt} (eV) ^b	E_{ox} (V/Fc ⁺ /Fc) ^c	E_{red} (V/Fc ⁺ /Fc) ^c	E_g^{el} (eV) ^c	HOMO (eV) ^d	LUMO (eV) ^d
Bz(T₁CAO)₂	498	51000	2.1	+1.01	-1.18	2.16	-6.4	-4.2
Bz(T₁CAEH)₂	497	55000	2.1	+0.99	-1.17	2.19	-6.4	-4.2
Bz(T₂CAO)₂	522	53440	2.0	+0.57	-1.34	1.91	-6.0	-4.05
Bz(T₂CAEH)₂	525	53440	2.0	+0.55	-1.37	1.92	-5.9	-4.0
BzT₂CAO	461		2.36	+0.85	-1.45	2.30	-6.24	-3.94

^aMeasurement in dichloromethane solution. ^bEvaluated from the onset absorption in dichloromethane solution ($E_g^{\text{opt}} = 1240/\lambda_{\text{onset}}$). ^cMeasured in CV in dichloromethane solution with FP₆TBA electrolyte. ^dEstimated by cyclic voltammetry, with Fc/Fc⁺ at 5.39 eV below vacuum.(329)

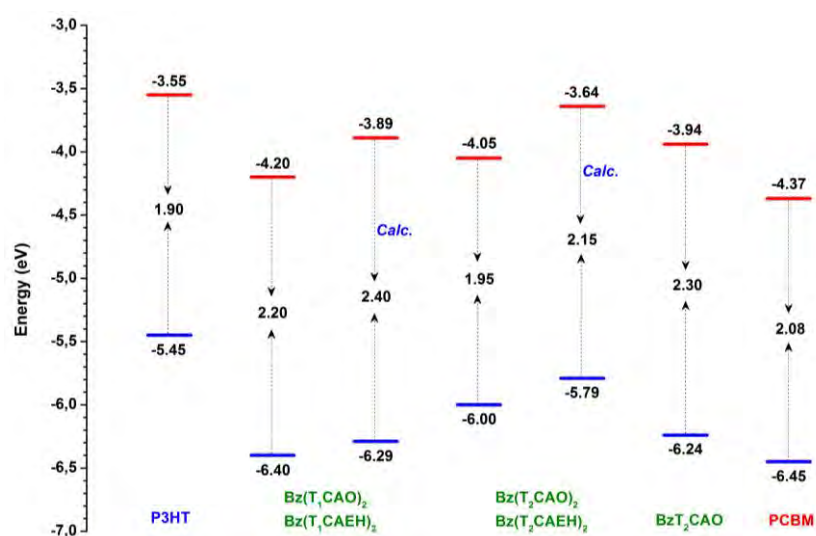


Figure IV-11: Diagram of the energy levels for the investigated molecules, P3HT and PCBM, estimated *via* electrochemical measurements. (All values have been measured in our laboratory in the same experimental conditions; *Calc.* represents calculated result)

CV measurements of molecules $\text{Bz}(\text{T}_1\text{CAO})_2$ and $\text{Bz}(\text{T}_1\text{CAEH})_2$ in thin films and their blend with P3HT (1:1 wt.) were also used to evaluate their electrochemical characteristics in OPV cells, as shown in Figure IV-12. Relevant data evaluated from the equations aforementioned are provided in Table IV-2. The oxidation and reduction potentials of $\text{Bz}(\text{T}_1\text{CAO})_2$ and $\text{Bz}(\text{T}_1\text{CAEH})_2$ in thin film show no difference to those in solution. For both case, their HOMO and LUMO energy levels are about -6.4 and -4.2 eV, respectively. In the blend, the HOMO energy level is increased about 1.0 eV but the LUMO maintains the same level, leading to a narrower gap. The first oxidation potential of P3HT: $\text{Bz}(\text{T}_1\text{CAO})_2$ blend is approximately the same as that of pure P3HT due to its lower oxidation potential relative to that of $\text{Bz}(\text{T}_1\text{CAO})_2$. Similarly, the reduction potential of P3HT: $\text{Bz}(\text{T}_1\text{CAO})_2$ blend is identical to that of pure molecule $\text{Bz}(\text{T}_1\text{CAO})_2$. It indicates that there is almost no change on their respective structure in solid state. Similarly, for P3HT: $\text{Bz}(\text{T}_1\text{CAEH})_2$ blend, the oxidation potential of is approximately identical to that of pure P3HT and the reduction potential is the same as that of pure molecule $\text{Bz}(\text{T}_1\text{CAEH})_2$. It confirms that molecules $\text{Bz}(\text{T}_1\text{CAO})_2$ and $\text{Bz}(\text{T}_1\text{CAEH})_2$ could be good electron acceptors candidates with P3HT as the donor.

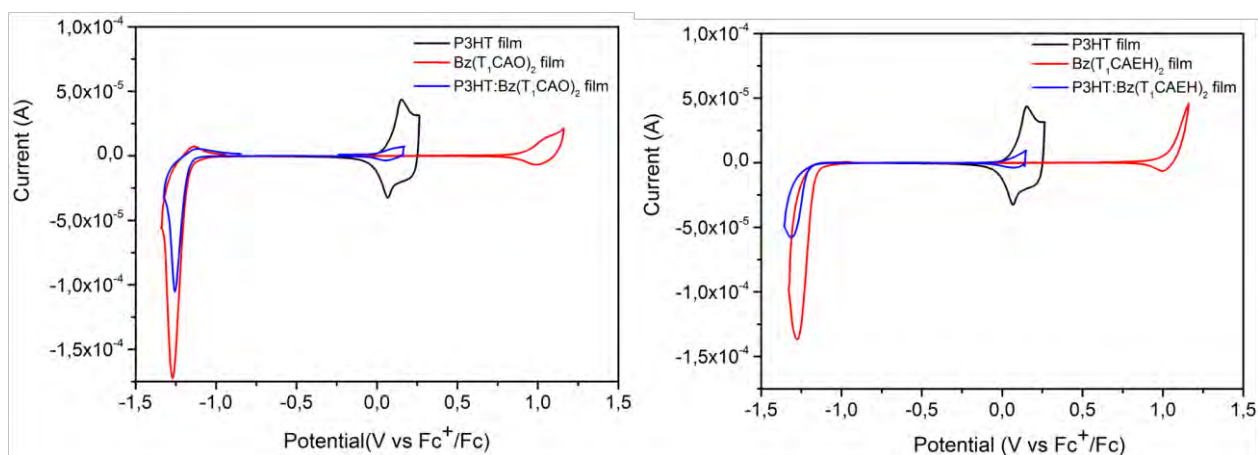


Figure IV-12: Cyclic voltammogram of pristine P3HT, $\text{Bz}(\text{T}_1\text{CAO})_2$, $\text{Bz}(\text{T}_1\text{CAEH})_2$ films and blend P3HT: $\text{Bz}(\text{T}_1\text{CAO})_2$ (1:1 wt.) and blend P3HT: $\text{Bz}(\text{T}_1\text{CAEH})_2$ (1:1 wt.) in 0.1 M PF_6TBA acetonitrile solution; Pt electrode; scan rate = 50 $\text{mV}\cdot\text{s}^{-1}$.

Table IV-2: Electronic properties of pristine P3HT, Bz(T₁CAO)₂, Bz(T₁CAEH)₂ films and blend P3HT:Bz(T₁CAO)₂ (1:1 wt.) and blend P3HT:Bz(T₁CAEH)₂ (1:1 wt.).

Films	E _{red} (V/Fc ⁺ /Fc) ^a	E _{ox} (V/Fc ⁺ /Fc) ^a	E _g ^{el} (eV) ^a	LUMO (eV) ^b	HOMO (eV) ^b
P3HT	-	0,06		-	-5.45
Bz(T ₁ CAO) ₂	-1.16	+0.93	2.09	-4,23	-6.32
Bz(T ₁ CAEH) ₂	-1.16	+1,03	2.19	-4,23	-6.42
P3HT:Bz(T ₁ CAO) ₂ (1:1 wt.)	-1.16	+0,01	1.17	-4,23	-5.40
P3HT:Bz(T ₁ CAEH) ₂ (1:1 wt.)	-1.19	+0,01	1.20	-4,20	-5.40

^aMeasured in CV in acetonitrile solution with FP₆TBA electrolyte. ^bEstimated by cyclic voltammetry, with Fc/Fc⁺ at 5.39 eV below vacuum.

Based on the design rules for donors in BHJ solar cells with regard to Scharber model,⁽⁶¹⁾ a minimum energy offset (ΔE , Figure IV-13) between the LUMO level of the donor material and the PCBM of approximately 0.3 eV has been demonstrated necessary to achieve efficient electron transfer from the LUMO of the donor to the LUMO of PCBM acceptor.^(61, 62, 78) On one hand, according to energy level diagram shown in Figure IV-11, molecules Bz(T₂CAO)₂, Bz(T₂CAEH)₂ and BzT₂CAO can be good candidates used as donors with PCBM as the acceptor. We can also predict that the power conversion efficiency based on Scharber model associated to Bz(T₂CAO)₂ and Bz(T₂CAEH)₂ may reach an ideal efficiency of 9.00 %, as the red cross marked in Figure IV-13. The blend using BzT₂CAO as donor and PCBM as acceptor in an OPV device may reach an ideal efficiency between 6.00% and 7.00%, according to the red dot marked in Figure IV-13. Despite achieving ideal efficiency requires an ideal morphology and sufficient charge transport, it confirms that Bz(T₂CAR)₂ and BzT₂CAO are promising donors for OPV devices. On the other hand, the energy level diagram of Figure IV-11 also suggests that all the five compounds may have the potential of being used as acceptors when blended with P3HT.

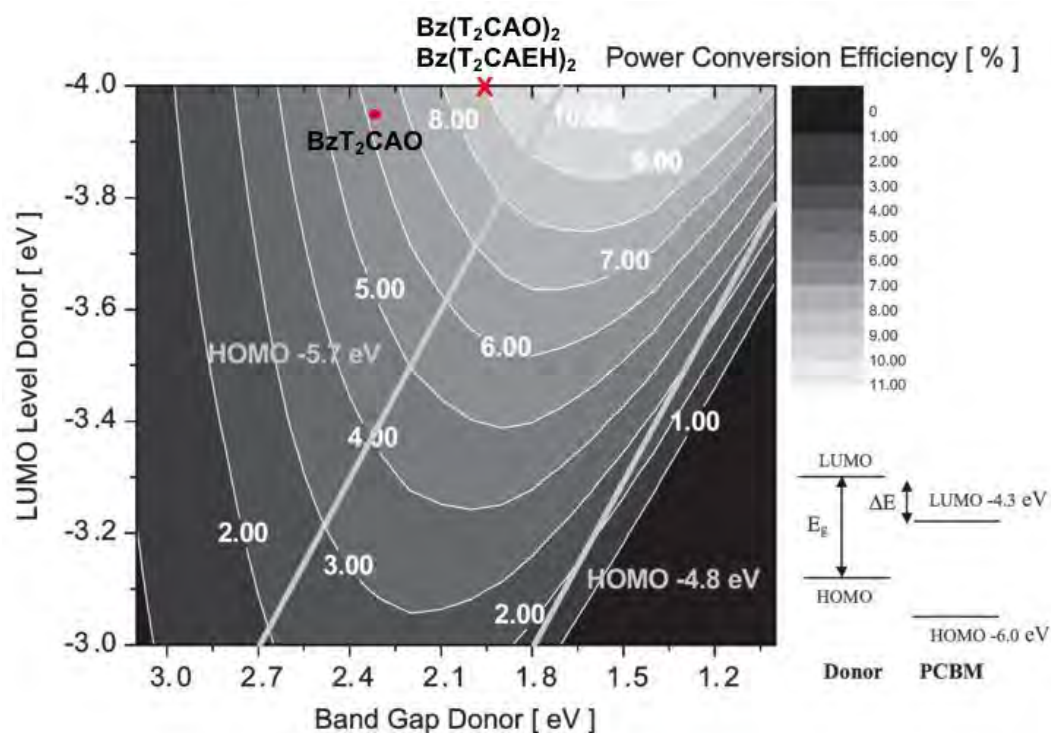


Figure IV-13: Outline plot showing the evaluated energy-conversion efficiency (contour lines and colours) versus the band gap and LUMO level of the donor based on Scharber model. A schematic energy diagram of a donor/PCBM system with the band gap energy (E_g) and the energy offset (ΔE) is also given.(61) Red cross indicates the ideal efficiency of $Bz(T_2CAEH)_2$ used as the donor with PCBM as the acceptor. Red point indicates the ideal efficiency of BzT_2CAO used as the donor with PCBM as the acceptor.

III Thermal properties

A highly thermal stability of the molecules is essential for estimating their use as active compounds in organic photovoltaic cells. The thermal properties of $Bz(T_1CAO)_2$, $Bz(T_1CAEH)_2$, $Bz(T_2CAO)_2$ and $Bz(T_2CAEH)_2$ were investigated using thermogravimetric analysis (TGA), as provided in Figure IV-14. It shows that their thermal degradation starts at 200°C for compounds $Bz(T_1CAO)_2$, whereas $Bz(T_1CAEH)_2$, $Bz(T_2CAO)_2$ and $Bz(T_2CAEH)_2$ are more thermally stable, revealing thermal degradation. The four molecules are sufficiently thermally stable enough for use in OPV applications at above 300°C under nitrogen atmosphere.

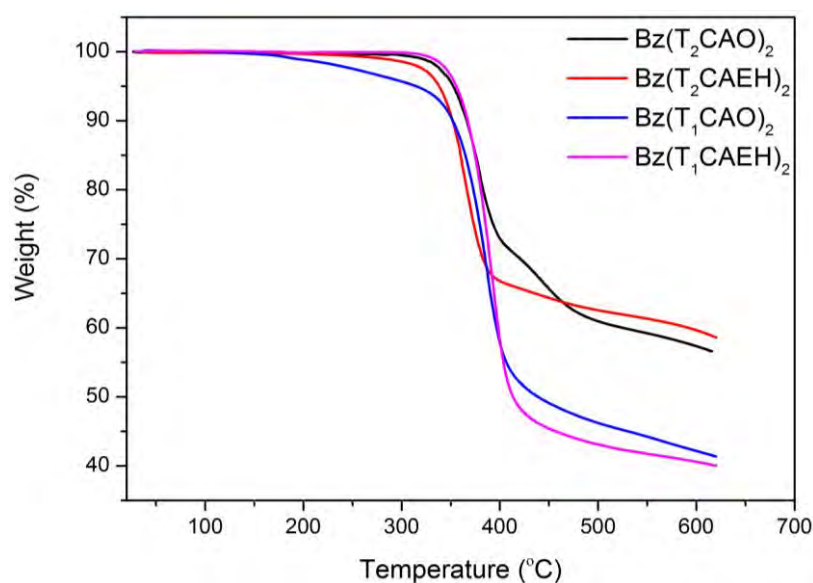


Figure IV-14: TGA plot of studied molecules with a heating rate of 10 °C/min under N₂ atmosphere.

IV Structural properties

Differential scanning calorimetry (DSC) was performed at 10°C/min on the materials, and the results are shown in Figure IV-15. On the first heating cycle (not shown here), Bz(T₂CAEH)₂ shows a sharp melting endothermic transition at 169°C which becomes broader on the following cycles ($\Delta H = 15 \text{ kJ mol}^{-1}$), demonstrating a low ability to recover a perfect crystalline state after thermal treatment, meanwhile the recrystallization occurs at 144°C ($\Delta H = 12 \text{ kJ mol}^{-1}$). For Bz(T₂CAO)₂, the sharp fusion peak recorded at 193°C during the first cycle (not shown here) is splitted into two transitions at 173°C ($\Delta H = 30 \text{ kJ mol}^{-1}$) and 186°C ($\Delta H = 10 \text{ kJ mol}^{-1}$), indicating the possible presence of conformational polymorphs due to thermal treatment. The recrystallization is characterized by a peak at 157 °C ($\Delta H = 25 \text{ kJ mol}^{-1}$) immediately followed by a broad and weak transition at around 142°C. Bz(T₁CAEH)₂ shows a large endothermic peak at around 175°C ($\Delta H = 32 \text{ kJ mol}^{-1}$), which corresponds to the phase transition from the crystalline solid (S) to the isotropic liquid (IL) state. During cooling, the corresponding recrystallization peak is observed at around 157°C ($\Delta H = 34 \text{ kJ mol}^{-1}$). Finally, Bz(T₁CAO)₂ possesses more complicated thermal properties. For this reason, it has been further investigated by DSC, Polarizing Optical Microscopy (POM), and Small Angle X-ray Scattering (SAXS). From the thermograms, upon heating Bz(T₁CAO)₂, a large exothermic peak ($\Delta H = 15 \text{ kJ mol}^{-1}$) at 100°C indicates a thermally induced crystallization phenomenon. A phase transition is also discernible at around 130°C, just before another sharp and intense peak at 141°C (total $\Delta H = 26 \text{ kJ mol}^{-1}$) corresponding to the transition to a liquid

crystalline (LC) phase, then the transition from the LC to IL states is observed at 177°C ($\Delta H = 3 \text{ kJ mol}^{-1}$). During the cooling process from IL, three low energetic transitions, typical of monotropic organizations, are recorded at 178°C, 128°C, and 69°C ($\Delta H = 3.0, 1.2, \text{ and } 4.3 \text{ kJ mol}^{-1}$), respectively.

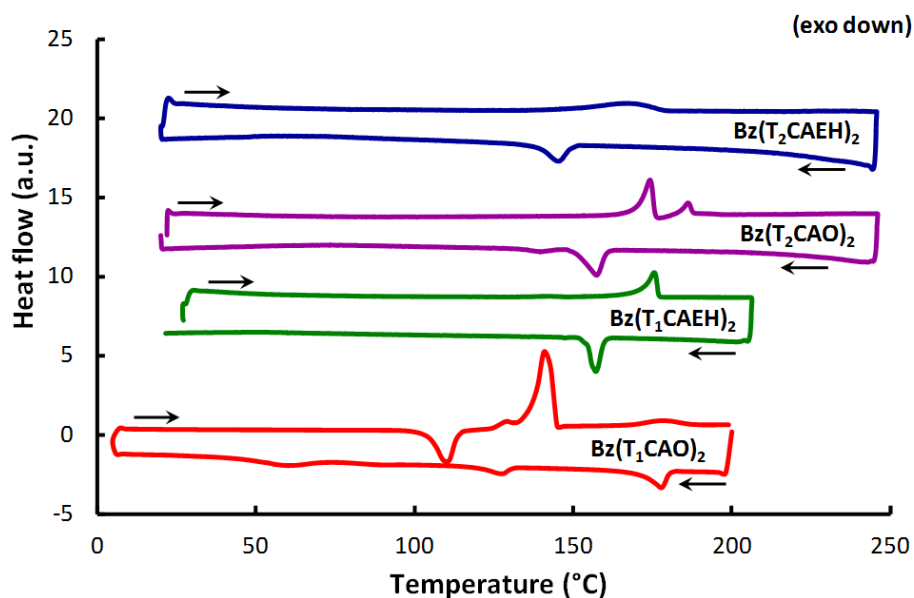


Figure IV-15: DSC thermograms of the molecules upon third heating and cooling cycles, measured at 10°C/min under nitrogen atmosphere.

SAXS patterns of $\text{Bz}(\text{T}_1\text{CAO})_2$ at 150°C (Figure IV-16) contain a unique sharp small-angle peak, corresponding to a layer spacing of 35.3 Å, and a broad wide-angle scattering due to liquid-like lateral distances between segregated chains and mesogens. Besides the usual signal from molten chains, h_{ch} , located at about 4.7 Å, two further maxima are observed for the rigid parts around 3.6 (h_{π}) and 7.2 Å ($2h_{\pi} + h_{\perp}$), respectively attributed to local-range face-to-face stacking and to overlapping contributions from face-to-face piled dimer and side-by-side lateral distances. Molecular areas A_{Mol} close to 30 Å² result from the ratio of estimated molecular volume ($1040 \pm 40 \text{ Å}^3$, $\rho \approx 1.15 \text{ g.cm}^{-3}$) and layer spacing. These values substantially exceed the cross-section of stretched chains (23.3 Å² at 150°C), which explains that the layer thickness is noticeably below the length of the entirely stretched molecule conformation (ca. 40 Å).

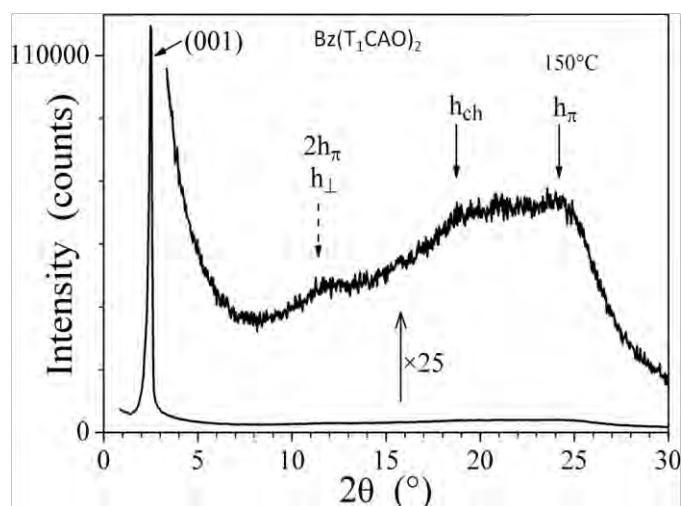


Figure IV-16: SAXS pattern of $Bz(T_1CAO)_2$ at $150^\circ C$, in the sanidic type smectic A phase.

SAXS shows that $Bz(T_1CAO)_2$ is crystalline in the pristine state (Figure A.8 left), melts around $135^\circ C$ to a smectic A phase with local stacking of the rigid parts (sanidic type smectic A phase - Figure IV-17a) (330) and gives rise to crystalline polymorphism upon cooling (Figure A.8 right). Cold crystallization however appears on the second heating in DSC and confirms that these monotropic organizations revealed by DSC are metastable and thus not accessible to the more time-demanding SAXS experiments which only evidenced crystalline phases (see Figure A.8). On the other hand, the metastable monotropic phases could be observed by POM analysis. $Bz(T_1CAO)_2$ revealed a batonnet-like texture (331) (Figure IV-17a) within a narrow temperature range from 185 to $180^\circ C$, corresponding to the formation of the monotropic smectic A (SmA) phase.(331) Then, a *fan-shaped* texture typical of a SmA phase is observed after maintaining the temperature at a constant value of $170^\circ C$ for 30 minutes (Figure IV-17b). On cooling, the DSC curve presents two further low energetic transitions at $135^\circ C$ and $60^\circ C$ ($\Delta H = 1.4$ and 2.2 kJ mol^{-1} , respectively), the broken fan-shaped POM texture of the upper phase suggesting a tilted smectic phase with in-plane order (Figure IV-17c).(331) Clearly, $Bz(T_1CAO)_2$ shows crystalline and ordered mesophases below the fluid SmA phase which may be helpful for morphology control and interesting for charge transfer.(332) The alkyls chains play a central role in the appearance of mesomorphism, but as depicted in Yongsheng Chen's work,(137, 333) they are also crucial for the photovoltaic performance, apart from having great impact on donor and acceptor mixtures as well as on the π -conjugation.

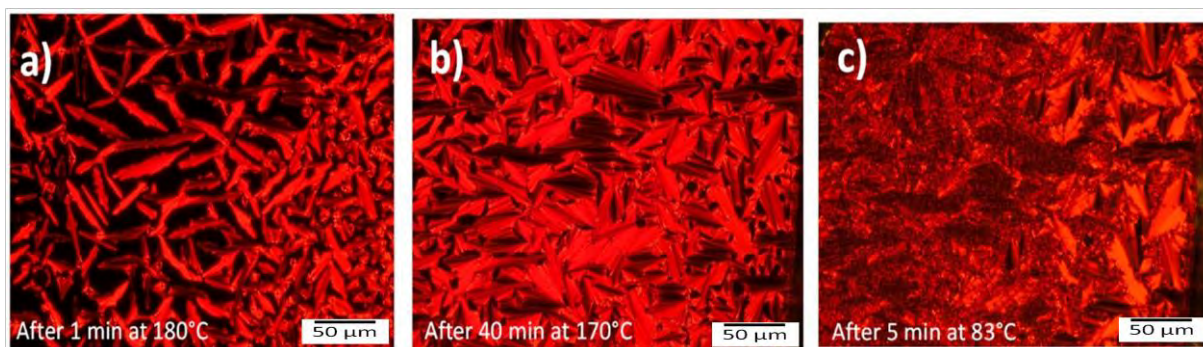


Figure IV-17: POM images of (a) the batonnet-like texture of Bz(T₁CAO)₂ at 183°C, (b) the SmA phase of Bz(T₁CAO)₂ at 170°C and (c) the smectic phase observed at 85°C.

V Conclusion

A series of π -conjugated small molecules were characterized in terms of various measurements. Their strong absorption in the region of 300-700 nm in solution is prerequisite for excitons generation. Their good thermal stability associated with their optoelectronic properties and ability to tolerate electron transfer make them interesting molecules to be tested as electron donors or acceptors in OPV applications. We show that a simple replacement of the branched (2-ethylhexyl) with linear (octyl) chain leads to a drastic change in their intermolecular interaction as supported by SAXS measurements. This property will presumably be beneficial for achieving appropriate thin film morphology (depending on the nature of the alkyl chain) for a given use. In that aim, further investigations on thin films of these molecules are also yet to be carried out to evaluate their potential performance in organic photovoltaics. Works are in progress to test them in these roles.

Chapter V: Experimental section

Chapter V : Experimental section

I Materials, equipment and methods

All used chemicals and solvents were purchased from chemical companies and used as received, unless otherwise mentioned. All reactions were performed under ambient atmosphere and under air exposition unless special indication. ^1H experiments were recorded in the listed deuterated solvents (internal standard) on a DPX 400 Bruker Spectrometer. Multiplicity of NMR signal was denoted as m (massif), s (singlet), d (doublet), t (triplet).

Mass analyses were performed at the Service de Spectrométrie de Masse de la Structure Fédérative Toulousaine en Chimie Moléculaire.

Elemental analyses (C, H, N) were carried out in the analysis service of the LCC laboratory.

Voltammetry measurements were carried out with a potentiostat Autolab PGSTAT100 controlled by GPES 4.09 software. Experiments were performed at room temperature in a homemade airtight three-electrode cell connected to a vacuum/argon line. The reference electrode consisted in a saturated calomel electrode (SCE) separated from the solution by a bridge compartment. The counter electrode was a platinum wire of ca 1cm^2 apparent surface. The working electrode was a Pt microdisk (0.5mm diameter) or a glassy carbon (1mm diameter). The supporting electrolyte (nBu₄N)[PF₆] (Fluka, 99% electrochemical grade) was used as received and simply degassed under argon. Dichloromethane was freshly distilled over CaH₂ prior to use. The solutions used during the electrochemical studies were typically $10^{-3}\text{ mol.L}^{-1}$ in compound and 0.1 mol.L^{-1} in supporting electrolyte. Before each measurement, the solutions were degassed by bubbling Ar and the working electrode was polished with a polishing machine (Presi P230).

UV-VIS-NIR absorption spectra were recorded on one Perkin Elmer Lambda 35 spectrometer, using dichloromethane as solvent. The solutions used for the electronic absorption analyses were typically about $10^{-5}\text{ mol.L}^{-1}$ in molecule.

Phase transition was determined by differential scanning calorimetry (DSC) thermograms, which were obtained on a DSC 204 NETZSCH system using 2-5 mg samples in 30 μl sample pans and a scan rate of $10^\circ\text{C min}^{-1}$. ΔH is the enthalpy associated with each phase transition and it is calculated in kJ.mol^{-1} .

Differential Scanning Calorimetry, DSC, was performed with a DSC 204 F1 Phoenix[®] system (NETZSCH). Samples (2-5 mg) were filled in 30 μ l perforated aluminium pans and measurements were conducted under nitrogen atmosphere. Three different heating/cooling cycles were registered for each sample in temperature ranges situated between 5°C and 250°C with a 10°C/min rate. With the exception of the first thermogram, all the cycles were reproducible. The values reported correspond to those determined from the position of the top of the peaks. ΔH is the enthalpy in kJ.mol⁻¹ associated with each phase transition.

LC textures were acquired with an Olympus BX53 polarized light microscope equipped with a Mettler FP82HT heating stage.

The SAXS patterns were obtained with a transmission Guinier-like geometry. A linear focalized monochromatic Cu K α 1 beam ($\lambda = 1.5405 \text{ \AA}$) was obtained using a sealed-tube generator (600 W) equipped with a bent quartz monochromator. In all cases, the crude powder was filled in Lindemann capillaries of 1 mm diameter and 10 μ m wall-thickness. The diffraction patterns were recorded with a curved Inel CPS120 counter gas-filled detector linked to a data acquisition computer (periodicities up to 90 \AA) and on image plates scanned by STORM 820 from Molecular Dynamics with 50 μ m resolution (periodicities up to 120 \AA). The sample temperature was controlled within $\pm 0.01 \text{ }^\circ\text{C}$, and exposure times were varied from 1 to 24 h.

II Computational details

Theoretical calculations were performed with Orca code 3.0.(183) Structural optimizations and subsequent frequency calculations (to confirm that the minimum energy ground state is reached without any imaginary frequency) were carried out using an all electron triple zeta basis set with one polarization functions on H,C,N,O and S atoms (Def₂-TZVP(-f)).(334) The B3LYP functional together with Grimme's D₃(BJ)(335, 336) model used to add molecular mechanics damped dispersion was applied for ground states calculation. Vertical excitations were computed with TD-DFT using BHandHLYP functional using the B3LYP optimized ground state structures. This hybrid functional which is Becke's half and half method(337) with LYP correlation,(338) is particularly well adapted in our case due to the presence of molecular species with delocalized electron. Bulk solvent effect, *i.e.* CH₂Cl₂, were included using the conductor like screening model (COSMO).(339) The terminal alkyl groups were

replaced by methyl groups, to gain computational time since experimental data concerning optoelectronic properties of the molecules (see Table IV-1) has been proven to be not affected by this simplification. Absorption spectra were simulated using the `orca_mapspc` program that applies Gaussian-type lineshape function to the calculated transition with a defined full-width-half-maximum of 1200 cm^{-1} . The nature of the transitions was determined using natural transition orbitals.(272, 340)

III Films elaboration

Electronic grade regioregular P3HT (PlexcoreVR average Mn 54 000–75 000; >98% head-to-tail regioregular) is purchased from Sigma-Aldrich and PCBM is acquired from LUMTEC (99.5%). ITO was purchased from SOLEMS: reference 1) ITO sol 30/1.1 and 30 ohm/cm^2 . 2) ITO sol 12/1.1 and 10 ohm/cm^2 , both used as received. All the materials, pristine and blended are dissolved in warm chlorobenzene (50°C) to produce 10 mg/mL concentration solutions. Solutions are filtered using $0.2\text{ }\mu\text{m}$ PTFE filters to remove any soluble aggregates. Films are prepared by spin coating at 1500 rpm for 30 s and then at 2000 rpm for 60 s on 120 nm thick indium tin oxide (ITO) covered glass substrates. The thicknesses of films were from 50 up to 100 nm . All the thin films were elaborated under clean-room conditions.

IV Synthetic procedure

In this part, the ^1H NMR spectrum was given for Bz-based target molecules and intermediates $\text{Bz}(\text{T}_1\text{CHO})_2$ and $\text{Bz}(\text{T}_2\text{CHO})_2$, not for the rest intermediates.

5,5'-(2,1,3-benzothiadiazole-4,7-diyl)bis-(2-thiophenecarboxaldehyde) - molecule $\text{Bz}(\text{T}_1\text{CHO})_2$

Route a: All solvents and basic solutions were previously degassed by bubbling through argon for 20 min . 2,1,3-benzothiadiazole-4,7-bis(boronic acid pinacol ester) (247 mg , 0.637 mmol , 1 eq) and 5-bromo-2-thiophenecarboxaldehyde (0.196 mL , 1.64 mmol , 2.5 eq) were placed in a three-necked flask which was brought under an inert atmosphere. Toluene (10 mL), K_2CO_3 (2.0 M , 5 mL), H_2O (4 mL) and Aliquat 336 ($4\text{--}5\text{ drops}$) were added and the mixture was vigorously stirred under argon for 10 min at room temperature. $\text{Pd}(\text{PPh}_3)_4$ (45 mg , $2.4\text{ mol}\%$) was then added and the mixture was allowed to react for 24 h at $80\text{ }^\circ\text{C}$. After cooling to room temperature, the solid crude mixture was filtered, washed with distilled water, ethyl acetate, then with a vol $1:1$ dichloromethane:petroleum ether mixture. After drying under vacuum, 230 mg of pure product were recovered (quantitative yield).

Route b: In a three-necked flask containing a stirring bar, Pd(OAc)₂ (7.6 mg, 0.034 mmol), P^tBu₂Me.HBF₄ (16.9 mg, 0.068 mmol), pivalic acid (35 mg, 0.34 mmol), 4,7-dibromobenzo-2,1,3-thiadiazole (100 mg, 0.34 mmol), potassium carbonate (141 mg, 1.0 mmol), and 2-thiophenecarboxaldehyde (84 mg, 0.75 mmol) were sequentially added under a flow of argon. Dry toluene (4 mL) was added and the reaction mixture was heated at 120°C in an oil bath for 5.5 h until judged complete by examining aliquots with TLC. After cooling to room temperature, the solid crude mixture was filtered, washed with distilled water, ethyl acetate, then with petroleum ether. After drying under vacuum, 119 mg of pure product were recovered (98% yield).

Route c: In a 100 mL three-necked round-bottomed flask, equipped with a thermometer, magnetic stirrer, condenser and rubber seal, 2-thiophenecarboxaldehyde (419 mg, 3.74 mmol, 2.2 eq) and DMA (6 mL) were added to a mixture of 4,7-dibromobenzo-2,1,3-thiadiazole (500 mg, 1.7 mmol, 1 eq), potassium acetate (334 mg, 3.4 mmol, 2 eq), and palladium acetate (1.9 mg, 8.4×10⁻³ mmol (0.5%)) in one portion under argon atmosphere. The reaction mixture was then heated to 150°C and stirred under vigorous reflux for 24 h. The dark red solution was cooled to ambient temperature and filtered. After washing with water, ethyl acetate, and then petroleum ether, the corresponding red diarylated product was dried, affording 430 mg of pure product (71% yield).

Table V-1 resumes the results obtained from various “r” molar ratios of 2-thiophenecarboxaldehyde/4,7-dibromobenzo-2,1,3-thiadiazole, and various amounts of palladium acetate (relative to 4,7-dibromobenzo-2,1,3-thiadiazole). The other parameters are fixed (quantity of 4,7-dibromobenzo-2,1,3-thiadiazole: 500 mg, KOAc: 334 mg, DMA: 6 mL, temperature of reaction: 150°C and time of reaction: 24 h)

Table V-1: Yields for molecule Bz(T₁CHO)₂ obtained from different Route c conditions.

r	palladium acetate	Yield of reaction
2.2	0.5%	71%
0.9	0.5%	100%
0.5	0.25%	100%

^1H NMR (400 MHz, CDCl_3) δ 10.02 (s, 2H), 8.29 (d, $J = 4$ Hz, 2H), 8.08 (s, 2H), 7.90 (d, $J = 4$ Hz, 2H); ^1H NMR (400 MHz, ^6d DMSO) δ 10.03 (s, 2H), 8.43 (s, 2H), 8.38 (d, $J = 4$ Hz, 2H), 8.17 (d, $J = 4$ Hz, 2H).

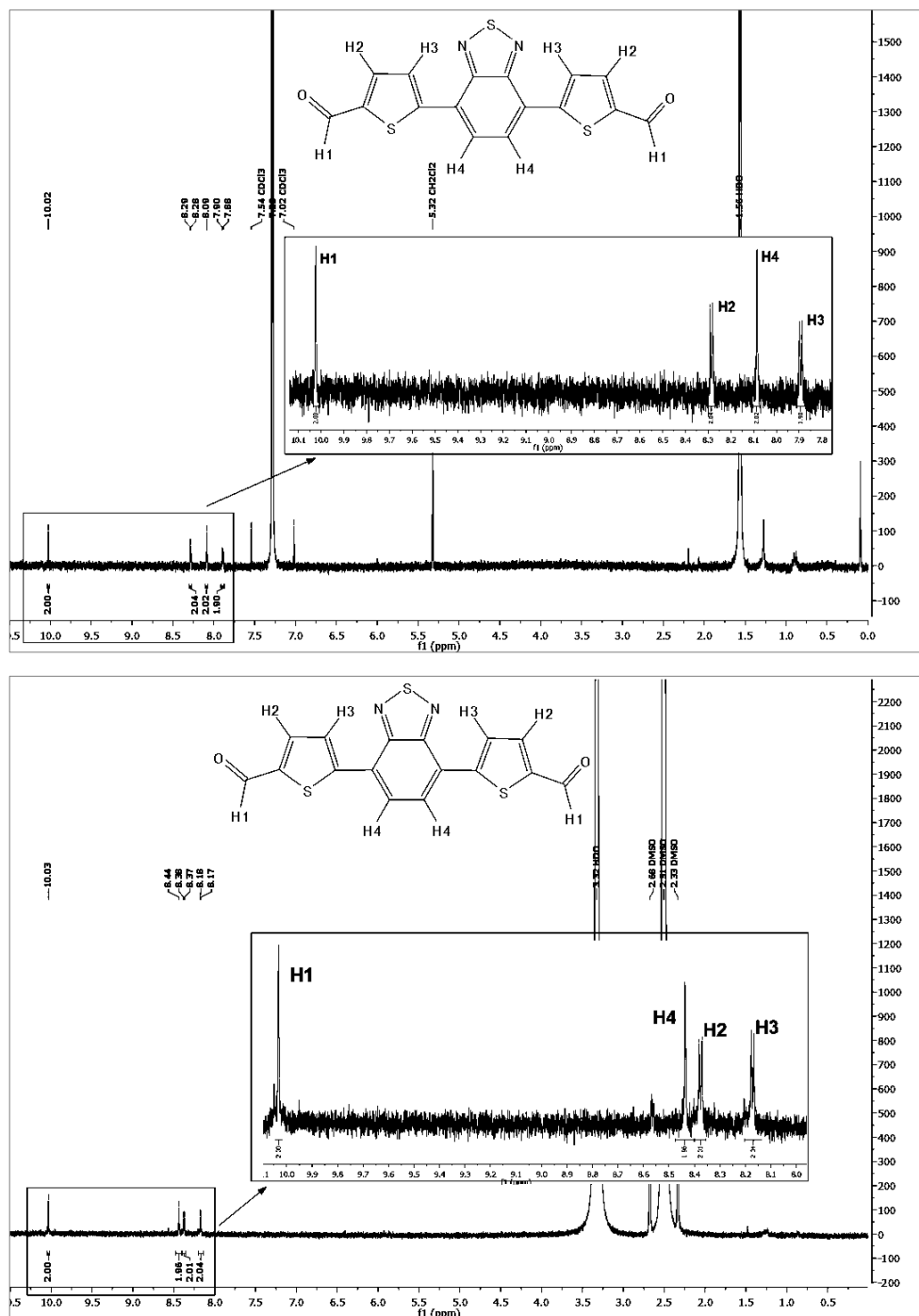


Figure V-1: ^1H NMR spectrum of $\text{Bz}(\text{T}_1\text{CHO})_2$ in CDCl_3 (top) and ^6d DMSO (down).

**5',5''-(2,1,3-benzothiadiazole-4,7-diyl)bis-[(2,2'-bithiophene)-5-carboxaldehyde]-
molecule Bz(T₂CHO)₂**

Route a: All solvents and basic solutions were previously degassed by bubbling through argon for 20 min. 2,1,3-benzothiadiazole-4,7-bis(boronic acid pinacol ester) (173 mg, 0.445 mmol, 1 eq) and 5'-bromo-2,2'-bithiophene-5-carboxaldehyde (305 mg, 1.11 mmol, 2.5 eq) were placed in a three-necked flask which was brought under an inert atmosphere. Toluene (25 mL), K₂CO₃ (2.0 M, 5 mL), H₂O (4 mL) and Aliquat 336 (2-3 drops) were added and the mixture was vigorously stirred under argon for 10 min at room temperature. Pd(PPh₃)₄ (38.5 mg, 3.0 mol%) was then added and the mixture was allowed to react for 24 h at 80 °C. After cooling to room temperature, the solid crude mixture was filtered, washed with distilled water, ethyl acetate, then with petroleum ether. After drying under vacuum, 230 mg of pure product were recovered (quantitative yield).

Route c: In a 100 mL three-necked round-bottomed flask, equipped with a thermometer, magnetic stirrer, condenser and rubber seal, 2,2'-bithiophene-5-carboxaldehyde (727 mg, 3.74 mmol, 2.2 eq) and DMA (6 mL) were added to a mixture of 4,7-dibromobenzo-2,1,3-thiadiazole (500 mg, 1.7 mmol, 1 eq), potassium acetate (334 mg, 3.4 mmol), and palladium acetate (1.9 mg, 8.4×10⁻³ mmol (0.5%)) in one portion under argon atmosphere. The reaction mixture was then heated to 150°C and stirred under vigorous reflux for 24 h. The dark red solution was cooled to ambient temperature and filtered. After washing with water, ethyl acetate, and then petroleum ether, the corresponding red diarylated product was dried, affording 811 mg of pure product (92% yield).

¹H NMR (400 MHz, CDCl₃) δ 9.92 (s, 2H), 8.12 (d, *J* = 4 Hz, 2H), 7.96 (s, 2H), 7.74 (d, *J* = 4 Hz, 2H), 7.50 (d, *J* = 4 Hz, 2H), 7.41 (d, *J* = 4 Hz, 2H); ¹H NMR (400 MHz, ⁶d DMSO) δ 9.90 (s, 2H), 8.32 (s, 2H), 8.03 (d, *J* = 4 Hz, 2H), 7.64 (d, *J* = 4 Hz, 2H), 7.52 (d, *J* = 4 Hz, 2H), 7.60 (d, *J* = 4 Hz, 2H).

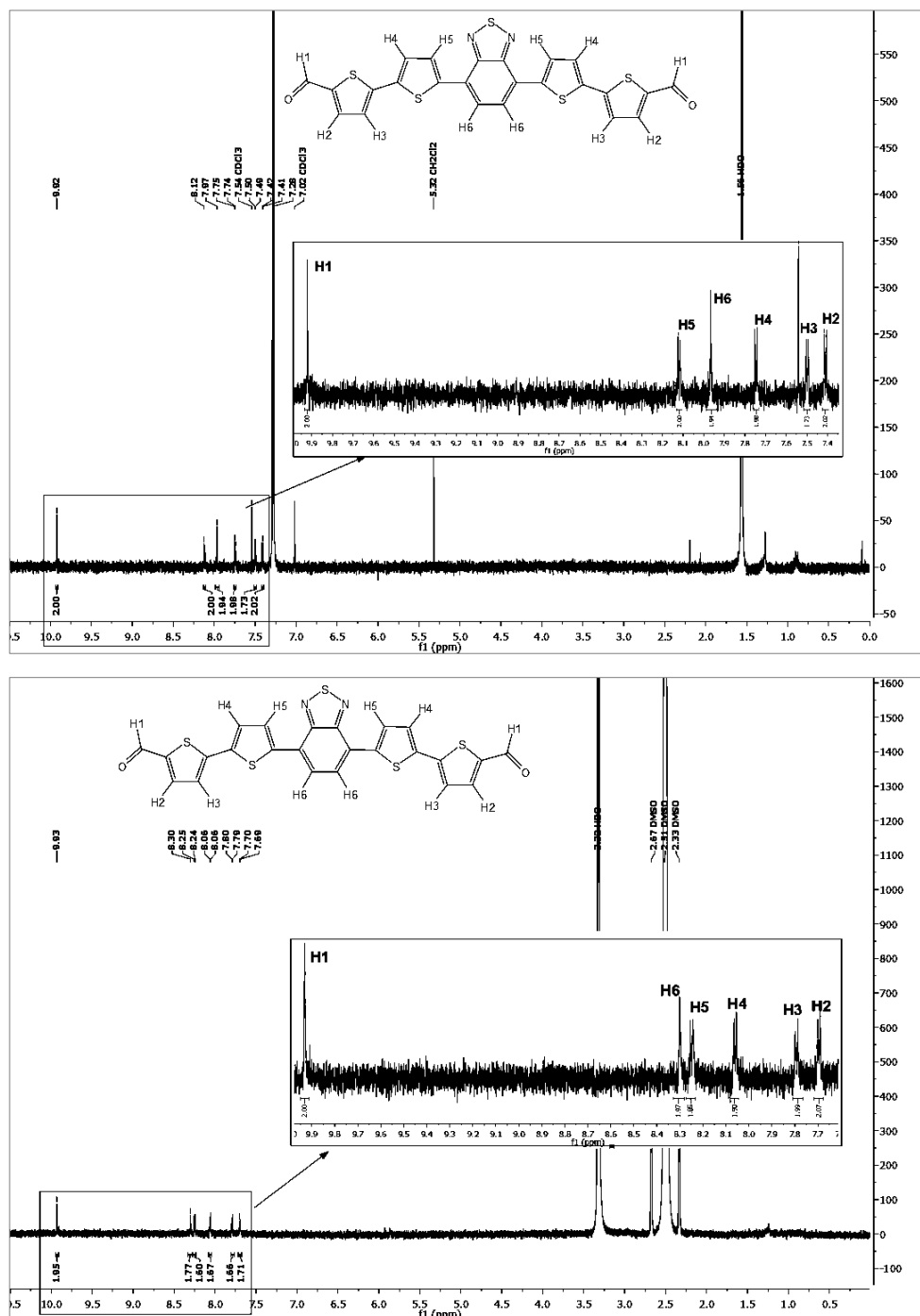


Figure V-2: ¹H NMR spectrum Bz(T₁CHO)₂ in CDCl₃ (top) and ⁶d DMSO (down).

Knoevenagel condensation:

Bz(T₁CAO)₂: Molecule Bz(T₁CHO)₂ (450 mg, 1.26 mmol) was dissolved in dry CH₂Cl₂ (30 mL). The mixture was deoxygenated with argon for 20 minutes. Triethylamine (2.3 mL) and octylcyanoacetate (2.7 mL, 12.7 mmol) were added successively. The resulting solution was stirred for 40 h under argon at room temperature (followed by TLC). After removal of solvent, the obtained powder was washed with distilled water (10 mL), then ethanol (10 mL)

and petroleum ether (30 mL), affording Bz(T₁CAO)₂ as dark solid, then further purified by recrystallization in 20 mL ethyl acetate, giving rise to 460 mg pure black solid (51% yield).

¹H NMR (400 MHz, CDCl₃): δ 8.38 (s, 2H), 8.32 (d, *J* = 4.4 Hz, 2H), 8.10 (s, 2H), 7.95 (d, *J* = 4.4 Hz, 2H), 4.34 (t, *J* = 6.8, 4H), 1.79 (m, 4H), 1.35 (m, 20H), 0.92 (m, 6H). MS (CI NH₃): calcd for C₃₈H₄₂N₄O₄S₃ [M]⁺, 714.24; found: 732.3 (100%) [M+NH₄]⁺; 714.3 (31%) [M]⁺. Element. Anal. Calc. for C₃₈H₄₂N₄O₄S₃: C, 63.86; H, 5.88; N, 7.84; found: C, 63.14; H, 5.94; N, 7.25. UV-vis (CH₂Cl₂): λ_{max} = 498 nm; ε = 51000 L·mol⁻¹·cm⁻¹; Optical Gap = 2.1 eV (λ_{onset} = 590 nm)

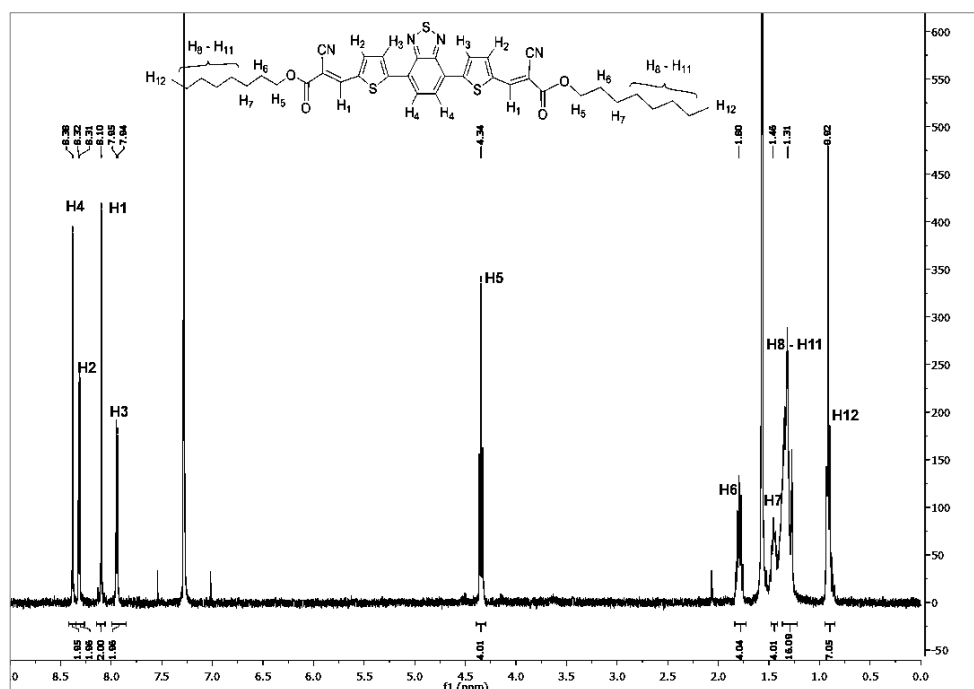


Figure V-3: ¹H NMR spectrum of Bz(T₁CAO)₂.

Bz(T₁CAEH)₂: Molecule Bz(T₁CHO)₂ (190 mg, 0.53 mmol) was dissolved in dry CH₂Cl₂ (20 mL). The mixture was deoxygenated with argon for 20 minutes. Triethylamine (0.96 mL) and 2-ethylhexylcyanoacetate (1.11 mL, 5.23 mmol) were added successively. The resulting solution was stirred for 40 h under argon at room temperature (followed by TLC). After removal of solvent, the obtained powder was washed with distilled water (10 mL), then ethanol (10 mL) and petroleum ether (20 mL), affording Bz(T₁CAEH)₂ as dark solid, then further purified by recrystallization in 8 mL ethyl acetate, giving rise to 180 mg pure black solid (47 % yield).

¹H NMR (400 MHz, CDCl₃): δ 8.38 (s, 2H), 8.32 (d, *J* = 4.4 Hz, 2H), 8.10 (s, 2H), 7.95 (d, *J* = 4.4 Hz, 2H), 4.28 (dd, *J* = 5.6 Hz, *J* = 1.6 Hz, 4H), 1.75 (m, 2H), 1.40 (m, 16H), 0.98 (m, 12H). MS (CI-NH₃): [M+NH₄]⁺ calcd for C₃₈H₄₂N₄O₄S₃, 732.96; found: 732.4. Element. Anal.

Calc. for $C_{38}H_{42}N_4O_4S_3$: C, 63.86; H, 5.88; N, 7.84; found: C, 63.28; H, 5.95; N, 7.51. UV-vis (CH_2Cl_2): $\lambda_{max} = 497$ nm; $\epsilon = 55000$ $L \cdot mol^{-1} \cdot cm^{-1}$; Optical Gap = 2.1 eV ($\lambda_{onset} = 590$ nm).

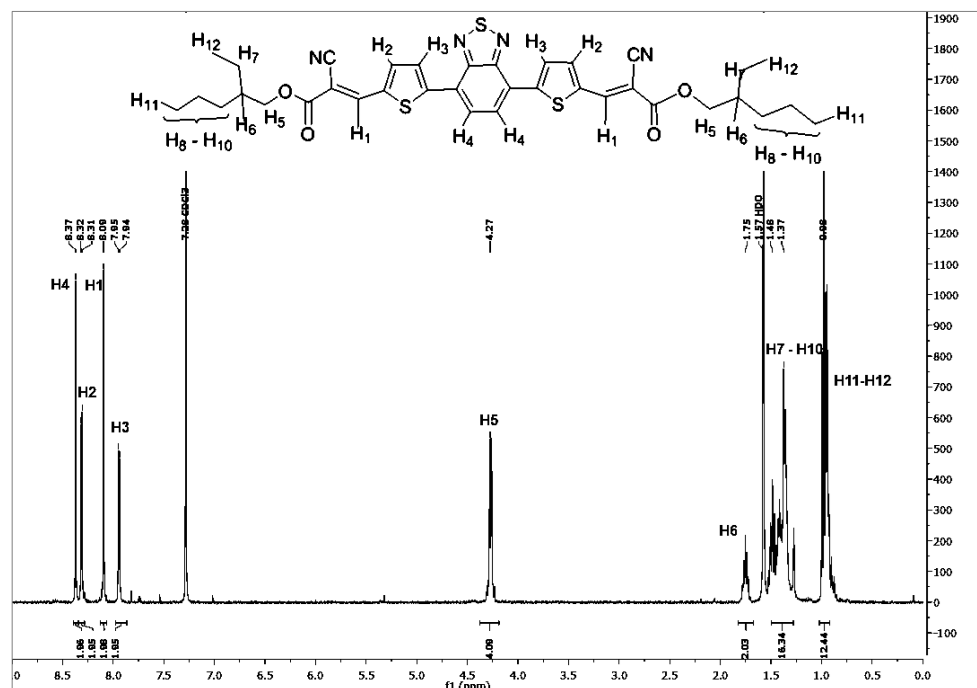


Figure V-4: 1H NMR spectrum of $Bz(T_1CAEH)_2$.

$Bz(T_2CAO)_2$: Molecule $Bz(T_2CHO)_2$ (500 mg, 0.96 mmol) was dissolved in dry CH_2Cl_2 (40 mL). The mixture was deoxygenated with argon for 20 minutes. Triethylamine (1.7 mL) and 2-ethylhexyl cyanoacetate (2 mL, 9.6 mmol) were added successively. The resulting solution was stirred for 29 h under argon at room temperature (followed by TLC). After removal of solvent, the obtained powder was washed with distilled water (10 mL), then ethanol (10 mL) and petroleum ether (20 mL), affording $Bz(T_2CAO)_2$ as dark solid, then further purified by recrystallization with 15 mL ethyl acetate, giving rise to 640 mg pure product (76% yield).

1HNMR (400MHz, $CDCl_3$): δ 8.30 (s, 2H), 8.12 (d, $J = 4$ Hz, 2H), 7.97 (s, 2H), 7.72 (d, $J = 4$ Hz, 2H), 7.53 (d, $J = 4$ Hz, 2H), 7.40 (d, $J = 4$ Hz, 2H), 4.33 (t, $J = 6.8$ Hz, 4H), 1.78 (m, 4H), 1.35 (m, 20H), 0.92 (m, 6H). MS (CI- NH_3): $[M]^+$ calcd for $C_{46}H_{46}N_4O_4S_5$: 878.2; found: 879.6. Element. Anal. Calcd for $C_{46}H_{46}N_4O_4S_5$: C, 62.84; H, 5.27; N, 6.37; found: C, 62.59; H, 5.04; N, 6.60. UV-vis (CH_2Cl_2): $\lambda_{max} = 522$ nm; $\epsilon = 53440$ $L \cdot mol^{-1} \cdot cm^{-1}$; Optical Gap = 2.0 eV ($\lambda_{onset} = 630$ nm).

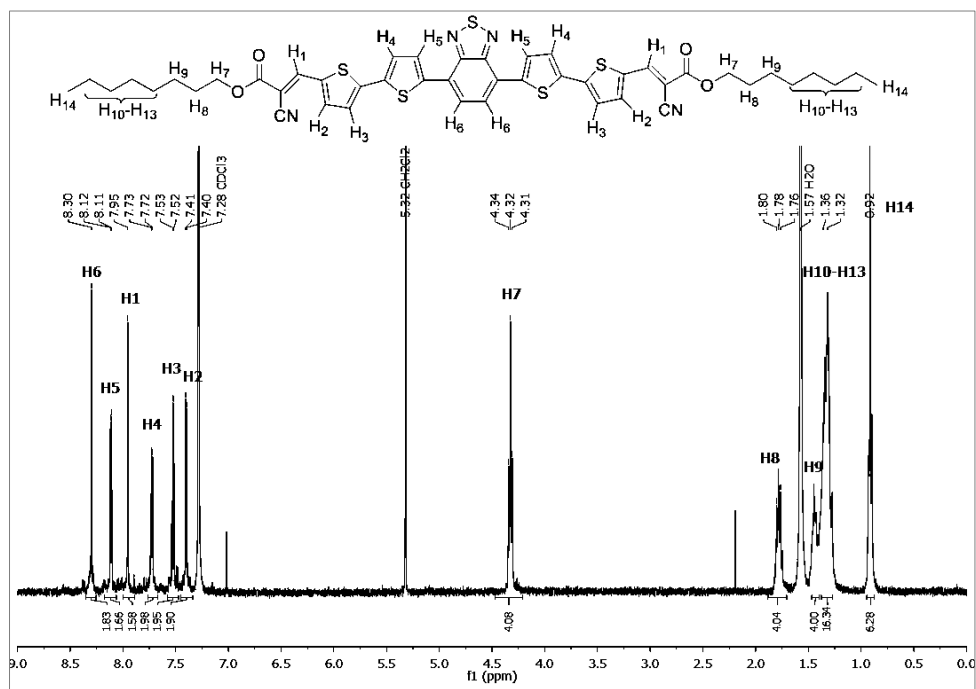


Figure V-5: ^1H NMR spectrum of $\text{Bz}(\text{T}_2\text{CAO})_2$.

$\text{Bz}(\text{T}_2\text{CAEH})_2$: Molecule $\text{Bz}(\text{T}_2\text{CHO})_2$ (500 mg, 0.96 mmol) was dissolved in dry CH_2Cl_2 (40 mL). The mixture was deoxygenated with argon for 20 minutes. Triethylamine (1.7 mL) and 2-ethylhexyl cyanoacetate (2mL, 9.6 mmol) were added successively. The resulting solution was stirred for 40 h under argon at room temperature (followed by TLC). After removal of solvent, the obtained powder was washed with distilled water (10 mL), then ethanol (10 mL) and petroleum ether (20 mL), affording $\text{Bz}(\text{T}_2\text{CAEH})_2$ as dark solid, then further purified by recrystallization with 15 mL ethyl acetate, giving rise to 570 mg pure product (68% yield).

$^1\text{HNMR}$ (400MHz, CDCl_3): δ 8.30 (s, 2H), 8.12 (d, $J = 4$ Hz, 2H), 7.97 (s, 2H), 7.73 (d, $J = 4$ Hz, 2H), 7.53 (d, $J = 4$ Hz, 2H), 7.41 (d, $J = 4$ Hz, 2H), 4.25(t, $J = 6.8$ Hz, 4H), 1.74 (m, 4H), 1.37 (m, 20H), 0.97 (m, 6H). MS (CI- NH_3): $[\text{M}]^+$ calcd for $\text{C}_{46}\text{H}_{46}\text{N}_4\text{O}_4\text{S}_5$: 878.2; found: 879.6. Element. Anal. Calcd for $\text{C}_{46}\text{H}_{46}\text{N}_4\text{O}_4\text{S}_5$: C, 62.84; H, 5.27; N, 6.37; found: C, 63.10; H, 5.53; N, 6.34. UV-vis (CH_2Cl_2): $\lambda_{\text{max}} = 525\text{nm}$; $\epsilon = 53440 \text{ L}\cdot\text{mol}^{-1}\cdot\text{cm}^{-1}$; Optical Gap = 2.0 eV ($\lambda_{\text{onset}} = 632\text{nm}$).

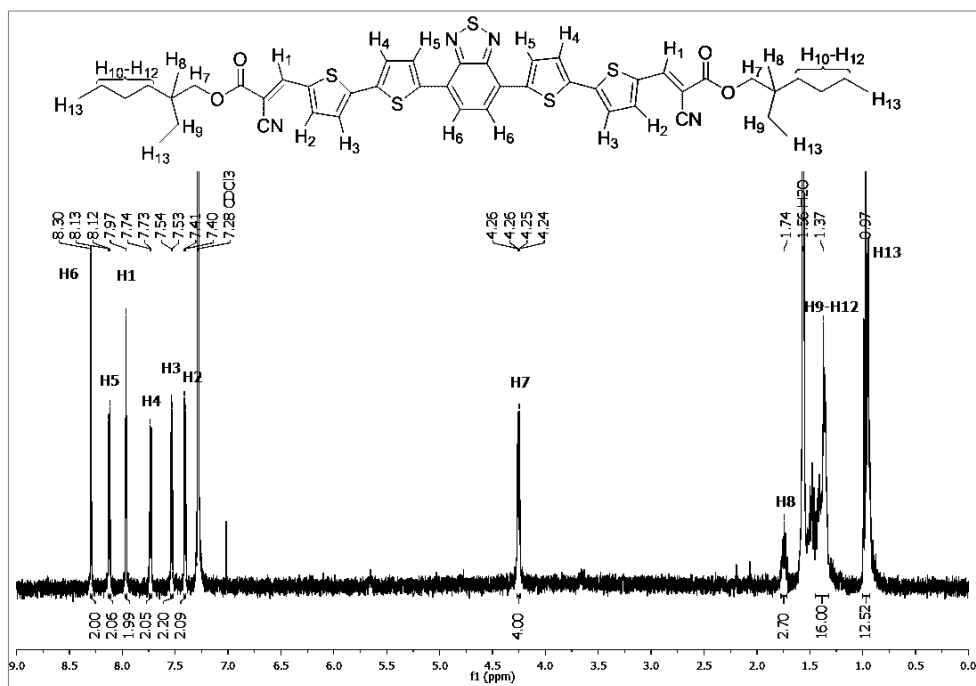
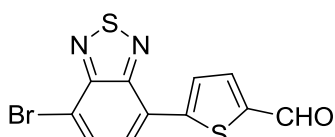


Figure V-6: ^1H NMR spectrum of $\text{Bz}(\text{T}_2\text{CAEH})_2$.

5-(7-bromo-2,1,3-benzothiadiazol-4-yl)- 2-thiophenecarboxaldehyde (BrBzT_1CHO)

Suzuki method


 4,7-dibromobenzo-2,1,3-thiadiazole (500 mg, 1.7 mmol) was placed in a three-necked flask which was brought under an inert atmosphere. All solvents and basic solutions were previously degassed by bubbling through argon for 20 min. Toluene (30 mL), K_2CO_3 (2.0 M, 2 mL), H_2O (6 mL) and Aliquat 336 (4–5 drops) were added and the mixture was vigorously stirred for 10 min at RT. $\text{Pd}(\text{PPh}_3)_4$ (3 mol%) was then added and the reaction continued to be under strong stirring until it reached 80 °C and last for 10 min. After, 5-formyl-2-thiopheneboronic acid pinacol ester (553 mg, 2.32 mmol) that was previously dissolved in 10 mL toluene and degassed for 15 min, was added very dropwisely for 40 min. The mixture was allowed to react overnight at 83 °C. After cooling to room temperature, the mixture was extracted with ether and dichloromethane. The organic extracts were dried over MgSO_4 , filtered and concentrated by evaporation under vacuum. The residue was purified by column chromatography in two times, first on basic alumina (dichloromethane: petroleum ether, 1:4 and gradually rise of the polarity until 1:1) and then on silica gel (petroleum ether: ethyl acetate, from 4:1 until 0:1) to a yellowish orange powder in 10% to 30% yield.

^1H NMR (400 MHz, CDCl_3): δ 10.01 (s, 1H), 8.21 (d, $J = 4.0$ Hz, 1H), 7.95 (d, $J = 7.6$ Hz, 1H), 7.88 (d, $J = 7.6$ Hz, 1H), 7.87 (d, $J = 4$ Hz 1H).

Direct arylation

Route b

The 4,7-dibromobenzo-2,1,3-thiadiazole (500 mg, 1.7 mmol, 1eq), 2-thiophenecarboxaldehyde (r eq) where “r” means molar ratios of 2-thiophenecarboxaldehyde/4,7-dibromobenzo-2,1,3-thiadiazole, various amount of ligand ($P^tBu_2Me.HBF_4$) and additive (pivalic acid) (relative to 4,7-dibromobenzo-2,1,3-thiadiazole), fixed amount of potassium carbonate (K_2CO_3 , 705 mg, 3eq) and palladium acetate ($Pd(OAc)_2$, 38 mg, 10% mol) (relative to 4,7-dibromobenzo-2,1,3-thiadiazole) were dissolved in 7.5 mL dry toluene (fixed parameter) under an argon atmosphere in a three-necked flask. The reaction mixture was refluxed at fixed temperature of oil bath (120 °C) for various reaction times (h). Then, the solvent was evaporated and the reaction yield was estimated from the 1H NMR spectrum of the crude product. All reaction conditions are resumed in Table V-2.

Table V-2: Yields for BrBzT₁CHO obtained from different Route b conditions.

r	Ligand	Additive	Time (h)	1H NMR	Yield
0.7	10%	30%	18	22%	
0.5	20%	1	6	5%	
1	20%	1	4	16%	
1	20%	1	4	10%	

Route c

i) The 4,7-dibromobenzo-2,1,3-thiadiazole (500 mg, 1.7 mmol, 1eq, fixed parameter), 2-thiophenecarboxaldehyde (191 mg, 1.7 mmol, 1eq) (molar ratio of 2-thiophenecarboxaldehyde/4,7-dibromobenzo-2,1,3-thiadiazole is 1), potassium acetate (KOAc, 250 mg, 2.55 mmol, 1.5 eq) and palladium acetate ($Pd(OAc)_2$, 4 mg, 1% relative to 4,7-dibromobenzo-2,1,3-thiadiazole) were dissolved in 6 mL DMA under an argon atmosphere in a schlenk. All of these parameters above were fixed. The reaction mixture was stirred at various temperatures (T) X °C for various reaction times (h). Then, the solvent was evaporated and the product was purified in the same way as the Suzuki coupling reaction (column on basic alumina and then on silica gel). The reaction yield was estimated from the 1H NMR spectrum of the crude product. All reaction yields are presented in Table V-4.

Table V-3: Yields for BrBzT₁CHO obtained from different Route c (i) conditions.

T (°C)*	Time (h)	¹ H NMR Yield
105	21	16%
115	2	20%
125	1.75	16%
140	24	0%

*T is the temperature of oil bath.

ii) The 4,7-dibromobenzo-2,1,3-thiadiazole (500 mg, 1.7 mmol, 1eq, fixed parameter), 2-thiophenecarboxaldehyde (r eq) where “r” means molar ratios of 2-thiophenecarboxaldehyde/4,7-dibromobenzo-2,1,3-thiadiazole, various amount of potassium acetate (KOAc) and catalyst palladium acetate (Pd(OAc)₂) (relative to 4,7-dibromobenzo-2,1,3-thiadiazole) were dissolved in fixed amount of DMA (6 mL) under an argon atmosphere in a three-necked flask. The reaction mixture was stirred at different temperatures (T, X °C) for various reaction times (h). Then, the solvent was evaporated and the product was purified in the same way as for the Suzuki cross-coupling reaction (column on basic alumina and then on silica gel). All reaction conditions are summarized in Table V-3.

Table V-4: Yields for BrBzT₁CHO obtained from different Route c (ii) conditions.

r	KOAc	Pd(OAc) ₂	T (°C)*	Time (h)	Isolate Yield
0.5	1.5	1%	105	21	35%
0.7	2	0.5%	45	2	10%
1	2	0.5%	45	1.75	10%
1	2	0.5%	60	7	10%
0.5	2	0.5%	105	24	trace
1	2	0.5%	105	24	30%
1	2	1%	105	24	trace
1	2	1%	85	6	trace

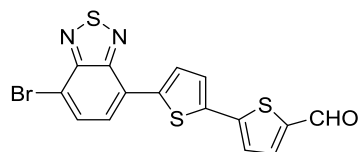
*T is the temperature of the reaction mixture. Note that the temperature of the reaction mixture is around 10°C below that of the oil bath.

¹H NMR (300 MHz, CDCl₃): δ 10.01 (s, 1H), 8.21 (d, *J* = 4.0 Hz, 1H), 7.95 (d, *J* = 7.7 Hz, 1H), 7.88 (d, *J* = 8 Hz, 1H), 7.87 (d, *J* = 4 Hz, 1H).

¹H NMR (400 MHz, CDCl₃): δ 10.01 (s, 1H), 8.21 (d, *J* = 4.0 Hz, 1H), 7.95 (d, *J* = 7.6 Hz, 1H), 7.89 – 7.86 (t, *J* = 4.0 Hz, *J* = 7.6 Hz, 2H).

5'-(7-bromo-2,1,3-benzothiadiazol-4-yl)-[2,2'-bithiophene]-5-carboxaldehyde

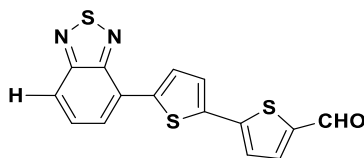
(BrBzT₂CHO)



To a 100 mL three-necked round-bottomed flask, containing a thermometer, stirring bar, and condenser, 4,7-dibromobenzo-2,1,3-thiadiazole (0.5g, 1.7 mmol), potassium acetate (334 mg, 3.4 mmol), and palladium acetate (4 mg, 0.017 mmol) were sequentially added and a rubber seal was used to rigorously keep the system anhydrous and under argon atmosphere. Then 2,2'-bithiophene-5-carboxaldehyde (330 mg, 1.7 mmol) and DMA (8 mL) were added to the mixture using syringe under argon atmosphere. The reaction mixture was then heated to 120°C (oil bath) and stirred under vigorous reflux for 24 hours. The red solution was cooled to room temperature and extracted with dichloromethane several times, then organic phase was evaporated, the residues (500-600mg) was subjected to flash chromatography using ethyl acetate and petroleum ether (from 0:1, 5:95; 1:9; 15:85 to 1:4) as eluent, giving rise to the corresponding red (or orange) mono-arylated product (50 mg, very pure, 8% yield)

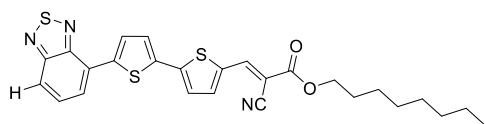
¹H NMR (400 MHz, CDCl₃): δ 9.92 (s, 1H), 8.07(d, *J* = 4 Hz, 1H), 7.91(d, *J* = 7.6 Hz, 1H), 7.78(d, *J* = 7.6 Hz, 1H), 7.74 (d, *J* = 4 Hz, 1H), 7.47 (d, *J* = 4 Hz, 1H), 7.39 (d, *J* = 4 Hz, 1H).

5'-(2,1,3-benzothiadiazol-4-yl)-[2,2'-bithiophene]-5-carboxaldehyde (BzT₂CHO)



To a 100 mL three-necked round-bottomed flask, containing a thermometer, stirring bar, and condenser, 4-bromobenzo-2,1,3-thiadiazole (500 mg, 2.33 mmol), potassium acetate (457 mg, 4.66 mmol), and palladium acetate (5.2 mg, 0.023 mmol) were sequentially added and a rubber seal was used to rigorously keep the system anhydrous and under argon atmosphere. Then 2,2'-bithiophene-5-carboxaldehyde (451 mg, 2.33 mmol) and DMA (8 mL) were added to the mixture using syringe under argon atmosphere. The reaction mixture was then heated to 150°C (oil bath) and stirred under vigorous reflux for 18 hours. The red solution was cooled to room temperature and extracted with dichloromethane and then filtered, the solvent was evaporated, then the residues was subjected to flash chromatography directly using ethyl acetate and petroleum (1:4) as eluent, giving rise to the corresponding orange red direct-arylated product (153 mg, 20% yield, very pure).

¹H NMR (400 MHz, CDCl₃): δ 9.91 (s, 1H), 8.09 (d, *J* = 4.0 Hz, 1H), 8.00 (dd, *J* = 8.8, 0.9 Hz, 1H), 7.92 (dd, *J* = 7.1, 0.9 Hz, 1H), 7.74 (d, *J* = 4.0 Hz, 1H), 7.68 (dd, *J* = 8.8, 7.1 Hz, 1H), 7.48 (d, *J* = 4.0 Hz, 1H), 7.39 (d, *J* = 4.0 Hz, 1H)

BzT₂CAO(211)

Compound 5'-(2,1,3-benzothiadiazol-4-yl)-[2,2'-bithiophene]-5-carboxaldehyde (388 mg, 1.2 mmol) was dissolved in dry CH₂Cl₂ (45 mL). The mixture

was deoxygenated with argon for 20 minutes. Triethylamine (2.17 mL) and octyl cyanoacetate (2.53 mL, 12 mmol) were added successively. The resulting solution was stirred for 25h under argon at room temperature (followed by TLC). After removal of solvent, the resulting mixture was first washed with petroleum ether, then, with distilled water, ethanol and petroleum ether, affording BzT₂CAO as red solid, giving rise to red product (415 mg, 68 % yield).

¹HNMR (400MHz, CDCl₃): δ 8.30 (s, 1H), 8.09 (d, *J* = 4.0 Hz, 1H), 8.00 (dd, *J* = 8.8, 0.8 Hz, 1H), 7.92 (dd, *J* = 7.0, 0.8 Hz, 1H), 7.73 (d, *J* = 4.0 Hz, 1H), 7.68 (dd, *J* = 8.8, 7.1 Hz, 1H), 7.52 (d, *J* = 4.0 Hz, 1H), 7.40 (d, *J* = 4.0 Hz, 1H), 4.33 (t, *J* = 6.8 Hz, 2H), 1.83 – 1.73 (m, 2H), 1.46 – 1.26 (m, 10H), 0.91 (d, *J* = 7.0 Hz, 3H). Element. Anal. Calc. for C₂₆H₂₅N₃O₂S₃: C, 61.51; H, 4.96; N, 8.28; found: C, 61.10; H, 4.85; N, 8.12.

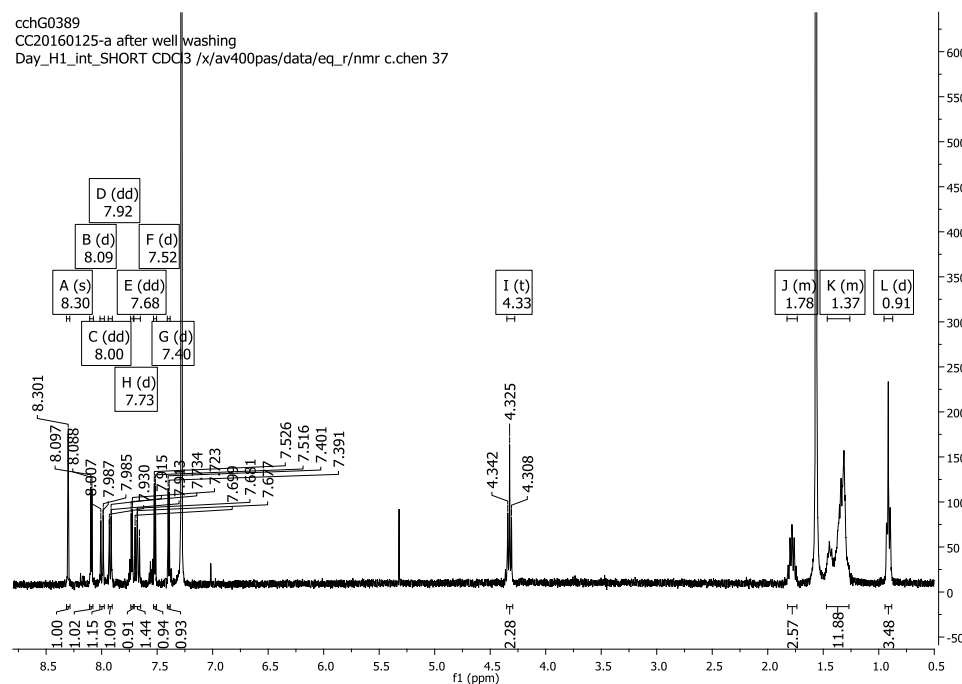
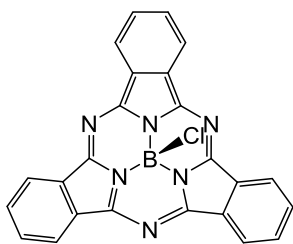


Figure V-7: ¹HNMR spectrum of BzT₂CAO.

Boron subphthalocyanine (SubPcBCl)



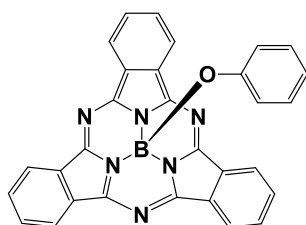
BCl_3 (2 mL, 2 mmol or 4 mL, 4 mmol, 1M solution in *p*-xylene, 1 eq) was added to dry phthalonitrile (256 mg, 2 mmol or 512 mg, 4 mmol, 1 eq) under an argon atmosphere. The reaction mixture was stirred under reflux for X h (or min). The purple solution was then flushed with argon. Treatment: i): The solvent was evaporated and crude product was extracted with toluene, and a purple solid was recovered after removal of the toluene. Then the resultant purple solid was thoroughly washed with methanol and hexane, yielding pure SubPcBCl. ii): The solvent was evaporated and the solid was dried overnight under reduced pressure, and then the crude product was directly washed thoroughly with methanol and hexane, giving rise to pure SubPcBCl. All reaction conditions and different treatment are presented in Table V-5.

Table V-5: Yields for SubPcBCl obtained from different conditions.

Treatment method	Reaction time	Isolated yield
i	3h	12%
i	30min	6%
ii	20min	7%
i + ii	1.5h	34%
ii	1h	47%

$^1\text{HNMR}$ (400MHz, CDCl_3): δ (ppm) = 8.93 (6H, dd), 7.98 (6H, dd). $^1\text{HNMR}$ (400MHz, C_6D_6): δ (ppm) = 8.69 (6H, dd), 7.35 (6H, dd). $^1\text{HNMR}$ (400MHz, $[\text{D}_6]\text{DMSO}$): δ (ppm) = 8.92 (6H, dd), 8.08 (6H, dd).

Phenoxy-SubPc



SubPcBCl (51.7 mg, 0.12 mmol) and phenol (56.5 mg, 0.6 mmol) were refluxed in dry toluene (2mL) for 5.5 h. The reaction mixture was cooled down to room temperature, the solvent evaporated under reduced pressure and the resulting purple solid was washed with methanol and hexane (herein, 40 mg of pink crude product was recovered) before being subjected to column chromatography on silica gel using toluene/ethyl acetate (20:1) as eluent, giving rise to 24 mg phenoxy-SubPc (41%). $^1\text{HNMR}$ (400MHz, CDCl_3): δ (ppm) = 8.87-8.77 (6H, m), 7.94-7.89 (6H, m), 6.77 (t, $J = 7.6$ Hz, 2H), 6.63 (t, $J = 7.6$ Hz, 1H), 5.40 (d, $J = 7.6$ Hz, 2H).

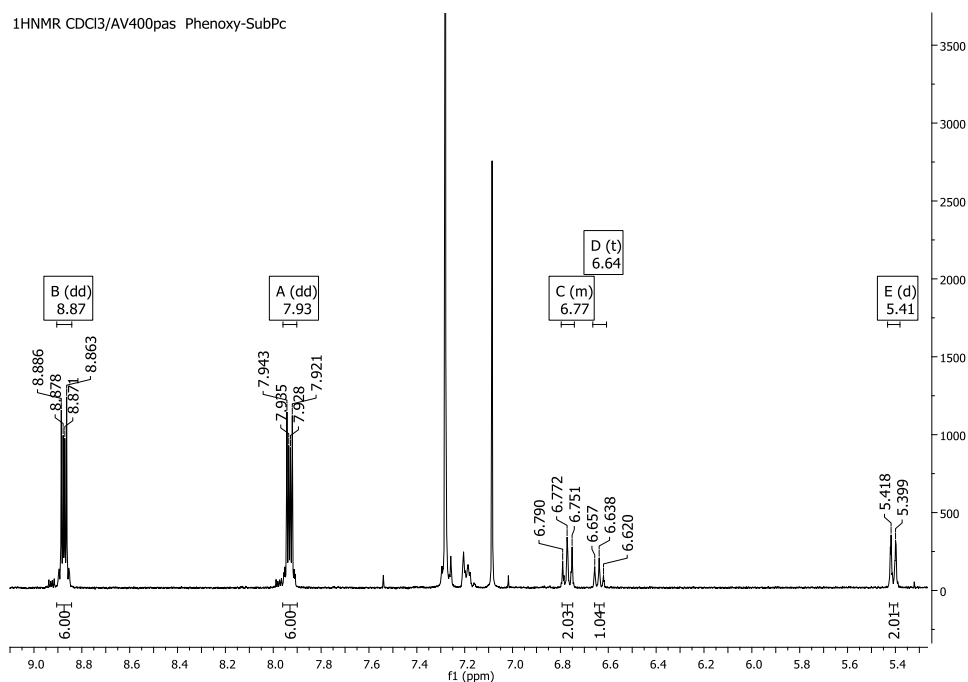
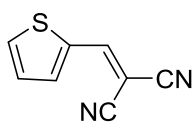


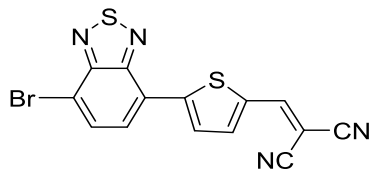
Figure V-8: ¹H NMR spectrum of phenoxy-SubPc

2-(2,2-dicyanovinyl)thiophene(34)



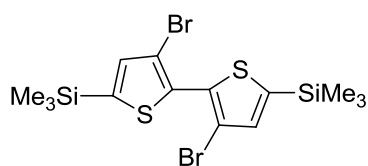
2-thiophenecarboxaldehyde (654 mg, 5.4 mmol), malononitrile (705 mg, 8.8 mmol), and basic aluminum oxide (2.55 g) were stirred in dry toluene (50 mL) for 11 h at 70°C. After cooling down to room temperature, the reaction solution was diluted with toluene and filtered through a pad of silica gel. After removal of solvent, the residue was purified by recrystallization from ethanol to yield yellow crystals in 88% yield (760 mg). ¹H NMR (400 MHz, CDCl₃): δ 7.90 (dd, *J* = 5.5, 1.5 Hz, 2H), 7.83 (d, *J* = 3.9 Hz, 1H), 7.31 – 7.29 (m, 1H).

2-[2-[5'-(7-bromo-2,1,3-benzothiadiazole-4-yl)]thienylmethylene]-propanedinitrile.



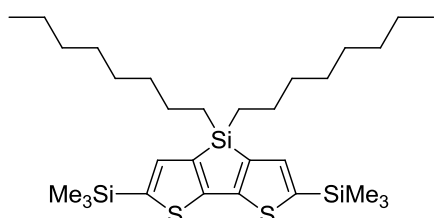
2-(2-thienylmethylene)-propanedinitrile (1 g, 6.21 mmol), 4,7-dibromobenzo-2,1,3-thiadiazole (555 mg, 1.89 mmol), potassium acetate (613 mg, 6.26 mmol), and PdCl(dppb) (36 mg, 0.070 mmol) were dissolved in cyclopentyl methyl ether (CPME) under argon atmosphere in a three-necked flask. The reaction mixture was stirred at 103°C for 28 h. After cooling down to room temperature, the solvent was evaporated under vacuum, and the residue was subjected to flash chromatography on silica gel using ethyl acetate and petroleum ether (1:4) three times to afford 18 mg orange solid (3% yield). ¹H NMR (400 MHz, CDCl₃) δ 8.26 (d, *J* = 4.0 Hz, 1H), 7.96 (d, *J* = 7.6 Hz, 1H), 7.91 (d, *J* = 7.6 Hz, 1H), 7.88 (s, 1H) 7.87 (d, *J* = 4.0 Hz, 1H).

3,3'-dibromo-5,5'-bis(trimethylsilyl)-2,2'-bithiophene(144)



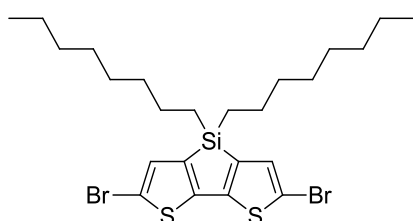
n-butyllithium solution in hexanes (2.5 M) (7.5 mL, 18.7 mmol) was added dropwisely over a period of 1 h to a solution of 3,3',5,5'-tetrabromo-2,2'-bithiophene (4.5 g, 9.3 mmol) in dry THF (110 mL), at -78 °C. The mixture was stirred for 30 min and di-*n*- chlorotrimethylsilane (3 mL, 23.25 mmol) was added in one portion, then the cooling bath was removed to warm the mixture to ambient temperature. The reaction mixture was stirred overnight, and then poured into water, extracted with diethyl ether. After removal of the solvent, the residue was purified by flash chromatography on silica gel using hexane as the eluent, giving a colourless oil in 50% yield (2.03 g). ¹H NMR (400 MHz, CDCl₃) δ 7.17 (s, 2H), 0.36 (s, 18H).

4,4'-dioctyl-2,6-bis(trimethylsilyl)dithieno[3,2-b:2',3'-d]silole(144, 314)



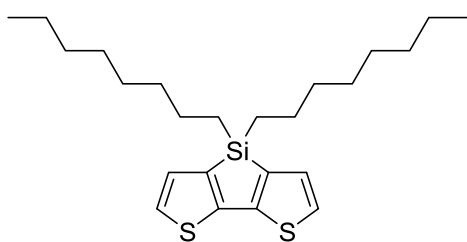
To a solution of 3,3'-dibromo-5,5'-bis(trimethylsilyl)-2,2'-bithiophene (1.98 g, 4.23 mmol) in dry THF (40 mL) was added a 2.5 M solution of *n*-butyllithium in hexanes (3.6 mL, 8.88 mmol) drop wisely at -78°C. After stirring at -78 °C for 15 min, di-*n*-chlorodioctylsilane (1.8 mL, 5.08 mmol) was introduced in one portion by syringe to the solution, and then the cooling bath was removed to warm the mixture to room temperature. After stirring for 2 h under room temperature, the mixture was poured into water and extracted with diethyl ether for several times. After removal of the solvent, the residue was purified by flash chromatography on silica gel using hexane as eluent to give yellow oil in 53% yield (1.24 g). ¹H NMR (400 MHz, CDCl₃) δ 7.18 (s, 2H), 1.50 - 1.40 (m, 4H), 1.34 - 1.20 (m, 20H), 1.0 - 0.9 (m, 10H), 0.39 (s, 18H)

4,4'-dioctyl-5,5'-dibromodithieno[3,2-b:2',3'-d]-silole(144)



NBS (822 mg, 4.62 mmol) was added in one portion to a solution of 4,4'-dioctyl-2,6-bis(trimethylsilyl)dithieno [3,2-b:2',3'-d]silole (1.24 g, 2.2 mmol) in THF (15 mL). After being stirred at ambient temperature for 4.5 h, the mixture was extracted with diethyl ether, and the volatiles were evaporated under vacuum. The residue was subjected to flash chromatography on silica gel using hexane as eluent to give light yellow oil (702 mg, 56% yield). ¹H NMR (400 MHz, CDCl₃) δ 7.05 (s, 2H), 1.40 - 1.28 (m, 28H), 0.94 (m, 6H).

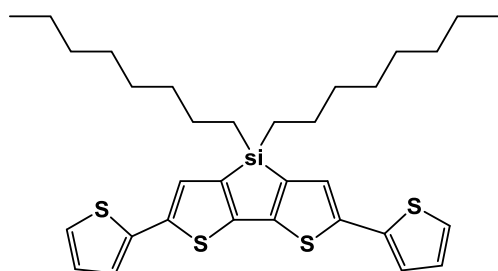
4,4'-dioctyl-dithieno[3,2-b:2',3'-d]-silole (144, 314, 341)



3,3'-dibromo-2,2'-bithiophene (1.4 g, 4.32 mmol) was dissolved in 45 mL dry THF and cooled down to -78°C by a liquid nitrogen-acetone bath. Then *n*-butyllithium solution in hexanes (2.5 M) (3.5 mL, 8.64 mmol) was added drop by drop in 10 mins. The

reaction mixture was stirred for 15 mins at -78°C , di-*n*-chlorosilane (1.5 mL, 4.32 mmol) was added in one portion, then the cooling bath was removed and the solution was stirred overnight. Then the solution was poured into water and extracted with diethyl ether for several times. The organic phase was dried over anhydrous MgSO_4 . After removal of the solvent, the residue was purified by flash chromatography on silica gel using hexane as eluent to yield light yellow oil (24 mg, 1%). $^1\text{H NMR}$ (400 MHz, CDCl_3) δ 7.22 (d, $J = 4.4$ Hz, 1H), 7.10 (d, $J = 4.8$ Hz, 1H), 1.47 (m, 4H), 1.30 (m, 20H), 0.93 (m, 10H).

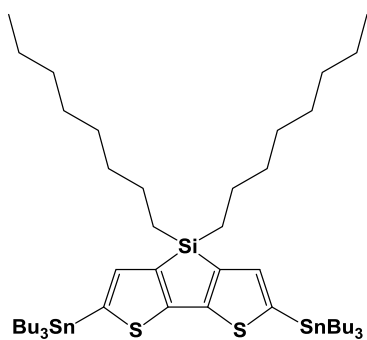
4,4'-dioctyl-2,6-di-(2-thienyl)-dithieno[3,2-b:2',3'-d]-silole



2-(tributylstannyl)thiophene (0.82 mL, 2.56 mmol) was added in a three-necked flask, then 4,4'-dioctyl-5,5'-dibromodithieno[3,2-b:2',3'-d]-silole (702 mg, 1.22 mmol) was dissolved in 5 mL dry toluene and degassed under argon for a while. Then the 5 mL solution was introduced to the flask by syringe in

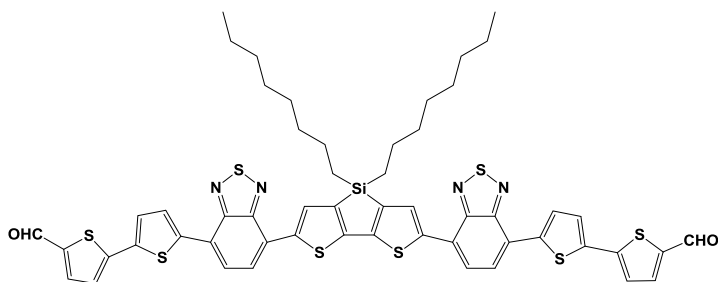
one portion, then 95 mL dry toluene was added in one portion. After, tetrakis(triphenylphosphine) ($\text{Pd}(\text{PPh}_3)_4$) (2.2 mol % relative to 2-(tributylstannyl)) was added and the mixture was refluxed for 15 h. After cooling down to room temperature, the reaction mixture was poured into water and extracted with diethyl ether. After removal of the solvent, the residue was purified by column chromatography on silica gel using hexane as eluent to give red oil (400 mg, 56%). $^1\text{H NMR}$ (400 MHz, CDCl_3) δ 7.21 (dd, $J = 5.1, 1.1$ Hz, 1H), 7.18 (dd, $J = 3.6, 1.1$ Hz, 1H), 7.15 (s, 1H), 7.04 (dd, $J = 5.1, 3.6$ Hz, 1H), 1.40 – 1.2 (m, 28H), 0.88 (m, 6H).

4,4'-di-n-octyl-5,5'-bis(tributyltin)-dithieno[3,2-b:2',3'-d]silole



To a 100 mL three-necked round-bottomed flask, containing a thermometer, stirring bar, and condenser, 2,6-dibromo-4,4'-di-n-octyl-4H-silolo[3,2-b:4,5-b']dithiophene (1.0 g, 1.74 mmol) was dissolved in 20 mL dry THF, then the solution was cooled down carefully to -78°C by a acetone-liquid nitrogen bath. Then 1.5 mL n-butyllithium solution in hexane (2.5 M) diluted in 5 mL THF was added drop wisely (last for 2h). After stirring for another 30mins at -78°C , 1.0 mL tri-n-butyttin chloride (1.19g, 3.65mmol) was added in one portion. Subsequently, the cooling bath was removed, and the argon was stopped. The reaction mixture was stirred at ambient temperature for 16h, followed by poured into water (35 mL) and extracted with diethyl ether for three times, affording 2.3 g of a yellow oil as crude product which was not able to be characterized properly. 67% ^1H NMR yield was however estimated from this crude product that was well dried and stored under argon without further purification for future work.

Fragment DTS(BzT₂CHO)₂(156)



A solution of crude compound 4,4'-di-n-octyl-5,5'-bis(tributyltin)-dithieno[3,2-b:2',3'-d]silole (320 mg, 0.22 mmol) and 5'-(7-bromo-2,1,3-benzothiadiazol-4-yl)-[2,2'-bithiophene]-5-carboxaldehyde (200 mg, 0.49 mmol) in dry toluene (12 mL) was degassed with argon for 25mins, following the addition of Pd(PPh₃)₄ (14 mg, 0.012 mmol). After stirring and refluxing for 24 h at 110°C with the protection of argon, the reaction mixture was poured into water (10 mL) and extracted with CH₂Cl₂ (10 mL x 2). The organic layer dried over anhydrous Na₂SO₄. After removal of solvent, the crude product was purified by silica gel using ethyl acetate:petroleum ether (1:4 to 1:1 to 1:0) as eluent to afford compound DTS(BzT₂CHO)₂. ^1H NMR (400 MHz, CDCl₃) δ 9.92 (s, 1H), 8.23 (s, 2H), 8.09 (d, $J = 4.0$ Hz, 1H), 7.94 (d, $J = 1.0$ Hz, 1H), 7.74 (d, $J = 4.0$ Hz, 1H), 7.49 (d, $J = 3.8$ Hz, 1H), 7.40 (d, $J = 4.0$ Hz, 1H), 1.42 – 1.34 (m, 4H), 1.32 – 1.20 (m, 20H), 1.09 (m, 4H), 0.89 – 0.80 (m, 6H).

**General conclusion
and
future work**

General conclusion

The objective of this thesis was to design and synthesize novel organic small molecules for applications in OPV devices. In this work, various π -conjugated organic molecules were designed and attempted to be synthesized.

A bibliographic review explains the work principle of organic photovoltaics. Then the important parameters for characterizing the performance of an organic solar cell are discussed with standard condition for testing efficiency of OPV cells. Hereafter different types of OPV device architectures are described. Finally, the state-of-the-art electronic materials for OPV devices are discussed. In particular, some representative and promising polymer-based donors, small-molecules based donors, fullerene based acceptors and fullerene-free based acceptors are deeply discussed together with their corresponding performances in OPV devices. It reveals that small molecule semiconductors are emerging and promising candidates for use as active materials in OPV cells.

The second chapter describes the molecular design. A set of small molecules comprised of benzothiadiazole (Bz) core, 4,4'-di-n-octyl-dithieno[3,2-b:2',3'-d]silole (DTS) core, and subphthalocyanines (SubPcs) unit are designed *via* DFT computations at B3LYP/Def2-TZVP(-f) level. Their synthetic strategies are also presented. It is anticipated that these designed molecules show promising potential for organic photovoltaic applications.

In the third chapter, the experimental methods for the molecules syntheses are mainly investigated. Three methods are involved throughout this work: traditional Suzuki cross-coupling, Stille cross-coupling and the emerging direct arylation. Particularly, the direct arylation method is emphatically discussed by means of E-factor (g waste / g product) and cost (€/g). It is demonstrated that direct arylation is an attractive green approach for the synthesis of electronic materials. Among all designed molecules, five molecules based on Bz core are obtained. For DTS and SubPc based target molecules, one more step needs done for obtaining the target molecules.

For obtained four small molecules: Bz(T₁CAO)₂, Bz(T₁CAEH)₂, Bz(T₂CAO)₂ and Bz(T₂CAEH)₂, they are deeply investigated as presented in the fourth chapter. Their optical properties are fully studied in terms of UV-Vis absorption and photoluminescence. The

evaluations of their electronic properties are studied by electrochemistry. Then the thermal and structural properties are studied by means of TGA, DSC and SAXS. We identify these molecules as promising materials for applications in OPV cells. Besides, the experimental results are consistent with theoretical calculation, which suggests that using theoretical calculation to design and predict new materials is a good methodology.

In conclusion, this thesis highlights the need to develop new organic electronic materials for photovoltaic applications and the need to develop green synthesis. Three synthetic approaches (Suzuki, Stille and direct arylation) were involved throughout this work. The E-factor is presented for assessing the environmental impact of two manufacturing processes: the emerging direct arylation method versus the traditional Suzuki cross-coupling method. It shows that direct arylation is a very promising synthetic method for green chemistry. We synthesized new small molecules, $\text{Bz}(\text{T}_1\text{CAO})_2$, $\text{Bz}(\text{T}_1\text{CAEH})_2$, $\text{Bz}(\text{T}_2\text{CAO})_2$ and $\text{Bz}(\text{T}_2\text{CAEH})_2$ for their use in active layers in solution-processed BHJ-OPVs. All four compounds may have the potential of being used as acceptor when blend with P3HT. Molecules $\text{Bz}(\text{T}_2\text{CAO})_2$, $\text{Bz}(\text{T}_2\text{CAEH})_2$ and BzT_2CAO may be potential candidates for use as electron donors with PCBM as the electron acceptor. The effect of alkyl chains on the morphology was also discussed. Further work is needed to better understand and optimize the performance of these materials in OPV devices.

Future work

First, concerning the initial molecules design, as illustrated in chapter II and III, further synthesis needs to be done to obtain corresponding DTS- and SubPc-based target molecules. Once the target molecules are obtained, various characterizations will be carried out to study their optoelectronic properties, thermal and structural properties together with the morphology study on their thin films. Then, to measure their charge transfer mobilities and to test them in OPV devices will be the final aim.

Second, molecules $\text{Bz}(\text{T}_1\text{CAO})_2$, and $\text{Bz}(\text{T}_1\text{CAEH})_2$ have been tested as acceptor with P3HT as donor in BHJ-OPV device, which was done by my colleague Dr. Daniel Hernandez Maldonado in collaboration with Dr. Jose-Luis Maldonado's laboratory. $\text{Bz}(\text{T}_1\text{CAO})_2$, and $\text{Bz}(\text{T}_1\text{CAEH})_2$ showed very low efficiencies (less than 0.1%), which may be caused by the annealing process as discussed in chapter IV. Thus, to fabricate devices *via* vacuum

deposition should be performed to improve the device performance. Works in that aim are under progress. To use DIP molecule as additive in order to improve the crystallinity thus to improve the active layer morphology will be another proposal.

Third, apart from Bz(T₁CAO)₂, and Bz(T₁CAEH)₂, we have also obtained Bz(T₂CAO)₂, Bz(T₂CAEH)₂, and BzT₂CAO that need to be further studied. The charge transfer mobilities need to be measured to know if they will behave as electron donors or acceptors. Their thin film morphologies need also to be studied. Finally, we need to fabricate BHJ devices *via* vacuum deposition and to test their power conversion efficiencies.

In addition, it will be necessary to study the morphology of the BHJ active layer.

The OPV device will be fabricated in Dr. Jose-Luis Maldonado's laboratory (Mexico). The charge transfer mobilities and BHJ device morphology will be performed by Dr. Isabell Séguy from LAAS laboratory and by collaboration with LAPLACE laboratory in Toulouse, respectively.

Annexes

Annexes

Annex 1

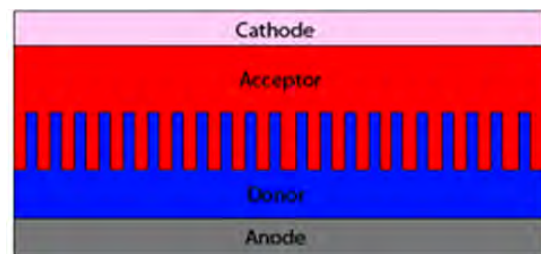


Figure A.1: Ideal or ordered heterojunction geometry of photovoltaic cells.(342)

Annex 2

Suzuki cross coupling

Suzuki and N. Miyaura first reported a stereoselective synthesis of arylated (E)-alkenes by the reaction of 1- alkenylboranes with aryl halides and a palladium catalyst. The Suzuki-Miyaura cross-coupling reaction permits the formation of C-C bonds between organoboron compounds and organic halides or triflates.(343) Suzuki cross-coupling exhibits several advantages: commercial availability of many organoboronic acids and esters, gentle reaction conditions, insensitive to water presence, and the coupling is predominantly stereo- and regioselective. These qualities allow Suzuki's cross-coupling method applicable for industrial produce.(344) However, one big disadvantage of this reaction is that by-products such as self-coupling products(345) or coupling products of phosphine-bound aryls are often formed. Recent developments in methods and catalyst have broadened its possible applications greatly, making the scope of the reaction reagents extend from aryls to alkyl, alkenyl and alkynyl. Potassium trifluoroborates and organoboronate esters or the classic boronic acids are often used as the reagents.

The general mechanism for Suzuki cross-coupling is described in Figure A.2, which can also be used for other cross-coupling methods. It can be summarized in four steps.(344) First, oxidative addition of an organic halide to the Pd(0)-species to generate Pd(II). This is the rate-determining step of the catalytic cycle. The organic halide in the presence of electron-deficient groups would be more reactive than those with electron-rich groups.(343) Second, metathesis that may involve an exchange of the anion adhered to the palladium for the anion of the base. Third, transmetallation transfers the organic group from metal boron to metal

palladium and thus to generate an intermediate containing organic groups in the coordination sphere of palladium. The base is necessary to activate the organoboron reagent. Finally, reductive elimination forms the C-C sigma bond between R^1 and R^2 . The catalyst $Pd(0)$ is regenerated so that it can participate again in the catalytic cycle. The general features of the catalytic cycle have been confirmed by observation of catalytic intermediates using electrospray mass spectrometry.(190)

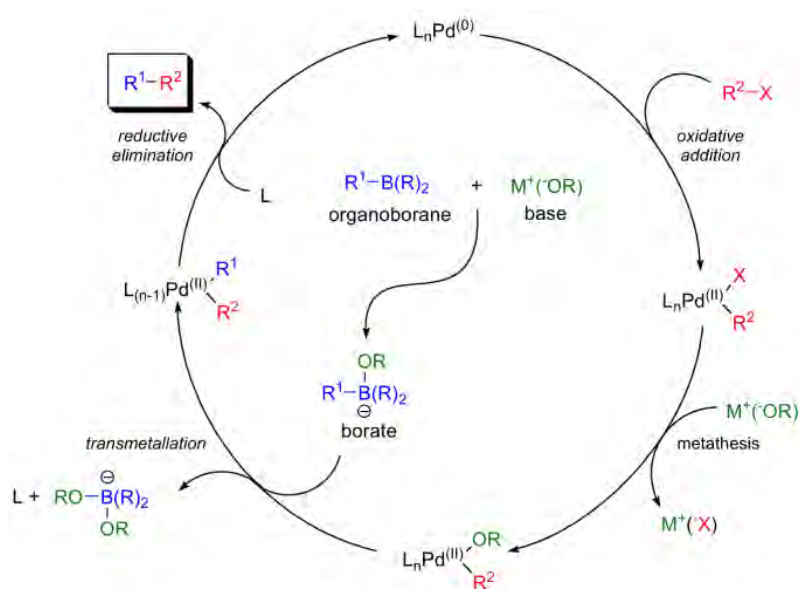


Figure A.2: Catalytic cycle of Suzuki-Miyaura cross-coupling reaction.

Annex 3

Stille cross coupling

The first palladium-catalysed reaction of organotin derivatives was reported by C. Eaborn *et al.* in 1976. Hereafter, M. Kosugi and T. Migita reported the formation of C-C-bond formation using organotin with aryl halides and acid chlorides in 1977. Inspired by the previous work, in 1978, J. K. Stille reported the coupling of several tin-derivatives reagents with different organic halides under milder reaction conditions and with much higher yields than the previous work. He described the mechanism which named after his name since then.(346)

Similar to that of Suzuki cross coupling, the mechanism of Stille cross-coupling reaction mainly involves three steps: oxidative addition; transmetalation; and reductive elimination. (see Figure A.3) Still cross-coupling is also a powerful synthetic strategy allows for the formation of C-C bonds with good yields. But the big drawback is the toxicity of tin derivatives and their low polarity.(347)

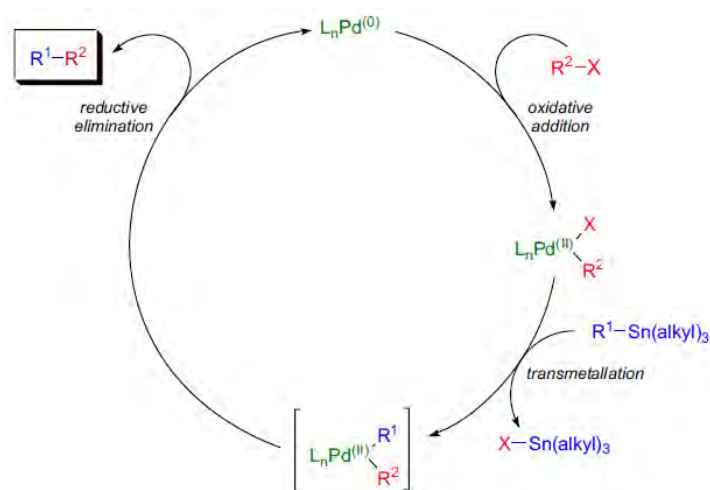


Figure A.3: Catalytic cycle of Stille cross-coupling reaction.

Annex 4

Direct arylation

Direct arylation is the coupling of transition-metal (palladium, Rhodium, Ruthenium) catalysed aryl C-H bonds with aryl halides. It proceeds *via* C-H bond activation without need of the preparation of organometallic. Thus it permits promising and atom-economical alternative to traditional cross-coupling reactions for the formation of new C-C bonds. It is considered to be more efficient and environmentally friendly, because it does not require the preparation of organometallic derivatives and provides either an organometallic or a salt as by-product. Besides, the low catalyst loading makes it a cost-effective procedure.(182, 348, 349)

This reaction was well described by Mario Leclerc, explaining that it could be considered as a combination of a traditional cross-coupling reaction (like Suzuki, Stille, etc.) and an oxidative coupling.(182) Proposed by Mario Leclerc, the catalytic cycle of direct arylation between a thiophene and bromobenzene using a carboxylate additive contains the following steps (see Figure A.4). First, oxidative addition of the carbon-halogen bond. Second, exchange of the halogen ligand for the carboxylate anion to form complex 1. Third, metalation-deprotonation: the complex 1 deprotonates the thiophene substrate while forming a metal-carbon bond at the same time and undergoes transition state (1-TS). Fourth, two possible paths: the phosphine ligands, or the solvent, can re-coordinate to the metal center following Pathway 1, or the carboxylate group can remain coordinated throughout the entire process (Pathway 2). Lastly, reductive elimination affords the coupled product.

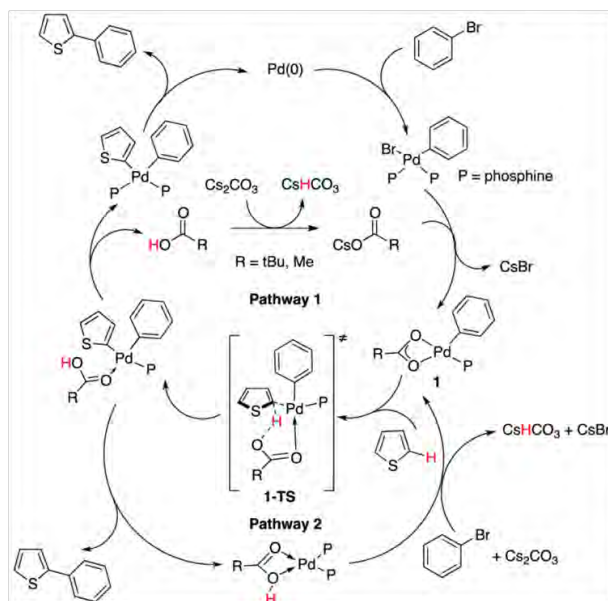


Figure A.4: Catalytic cycle of direct arylation between a thiophene and bromobenzene using a carboxylate additive.(182)

Annex 5

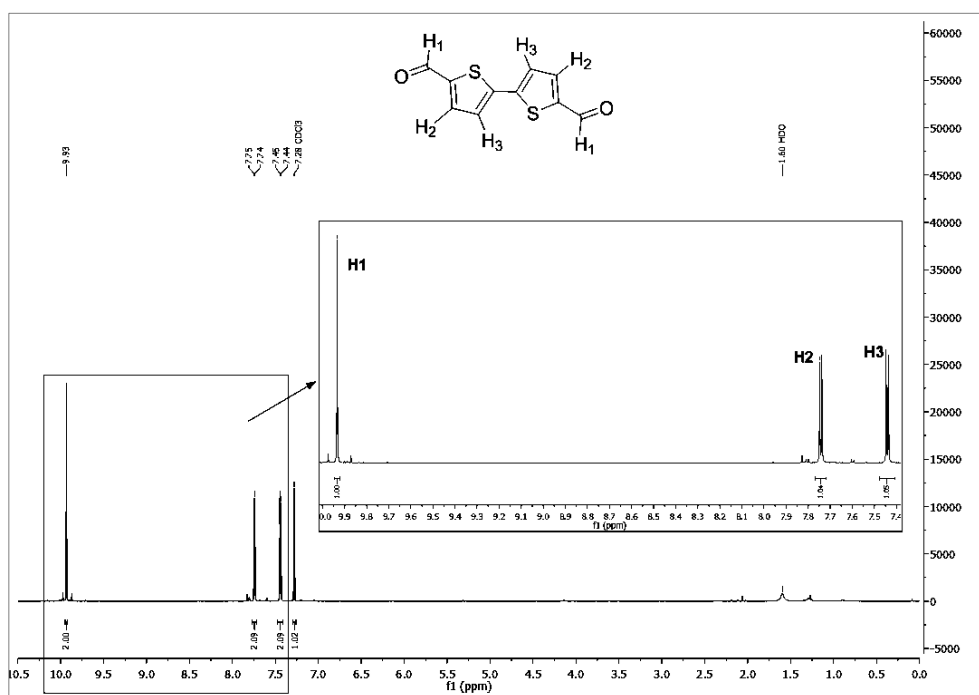


Figure A.5: ¹H NMR spectrum of Homocoupling product of thiophene carboxaldehyde in CDCl₃. (300 MHz) δ 9.93 (s, 2H), 7.75 (d, J = 4.0 Hz, 2H), 7.45 (d, J = 4.0 Hz, 2H).

Annex 6

E-factor and costs

Prices are calculated from raw materials purchased from Aldrich unless indicated

Table A6-I: Molecule 5 obtained *via* **Route a, b, and c.**

reagent	amount (g)	amount (mL)	density (g/mL)	total mass (g)	price (€/g or €/mL)	total price (€)	
Route a							
2,1,3-benzothiadiazole-4,7-bis(boronic acid pinacol ester)	0.247			0.247	138.000	34.086	
5-Bromo-2-thiophenecarboxaldehyde (1.607 g/mL at 25 °C)	0.314			0.314	3.170	0.995	
toluene		10	0.865	8.650	0.050	0.500	
K ₂ CO ₃ 2mol/L (= 280 g/L)		5		1.400	0.140	0.196	
H ₂ O		29	1	29.000			
Aliquat 336		4-5 drops = 0.25	0.884	0.221	0.150	0.033	
Pd(PPh ₃) ₄	0.045			0.045	30.000	1.350	
ethyl acetate		20	0.902	22.173	0.085	1.700	
dichloromethane		20	1.33	26.600	0.059	1.180	
petroleum ether 40-60°C		20	0.65	13.000	0.020	0.400	
total masses		101.650					
amount of product		0.230					
E-Factor route a		(total masses - amount)/amount					440.96
cost (€/g)							175.83
Route b							
reagent	amount (g)	amount (mL)	density (g/mL)	total mass (g)			
4,7-Dibromobenzo-2,1,3-thiadiazole ^a	0.100			0.100	6.600	0.660	
2-thiophenecarboxaldehyde ^b	0.084			0.084	0.330	0.028	
Pd(OAc) ₂ ^c	0.008			0.008	69.000	0.524	
PtBu2Me.HBF ₄	0.017	5		0.017	63.000	1.065	
PivOH	0.035			0.035	0.270	0.009	
K ₂ CO ₃	0.141			0.141	0.140	0.020	
toluene		4	0.865	3.460	0.050	0.173	
H ₂ O		20	1	20.000			
ethyl acetate		20	0.902	22.173	0.085	1.700	
petroleum ether 40-60°C		20	0.65	13.000	0.020	0.400	
total masses		59.018					
amount of product		0.119					
E-Factor route b		(total masses - amount)/amount					494.95
cost (€/g)							38.48
Route c							
reagent	amount (g)	amount (mL)	density (g/mL)	total mass (g)			
4,7-Dibromobenzo-2,1,3-thiadiazole	0.500			0.500	6.600	3.300	
2-thiophenecarboxaldehyde	0.419			0.419	0.280	0.117	
DMA		6	0.937	5.622	0.040	0.240	
KOAc	0.334			0.334	0.300	0.100	
Pd(OAc) ₂	0.002			0.002	63.000	0.120	
H ₂ O		20	1	20.000			
ethyl acetate		20	0.902	22.173	0.085	1.700	
petroleum ether 40-60°C		20	0.65	13.000	0.020	0.400	
total masses		62.050					
amount of product		0.430					
E-Factor route c		(total masses - amount)/amount					143.30
cost (€/g)							13.90

a, b, c: purchased from Interchim, Alfa Aesar, and Strem, respectively

Table A6-II: Molecule 5 obtained *via Route c* and different ratios (**r**), **b**, and **c**.

Route c / r = 2.2							
reagent	amount (g)	amount (mL)	density (g/mL)	total mass (g)			
4,7-Dibromobenzo-2,1,3-thiadiazole	0.500			0.500	6.600	3.300	
2-thiophenecarboxaldehyde	0.419			0.419	0.280	0.117	
DMA		6	0.937	5.622	0.040	0.240	
KOAc	0.334			0.334	0.300	0.100	
Pd(OAc) ₂	0.002			0.002	63.000	0.120	
H ₂ O		20	1	20.000			
ethyl acetate		20	0.902	22.173	0.085	1.700	
petroleum ether 40-60°C		20	0.65	13.000	0.020	0.400	
total masses		62.050					
amount of product		0.430					
E-Factor route c		(total masses - amount)/amount					143.30
cost (€/g)							13.90
Route c / r = 0.9							
reagent	amount (g)	amount (mL)	density (g/mL)	total mass (g)			
4,7-Dibromobenzo-2,1,3-thiadiazole	0.500			0.500	6.600	3.300	
2-thiophenecarboxaldehyde	0.172			0.172	0.280	0.048	
DMA		6	0.937	5.622	0.040	0.240	
KOAc	0.334			0.334	0.300	0.100	
Pd(OAc) ₂	0.002			0.002	63.000	0.120	
H ₂ O		20	1	20.000			
ethyl acetate		20	0.902	22.173	0.085	1.700	
petroleum ether 40-60°C		20	0.65	13.000	0.020	0.400	
total masses		61.803					
amount of product		0.272					
E-Factor route c		(total masses - amount)/amount					226.22
cost (€/g)							21.72
Route c / r = 0.5							
reagent	amount (g)	amount (mL)	density (g/mL)	total mass (g)			
4,7-Dibromobenzo-2,1,3-thiadiazole	0.500			0.500	6.600	3.300	
2-thiophenecarboxaldehyde	0.095			0.095	0.280	0.027	
DMA		6	0.937	5.622	0.040	0.240	
KOAc	0.334			0.334	0.300	0.100	
Pd(OAc) ₂	0.002			0.002	63.000	0.120	
H ₂ O		20	1	20.000			
ethyl acetate		20	0.902	22.173	0.085	1.700	
petroleum ether 40-60°C		20	0.65	13.000	0.020	0.400	
total masses		61.726					
amount of product		0.151					
E-Factor route c		(total masses - amount)/amount					407.78
cost (€/g)							38.98

Table A6-III: Molecule 7 obtained via Routes a and c.

reagent	amount (g)	amount (mL)	density (g/mL)	total mass (g)	price (€/g or €/mL)	total price (€)
Route a						
2,1,3-benzothiadiazole-4,7-bis(boronic acid pinacol ester)	0.173			0.173	138.000	23.874
5'-Bromo-2,2'-bithiophene-5-carboxaldehyde	0.305			0.305	54.000	16.470
toluene		25	0.865	21.625	0.050	1.250
K ₂ CO ₃ 2mol/L (= 280 g/L)		5		1.400	0.140	0.196
H ₂ O		29	1	29.000		
Aliquat 336		4-5 drops = 0.25	0.884	0.221	0.150	0.033
Pd(PPh ₃) ₄	0.039			0.039	30.000	1.155
ethyl acetate		20	0.902	22.173	0.085	1.700
dichloromethane		20	1.33	26.600	0.059	1.180
petroleum ether 40-60°C		20	0.65	13.000	0.020	0.400
total masses		114.536				
amount of product		0.230				
E-Factor route a		(total masses - amount)/amount				496.98
cost (€/g)						201.12
Route c						
reagent	amount (g)	amount (mL)	density (g/mL)	total mass (g)		
4,7-Dibromobenzo-2,1,3-thiadiazole	0.500			0.500	6.600	3.300
2,2'-bithiophene-5-carbaldehyde ^d	0.727			0.727	37.000	26.899
DMA		6	0.937	5.622	0.040	0.240
KOAc	0.334			0.334	0.300	0.100
Pd(OAc) ₂	0.002			0.002	63.000	0.120
H ₂ O		20	1	20.000		
ethyl acetate		20	0.902	22.173	0.085	1.700
petroleum ether 40-60°C		20	0.65	13.000	0.020	0.400
total masses		62.358				
amount of product		0.811				
E-Factor route c		(total masses - amount)/amount				75.89
cost (€/g)						40.39

Table A6-IV: Bz(T₁CAO)₂

reagent	amount (g)	amount (mL)	density (g/mL)	total mass (g)	price (€/g or €/mL)	total price (€)
molecule 5	0.450			0.450	14.000	6.300
triethylamine	1.680	2.3	0.73	1.680	0.283	0.651
octylcyanoacetate	2.500	2.7	0.924	2.500	3.750	9.375
dichloromethane		30	1.33	39.900	0.059	1.770
water		10	1	10.000		
ethanol		10	1	10.000	0.032	0.320
petroleum ether 40-60°C		30	0.65	19.500	0.020	0.600
ethyl acetate		20	0.902	22.173	0.085	1.700
total masses		106.203				
amount of product		0.460				
E-Factor route c		(total masses - amount)/amount				229.88
cost (€/g)						45.03

Table A6-V: Bz(T₁CAEH)₂

reagent	amount (g)	amount (mL)	density (g/mL)	total mass (g)	price (€/g or €/mL)	total price (€)
molecule 5	0.190			0.190	14.000	2.660
triethylamine	0.700	0.96	0.73	0.700	0.283	0.272
2-ethylhexylcyanoacetate ^d	1.050	1.11	0.95	1.050	1.080	1.199
dichloromethane		20	1.33	26.600	0.059	1.180
water		10	1	10.000		
ethanol		10	1	10.000	0.032	0.320
petroleum ether 40-60°C		20	0.65	13.000	0.020	0.400
ethyl acetate		8	0.902	7.216	0.085	0.680
total masses		68.756				
amount of product		0.180				
E-Factor route c		(total masses - amount)/amount				380.98
cost (€/g)						37.28

d: purchased from TCI Europe

Table A6-VI: Bz(T₂CAO)₂

reagent	amount (g)	amount (mL)	density (g/mL)	total mass (g)	price (€/g or €/mL)	total price (€)
molecule 7	0.500			0.500	40.000	20.000
triethylamine ^d	1.240	1.7	0.73	1.241	0.283	0.481
octylcyanoacetate	1.850	2	0.924	1.848	3.750	7.500
dichloromethane		40	1.33	53.200	0.059	2.360
ethanol		10	1	10.000	0.032	0.320
petroleum ether 40-60°C		20	0.65	13.000	0.020	0.400
ethyl acetate		15	0.902	13.530	0.085	1.275
total masses		93.319				
amount of product		0.640				
E-Factor route c		(total masses - amount)/amount				144.81
cost (€/g)						50.53

d: purchased from TCI Europe

Table A6-VII: Bz(T₂CAEH)₂

reagent	amount (g)	amount (mL)	density (g/mL)	total mass (g)	price (€/g or €/mL)	total price (€)
molecule 7	0.500			0.500	40.000	20.000
triethylamine ^d	1.240	1.7	0.73	1.241	0.283	0.481
2-ethylhexylcyanoacetate	1.900	2	0.95	1.900	1.080	2.160
dichloromethane		40	1.33	53.200	0.059	2.360
ethanol		10	1	10.000	0.032	0.320
petroleum ether 40-60°C		20	0.65	13.000	0.020	0.400
ethyl acetate		15	0.902	13.530	0.085	1.275
total masses		93.371				
amount of product		0.570				
E-Factor route c		(total masses - amount)/amount				162.81
cost (€/g)						47.36

d: purchased from TCI Europe

Annex 7

Theoretical calculations

Table A7-I: Ground-state Cartesian coordinates of Bz(T₁CAME)₂ in CH₂Cl₂

C	3.52188127462369	-3.50865462434769	-0.02312086412719
H	6.05939949349445	0.34079056482612	-0.16504781892921
N	8.34754466317542	-3.61580969983038	-0.39850122729142
S	7.78134230640971	-5.12995119833919	-0.41132145162661
N	6.19618920219010	-4.83712977703144	-0.29639133286658
C	6.03685701268153	-3.51060996373109	-0.24056115463085
C	7.29540800677292	-2.79546367637270	-0.30402323959877
C	4.78835992851491	-2.81384498607865	-0.13664327250968
C	4.88389087188389	-1.43301340167563	-0.13159319269990
C	6.10262632415653	-0.74003211549418	-0.19453001055549
C	7.33712935706796	-1.36252408278048	-0.26993413768217
S	8.56954225326217	1.12263303004226	-0.29344593719670
C	8.57762518478992	-0.61370506658070	-0.30053210408760
C	9.88321744961530	-1.08416482328796	-0.32723821496625
C	10.85023200733237	-0.07280873791571	-0.34172332566478
C	10.31254966787906	1.20514797741097	-0.33005747589957
H	10.11406053777243	-2.13560822455464	-0.33794518110014
H	11.91028457782639	-0.26775026570512	-0.36430544083503
H	3.98084514931512	-0.84213875439689	-0.05211909215821
C	10.91024054080739	2.49624361713146	-0.34754125491095
C	12.22597362628845	2.84551792901466	-0.37544226368309
H	10.23211346392808	3.34239410790516	-0.34899807262004
C	13.25365766837061	1.87128511437694	-0.44599225781470
N	14.07593508392382	1.06407276748994	-0.52184675213081
C	12.52617937758235	4.31799670827946	-0.44366363569693
O	11.69921152568739	5.09793067390376	-0.84241946595305
O	13.73593848469114	4.77769252563035	-0.07832427552227
C	14.62228655700479	4.05698470184201	0.79695399167566
H	15.18272033341919	4.82130202459810	1.33032028348594
H	14.06880680258562	3.45104458856012	1.51314960989640
H	15.30001802495926	3.43020128694078	0.22187604487296
S	2.00966048791308	-2.65601668233909	-0.06791409326934
C	3.29969902312667	-4.86470977431273	0.16077461143412
C	1.95110273866125	-5.20811511097430	0.28054812227799
H	4.10579180022806	-5.57562265383982	0.20879634646427
H	1.60914873140766	-6.21797277178447	0.43685724381129
C	1.09363248732899	-4.12343936431457	0.17869295131518
C	-0.32578079743771	-4.03448690504576	0.22812633866813
C	-1.24307122332730	-5.01685483006144	0.44691508661511
H	-0.75912302713140	-3.05165612662592	0.08016765792875
C	-0.85790637251548	-6.34501901647474	0.75767625068832
N	-0.52905473371920	-7.41781575858922	1.02971138566497
C	-2.68827552642340	-4.60505211956293	0.47144125465656
O	-3.00294546205531	-3.46204849561969	0.68348862096789
O	-3.64948579827646	-5.52730634719019	0.28269727148835

C	-3.43328962670595	-6.77580969871453	-0.40196358392883
H	-4.36826928238882	-6.98741321944136	-0.91549299006198
H	-2.63201635444213	-6.69906220231025	-1.13506158299990
H	-3.21178882225456	-7.56508214262861	0.31208763110612

Table A7-II: Ground-state Cartesian coordinates of Bz(T₂CAMe)₂ in CH₂Cl₂

C	3.34397615474397	-3.36444939449446	0.32636020626414
H	5.71170221841585	0.59725040409583	0.33604861771635
N	8.17006785306471	-3.23946094206575	-0.03554584845209
S	7.67530567705331	-4.77716374647891	-0.10650983001549
N	6.07714047453702	-4.56190121214709	0.01497562164131
C	5.85610735592532	-3.24724074003635	0.11809057044102
C	7.08159697655619	-2.47377458384515	0.08702339206960
C	4.57650542985758	-2.61115745483943	0.24297622512345
C	4.61525246756855	-1.22758313993114	0.29615897962728
C	5.80285693937480	-0.47922823528582	0.26694904662554
C	7.06417900642246	-1.04262597888611	0.17737173493329
S	8.20689171411887	1.49325753420363	0.26011223202984
C	8.27618377204463	-0.25390806920209	0.18646048265958
C	9.59292075747857	-0.67333201426819	0.15872968030302
C	10.52110049668406	0.37790340196747	0.19873446970869
C	9.94218639973843	1.62725227549200	0.25851277277009
H	9.86536054995040	-1.71332442056120	0.11047916562074
H	11.59144275058109	0.22643970952988	0.18502190472244
H	3.68730321007410	-0.67809032859434	0.38555380708297
C	13.43990941708773	5.57048047468734	0.31578361541561
C	14.77032782397694	5.27507408948561	0.27481763868192
H	13.21641479628499	6.63171533160719	0.32853753976167
C	15.23455713908139	3.93997737312530	0.17830111862692
N	15.60082764514565	2.84933609206961	0.07444803203303
C	15.70960220292820	6.44115946507010	0.19850330813517
O	15.33137381308462	7.50990204172196	-0.20926187518677
O	16.99664382438647	6.30063069584158	0.56663560698190
C	17.47137530548624	5.23783657076521	1.41113172980852
H	18.30078524215240	5.66713313719825	1.96860270079816
H	16.70455562011443	4.90336073507709	2.10833956307816
H	17.81751112257238	4.40013982076536	0.80997031680404
S	1.79641541514106	-2.55735446447629	0.43271380503160
C	3.16573924608899	-4.73363217317148	0.37035412753538
C	1.82426635480318	-5.12606442582424	0.49137816733082
H	3.99188952785725	-5.42099923780805	0.31849002741412
H	1.50946398875822	-6.15853894909413	0.54110191086338
C	0.93803258868694	-4.07027191816624	0.53938186949476
C	-4.11888827127637	-5.51826120757370	1.02001685365769
C	-4.43228552599023	-6.84051102983293	1.12427285908194
H	-4.97437436571082	-4.85164533506268	1.03346465476218
C	-3.42613756945301	-7.83575358813215	1.20476979437528
N	-2.59766368464667	-8.63623522357434	1.28970428077655
C	-5.88732329620406	-7.18103013107218	1.26243908937701
O	-6.68179563059622	-6.36663242922519	1.65951633293394

O	-6.31949202870346	-8.41964690203890	0.95644379872917
C	-5.60464428095372	-9.30620867626890	0.07775189926335
H	-6.37036890289432	-9.89076106764908	-0.42725464393152
H	-5.02637887369920	-8.75459230476138	-0.66199768091196
H	-4.95026428432677	-9.96115771552098	0.64876157171191
C	-0.48959367210441	-4.11809784434672	0.65851645597074
C	-1.39658717366572	-3.06937534472384	0.65222623953923
C	-2.72125058022714	-3.49263528908532	0.78181104250788
C	-2.86528133476066	-4.86863193742348	0.89620926289836
S	-1.29962235030570	-5.64455037526270	0.84119794860914
H	-1.10048602394481	-2.03578862440196	0.55040263589144
H	-3.57322494054688	-2.82782806479728	0.79160160722822
C	10.59698983512611	2.89946833105371	0.30479440724380
C	10.03748937027617	4.16470205524521	0.38335695884938
C	10.99353816252661	5.18311180587623	0.39569035719274
C	12.30364276096685	4.72621212041563	0.33085552723408
S	12.32959386042040	2.97972766140094	0.25400939896717
H	8.97180456852473	4.33737539311894	0.42776438459249
H	10.75552695434228	6.23637500011609	0.44913652996973

Table A7-III: Ground-state Cartesian coordinates of the oxidized form of Bz(T₂CAMe)₂ in CH₂Cl₂ and its SOMO

C	3.33671792757404	-3.30059305982861	0.39114359685763
H	5.64840368976492	0.66388324131837	0.37444214119899
N	8.15081500512980	-3.17737119824655	0.07029275484481
S	7.67109453674612	-4.71979250559196	0.00388316830933
N	6.07198745069536	-4.50731469209620	0.11164340929084
C	5.84419067805861	-3.19707408279657	0.20621859841632
C	7.05980027657614	-2.42013381356566	0.18077595131835
C	4.55104793513201	-2.56379814781528	0.31210803302313
C	4.58056190166238	-1.15729285172429	0.34628067013296
C	5.74726804847273	-0.41281890424129	0.32370893829720
C	7.03298184869401	-0.97849658502586	0.25814507621848
S	8.14641583833998	1.56909958156015	0.32527815906977
C	8.21346255546345	-0.18592301294641	0.27241350396583
C	9.55098243281038	-0.60823269071627	0.25729966386809
C	10.46540820643730	0.42742439936936	0.28383800519813
C	9.87884116408878	1.69388879793314	0.32179679627597
H	9.82903981614142	-1.64777928842230	0.22804246720034
H	11.53529827992181	0.27275445000185	0.27913154205099
H	3.64826986195373	-0.61217722487027	0.41333502606814
C	13.47266743224797	5.54196900129400	0.27338999191996
C	14.79356801103553	5.21638398287138	0.17973873667706
H	13.26402834976570	6.60540098557652	0.30966848070580
C	15.23500872503406	3.87399816024423	0.05615588405826
N	15.58730804787895	2.78190795917506	-0.07506435852326
C	15.77220022527028	6.35153296594781	0.07372406867797
O	15.42606434722655	7.41873625337077	-0.38065525164538
O	17.04460236253065	6.19221426554201	0.44919424268413
C	17.50835650046780	5.14854890296886	1.34210194539574

H	18.30726452639465	5.60636222654416	1.91927226994220
H	16.71909399250280	4.82016952045407	2.01471763754764
H	17.89459276800478	4.31538602053937	0.76062413969671
S	1.77432263918056	-2.50622974381978	0.46253500954627
C	3.16502154200480	-4.69071339837521	0.45238860524511
C	1.84557438511921	-5.08899139730241	0.55876273749105
H	3.99530298936181	-5.37505442176528	0.42495110068935
H	1.54205167621454	-6.12422485627459	0.62122769988280
C	0.93810083039681	-4.02675237397898	0.57655824809700
C	-4.09154687801179	-5.57682302592942	0.95993992502733
C	-4.40354827483153	-6.89903933070771	1.07138459682644
H	-4.94434603641970	-4.90745885161013	0.94201463257166
C	-3.40265785903024	-7.89808209036161	1.18533128113320
N	-2.57913705418001	-8.69869881250359	1.30626667705839
C	-5.86200384675508	-7.24650556482607	1.18726392493458
O	-6.65618917172524	-6.43689158081757	1.61133730130236
O	-6.30368037688369	-8.46085225919447	0.84561121731872
C	-5.58887393571605	-9.36513894264461	-0.03320888891006
H	-6.36168934332649	-9.92394459598497	-0.55409161024597
H	-4.98825973683260	-8.81693467372442	-0.75569039155671
H	-4.97194163524490	-10.04015382695236	0.55447294346059
C	-0.48044469748910	-4.10773905425685	0.67042760998330
C	-1.41420800933187	-3.07509195807345	0.65571068841694
C	-2.72574241836834	-3.52744729364600	0.75482458208817
C	-2.83736672124867	-4.91285188219065	0.85689494936751
S	-1.26416292317516	-5.65704663729099	0.82440607591467
H	-1.14495617339902	-2.03213706139874	0.56887190810596
H	-3.59210333612016	-2.88154915860793	0.75305222150126
C	10.55731470334350	2.94453917556990	0.34554156083234
C	10.03312583976361	4.23117722875742	0.42159259513404
C	11.01482620368357	5.21827943040310	0.41073062995646
C	12.31361456875667	4.71919347981185	0.32207442354456
S	12.29568557055873	2.98013323266671	0.25956560168408
H	8.97444125331409	4.44057184443479	0.48526277644889
H	10.80682748436899	6.27797274377046	0.46353807840767

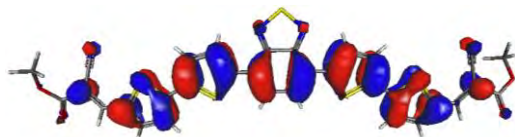


Figure A7-I: SOMO of the oxidized form of Bz(T₂CAMe)₂.

Table A7-IV: Ground-state Cartesian coordinates of the reduced form of Bz(T₂CAMe)₂ in CH₂Cl₂ and its SOMO

C	3.35895909524314	-3.37164724059587	0.29022931381003
H	5.73541349547162	0.56799075606796	0.22243844999261
N	8.18701116850452	-3.30502626286746	-0.03675564128488
S	7.68568188369451	-4.85590815688089	-0.08130038118649
N	6.07685184633117	-4.61300844285625	0.02208076110208
C	5.86740083934319	-3.29714320499971	0.09637432027708

C	7.10498918784651	-2.53074892664984	0.05964617846440
C	4.58731071258894	-2.64606243358906	0.19815415005969
C	4.63952078144021	-1.23991648876762	0.21931054447602
C	5.81778635180327	-0.51139364321706	0.18411246245531
C	7.09705949960382	-1.09259726235016	0.11908006368127
S	8.23045142478012	1.44703422906438	0.18468612131428
C	8.29413942674155	-0.31174499055040	0.12245549041981
C	9.62917259128030	-0.72274993859803	0.09522910783444
C	10.55000281356521	0.31937499642416	0.12615108393080
C	9.98006219411350	1.58636110819332	0.17865214523154
H	9.90810379511618	-1.76199101431194	0.05563882475298
H	11.62023583240350	0.15999283294871	0.11233138189950
H	3.71348800806978	-0.68238580830790	0.28440855706167
C	13.43244048174864	5.56816362210001	0.31664661325832
C	14.80160407940782	5.33389368875389	0.33094108093965
H	13.16590144683315	6.61889013692220	0.35103684214115
C	15.33056190825830	4.03051074343705	0.20325980657642
N	15.74719799073552	2.95849027201528	0.06701038801340
C	15.67927981058541	6.52037572763876	0.34144775997717
O	15.28063012619659	7.62180370360900	0.00613341750629
O	16.97833881239366	6.42306838416633	0.70466022824209
C	17.50383022758477	5.36913706282680	1.54101097810199
H	18.29824454874847	5.83452133104758	2.12034890383726
H	16.74340552371990	4.98107543737790	2.21602535204497
H	17.91066638430890	4.56832161925982	0.92799696078296
S	1.80639107780418	-2.54739215729235	0.38300661744709
C	3.15107285517194	-4.75066668477514	0.35357573503387
C	1.81863807236999	-5.12512807926553	0.48092821791760
H	3.96608593861396	-5.45259888834614	0.31344282460768
H	1.50130822824963	-6.15685169106719	0.54852373581769
C	0.92331915053963	-4.06062934333361	0.51576136976472
C	-4.12191108571751	-5.49822377651214	1.04850944665940
C	-4.46737492650425	-6.83885200304498	1.15528710882607
H	-4.96757302688397	-4.81938048292557	1.06576450924957
C	-3.48946261511562	-7.85572391218218	1.23637856029514
N	-2.68535705521120	-8.68372233727379	1.33158026303652
C	-5.89879046849519	-7.16086410514386	1.31430922826040
O	-6.71424323390643	-6.34025466019162	1.69632322830673
O	-6.35157606224516	-8.41163497809232	1.06508568863206
C	-5.71187145382249	-9.31643256937167	0.13803191535565
H	-6.52116180562327	-9.86526092708895	-0.33866730773163
H	-5.14870095509862	-8.77200792740208	-0.61738111053521
H	-5.06155314376547	-10.00376828070193	0.67413509508489
C	-0.48439035766207	-4.11060884756480	0.64504575569410
C	-1.41027683705442	-3.05855002487043	0.65555776845411
C	-2.72199906518843	-3.47668680203439	0.79628624648173
C	-2.88390991419423	-4.86518046592501	0.90997883894359
S	-1.30638920639706	-5.64501268110584	0.82810751056555
H	-1.11890644174052	-2.02247957081382	0.55640140750385
H	-3.57040726821134	-2.80607443118679	0.81770566787584
C	10.63082213871279	2.84003049823419	0.22256915467928

C	10.06390592353170	4.11944344323369	0.27597306449804
C	10.99914367659964	5.13798219871979	0.30576247725508
C	12.33445078592207	4.70651862145570	0.28010269452097
S	12.37637496883122	2.94475239265120	0.21395982966100
H	8.99577700999226	4.28654598833022	0.29171829579334
H	10.74351680803598	6.18840764757638	0.34898889633153

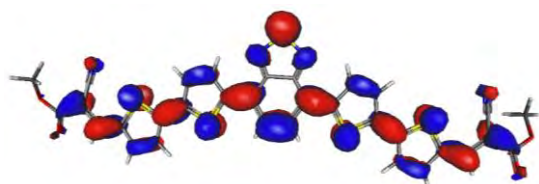
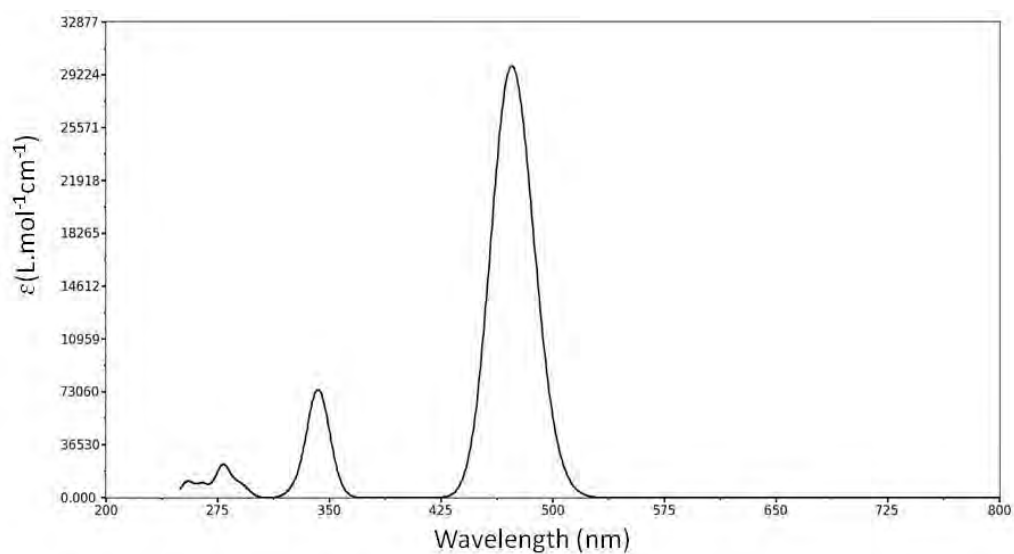
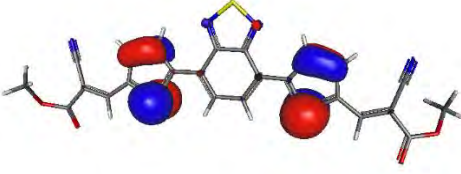
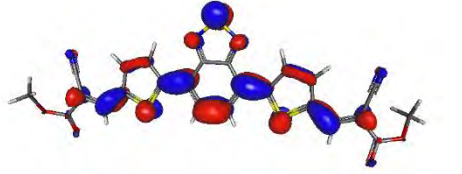
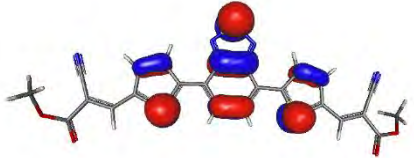
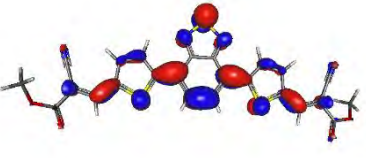
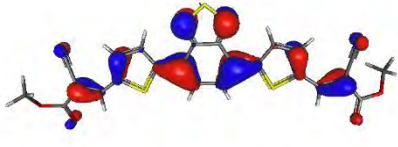
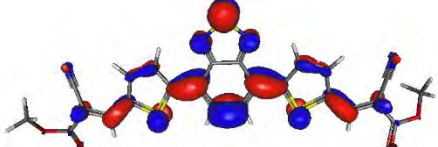
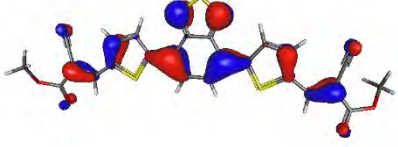
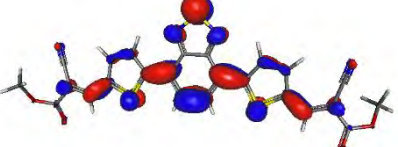
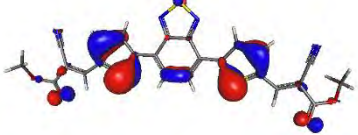

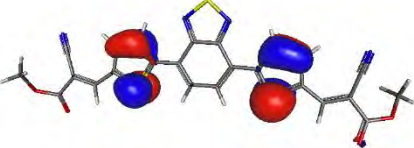
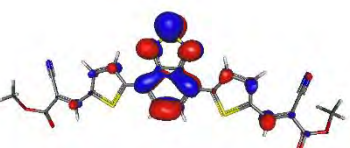
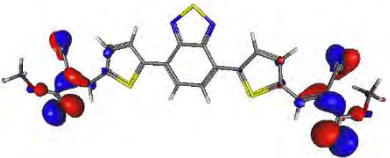
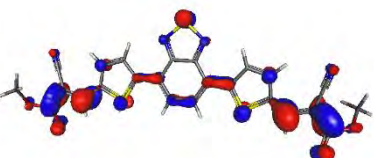




Figure A7-II: SOMO of the reduced form of Bz(T₂CAME)₂.



State, f, λ (nm), n	Hole	Electron
S ₁ , 2.07, 472.7, 0.93		
S ₂ , 0.088, 343, 0.88		
S ₃ , 0.422, 342.8, 0.93		

S ₆ , 0.06, 290.6, 0.84		
S ₇ , 0.15, 278.7, 0.77		
S ₈ , 0.06, 265.2, 0.83		
S ₉ , 0.07, 255.0, 0.83		
S ₁₂ , 0.05, 239.8, 0.44		
S ₁₂ , 0.05, 239.8, 0.29		
S ₁₂ , 0.05, 239.8, 0.19		
S ₁₅ , 0.08, 238.2, 0.42		

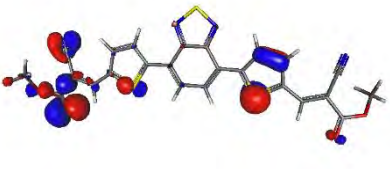
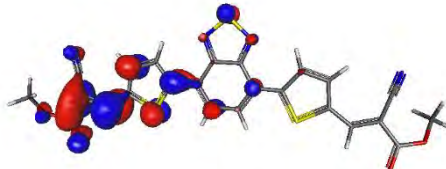
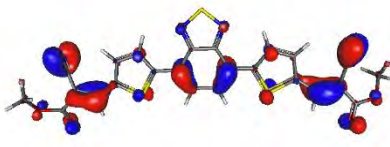
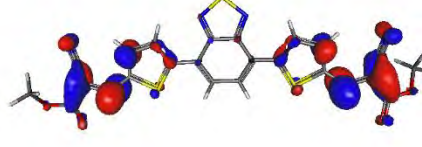
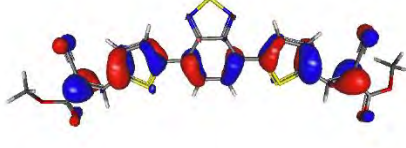
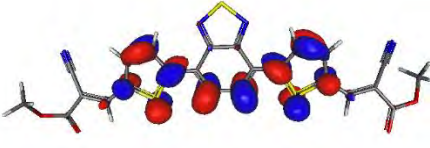
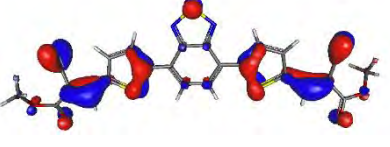
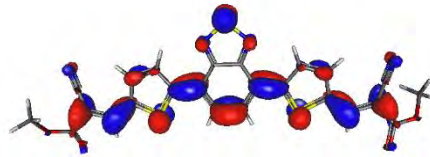
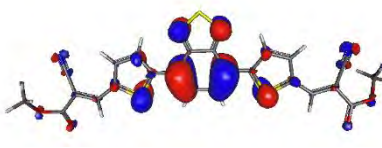


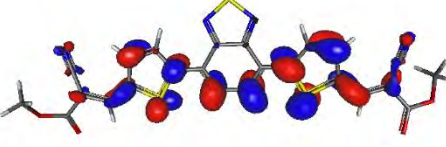
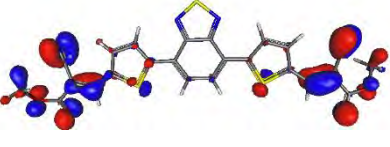
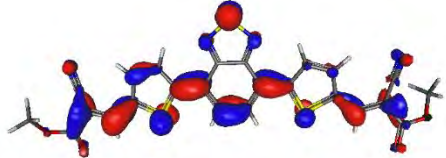
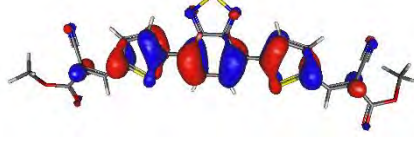
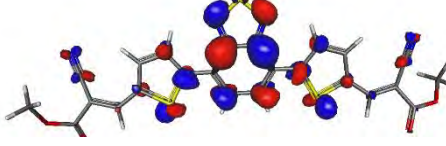
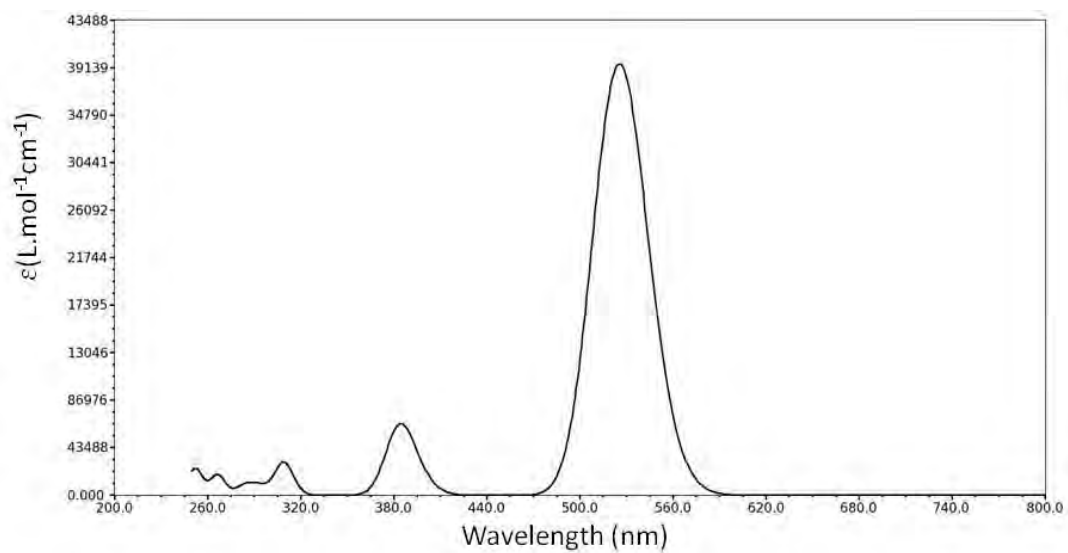
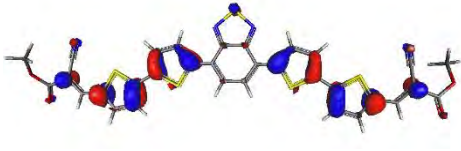
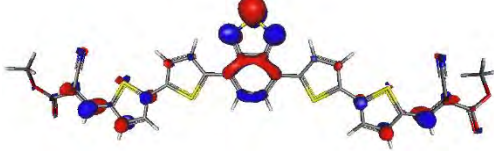
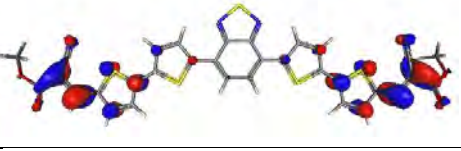
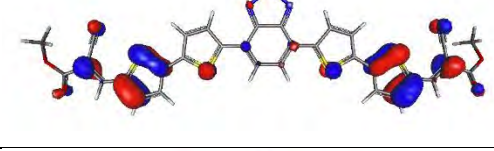

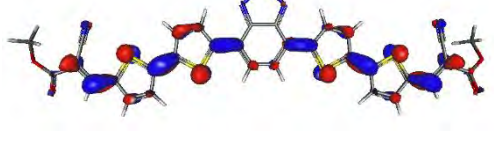
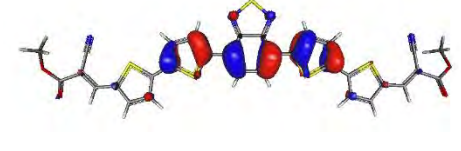
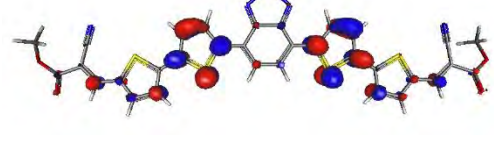
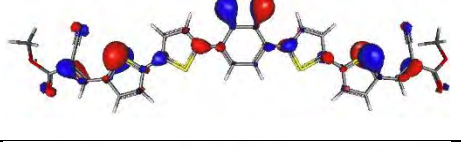
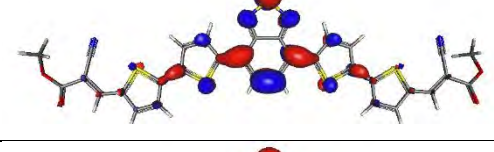
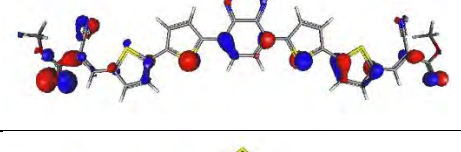
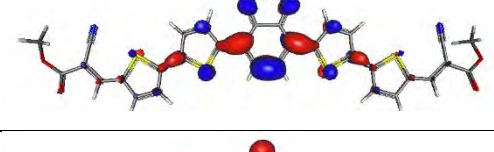
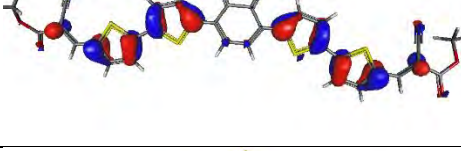
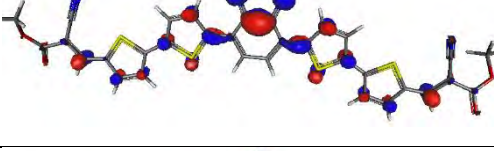
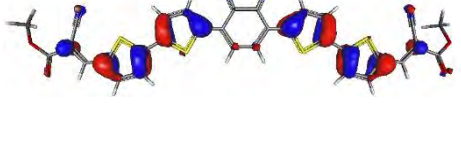
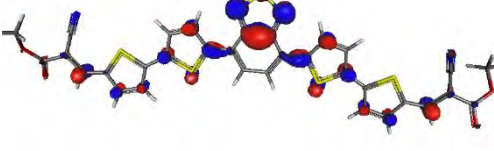
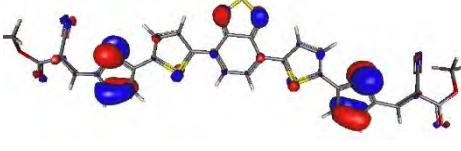
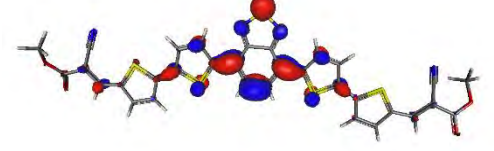
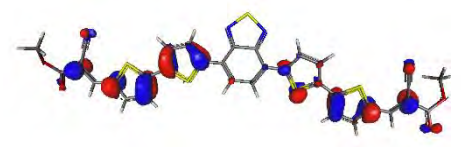
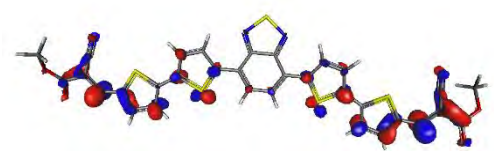
S ₁₅ , 0.08, 238.2, 0.34		
S ₂₂ , 0.05, 219.7, 0.47		
S ₂₂ , 0.05, 219.7, 0.25		
S ₂₂ , 0.05, 219.7, 0.17		
S ₂₅ , 0.07, 209.8, 0.32		
S ₂₅ , 0.07, 209.8, 0.29		
S ₂₅ , 0.07, 209.8, 0.24		
S ₂₉ , 0.13, 206.6, 0.63		

Figure A7-III: Simulated absorption spectrum of Bz(T₁CAMe)₂ in CH₂Cl₂ and Natural transitions orbital isodensity surface for main transitions ($f > 0.05$) of Bz(T₁CAMe)₂



State, f, λ (nm), n	Hole	Electron
S ₁ , 2.73, 525.7, 0.90		
S ₂ , 0.05, 398.1, 0.73		
S ₃ , 0.43, 384.3, 0.89		
S ₅ , 0.20, 309.2, 0.54		
S ₅ , 0.20, 309.2, 0.39		
S ₇ , 0.05, 293.6, 0.67		

S ₇ , 0.05, 293.6, 0.20		
S ₁₃ , 0.11, 266.7,		
S ₁₅ , 0.14, 255.0, 0.34		
S ₁₅ , 0.14, 255.0, 0.29		
S ₂₅ 0.05, 239.8, 0.49		
S ₂₅ 0.05, 239.8, 0.21		
S ₂₆ , 0.08, 238.2, 0.57		
S ₂₆ , 0.08, 238.2, 0.17		
S ₂₈ , 0.05, 219.7, 0.32		
S ₂₈ , 0.05, 219.7, 0.22		

S ₂₈ , 0.05, 219.7, 0.14		
S ₃₅ , 0.07, 209.8, 0.41		
S ₃₅ , 0.07, 209.8, 0.37		
S ₃₈ , 0.13, 206.6, 0.43		
S ₃₈ , 0.13, 206.6, 0.22		

Figure A7-IV: Simulated absorption spectrum of Bz(T₂CAMe)₂ in CH₂Cl₂ and Natural transitions orbital isodensity surface for main transitions ($f > 0.05$) of Bz(T₂CAMe)₂.

Annex 8

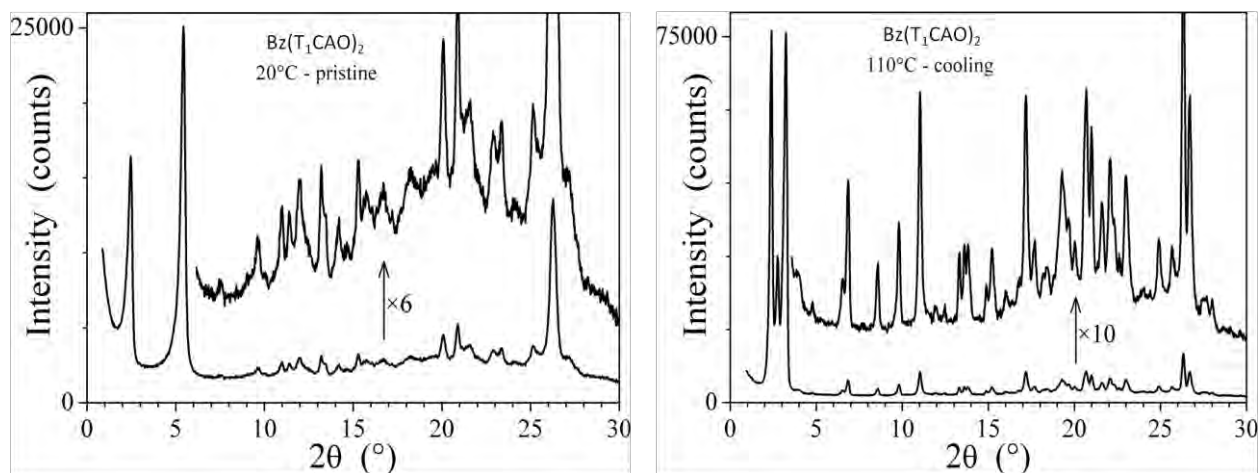


Figure A.8: SAXS patterns of Bz(T₁CAO)₂ in the pristine state (left) and at 110°C in the crystalline phase obtained on cooling from the smectic A phase (right).

Figure list

Figure list

Figure I-1: World total primary energy supply in 2013, provided by International Energy Agency. <i>Coal</i> : peat and oil shale are aggregated with coal, <i>other</i> : geothermal, solar, wind, heat, etc., are included.(7)	5
Figure I-2: U.S. energy consumption by energy source in 2014. Source: U.S. Energy Information Administration.(11)	6
Figure I-3: The spectrum of solar radiation.(12)	6
Figure I-4: Device architecture of a bulk heterojunction photovoltaic cell.	7
Figure I-5: Number of publications dealing with organic solar cells during the period of 1980-2016 (Source Scopus).	7
Figure I-6: The latest chart on record cell efficiencies, provided by The National Center for Photovoltaics (NCPV) at National Renewable Energy Laboratory (NREL).(33) Progress in photovoltaic power conversion efficiencies is tracked six monthly by Green <i>et al.</i> (34)	8
Figure I-7: Basic energy level diagram and illustration of energy gap in molecular case of an organic semiconductor.(53)	10
Figure I-8: Functional principle of a D/A solar cell.	11
Figure I-9: Absorption coefficients of films of commonly used materials are depicted in comparison with the standard AM 1.5 terrestrial solar spectrum (up)(according to Ref.(56)), and the structures of the materials (down).	12
Figure I-10: Standard Solar Spectra for space and terrestrial use. (Source: pveducation)	14
Figure I-11: Scheme of the sunlight path length, in units of Air Mass and dependent on the angle from the vertical (zenith angle θ). (Source: pveducation)	15
Figure I-12: Current density <i>versus</i> voltage schematic diagram of organic solar cells in the dark and under illumination.	15
Figure I-13: Schematic energy level diagram between an ideal polymer and a PC ₆₁ BM acceptor.(63)	16
Figure I-14: Efficiency of a D/A OPV cell <i>vs</i> the band gap energy of the donor, and the LUMO offset between the two materials.(79)	18
Figure I-15: The architecture structure of (a) bilayer heterojunction and (b) BHJ OPV devices.(84)	20
Figure I-16: Schematic energy level diagram of an OPV, revealing the anode and cathode work functions, the HOMO and LUMO offsets (Δ HOMO and Δ LUMO, respectively) and the maximum open-circuit voltage (V_{oc}). (87)	21
Figure I-17: Schematic architecture of an organic tandem solar cell including two sub-cells with different and complementary absorption spectra.(79)	23
Figure I-18: <i>trans</i> -polyacetylene and its schematic π orbital.	25

Figure I-19: Illustration of energy binding mechanism with increase in the conjugation length of the ethylene in polyacetylene.....	26
Figure I-20: Schematic band diagram for π -conjugated polymers (left) and π - π^* interband transition associated with generation of a mobile electron and a mobile hole in the π^* -band and π -band respectively (right).(26).....	27
Figure I-21: One difference of hopping transport from coherent (band) transport is that there is no need for charge carrier to move from one unit to the next. (a) This involves intrachain transport that may occur by a hopping mechanism, particularly when defects are existed in the chain. (b) It is possible that both coherent transport and hopping can occur in conjugated polymers, with the charge carrier hopping from one chain to another. (c) Only hopping transport exhibits in some polymers like poly(vinyl carbazole), due to lack of conjugated backbone.(125).....	28
Figure I-22: Structures of some (a) electron donor and (b) electron acceptor units.	29
Figure I-23: Chemical structures of representative polymers acting as donors in OPV devices.	29
Figure I-24: The development of heterojunction solar cells based on polymers and small molecules.(30).....	32
Figure I-25: Chemical structures of representative small molecular-based donors.	33
Figure I-26: Common fullerene and its derivatives acceptor materials.	35
Figure I-27: Chemical structures of fullerene-free acceptors for OPVs.	37
Figure II-1: The 26 building blocks (including chemical connections indicated by 'X') of the resulting CEP molecular candidate library. Five most efficient moieties in the top PCE are highlighted in green, and red indicates the five less efficient moieties.(188).....	46
Figure II-2: Ranking of building blocks related to calculated PCE $\geq 10\%$.(188).....	46
Figure II-3: Chemical structures of some top candidates gathered in the CEPDB.	47
Figure II-4: Pentacene-C ₆₀ bilayer interface simulated by molecular dynamics.....	48
Figure II-5: Chemical structures of designed small molecules based on Bz core.....	50
Figure II-6: Chemical structures of some donor materials based on DTS core (C8 = octyl)...	52
Figure II-7: 3D structure of SubPcBCl illustrating its unique bowl-shaped structure: a top view (left) and side view (right). (white sticks: H; grey sticks:C; blue sticks: N; yellow sticks: B; green stick: Cl).(221).....	57
Figure II-8: The axial and peripheral positions on SubPcBCl. (white sticks: H; grey sticks:C; blue sticks: N; yellow sticks: B; green sticks: Cl).(221).....	58
Figure II-9: Chemical structures of some materials associated with SubPcs in OPV application.	59
Figure II-10: Conformations of diTBz characterized by dihedral angles (θ_A and θ_B).	61
Figure II-11: Frontier molecular orbitals of diTBz in different conformations at the B3LYP/Def2-TZVP(-f) level.	61

Figure II-12: Structures of designed molecules with different conjugation lengths.	62
Figure II-13: The scheme of dihedral angles for structural analysis.	63
Figure II-14: Frontier molecular orbitals of Bz(T ₁ CAMe) ₂ , Bz(T ₂ CAMe) ₂ , Bz(T ₃ CAMe) ₂ and Bz(T ₄ CAMe) ₂ in their optimized geometries at B3LYP/Def2-TZVP(-f) level.	64
Figure II-15: NTOs isodensity surface for the strongest transition are represented and the associated wavelengths are indicated for Bz(T ₁ CAMe) ₂ and Bz(T ₂ CAMe) ₂ in CH ₂ Cl ₂ at B3LYP/Def2-TZVP(-f) level.	65
Figure II-16: Simulated absorption spectra of Bz(T ₁ CAMe) ₂ (left) and Bz(T ₂ CAMe) ₂ (right) with different functionals with Def2-TZVP(-f) basis set.	66
Figure II-17: Frontier molecular orbitals and electronic properties of diTBz and diTffBz with different conformations calculated by DFT at B3LYP/Def2-TZVP(-f) level.	68
Figure II-18: Frontier molecular orbitals and electronic properties of ffBz(T ₁ CAMe) ₂ , ffBz(T ₂ CAMe) ₂ , ffBz(T ₃ CAMe) ₂ and ffBz(T ₄ CAMe) ₂ at B3LYP/Def2-TZVP(-f) level.	69
Figure II-19: Simulated absorption spectra of Bz(T ₁ CAMe) ₂ , ffBz(T ₁ CAMe) ₂ , Bz(T ₂ CAMe) ₂ , ffBz(T ₂ CAMe) ₂ at BHandHLYP/ Def2-TZVP(-f) level.	70
Figure II-20: The scheme of dihedral angles for structural analysis.	71
Figure II-21: Frontier molecular orbitals and electronic properties of DTS-based small molecules calculated by DFT at B3LYP/Def2-TZVP(-f) level.	72
Figure II-22: Chemical structures of calculated SubPcs-based small molecules.	73
Figure II-23: Frontier molecular orbitals and electronic properties of SubPcs-based small molecules calculated by DFT at B3LYP/Def2-TZVP(-f) level.	74
Figure II-24: Structure of axial substituents.	74
Figure II-25: Frontier molecular orbitals and electronic properties of axial substituents calculated by DFT at B3LYP/Def2-TZVP(-f) level.	75
Figure II-26: Energy level diagram of molecules calculated by DFT at B3LYP/Def2-TZVP(-f) level.	76
Figure III-1: Chemical structures of the synthesized molecules.	82
Figure III-2: Chemical structures of various fragments for DTS-based target molecules.	89
Figure III-3: Products found in the crude product of Suzuki reaction for fragment BrBzT ₁ CHO.	90
Figure III-4: Normalized absorption spectra of SubPcBCl and phenoxy-SubPc in CH ₂ Cl ₂ solution.	99
Figure IV-1: Absorption spectra of the four molecules under study in DCM solution with concentrations as indicated.	103
Figure IV-2: Experimental and simulated absorption spectra of Bz(T ₁ CAMe) ₂ and Bz(T ₂ CAMe) ₂ in DCM solution (simulation performed at BHandHLYP/Def2-TZVP level).	104

Figure IV-3: UV-vis absorption spectra of molecules Bz(T ₁ CAMe) ₂ and ffBz(T ₁ CAMe) ₂ under study in DCM solution and by DFT at BHandHLYP/Def2-TZVP level. (Exp. indicates experimental absorption; Cal. means calculated absorption).....	105
Figure IV-4: Emission spectra of the four molecules under study in DCM solution with concentrations as indicated.....	105
Figure IV-5: Normalized absorption and excitation spectra of Bz(T ₁ CAO) ₂ in dichloromethane (left) and of Bz(T ₂ CAR) ₂ in DCM (right).	106
Figure IV-6: Normalized absorption spectra of Bz(T ₁ CAO) ₂ and Bz(T ₁ CAEH) ₂ in thin film in DCM solution.....	107
Figure IV-7: UV-vis absorption spectra of Bz(T ₁ CAEH) ₂ film spin coated from chlorobenzene solution at room temperatures and annealed as indicated. The film was sequentially annealed at increasing temperature for 20 minutes.....	108
Figure IV-8: Normalized absorption spectra of pure P3HT, Bz(T ₁ CAO) ₂ and Bz(T ₁ CAEH) ₂ and 1:1 wt. blends in thin films.	109
Figure IV-9: Cyclic voltammetry of Bz(T ₁ CAO) ₂ in 0.1 M PF ₆ TBA dichloromethane solution; Pt electrode; scan rate = 200 mV.s ⁻¹	109
Figure IV-10: Cyclic voltammetry of Bz(T ₂ CAEH) ₂ in 0.1 M PF ₆ TBA dichloromethane solution; Pt electrode; scan rate = 200 mV.s ⁻¹	110
Figure IV-11: Diagram of the energy levels for the investigated molecules, P3HT and PCBM, estimated <i>via</i> electrochemical measurements. (All values have been measured in our laboratory in the same experimental conditions; <i>Calc.</i> represents calculated result)	111
Figure IV-12: Cyclic voltammogram of pristine P3HT, Bz(T ₁ CAO) ₂ , Bz(T ₁ CAEH) ₂ films and blend P3HT:Bz(T ₁ CAO) ₂ (1:1 wt.) and blend P3HT:Bz(T ₁ CAEH) ₂ (1:1 wt.) in 0.1 M PF ₆ TBA acetonitrile solution; Pt electrode; scan rate = 50 mV.s ⁻¹	112
Figure IV-13: Outline plot showing the evaluated energy-conversion efficiency (contour lines and colours) versus the band gap and LUMO level of the donor based on Scharber model. A schematic energy diagram of a donor/PCBM system with the band gap energy (E _g) and the energy offset (ΔE) is also given.(61) Red cross indicates the ideal efficiency of Bz(T ₂ CAR) ₂ used as the donor with PCBM as the acceptor. Red point indicates the ideal efficiency of BzT ₂ CAO used as the donor with PCBM as the acceptor.	114
Figure IV-14: TGA plot of studied molecules with a heating rate of 10 °C/min under N ₂ atmosphere.	115
Figure IV-15: DSC thermograms of the molecules upon third heating and cooling cycles, measured at 10°C/min under nitrogen atmosphere.	116
Figure IV-16: SAXS pattern of Bz(T ₁ CAO) ₂ at 150°C, in the sanidic type smectic A phase.	117
Figure IV-17: POM images of (a) the batonnet-like texture of Bz(T ₁ CAO) ₂ at 183°C, (b) the SmA phase of Bz(T ₁ CAO) ₂ at 170°C and (c) the smectic phase observed at 85°C.....	118
Figure V-1: ¹ H NMR spectrum of Bz(T ₁ CHO) ₂ in CDCl ₃ (top) and ⁶ d DMSO (down).....	125
Figure V-2: ¹ H NMR spectrum Bz(T ₁ CHO) ₂ in CDCl ₃ (top) and ⁶ d DMSO (down).....	127

Figure list

Figure V-3: ^1H NMR spectrum of $\text{Bz}(\text{T}_1\text{CAO})_2$	128
Figure V-4: ^1H NMR spectrum of $\text{Bz}(\text{T}_1\text{CAEH})_2$	129
Figure V-5: ^1H NMR spectrum of $\text{Bz}(\text{T}_2\text{CAO})_2$	130
Figure V-6: ^1H NMR spectrum of $\text{Bz}(\text{T}_2\text{CAEH})_2$	131
Figure V-7: ^1H NMR spectrum of BzT_2CAO	135
Figure V-8: ^1H NMR spectrum of phenoxy-SubPc.....	137

Scheme list

Scheme list

Scheme II-1: Synthesis strategies designed for obtaining Bz-based small molecules (R= octyl cyanoacete and 2-ethylhexyl cyanoacetate).	51
Scheme II-2: Chemical structures of designed target molecules based on DTS core.	54
Scheme II-3: Synthesis routes to obtain precursors for DTS-based target molecules.	55
Scheme II-4: General procedure to synthesize the DTS cores for the target molecules.	56
Scheme II-5: Envisaged synthesis routes for Bz-based fragments <i>via</i> direct arylation.	56
Scheme II-6: Designed SubPcs derivatives and synthesis strategies <i>via</i> axial substitution.	60
Scheme III-1: Classical coupling (Route a) to molecule Bz(T ₁ CHO) ₂	83
Scheme III-2: Direct arylation Route b to molecule Bz(T ₁ CHO) ₂	83
Scheme III-3: Direct arylation Route c to molecule Bz(T ₁ CHO) ₂	83
Scheme III-4: Classical (top) and new (bottom) routes to molecule Bz(T ₂ CHO) ₂	85
Scheme III-5: Different strategies to synthesize fragment BrBzT ₁ CHO.	90
Scheme III-6: Other protocols to obtain fragment BrBzT ₁ CHO.	92
Scheme III-7: Synthetic route to obtain fragment BrBzT ₂ CHO.	93
Scheme III-8: Strategy to obtain non-symmetric molecule BzT ₂ CAO.	93
Scheme III-9: General procedures to synthesize the DTS cores for the target molecules.	94
Scheme III-10: One strategy supposed to obtain DTS(BzT ₂ CHO) ₂	95
Scheme III-11: Second strategy for obtaining DTS(BzT ₂ CHO) ₂	96
Scheme III-12: The strategy for obtaining DTS(TBzT ₁ CHO) ₂	96
Scheme III-13: Synthesis route to SubPcBCl.	97
Scheme III-14: Synthesis route to phenoxy-SubPc.	98

Table list

Table list

Table I-1: Electronic properties and OPV performance of some typical polymer-based donors.	30
Table I-2: Electronic properties and OPV performance of some typical small molecular donors.	34
Table I-3: Electronic properties and OPV performance of typical fullerene and its derivatives as acceptors.	35
Table I-4: Electronic properties and OPV performance of some typical non-fullerene acceptors.	38
Table II-1: Electronic properties and OPV performance of some typical donors based on dithienosilole core.	53
Table II-2: Performance of some OPV devices based on SubPcs.	59
Table II-3: Total energy, orbital energy levels and dihedral angles of diTBz.	61
Table II-4: Dihedral angles (°) in Bz(T ₁ CAMe) ₂ , Bz(T ₂ CAMe) ₂ , Bz(T ₃ CAMe) ₂ and Bz(T ₄ CAMe) ₂	63
Table II-5: Theoretical open-circuit voltage and energy offset in blends of Bz(T ₁ CAMe) ₂ , Bz(T ₂ CAMe) ₂ , Bz(T ₃ CAMe) ₂ and Bz(T ₄ CAMe) ₂ with PCBM.	66
Table II-6: Dihedral angles (°) in ffBz(T ₁ CAMe) ₂ , ffBz(T ₂ CAMe) ₂ , ffBz(T ₃ CAMe) ₂ and ffBz(T ₄ CAMe) ₂	68
Table II-7: Dihedral angles (°) in DTS(BzT ₂ CAMe) ₂ and DTS(TBzT ₁ CAMe) ₂	71
Table III-1: Reaction yields, E-factors and costs calculated for Bz(T ₁ CHO) ₂ obtained <i>via</i> the three investigated routes.	86
Table III-2: Reaction yields, E-factors and costs calculated for the synthesis of Bz(T ₁ CHO) ₂ obtained <i>via</i> Route c with decreasing the TCHO/diBrBz ratios (r).	87
Table III-3: Reaction yields, E-factors and costs calculated for Bz(T ₂ CHO) ₂ obtained <i>via</i> Route a and Route c.	87
Table III-4: Reaction yields for Knoevenagel condensation, and total E-factors and costs calculated for the target molecules obtained <i>via</i> Route c followed by Knoevenagel condensation.	88
Table IV-1: Optoelectronic properties of the target molecules.	111
Table IV-2: Electronic properties of pristine P3HT, Bz(T ₁ CAO) ₂ , Bz(T ₁ CAEH) ₂ films and blend P3HT:Bz(T ₁ CAO) ₂ (1:1 wt.) and blend P3HT:Bz(T ₁ CAEH) ₂ (1:1 wt.).	113
Table V-1: Yields for molecule Bz(T ₁ CHO) ₂ obtained from different Route c conditions. ...	124
Table V-2: Yields for BrBzT ₁ CHO obtained from different Route b conditions.	132
Table V-3: Yields for BrBzT ₁ CHO obtained from different Route c (i) conditions.	133

Table list

Table V-4: Yields for BrBzT₁CHO obtained from different Route c (ii) conditions..... 133

Table V-5: Yields for SubPcBCl obtained from different conditions..... 136

Résumé de thèse

Résumé de thèse

INTRODUCTION GENERALE

L'énergie est aujourd'hui un problème important et urgent auquel nous devons faire face, la demande mondiale en énergie renouvelable étant en croissance constante. Les combustibles fossiles tels que le pétrole, le gaz, le charbon et d'autres énergies non renouvelables sont actuellement les principales sources d'énergie. Leur production et leur combustion sont devenues un problème sérieux pour notre environnement, en raison des fortes émissions en dioxyde de carbone (CO₂), constituant un facteur clé du réchauffement climatique. Les combustibles fossiles ne sont pas en mesure de satisfaire nos besoins futurs en énergie car leurs ressources sont limitées, ce qui conduit à un besoin urgent de sources d'énergie propres, renouvelables et durables. Atteindre cet objectif est l'un des plus grands défis de l'humanité.

Le soleil peut constituer pour notre planète une source inépuisable et infinie de l'énergie : la Terre reçoit suffisamment d'énergie solaire chaque heure pour satisfaire la demande annuelle en énergie de l'homme. L'énergie solaire irradiée en surface de la Terre représente par année le double de l'énergie de toutes les sources fossiles et de l'énergie nucléaire. L'énergie solaire est donc une alternative prometteuse à ces sources d'énergie non renouvelables et pourrait contribuer à répondre à notre demande croissante en énergie.

Les cellules photovoltaïques organiques (cellules OPV) permettent de réaliser la conversion de l'énergie solaire en énergie électrique. Elles font partie d'une des stratégies à long terme les plus prometteuses pour fournir de l'énergie propre et renouvelable à notre planète. Les cellules OPV constituent des candidats prometteurs, en raison de leurs excellentes propriétés, telles que la facilité de fabrication, leur flexibilité mécanique, et leur potentiel comme source potentielle d'énergie renouvelable et verte à faible coût.(1-5) Récemment, un rendement de conversion en puissance (PCE) de 13.2% pour une cellule OPV multi-jonction a été atteint par la Société Heliatek.(6) Le développement et la synthèse de nouveaux matériaux organiques pour leur utilisation dans la couche active, de même que les progrès technologiques dans le domaine de la fabrication des dispositifs OPV à haute performance, sont d'une grande importance. Les petites molécules pour l'OPV ont récemment émergé comme alternative pertinente à leurs homologues polymères, en raison de leurs structures chimiques bien définies, plus faciles d'accès avec une grande pureté et permettant un contrôle plus aisé de leurs caractéristiques électroniques.

Les travaux rapportés ici se concentrent sur le développement et la synthèse de petites molécules pour l'OPV. La motivation ultime est d'obtenir des petites molécules originales pour leur utilisation comme matériaux actifs par voie de synthèse verte, de façon aussi simple que possible. Dans ce travail, nous avons étudié quelques nouveaux matériaux, depuis leur conception initiale à la synthèse et à la caractérisation.

CHAPITRE I : BIBLIOGRAPHIE

Dans cette revue bibliographique concise et ciblée, nous présentons le principe de fonctionnement et caractérisations importantes des cellules OPV, et les différents types de dispositifs avant de nous concentrer sur les matériaux actuels les plus performants :

Comme décrit simplement la Figure I, une telle cellule est constituée de deux matériaux semi-conducteurs organiques, respectivement donneur (D) et accepteur (A) d'électrons. La conversion de la lumière du soleil en électricité dans une cellule photovoltaïque organique peut être décrite comme un processus en quatre étapes: (27,55) (i) absorption d'un photon et génération d'un exciton (paire électron-trou); (ii) diffusion de l'exciton à l'interface D/A; (iii) dissociation de l'exciton en porteurs de charge libres (électrons et trous), et (iv) transport et collecte des charges aux électrodes, générant un courant électrique dans le circuit externe. Chacune des quatre étapes intervenant de façon cruciale dans le processus global, il convient de les optimiser par le choix de matériaux D et A stables qui devront participer de façon la plus active possible à l'absorption de la lumière, posséder des niveaux d'énergie en faveur de la dissociation des charges, s'organiser en film mince de façon à favoriser le transport des charges et transférer aux électrodes les charges générées.

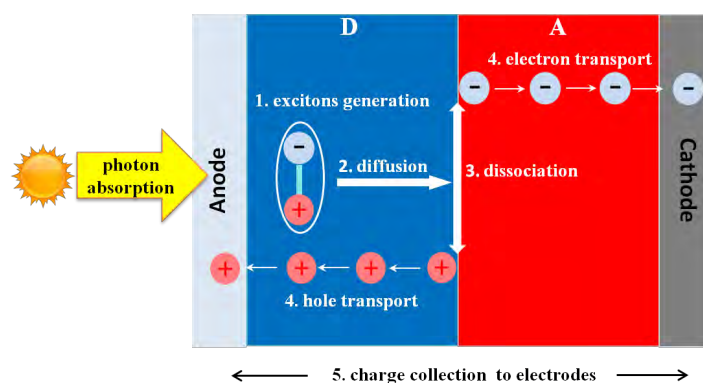


Figure 1: Principe de fonctionnement d'une cellule organique à hétérojonction donneur/accepteur.

Les performances des cellules prototypes sont évaluées par tracé de leurs caractéristiques électriques (courbes I(V)) comme représenté en Figure 2, dans le noir et sous illumination avec un simulateur solaire.

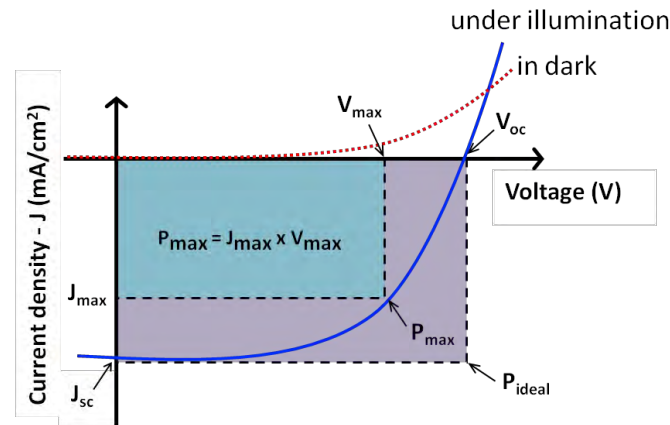


Figure 2: Courbes I(V) dans le noir et sous illumination d'une cellule OPV.

L'analyse des courbes obtenues permet d'évaluer le rendement de conversion en puissance (PCE) qui s'exprime selon la relation :

$$PCE = P_{max} / P_{in} = (FF \times J_{sc} \times V_{oc}) / P_{in}$$

Où P_{max} est la puissance maximale créée dans le circuit externe ; celle-ci est déduite du produit de J_{sc} (courant mesuré sous illumination à tension nulle), de V_{oc} (tension mesurée sous illumination à courant nul) et de FF (facteur de forme) qui traduit la qualité de la réponse en I(V) du composant, déterminé par le rapport de la surface bleue et de la surface violette de la Figure 2.

Les cellules OPV sont conçues selon différentes architectures, principalement en structure bicouche (ou planaire) ou en mélange en volume (BHJ), en cellule simple ou en cellule tandem. La première cellule photovoltaïque organique décrite était constituée d'une bicouche délivrant un rendement de conversion proche de 1%.⁽¹⁾ Ce premier résultat a ouvert la voie vers de nombreux travaux, les meilleures performances actuelles approchant les 10 à 11 %.

Parmi les matériaux utilisés en OPV, on distingue principalement les polymères et les petites molécules, leurs performances record respectives étant aujourd'hui similaires en termes de PCE, des améliorations étant attendues en termes de stabilité, en particulier pour les petites molécules. Les structures chimiques de matériaux polymères et des petites molécules utilisés comme donneurs d'électrons sont illustrées en Figure 3, celles des matériaux accepteurs d'électrons sont données en Figure 4.

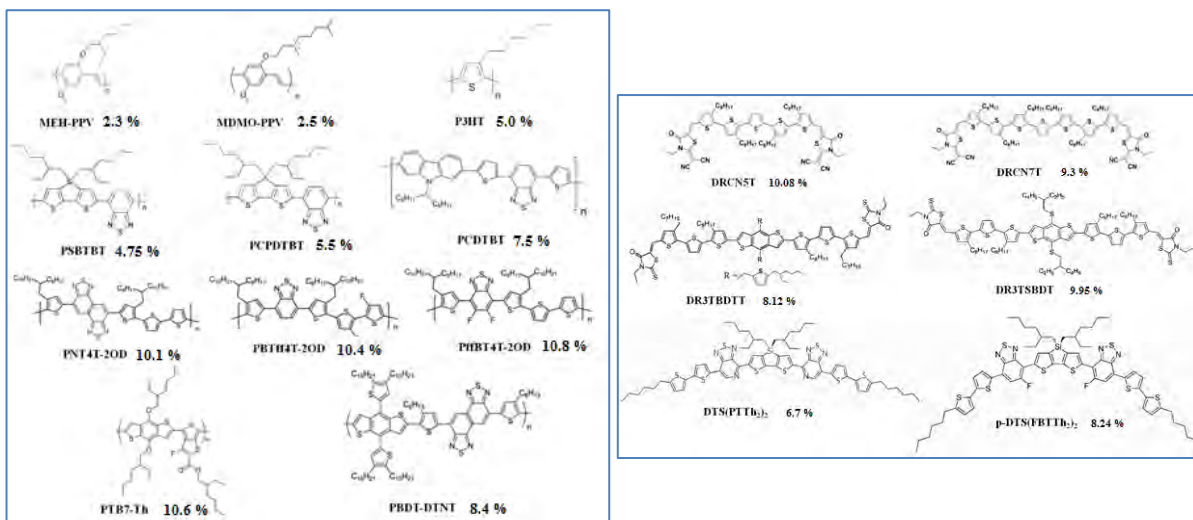


Figure 3: Structures chimiques de polymères (gauche), et petites molécules (droite) donneurs d'électrons et de dérivés du fullerène (bas) et PCE associés.

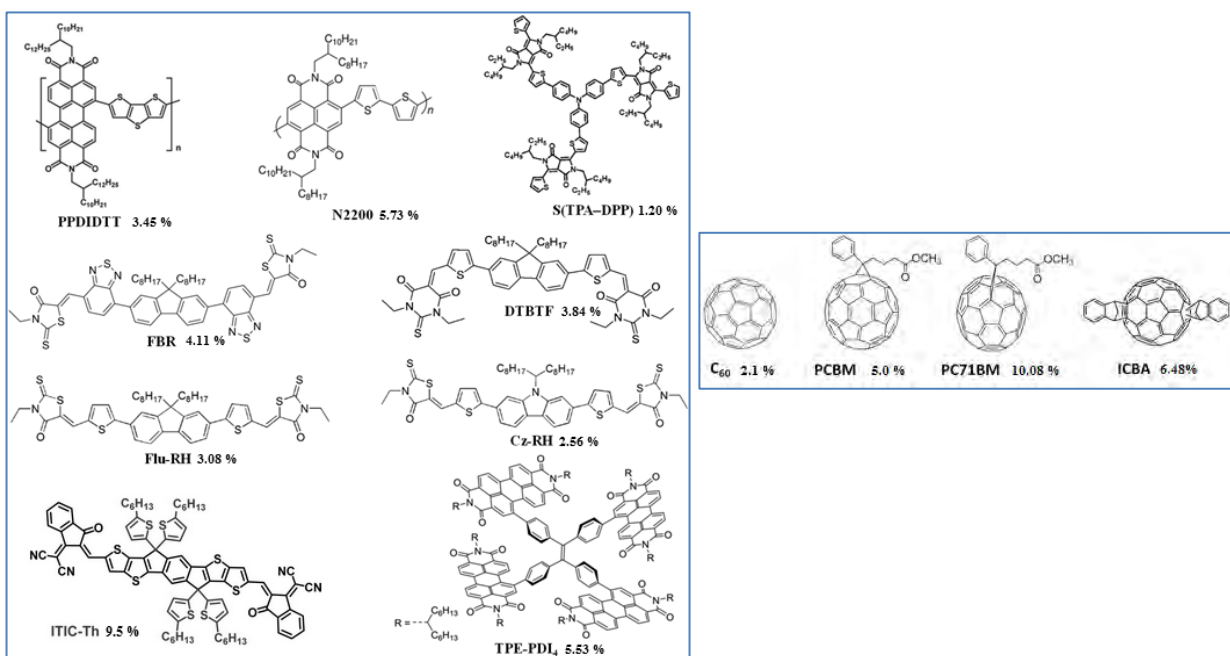


Figure 4: Structures chimiques de matériaux accepteurs d'électrons non-fullerène (gauche) et de dérivés du fullerène (droite) et PCE associés.

Un résumé des performances de différents semi-conducteurs organiques utilisés comme donneurs d'électrons dans les cellules OPV est donné en Figure 5, les matériaux organiques utilisés comme accepteurs délivrant actuellement des rendements record de l'ordre de 9.5%.⁽¹⁶⁵⁾ Ces progrès remarquables encouragent les chimistes à concevoir et synthétiser de nouveaux matériaux conjugués. Dans ce contexte, notre but était de proposer de nouvelles petites molécules. Selon la littérature, abondante dans ce sujet, les structures de type « push-

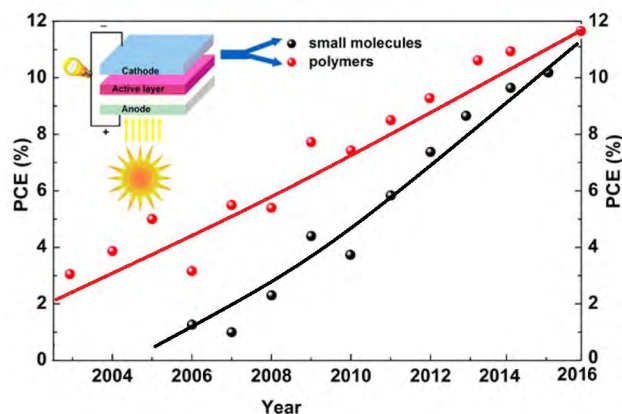


Figure 5: Evolution comparée depuis 2003 des performances des cellules OPV respectivement à base de matériaux polymères et de petites molécules, utilisés comme donneurs d'électrons.(19,21,30,94,156)

pull » permettent d'obtenir des molécules à propriétés physiques et optoélectroniques idéales pour l'OPV. Nous avons par conséquent choisi d'explorer cette voie. Nous avons en premier lieu réalisé une étude théorique en collaboration avec le Laboratoire de Chimie et Physique Quantiques (LCPQ) sur des molécules virtuelles, afin de préciser leurs propriétés structurales et électroniques et avant d'en entreprendre la synthèse, puis de les caractériser. Cela fait l'objet des chapitres suivants.

CHAPITRE II : CONCEPTION DES MOLECULES

Une méthode de conception moléculaire, très classiquement utilisée, consiste à imaginer des nouvelles molécules sur la base de la bibliographie, d'en réaliser la synthèse puis de les tester en cellule OPV. L'inconvénient majeur de cette méthode est qu'elle est coûteuse en temps et en moyens pour un résultat non garanti.

Une autre stratégie récemment proposée consiste à réaliser un criblage virtuel à grande échelle par calculs théoriques. C'est précisément l'objet du projet « Clean Energy Project » (CEP),(187-189) initié en 2008 par le groupe d'Alán Aspuru-Guzik de l'Université de Harvard et soutenu par de nombreux contributeurs et collaborateurs externes.(190,191) Selon ce projet, 26 blocs génériques, constitués de cycles ou hétérocycles aromatiques, ont été utilisés pour générer 2,3 millions de motifs moléculaires, tous virtuels, constituant une base de données de référence massive concernant des matériaux semi-conducteurs organiques pour une application en photovoltaïque organique.(192) Les performances des molécules virtuellement générées ont été évaluées en OPV par calculs théoriques : leurs structures ont été optimisées, puis les niveaux de leurs orbitales frontières calculés. Enfin, à l'aide du modèle de Scharber,(61) les performances de composants constitués de ces molécules,

considérées comme donneuses d'électrons, associées au PCBM comme accepteur d'électrons, ont été évaluées. Parmi les 2.3 millions de molécules virtuelles étudiées, environ 1000 auraient la capacité à mener à un PCE supérieur à 11%, la majorité des candidats menant à un PCE inférieur à 4%.⁽¹⁸⁸⁾ Toutefois, il convient de souligner que la plupart des candidats prometteurs seraient difficiles (voire impossible) à synthétiser en raison de leur complexité structurale (hétérocycles complexes fusionnés). De plus, l'ajout de chaînes alkyles indispensable à rendre solubles ces molécules virtuelles constitue une difficulté de synthèse supplémentaire non négligeable. Parmi les 26 blocs de base, le 4,7-dibromobenzo-2,1,3-thiadiazole (diBrBz) figure parmi les fragments menant aux candidats les plus prometteurs, ce qui pourrait être un guide dans la conception de nos molécules. Par ailleurs, nous constatons que la majorité des structures moléculaires générées sont asymétriques, alors que généralement les molécules synthétisées, testées en OPV et décrites dans la littérature sont symétriques, pour des raisons de synthèse, principalement.

Des investigations théoriques avancées d'une tout autre nature ont été réalisées afin d'étudier les interactions à l'interface d'un système bicouche, pour en donner une représentation visuelle simple et pédagogique. Ainsi, les groupes de Cantrell (195-197) et de Brédas (194) ont étudié en détail les interactions entre le fullerène (C₆₀) et le pentacène par modélisation en dynamique moléculaire. Les résultats obtenus décrivent la complexité morphologique à l'interface de la couche active qui affectera le processus électronique au cours de l'effet photovoltaïque. D'autre part, des simulations de morphologie réalisées à l'aide du modèle de Monte Carlo ont prédit l'importance de la qualité de la morphologie d'un mélange donneur-accepteur sur les performances de cellules de type BHJ (198).

Tous ces travaux théoriques nous donnent des pistes pour la conception des molécules futures, aussi bien du point de vue moléculaire, grâce à des descriptions structurales moléculaires avancées, que du point de vue du matériau avec des descriptions théoriques des interfaces et des morphologies de plus en plus fines.

Pour notre part, sur la base d'une synthèse bibliographique (partie II.5-4 du chapitre I), nous proposons ici des nouvelles structures moléculaires que nous avons soumises à des calculs théoriques dans le but d'anticiper les niveaux d'énergie de leurs orbitales frontières (HOMO et LUMO) et de valider leur utilité potentielle en OPV. Cette validation obtenue, nous pourrions alors envisager de les synthétiser. Ces dernières années, de nombreux efforts ont été consacrés à la conception et à la synthèse de petites molécules ou polymères à faible largeur de bande interdite et conçus selon une alternance de fragments donneur et accepteur (D/A). Nous avons suivi cette stratégie afin d'obtenir des matériaux absorbant fortement dans

la région visible et proche infrarouge du spectre solaire.(199-201) Pour des raisons de facilité synthétique, nous avons ciblé des petites molécules symétriques dont la synthèse comporte peu d'étapes intermédiaires, 2 à 3 étapes s'avérant être un minimum. Les calculs, effectués avec le programme OCRA (183) utilisant la théorie fonctionnelle de densité (DFT) (184), ont pour but principal d'évaluer les niveaux d'énergie des orbitales frontières (HOMO et LUMO) de ces molécules cibles. Ils ont été conduits sur une série de petites molécules à base de benzothiadiazole (Bz), de 4,4'-di-n-octyl-dithiénylsilane (ou dithiénylsilane, DTS) et de subphthalocyanines (SubPcs). Les molécules étudiées (voir Figure 6) ici sont de trois types, leurs structures ainsi que les voies de synthèses envisagées sont présentées:

- Centrées sur le fragment benzothiadiazole, avec structures symétriques simples de type A-D-A-D-A.
- Centrées sur le fragment dithiénylsilane (DTS), ce dernier étant un donneur d'électron reconnu pour sa stabilité chimique et fréquemment utilisé dans les matériaux efficaces en OPV (206-209,144). Nous avons proposé les structures de type A-D-A-D-A-D-A, plus étendues que les précédentes.
- A base de subphthalocyanine (SubPc), qui se sont révélé être de bons matériaux donneurs (252-255) ou accepteurs (256) d'électrons pour des applications en OPV (216,218).

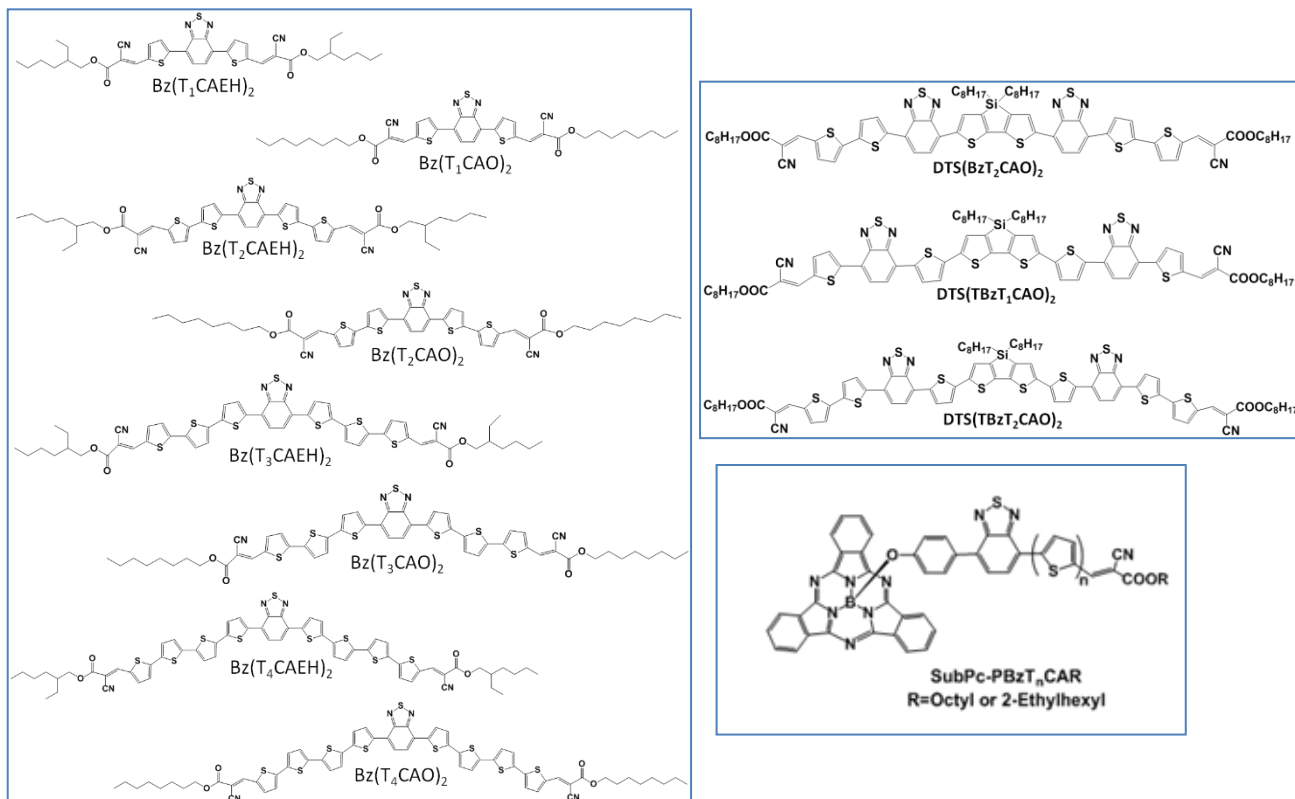


Figure 6: Structures molécules à base de benzothiadiazole (gauche), de dithiénylsilane (haut droite) et de subphthalocyanine (bas droite).

Une fois ces molécules conçues, des calculs théoriques ont été effectués pour prédire leurs propriétés électroniques. Les méthodes DFT (184) et TD-DFT (266-268) sont couramment utilisées et les résultats obtenus présentent de bon accords avec les résultats expérimentaux.(269, 270) Ainsi, pour prédire les propriétés électroniques de toutes les molécules conçues ci-dessus, nous avons effectué tous les calculs en utilisant la méthode DFT au niveau B3LYP/Def2-TZVP (-f). Pour faciliter le calcul, les chaînes terminales octyles (O) ou 2-éthylhexyle (EH) ont été remplacées par des groupes méthyle (Me).

Les structures des molécules centrées sur le fragment benzothiadiazole ont été modélisées, la conformation des molécules et les angles dièdres entre les différents fragments ont été discutés. Il ressort de cette étude que les molécules cibles présentent des énergies d'orbitales frontières HOMO et LUMO compatibles avec une utilisation en qualité de donneurs d'électrons en association avec le PCBM comme accepteur. Les principaux résultats, ainsi que les paramètres OPV calculés selon le modèle de Scharber(61) pour des dispositifs conçus avec ces matériaux, ont été consignés dans le tableau suivant :

Tableau 1: Energies des orbitales frontières HOMO et LUMO des molécules, tension de circuit ouvert (V_{oc}) et différence d'énergies des niveaux LUMO des molécules et du PCBM pour des dispositifs conçus à base de ces molécules associées au PCBM comme accepteur d'électron.

	HOMO	LUMO	V_{oc} (V)	ΔE (eV)
Bz(T ₁ CAMe) ₂	-6.29	-3.89	1.7	0.4
Bz(T ₂ CAMe) ₂	-5.79	-3.64	1.2	0.66
Bz(T ₃ CAMe) ₂	-5.56	-3.51	0.96	0.8
Bz(T ₄ CAMe) ₂	-5.37	-3.39	0.77	0.9

Des calculs similaires ont été conduits sur les molécules à base de DTS. Ces molécules étant beaucoup plus complexes que les précédentes (voir Figure 7), les calculs nécessaires nécessitent des temps plus long pour en optimiser la géométrie puis, par calculs de fréquence de vibration, vérifier que nous avons bien atteint bien un minimum d'énergie moléculaire correspondant à l'état fondamental le plus stable. Les calculs actuels n'ont pas encore, de notre point de vue, atteint tout à fait leur terme, mais nous pouvons estimer que les structures calculées sont actuellement très proches de structures à l'état fondamental, ce qui nous permet d'ores et déjà d'avoir une vision claire de l'influence de la longueur de conjugaison sur la

structure moléculaire. En particulier, nous avons examiné l'effet de l'extension moléculaire sur les torsions des structures suivantes, les valeurs des angles étant données dans le Tableau 2 :

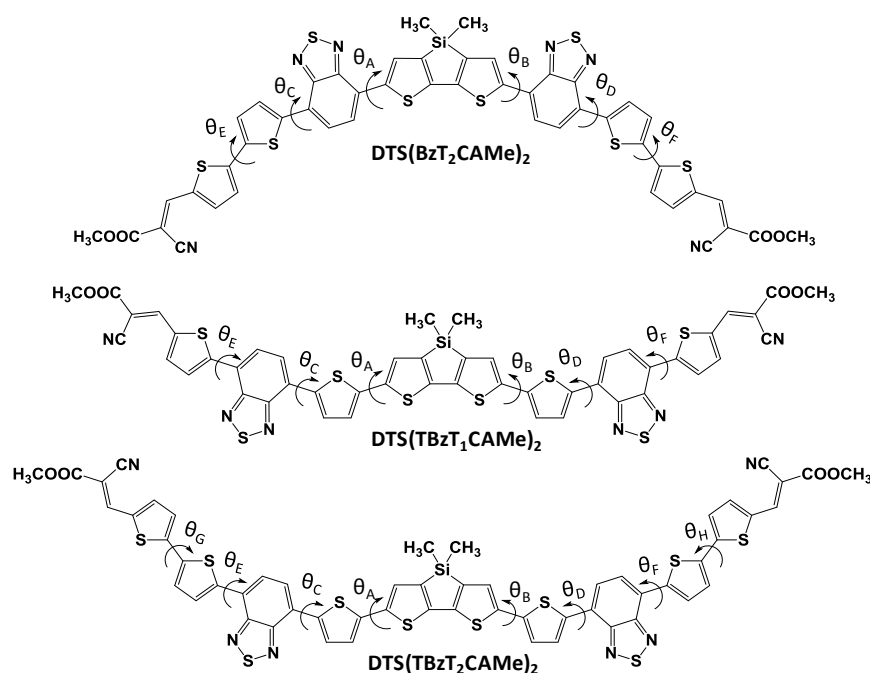


Figure 7: Structures des molécules étudiées et angles dièdres examinés.

Tableau 2: Valeurs calculées des angles dièdres.

	θ_A	θ_B	θ_C	θ_D	θ_E	θ_F	θ_G	θ_H
DTS(BzT ₂ CAMe) ₂	0.48	0.56	1.02	1.01	0.27	0.37		
DTS(TBzT ₁ CAMe) ₂	4.43	4.36	0.26	0.60	7.00	1.42		
DTS(TBzT ₂ CAMe) ₂	*	*	*	*	*	*	*	*

* données non disponibles actuellement pour des raisons de durée de calcul.

De ces résultats, il ressort que les structures modélisées des molécules sont relativement planaires, les angles dièdres entre les cycles constitutifs étant en général faibles. Cela est très certainement lié à la structure de type A-D de ces composés qui possèdent une conjugaison de type π très marquée. De la même façon que précédemment, les paramètres électroniques de ces composés ont également été évalués. Il s'avère que les énergies de leurs orbitales frontières sont très proches, de l'ordre de -5.35 eV pour l'énergie de la HOMO et de -3.6 eV pour l'énergie de la LUMO, leur gap électronique étant de l'ordre de 1.8 eV. Ces valeurs sont très proches de celles d'un composé donneur idéal, selon le modèle de Scharber,

qui préconise comme valeurs optimisées d'énergie de HOMO et LUMO respectivement -5.4 eV et -3.9 eV. Ces résultats nous encouragent par conséquent à poursuivre ce travail par la réalisation de la synthèse de ces molécules.

Des composés à base de SubPc ont également fait l'objet d'investigations théoriques : pour cela, nous avons considéré le fragment SubPc chloré dont nous avons substitué l'atome de chlore par un fragment axial, aucune substitution n'étant envisagée en position périphérique de la subphthalocyanine. Le choix des substituants axiaux a été guidé par le travail effectué sur les molécules précédemment envisagées, en tenant compte des contraintes synthétiques liées aux structures ciblées : les chloro-subphthalocyanines de bore subissent de façon relativement aisée une substitution de l'atome de chlore par le phénol et ses dérivés, les molécules obtenues étant généralement stabilisées photochimiquement.(186) Nous avons par conséquent envisagé d'introduire en position para- du phénol un fragment Bz(T)_nCAMe, les structures des substituants ciblés étant présentées dans la figure suivante :

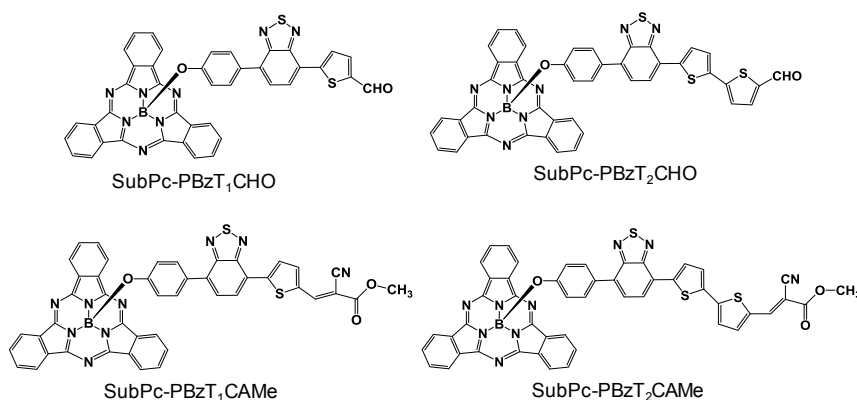
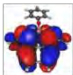
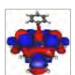

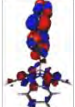
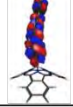
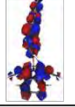

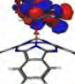

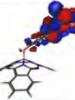


Figure 8: Structure des substituants axiaux de la chloro-subphthalocyanines de bore

Les calculs effectués sur ces molécules sont résumés dans le tableau 3. Nous avons considéré, pour comparaison, la molécule simple de SubPc substituée par le phénol, nommée « Phenoxy-SubPc » : les calculs révèlent que dans ce cas les deux orbitales frontières, HOMO et LUMO, sont centrées sur le fragment SubPc. La situation est différente dans le cas de nos molécules : la HOMO est centrée sur la SubPc sauf pour SubPc-PBzT₂CHO où elle est centrée sur le substituant axial, certainement grâce à la présence du fragment bithiophène. Plus intéressant encore, le déplacement de la LUMO vers le substituant axial est observé pour nos molécules, de façon sensible dans le cas des intermédiaires porteurs de la fonction aldéhyde terminale, et de façon exclusive dans le cas des molécules cibles porteuses de fonction alkyle cyanoacétate terminale. Nous constatons ici l'effet électro attracteur du substituant axial. Les cas rapportés dans la littérature où la HOMO est centrée uniquement sur la SubPc et la LUMO uniquement

sur le substituant axial sont très rares (262). Ainsi, dans la même molécule, le fragment SubPc peut jouer le rôle de donneur d'électron, et le substituant axial peut jouer le rôle d'accepteur d'électron. Cette propriété quasi-unique des molécules cibles proposées dans ce travail ouvre par conséquent la voie vers des composés originaux qui, à l'état excité, peuvent présenter des états de charges séparées favorables aux processus photovoltaïques.

Tableau 3: Orbitales frontières et propriétés électroniques des petites molécules à base de SubPcs calculées par DFT.

	HOMO	LUMO	HOMO/LUMO (eV)	E_g (eV)
Phenoxy-SubPc			-5.44/-2.72	2.72
SubPc-PBzT ₁ CHO			-5.59/-2.93	2.67
SubPc-PBzT ₂ CHO			-5.51/-2.90	2.61
SubPc-PBzT ₁ CAMe			-5.56/-3.23	2.33
SubPc-PBzT ₂ CAMe			-5.59/-3.19	2.40

En résumé, trois séries de petites molécules très différentes, de très faibles masses moléculaires à base de BZ, de taille plus conséquente à base de DTS, et à base de SubPc de bore, ont été conçues et étudiées par des calculs théoriques, leurs géométries et propriétés électroniques ayant été explorées. Selon le diagramme des niveaux d'énergie de leurs orbitales frontières, donné en Figure 9, chacune de ces molécules peut être un candidat prometteur pour une utilisation en cellule OPV.

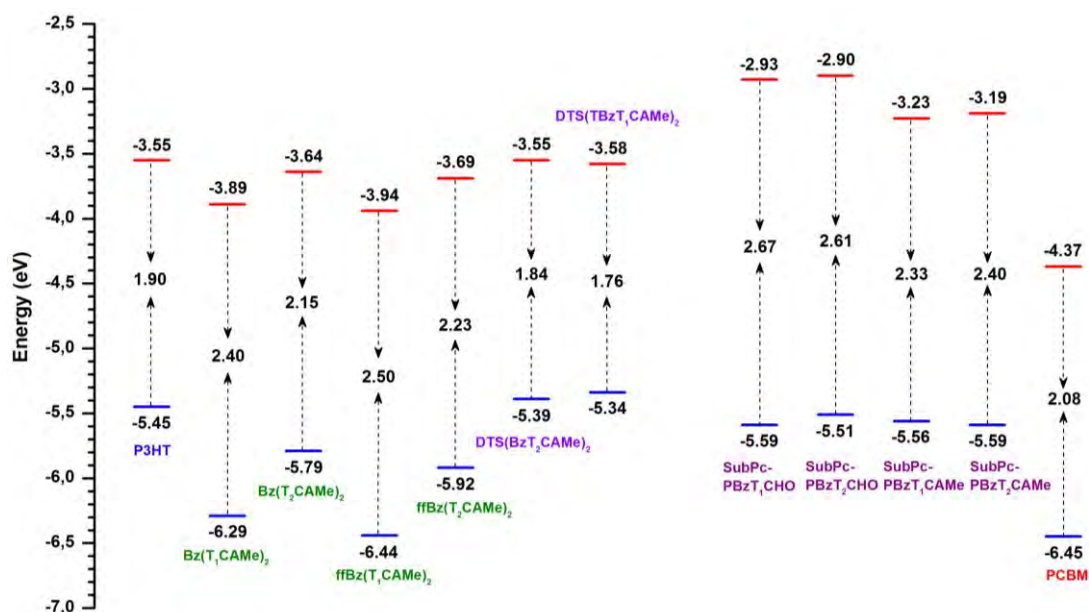


Figure 9: Diagramme d'énergie des orbitales frontières des molécules cible.

Pour ce qui concerne leur synthèse, les molécules à base de Bz peuvent être obtenues en seulement deux étapes, les molécules à base de DTS peuvent être obtenues en trois étapes au minimum et les molécules à base de SubPc pourraient être obtenues en quatre étapes au minimum. Les deux derniers types de molécules nécessitent pour leur synthèse des fragments non symétriques intermédiaires (en particulier le fragment Bz-thiophène), ce qui rend leur obtention plus difficile. C'est pourquoi nous avons choisi de synthétiser dans un premier temps des molécules à base de Bz, puis des molécules à base DTS, et enfin des molécules à base de SubPc. Les détails de ces synthèses sont présentés dans le chapitre suivant.

CHAPITRE III : SYNTHÈSE DES MOLECULES PAR UNE APPROCHE CHIMIE VERTE

Le troisième chapitre décrit les méthodes synthétiques utilisées pour les molécules préalablement conçues. En particulier, nous décrivons l'emploi de l'arylation directe comme approche synthétique appartenant à la chimie verte.

Parmi les molécules à base de Bz présentées précédemment, nous avons choisi de synthétiser Bz (T₁CAO)₂, Bz (T₁CAEH)₂, Bz (T₂CAO)₂ et Bz (T₂CAEH)₂ parce qu'elles sont isolables en deux étapes. Leurs précurseurs Bz(T₁CHO)₂ et Bz (T₂CHO)₂ peuvent être obtenus à partir de réactifs disponibles dans le commerce, tels que diBrBz, et TCHO T₂CHO.

Trois protocoles de synthèse pour l'obtention des molécules intermédiaires $Bz(T_1CHO)_2$ et $Bz(T_2CHO)_2$ ont été comparés: i) le couplage de Suzuki classique (ci-après appelé **Voie a**) utilisant un intermédiaire boronylé qui est assez coûteux et génère des déchets polluants, ii) une procédure d'hétéroarylation directe (**Voie b**) conduite sans réactif organométallique ni composé boronylé intermédiaire, mais nécessitant un catalyseur au palladium, des ligand de type phosphine et de l'acide pivalique en combinaison avec du carbonate de potassium, enfin, iii) la procédure directe hétéroarylation (**Voie c**) procédant sans ligand ni acide pivalique, mais uniquement avec de l'acétate de palladium comme catalyseur et de l'acétate de potassium comme base. Ces protocoles sont présentés en Schéma 1 :

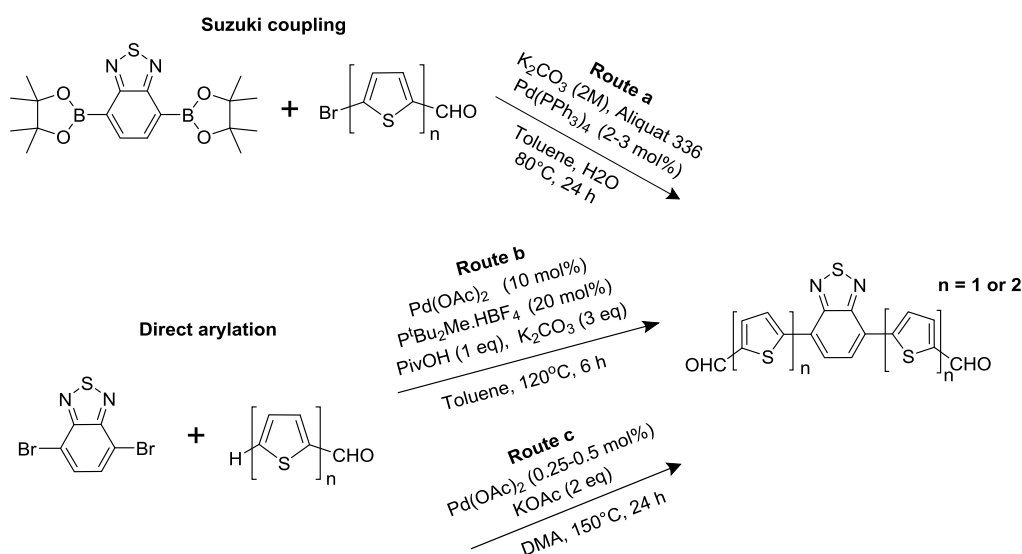


Schéma 1: Protocoles utilisés pour la synthèse des intermédiaires $Bz(T_1CHO)_2$ et $Bz(T_2CHO)_2$.

Les rendements globaux et le E-facteur (masse de déchets/masse de produit) sont des paramètres de chimie « verte » quantifiables utilisées pour évaluer l'impact environnemental associé à la production de matières organiques pour des applications durables. (311, 312) Ces grandeurs ont été évaluées pour les molécules élaborées (voir le tableau 4). Une amélioration conséquente du E-Facteur est obtenue pour l'arylation directe sans ligand (**Voie c**). Ce procédé implique une faible quantité de catalyseur (0.5 % mole d'acétate de palladium) et l'absence de tout additif, menant par conséquent à un protocole très simple avec un E-facteur de 143g/g, qui représente environ un tiers de celui obtenu à partir des deux autres voies. En outre, le coût de $Bz(T_1CHO)_2$ est considérablement réduit. Cela représente une grande amélioration en termes de production et le coût des déchets pour la synthèse de cet

intermédiaire. La même tendance est observée concernant l'intermédiaire $Bz(T_2CHO)_2$ qui est obtenu *via* la **Voie c** avec un E-Facteur de 76 et un coût de 40 €/g.

Tableau 4: Rendements de réaction, E-facteurs et coûts calculés pour $Bz(T_1CHO)_2$ obtenus pour les trois voies explorées.

	Voie a	Voie b	Voie c
Rd ^t (%)	100%	98%	71%
E-factor (g/g)	441	495	143
Coût (€/g)	176	38.5	14

Enfin, ces intermédiaires conduisent aux molécules cibles par condensation de Knoevenagel, menée de façon classique. La purification finale est réalisée par simple recristallisation dans l'acétate d'éthyle, ce qui réduit le problème des déchets liés au procédé de synthèse. Le tableau suivant résume les paramètres de synthèse des 4 molécules isolées.

Tableau 5: Rendements de la condensation Knoevenagel, E-facteurs globaux et coûts calculés pour les molécules cible obtenues *via* la **Voie c**.

		$Bz(T_1CAO)_2$	$Bz(T_1CAEH)_2$	$Bz(T_2CAO)_2$	$Bz(T_2CAEH)_2$
Rd ^t	Cond.	51%	47%	76%	68%
E-facteur	global	230	380	144	162
Coût total (€/g)		45	37	50	47

La synthèse des molécules base de DTS s'est avérée beaucoup plus complexe car le nombre d'étapes nécessaires était plus important et l'obtention et purification de certains synthons s'est révélée délicate. Les voies de synthèse des précurseurs di-aldéhydiques des molécules cibles sont schématisées ci-dessous :

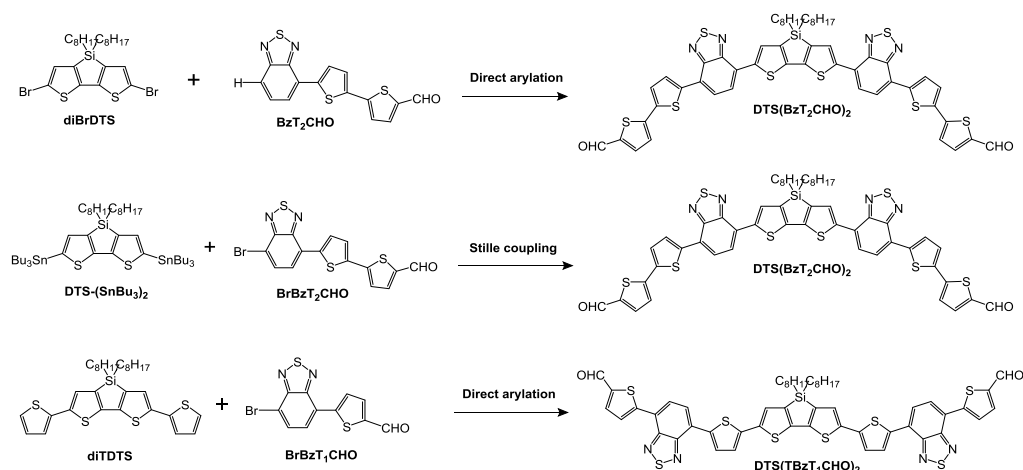


Schéma 2: Voies de synthèse des dialdéhydes à base de DTS.

Parmi les synthons nécessaires, nous avons isolé tous les réactifs (à gauche) des réactions ci-dessus ainsi que le produit dialdéhyde $\text{DTS}(\text{BzT}_2\text{CHO})_2$. Par manque de temps, nous n'avons pas poursuivi les synthèses initialement prévues.

La synthèse des molécules à base de SubPc n'a pas non plus pu être menée à terme. Il s'est avéré que les rendements de réactions annoncés dans la littérature pour la synthèse de la SubPcBCl sont beaucoup plus optimistes que ceux que nous avons pu atteindre en utilisant les protocoles décrits. Nous avons néanmoins pu isoler la SubPcBCl avec un rendement de 12%, puis effectuer la substitution de l'atome de chlore avec un rendement de 41%.

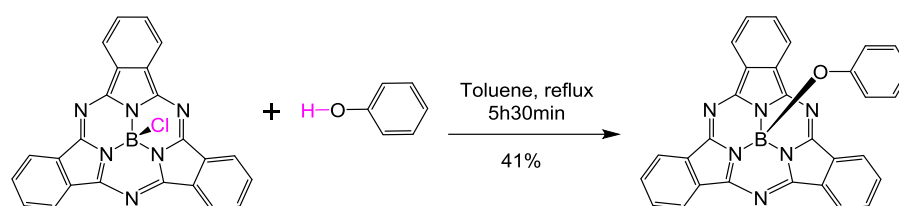


Schéma 3: Synthèse du phenoxy-SubPc à partir de la SubPcBCl.

Ce travail préliminaire, nécessaire à l'acquisition du savoir-faire dans la synthèse des dérivés de subphthalocyanines, sera poursuivi au laboratoire dans le futur. Pour cela, il est envisagé d'utiliser un phénol substitué en position para- par un fragment très proche de ceux vus précédemment, puis de le faire réagir sur la SubPcBCl pour obtenir les molécules cibles présentées en Figure 8. Le schéma réactionnel global est le suivant:

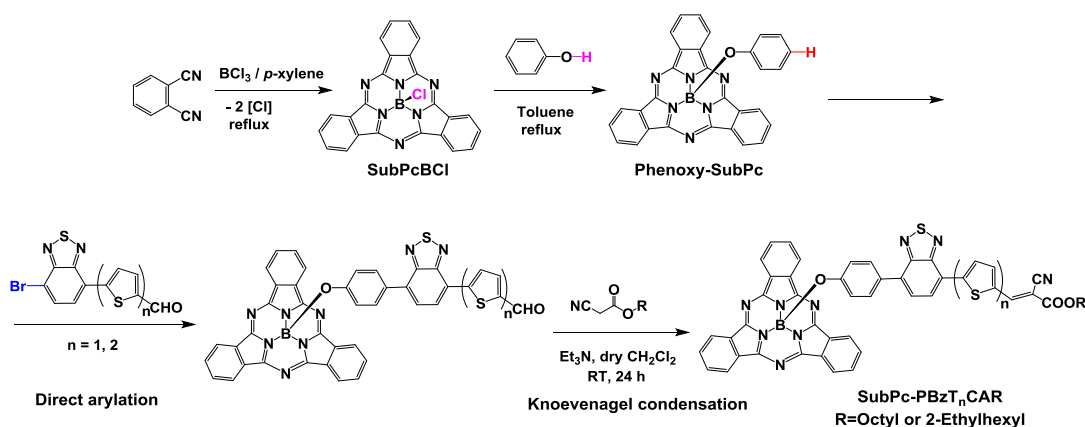


Schéma 4: Dérivés SubPcs cibles et stratégies de synthèse par substitution axiale.

CHAPITRE IV : CARACTERISATION DES MATERIAUX

Dans cette section, les composés $Bz(T_1CAO)_2$, $Bz(T_1CAEH)_2$, $Bz(T_2CAO)_2$, $Bz(T_2CAEH)_2$ et BzT_2CAO sont étudiés en termes de propriétés optiques, électrochimiques, et thermiques afin d'évaluer leur potentielle utilisation en application photovoltaïque organique.

Les composés symétriques montrent, pour une longueur de conjugaison équivalente, des spectres d'absorption et d'émissions similaires : la nature des chaînes alkyle n'est pas un facteur influant sur leurs propriétés optiques. L'addition d'un noyau thiophène dans le chemin de conjugaison moléculaire provoque un effet bathochrome sur le spectre d'absorption électronique.

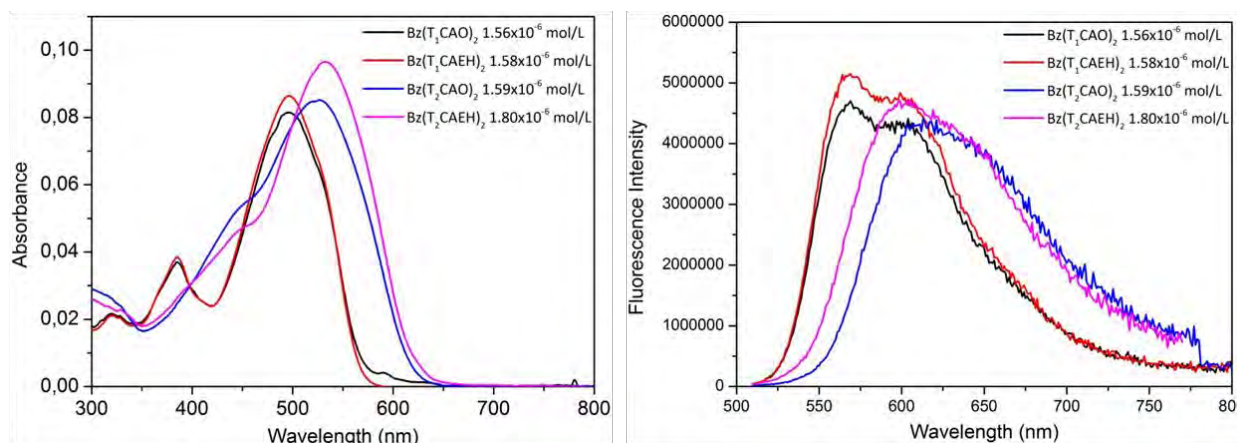


Figure 10: Spectre d'absorption (à gauche) et d'émission (à droite) des molécules symétriques à base de Bz.

L'examen en température des spectres d'absorption électronique de $Bz(T_1CAEH)_2$ déposée à la tournette en film mince sur ITO/verre à partir d'une solution de chlorobenzène révèle une nette diminution en intensité de son absorption dès lors que le film a été chauffé à 100°C . Cela indique que la morphologie de films réalisés avec ces molécules seront certainement sensibles au recuit thermique. Ce paramètre devra être étudié et pris en compte pour la réalisation de cellule OPV prototype.

L'étude par électrochimie de ces molécules révèlent leur grande stabilité au transfert électronique (signaux redox réversibles) en oxydation et en réduction. Les caractéristiques électroniques des composés sont résumées dans le tableau suivant :

Tableau 6: Paramètres optoélectroniques des molécules cibles.

	λ_{\max} (nm) ^a	ϵ (M ⁻¹ cm ⁻¹)	E_g^{opt} (eV) ^b	E_{ox} (V/Fc ⁺ /Fc) ^c	E_{red} (V/Fc ⁺ /Fc) ^c	E_g^{el} (eV) ^c	HOMO (eV) ^d	LUMO (eV) ^d
Bz(T ₁ CAO) ₂	498	51000	2.1	+1.01	-1.18	2.16	-6.4	-4.2
Bz(T ₁ CAEH) ₂	497	55000	2.1	+0.99	-1.17	2.19	-6.4	-4.2
Bz(T ₂ CAO) ₂	522	53440	2.0	+0.57	-1.34	1.91	-6.0	-4.05
Bz(T ₂ CAEH) ₂	525	53440	2.0	+0.55	-1.37	1.92	-5.9	-4.0
BzT ₂ CAO	461		2.36	+0.85	-1.45	2.30	-6.24	-3.94

Le diagramme d'énergie de leurs orbitales frontières a été établi sur la base des résultats expérimentaux et théoriques (Figure 11). Notons que les niveaux d'énergie des HOMO et LUMO des composés symétriques sont plus élevés selon les calculs théoriques en comparaison aux valeurs expérimentales. Globalement, il ressort que les 5 molécules peuvent être utilisées comme matériaux accepteurs d'électrons en association avec le P3HT comme donneur d'électron. Par ailleurs, les molécules comportant des fragments bithiophène Bz(T₂CAO)₂, Bz(T₂CAEH)₂ et BzT₂CAO peuvent être utilisées comme donneurs d'électrons en association avec le PCBM comme accepteur d'électrons. Dans ce cas, et selon le modèle Scharber, les molécules symétriques permettraient d'élaborer des cellules OPV avec un PCE optimisé de 9 %, et la molécule non symétrique un PCE optimisé de 6%.

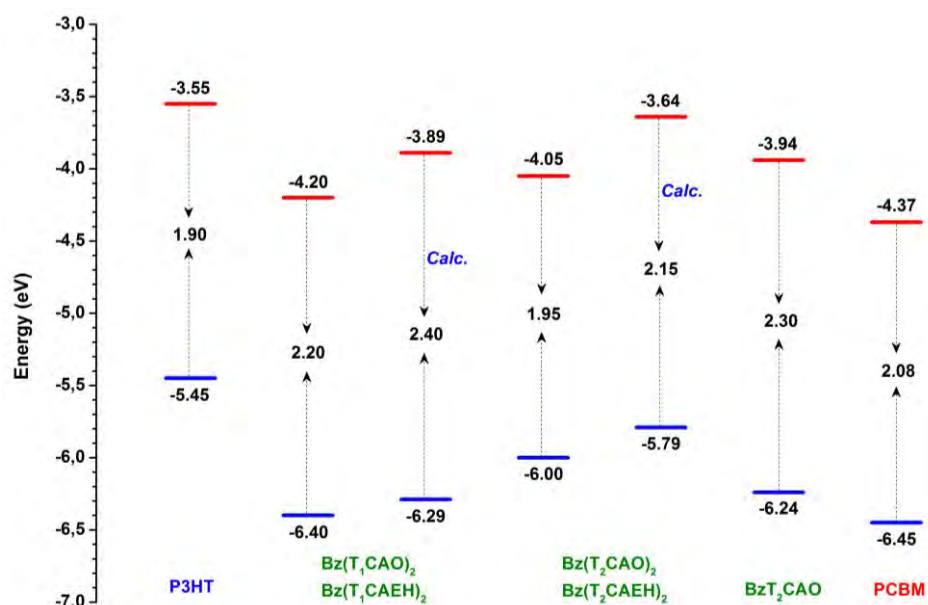


Figure 11: Niveaux d'énergie des HOMO et LUMO pour les molécules étudiées, P3HT et PCBM, estimés par mesures électrochimiques et calculés. (Toutes les valeurs ont été mesurées dans notre laboratoire dans les mêmes conditions expérimentales.

Les propriétés thermiques de ces matériaux ont été étudiées par analyses thermogravimétriques et thermique différentielle. Elles sont toutes des stables thermiquement jusque 300 °C. Trois d'entre elles présentent des comportements cristallins classiques, seuls la molécule $Bz(T_1CAO)_2$ révèlent un comportement cristal liquide (voir Figure 12), confirmé par ailleurs par examen en microscopie sous polariseur croisé (POM) et analyse aux rayons X aux petits angles (SAXS). La phase cristalline liquide identifiée est la phase smectique A se formant au refroidissement à 178 °C, puis se transformant vraisemblablement en phase smectique C à 128°C. Ce comportement original, lié à la présence des chaînes octyles en bout de molécule, peut être un atout pour l'organisation moléculaire en film mince.

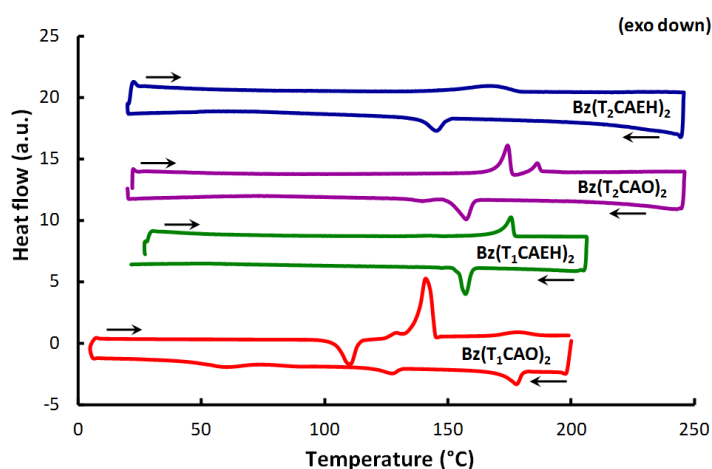


Figure 12: Thermogrammes des molécules symétriques enregistrés au troisième cycle de chauffage à 10°C/min sous atmosphère d'azote.

En conclusion, une série de petites molécules de π -conjuguées a été caractérisée par différentes techniques analytiques. Leur forte absorption dans la région allant de 300 à 700 nm en solution est une condition préalable pour la production d'excitons sous la lumière du soleil. Leur bonne stabilité thermique associée à leurs propriétés optoélectroniques et leur capacité à tolérer le transfert d'électrons rendent ces molécules intéressantes à tester en tant que matériaux donneurs ou accepteurs d'électrons pour des applications en OPV. Nous montrons que le simple remplacement d'une chaîne ramifiée (2-éthylhexyle) par une chaîne linéaire (octyle) conduit à un changement radical des interactions intermoléculaires et donc des propriétés d'organisation en film mince. Cette propriété sera vraisemblablement bénéfique pour la réalisation de films minces à morphologie appropriée (en fonction de la nature de la chaîne alkyle) pour une utilisation donnée. Dans ce but, de nouvelles investigations sur des films minces de ces molécules devront être effectuées pour évaluer leurs performances potentielles en photovoltaïque organique.

CHAPITRE V : PARTIE EXPERIMENTALE

Ce cinquième chapitre présente les procédures expérimentales liées aux travaux effectués au long de ce travail.

CONCLUSION GENERALE

L'objectif de cette thèse était de concevoir et de synthétiser des petites molécules organiques pour des applications dans des dispositifs OPV. Dans ce travail, diverses molécules organiques π -conjugués ont été conçues et leurs synthèses entreprises.

Après avoir exposé le principe de fonctionnement d'une cellule organique pour l'OPV, les paramètres importants mesurés en conditions standards pour caractériser leurs performances ont été discutés. Les différents types d'architectures des dispositifs OPV ont été décrits. Enfin, les matériaux semi-conducteurs organiques les plus performants ont été présentés et discutés. En particulier, certains matériaux donneurs ou accepteurs d'électrons parmi les plus prometteurs à base de polymères ou de petites molécules organiques, ainsi que des accepteurs à base de PCBM ont été discutés sur la base de leurs structures et de leurs performances respectives en utilisation dans les dispositifs OPV. Cette revue bibliographique révèle que les petites molécules semi-conductrices organiques sont des candidats prometteurs en OPV.

Le deuxième chapitre décrit notre approche de conception moléculaire. Un ensemble de petites molécules composées de benzothiadiazole (Bz) de base, le 4,4'-di-n-octyl-dithieno [3,2-b: 2', 3'-d] silole (DTS) de base, et subphthalocyanines (SubPcs) unité ont été conçues puis étudiées par des calculs DFT à B3LYP/Def2-TZVP(-f) niveau. Leurs stratégies de synthèse ont également été présentées, ces molécules présentant un potentiel prometteur pour des applications en OPV.

Dans le troisième chapitre, les méthodes de synthèse de ces molécules sont présentées. Pour les molécules à base de Bz, trois méthodes ont été étudiées: le couplage de Suzuki, le couplage de Stille et l'hétéroarylation directe. La méthode d'hétéroarylation directe a été étudiée en détail, avec évaluation du E-facteur de la synthèse et du coût de la molécule considérée. Il a démontré que l'hétéroarylation directe est une approche verte attrayante pour la synthèse de matériaux semiconducteurs organiques. Parmi toutes les molécules conçues, cinq molécules à base de noyau Bz ont été obtenues. La synthèse des molécules cible à base de DTS et SubPc ont été entreprises, mais pas encore menées à leur terme pour des raisons de temps.

Les quatre petites molécules symétriques obtenues: Bz(T₁CAO)₂, Bz(T₁CAEH)₂, Bz(T₂CAO)₂ et Bz(T₂CAEH)₂, ont été étudiées en détail, comme présenté dans le quatrième chapitre. Leurs propriétés optiques ont été étudiées par absorption électronique UV-visible et de photoluminescence. L'évaluation de leurs paramètres électroniques a été réalisée par électrochimie. Les résultats expérimentaux sont en accord avec les calculs théoriques, ce qui valide notre approche selon laquelle l'utilisation de calculs théoriques pour concevoir et prévoir de nouveaux matériaux est une bonne méthodologie. Ensuite, les propriétés thermiques et structurales ont été étudiées au moyen de l'analyse thermique différentielle, l'analyse thermogravimétrique, la microscopie sous polariseurs croisés et la diffraction des rayons X aux petits angles en température. Ces molécules se révèlent sous leurs différents aspects, électroniques et structuraux, comme matériaux prometteurs pour des applications dans les cellules OPV.

PERSPECTIVES

Concernant les molécules cible, il nous faudra poursuivre les synthèses précédemment décrites pour obtenir des composés à base de DTS et ceux à base de SubPc. Leurs caractérisations complètes devront être réalisées et comparées, pour les paramètres électroniques, avec les résultats des calculs théoriques.

L'étude de la morphologie des films minces réalisés avec toutes les molécules cible devra être réalisée et les mesures leurs mobilités de charge effectuées. Enfin, nous devons les tester dans des dispositifs prototypes OPV afin d'atteindre tous nos objectifs. Nous pourrons en particulier tester l'utilisation de DIP pour améliorer la cristallinité des films de molécules à base de Bz et ainsi améliorer la morphologie de leur couche active.

References

References

1. C. W. Tang, Two-layer organic photovoltaic cell. *Applied Physics Letters* **48**, 183-185 (1986).
2. M. Granström *et al.*, Laminated fabrication of polymeric photovoltaic diodes. *Nature* **395**, 257-260 (1998).
3. C. J. Brabec *et al.*, Polymer–fullerene bulk-heterojunction solar cells. *Advanced Materials* **22**, 3839-3856 (2010).
4. P. Peumans, A. Yakimov, S. R. Forrest, Small molecular weight organic thin-film photodetectors and solar cells. *Journal of Applied Physics* **93**, 3693-3723 (2003).
5. J. Halls *et al.*, Efficient photodiodes from interpenetrating polymer networks. *Nature* **376**, 498-500 (1995).
6. Heliatek, <http://www.heliatek.com/>.
7. <http://www.iea.org/publications/freepublications/publication/key-world-energy-statistics-2015.html>.
8. http://www.eia.gov/energyexplained/index.cfm?page=renewable_home.
9. J. Goldemberg, T. B. Johansson, D. Anderson, *World energy assessment: overview: 2004 update*. (United Nations Development Programme, Bureau for Development Policy, 2004).
10. N. Armaroli, V. Balzani, The future of energy supply: challenges and opportunities. *Angewandte Chemie International Edition* **46**, 52-66 (2007).
11. U. S. E. I. A. http://www.eia.gov/energyexplained/index.cfm?page=renewable_home. eia.
12. A. M. a. M. G. Krzysztof Biernat, Z. F. (Ed.), Ed. (2013).
13. Y.-J. Cheng, S.-H. Yang, C.-S. Hsu, Synthesis of Conjugated Polymers for Organic Solar Cell Applications. *Chemical reviews* **109**, 5868-5923 (2009).
14. S. Günes, H. Neugebauer, N. S. Sariciftci, Conjugated Polymer-Based Organic Solar Cells. *Chemical reviews* **107**, 1324-1338 (2007).
15. J. Chen, Y. Cao, Development of Novel Conjugated Donor Polymers for High-Efficiency Bulk-Heterojunction Photovoltaic Devices. *Accounts of chemical research* **42**, 1709-1718 (2009).
16. C. Li, M. Liu, N. G. Pschirer, M. Baumgarten, K. Müllen, Polyphenylene-Based Materials for Organic Photovoltaics. *Chemical reviews* **110**, 6817-6855 (2010).
17. L.-M. Chen, Z. Hong, G. Li, Y. Yang, Recent Progress in Polymer Solar Cells: Manipulation of Polymer:Fullerene Morphology and the Formation of Efficient Inverted Polymer Solar Cells. *Advanced Materials* **21**, 1434-1449 (2009).
18. P. M. Beaujuge, J. M. J. Fréchet, Molecular Design and Ordering Effects in π -Functional Materials for Transistor and Solar Cell Applications. *Journal of the American Chemical Society* **133**, 20009-20029 (2011).
19. B. Kan *et al.*, A Series of Simple Oligomer-like Small Molecules Based on Oligothiophenes for Solution-Processed Solar Cells with High Efficiency. *Journal of the American Chemical Society* **137**, 3886-3893 (2015).
20. B. Kan *et al.*, Small Molecules Based on Alkyl/Alkylthio-thieno[3,2-b]thiophene-Substituted Benzo[1,2-b:4,5-b']dithiophene for Solution-Processed Solar Cells with High Performance. *Chemistry of Materials* **27**, 8414-8423 (2015).
21. J. Zhao *et al.*, Efficient organic solar cells processed from hydrocarbon solvents. *Nature Energy* **1**, 15027 (2016).
22. S. Holliday *et al.*, A rhodanine flanked nonfullerene acceptor for solution-processed organic photovoltaics. *Journal of the American Chemical Society* **137**, 898-904 (2015).
23. H. Zhou *et al.*, Polymer Homo-Tandem Solar Cells with Best Efficiency of 11.3%. *Advanced Materials* **27**, 1767-1773 (2015).
24. K. Sun *et al.*, A molecular nematic liquid crystalline material for high-performance organic photovoltaics. *Nature Communications* **6**, (2015).

25. C.-C. Chen *et al.*, An Efficient Triple-Junction Polymer Solar Cell Having a Power Conversion Efficiency Exceeding 11%. *Advanced Materials* **26**, 5670-5677 (2014).
26. A. J. Heeger, Semiconducting polymers: the third generation. *Chemical Society Reviews* **39**, 2354-2371 (2010).
27. A. J. Heeger, 25th Anniversary Article: Bulk Heterojunction Solar Cells: Understanding the Mechanism of Operation. *Advanced Materials* **26**, 10-28 (2014).
28. S. H. Park *et al.*, Bulk heterojunction solar cells with internal quantum efficiency approaching 100%. *Nature Photonics* **3**, 297-302 (2009).
29. Y. Sun *et al.*, Solution-processed small-molecule solar cells with 6.7% efficiency. *Nature materials* **11**, 44-48 (2012).
30. Y. Chen, X. Wan, G. Long, High Performance Photovoltaic Applications Using Solution-Processed Small Molecules. *Accounts of chemical research* **46**, 2645-2655 (2013).
31. K. Cnops *et al.*, 8.4% efficient fullerene-free organic solar cells exploiting long-range exciton energy transfer. *Nature communications* **5**, (2014).
32. K. A. Mazzi, C. K. Luscombe, The future of organic photovoltaics. *Chemical Society Reviews* **44**, 78-90 (2015).
33. <http://www.nrel.gov/ncpv/>, National Center for Photovoltaics, NREL.
34. M. A. Green, K. Emery, Y. Hishikawa, W. Warta, E. D. Dunlop, Solar cell efficiency tables (version 47). *Progress in Photovoltaics: Research and Applications* **24**, 3-11 (2016).
35. G. Yu, J. Gao, J. C. Hummelen, F. Wudl, A. J. Heeger, Polymer photovoltaic cells: Enhanced efficiencies via a network of internal donor-acceptor heterojunctions. *Science* **270**, 1789 (1995).
36. G. Li *et al.*, High-efficiency solution processable polymer photovoltaic cells by self-organization of polymer blends. *Nature materials* **4**, 864-868 (2005).
37. B. C. Thompson, J. M. J. Fréchet, Polymer–Fullerene Composite Solar Cells. *Angewandte Chemie International Edition* **47**, 58-77 (2008).
38. G. Li, R. Zhu, Y. Yang, Polymer solar cells. *Nature Photonics* **6**, 153-161 (2012).
39. N. Sariciftci, L. Smilowitz, A. J. Heeger, F. Wudl, Photoinduced electron transfer from a conducting polymer to buckminsterfullerene. *Science* **258**, 1474-1476 (1992).
40. J. You *et al.*, A polymer tandem solar cell with 10.6% power conversion efficiency. *Nature Communications* **4**, 1446 (2013).
41. Z. He *et al.*, Enhanced power-conversion efficiency in polymer solar cells using an inverted device structure. *Nature Photonics* **6**, 591-595 (2012).
42. L. Dou *et al.*, Tandem polymer solar cells featuring a spectrally matched low-bandgap polymer. *Nature Photonics* **6**, 180-185 (2012).
43. Y. Kim, C. E. Song, S.-J. Moon, E. Lim, Rhodanine dye-based small molecule acceptors for organic photovoltaic cells. *Chemical Communications* **50**, 8235-8238 (2014).
44. F. C. Krebs, Fabrication and processing of polymer solar cells: A review of printing and coating techniques. *Solar Energy Materials and Solar Cells* **93**, 394-412 (2009).
45. Q. Zhang *et al.*, A solution-processed high performance organic solar cell using a small molecule with the thieno [3, 2-b] thiophene central unit. *Chemical Communications* **51**, 15268-15271 (2015).
46. Q. Zhang *et al.*, Small-molecule solar cells with efficiency over 9%. *Nature Photonics* **9**, 35-41 (2015).
47. J. Y. Kim *et al.*, Efficient tandem polymer solar cells fabricated by all-solution processing. *Science* **317**, 222-225 (2007).
48. J. Peet *et al.*, Efficiency enhancement in low-bandgap polymer solar cells by processing with alkane dithiols. *Nature materials* **6**, 497-500 (2007).
49. H.-Y. Chen *et al.*, Polymer solar cells with enhanced open-circuit voltage and efficiency. *Nature Photonics* **3**, 649-653 (2009).
50. X. Guo *et al.*, Polymer solar cells with enhanced fill factors. *Nature Photonics* **7**, 825-833 (2013).

51. A.-E. Becquerel, Mémoire sur les effets électriques produits sous l'influence des rayons solaires. *Comptes Rendus* **9**, 1839 (1839).
52. D. M. Chapin, C. Fuller, G. Pearson, A new silicon p-n junction photocell for converting solar radiation into electrical power. *Journal of Applied Physics* **25**, 676-677 (1954).
53. J.-L. Bredas, Mind the gap! *Materials Horizons* **1**, 17-19 (2014).
54. Energy of Photon. PVEDUCATION.ORG. <http://www.pveducation.org/pvcdrom/properties-of-sunlight/energy-of-photon>.
55. J.-M. Nunzi, Organic photovoltaic materials and devices. *Comptes Rendus Physique* **3**, 523-542 (2002).
56. H. Hoppe, N. S. Sariciftci, Organic solar cells: An overview. *Journal of Materials Research* **19**, 1924-1945 (2004).
57. M. C. Scharber, N. S. Sariciftci, Efficiency of bulk-heterojunction organic solar cells. *Progress in Polymer Science* **38**, 1929-1940 (2013).
58. P. B. Miranda, D. Moses, A. J. Heeger, Ultrafast photogeneration of charged polarons in conjugated polymers. *Physical Review B* **64**, 081201 (2001).
59. S. D. Dimitrov *et al.*, Singlet Exciton Lifetimes in Conjugated Polymer Films for Organic Solar Cells. *Polymers* **8**, 14 (2016).
60. A. J. Mozer, N. S. Sariciftci, Conjugated polymer photovoltaic devices and materials. *Comptes Rendus Chimie* **9**, 568-577 (2006).
61. M. C. Scharber *et al.*, Design rules for donors in bulk-heterojunction solar cells—Towards 10% energy-conversion efficiency. *Advanced Materials* **18**, 789-794 (2006).
62. J.-L. Brédas, D. Beljonne, V. Coropceanu, J. Cornil, Charge-Transfer and Energy-Transfer Processes in π -Conjugated Oligomers and Polymers: A Molecular Picture. *Chemical reviews* **104**, 4971-5004 (2004).
63. T. Wang, A. J. Pearson, D. G. Lidzey, Correlating molecular morphology with optoelectronic function in solar cells based on low band-gap copolymer: fullerene blends. *Journal of Materials Chemistry C* **1**, 7266-7293 (2013).
64. C. Vijila *et al.*, Relation between charge carrier mobility and lifetime in organic photovoltaics. *Journal of Applied Physics* **114**, 184503 (2013).
65. R. Schlaf, H. Murata, Z. H. Kafafi, Work function measurements on indium tin oxide films. *Journal of Electron Spectroscopy and Related Phenomena* **120**, 149-154 (2001).
66. T. Yamanari, T. Taima, J. Sakai, K. Saito, Origin of the open-circuit voltage of organic thin-film solar cells based on conjugated polymers. *Solar Energy Materials and Solar Cells* **93**, 759-761 (2009).
67. V. Shrotriya *et al.*, Accurate Measurement and Characterization of Organic Solar Cells. *Advanced functional materials* **16**, 2016-2023 (2006).
68. J. K. J. van Duren *et al.*, Relating the Morphology of Poly(p-phenylene vinylene)/Methanofullerene Blends to Solar-Cell Performance. *Advanced functional materials* **14**, 425-434 (2004).
69. H. Hoppe *et al.*, Efficiency limiting morphological factors of MDMO-PPV: PCBM plastic solar cells. *Thin solid films* **511**, 587-592 (2006).
70. H. Hoppe *et al.*, Nanoscale Morphology of Conjugated Polymer/Fullerene-Based Bulk-Heterojunction Solar Cells. *Advanced functional materials* **14**, 1005-1011 (2004).
71. D. Gebeyehu *et al.*, The interplay of efficiency and morphology in photovoltaic devices based on interpenetrating networks of conjugated polymers with fullerenes. *Synthetic Metals* **118**, 1-9 (2001).
72. T. Martens *et al.*, Disclosure of the nanostructure of MDMO-PPV:PCBM bulk hetero-junction organic solar cells by a combination of SPM and TEM. *Synthetic Metals* **138**, 243-247 (2003).
73. A. Gadisa, M. Svensson, M. R. Andersson, O. Inganäs, Correlation between oxidation potential and open-circuit voltage of composite solar cells based on blends of polythiophenes/fullerene derivative. *Applied Physics Letters* **84**, 1609-1611 (2004).

74. K. L. Mutolo, E. I. Mayo, B. P. Rand, S. R. Forrest, M. E. Thompson, Enhanced Open-Circuit Voltage in Subphthalocyanine/C60 Organic Photovoltaic Cells. *Journal of the American Chemical Society* **128**, 8108-8109 (2006).
75. M. D. McGehee, M. A. Topinka, Solar cells: pictures from the blended zone. *Nature materials* **5**, 675-676 (2006).
76. J. Nelson, Organic photovoltaic films. *Current Opinion in Solid State and Materials Science* **6**, 87-95 (2002).
77. M. D. Archer, R. Hill, *Clean electricity from photovoltaics*. (World Scientific, 2001).
78. L. J. A. Koster, V. D. Mihailetschi, P. W. M. Blom, Bimolecular recombination in polymer/fullerene bulk heterojunction solar cells. *Applied Physics Letters* **88**, 052104 (2006).
79. T. Ameri, G. Dennler, C. Lungenschmied, C. J. Brabec, Organic tandem solar cells: A review. *Energy & Environmental Science* **2**, 347-363 (2009).
80. B. Kippelen, J.-L. Brédas, Organic photovoltaics. *Energy & Environmental Science* **2**, 251-261 (2009).
81. H. Zhou, L. Yang, W. You, Rational Design of High Performance Conjugated Polymers for Organic Solar Cells. *Macromolecules* **45**, 607-632 (2012).
82. P. Peumans, S. Uchida, S. R. Forrest, Efficient bulk heterojunction photovoltaic cells using small-molecular-weight organic thin films. *Nature* **425**, 158-162 (2003).
83. C. J. Brabec *et al.*, Origin of the open circuit voltage of plastic solar cells. *Advanced functional materials* **11**, 374-380 (2001).
84. Y. Lin, Y. Li, X. Zhan, Small molecule semiconductors for high-efficiency organic photovoltaics. *Chemical Society Reviews* **41**, 4245-4272 (2012).
85. Y. Liu *et al.*, Solution-processed small-molecule solar cells: breaking the 10% power conversion efficiency. *Scientific Reports* **3**, 3356 (2013).
86. R. R. Lunt, N. C. Giebink, A. A. Belak, J. B. Benziger, S. R. Forrest, Exciton diffusion lengths of organic semiconductor thin films measured by spectrally resolved photoluminescence quenching. *Journal of Applied Physics* **105**, 053711 (2009).
87. M. T. Greiner, Z.-H. Lu, Thin-film metal oxides in organic semiconductor devices: their electronic structures, work functions and interfaces. *NPG Asia Materials* **5**, e55 (2013).
88. H. Frohne *et al.*, Influence of the Anodic Work Function on the Performance of Organic Solar Cells. *ChemPhysChem* **3**, 795-799 (2002).
89. R. Fitzner *et al.*, Correlation of π -Conjugated Oligomer Structure with Film Morphology and Organic Solar Cell Performance. *Journal of the American Chemical Society* **134**, 11064-11067 (2012).
90. M. Riede *et al.*, Efficient Organic Tandem Solar Cells based on Small Molecules. *Advanced functional materials* **21**, 3019-3028 (2011).
91. F. Padinger, R. S. Rittberger, N. S. Sariciftci, Effects of Postproduction Treatment on Plastic Solar Cells. *Advanced functional materials* **13**, 85-88 (2003).
92. B. Walker, C. Kim, T.-Q. Nguyen, Small Molecule Solution-Processed Bulk Heterojunction Solar Cells. *Chemistry of Materials* **23**, 470-482 (2011).
93. J.-D. Chen *et al.*, Single-Junction Polymer Solar Cells Exceeding 10% Power Conversion Efficiency. *Advanced Materials* **27**, 1035-1041 (2015).
94. Y. Liu *et al.*, Aggregation and morphology control enables multiple cases of high-efficiency polymer solar cells. *Nature communications* **5**, (2014).
95. H. Kang *et al.*, Simplified Tandem Polymer Solar Cells with an Ideal Self-Organized Recombination Layer. *Advanced Materials* **27**, 1408-1413 (2015).
96. Z. He *et al.*, Single-junction polymer solar cells with high efficiency and photovoltage. *Nature Photonics* **9**, 174-179 (2015).
97. S. Zhang *et al.*, Realizing over 10% efficiency in polymer solar cell by device optimization. *Science China Chemistry* **58**, 248-256 (2015).

98. C. Liu *et al.*, Single-Junction Polymer Solar Cells with Over 10% Efficiency by a Novel Two-Dimensional Donor–Acceptor Conjugated Copolymer. *ACS Applied Materials & Interfaces* **7**, 4928-4935 (2015).
99. S. Liu *et al.*, Enhanced efficiency of polymer solar cells by adding a high-mobility conjugated polymer. *Energy & Environmental Science* **8**, 1463-1470 (2015).
100. J. K. Lee *et al.*, Processing Additives for Improved Efficiency from Bulk Heterojunction Solar Cells. *Journal of the American Chemical Society* **130**, 3619-3623 (2008).
101. C. J. Brabec, N. S. Sariciftci, J. C. Hummelen, Plastic solar cells. *Advanced functional materials* **11**, 15-26 (2001).
102. G. Yu, C. Zhang, A. J. Heeger, Dual-function semiconducting polymer devices: Light-emitting and photodetecting diodes. *Applied Physics Letters* **64**, 1540-1542 (1994).
103. J. You, L. Dou, Z. Hong, G. Li, Y. Yang, Recent trends in polymer tandem solar cells research. *Progress in Polymer Science* **38**, 1909-1928 (2013).
104. M. Wanlass *et al.*, Practical considerations in tandem cell modeling. *Solar cells* **27**, 191-204 (1989).
105. W. Li, A. Furlan, K. H. Hendriks, M. M. Wienk, R. A. J. Janssen, Efficient Tandem and Triple-Junction Polymer Solar Cells. *Journal of the American Chemical Society* **135**, 5529-5532 (2013).
106. J. Jo *et al.*, Enhanced Efficiency of Single and Tandem Organic Solar Cells Incorporating a Diketopyrrolopyrrole-Based Low-Bandgap Polymer by Utilizing Combined ZnO/Polyelectrolyte Electron-Transport Layers. *Advanced Materials* **25**, 4783-4788 (2013).
107. J. Yang *et al.*, A Robust Inter-Connecting Layer for Achieving High Performance Tandem Polymer Solar Cells. *Advanced Materials* **23**, 3465-3470 (2011).
108. J. Yang *et al.*, Plasmonic Polymer Tandem Solar Cell. *Acs Nano* **5**, 6210-6217 (2011).
109. J. Lee, H. Kang, J. Kong, K. Lee, A Depletion-Free, Ionic, Self-Assembled Recombination Layer for Tandem Polymer Solar Cells. *Advanced Energy Materials* **4**, (2014).
110. I. Riedel, V. Dyakonov, Influence of electronic transport properties of polymer-fullerene blends on the performance of bulk heterojunction photovoltaic devices. *physica status solidi (a)* **201**, 1332-1341 (2004).
111. A. R. bin Mohd Yusoff, D. Kim, F. K. Shneider, W. J. da Silva, J. Jang, Au-doped Single Layer Graphene Nanoribbons for a Record-High Efficiency ITO-Free Tandem Polymer Solar Cells. *Energy & Environmental Science*, (2015).
112. P. Kumar, S. Chand, Recent progress and future aspects of organic solar cells. *Progress in Photovoltaics: Research and Applications* **20**, 377-415 (2012).
113. M. Bhatt *et al.*, Poly (3-Hexylthiophene) nanostructured materials for organic electronics applications. *Journal of nanoscience and nanotechnology* **14**, 1033-1050 (2014).
114. L. Duan, K. Xie, Y. Qiu, Review Paper: Progress on efficient cathodes for organic light-emitting diodes. *Journal of the Society for Information Display* **19**, 453-461 (2011).
115. M. C. Gather, A. Koehnen, A. Falcou, H. Becker, K. Meerholz, Solution-Processed Full-Color Polymer Organic Light-Emitting Diode Displays Fabricated by Direct Photolithography. *Advanced functional materials* **17**, 191-200 (2007).
116. J. Burroughes *et al.*, Light-emitting diodes based on conjugated polymers. *Nature* **347**, 539-541 (1990).
117. Z. Bao, A. Dodabalapur, A. J. Lovinger, Soluble and processable regioregular poly(3-hexylthiophene) for thin film field-effect transistor applications with high mobility. *Applied Physics Letters* **69**, 4108-4110 (1996).
118. H. Bronstein *et al.*, Thieno[3,2-b]thiophene–Diketopyrrolopyrrole-Containing Polymers for High-Performance Organic Field-Effect Transistors and Organic Photovoltaic Devices. *Journal of the American Chemical Society* **133**, 3272-3275 (2011).
119. G. Horowitz, Organic field-effect transistors. *Advanced Materials* **10**, 365-377 (1998).

120. H. Shirakawa, E. J. Louis, A. G. MacDiarmid, C. K. Chiang, A. J. Heeger, Synthesis of electrically conducting organic polymers: halogen derivatives of polyacetylene, (CH)_x. *Journal of the Chemical Society, Chemical Communications*, 578-580 (1977).
121. A. J. Heeger, Semiconducting and Metallic Polymers: The Fourth Generation of Polymeric Materials (Nobel Lecture). *Angewandte Chemie International Edition* **40**, 2591-2611 (2001).
122. A. J. Heeger, Nobel Lecture: Semiconducting and metallic polymers: The fourth generation of polymeric materials. *Reviews of Modern Physics* **73**, 681-700 (2001).
123. V. Coropceanu *et al.*, Charge Transport in Organic Semiconductors. *Chemical reviews* **107**, 926-952 (2007).
124. A. J. Heeger, S. Kivelson, J. R. Schrieffer, W. P. Su, Solitons in conducting polymers. *Reviews of Modern Physics* **60**, 781-850 (1988).
125. M. Geoghegan, G. Hadziioannou, *Polymer electronics*. (OUP Oxford, 2013).
126. B. Fu *et al.*, High Charge Carrier Mobility, Low Band Gap Donor–Acceptor Benzothiadiazole-oligothiophene Based Polymeric Semiconductors. *Chemistry of Materials* **24**, 4123-4133 (2012).
127. H. Zhou *et al.*, Development of fluorinated benzothiadiazole as a structural unit for a polymer solar cell of 7% efficiency. *Angewandte Chemie* **123**, 3051-3054 (2011).
128. Y. Fang *et al.*, A narrow optical gap small molecule acceptor for organic solar cells. *Advanced Energy Materials* **3**, 54-59 (2013).
129. J. E. Coughlin, Z. B. Henson, G. C. Welch, G. C. Bazan, Design and Synthesis of Molecular Donors for Solution-Processed High-Efficiency Organic Solar Cells. *Accounts of chemical research* **47**, 257-270 (2014).
130. A. Mishra, P. Bäuerle, Small Molecule Organic Semiconductors on the Move: Promises for Future Solar Energy Technology. *Angewandte Chemie International Edition* **51**, 2020-2067 (2012).
131. C. J. Takacs *et al.*, Solar Cell Efficiency, Self-Assembly, and Dipole–Dipole Interactions of Isomorphous Narrow-Band-Gap Molecules. *Journal of the American Chemical Society* **134**, 16597-16606 (2012).
132. G. C. Welch *et al.*, A modular molecular framework for utility in small-molecule solution-processed organic photovoltaic devices. *Journal of Materials Chemistry* **21**, 12700-12709 (2011).
133. J. Roncali, P. Leriche, P. Blanchard, Molecular Materials for Organic Photovoltaics: Small is Beautiful. *Advanced Materials* **26**, 3821-3838 (2014).
134. Y. Lin, X. Zhan, Non-fullerene acceptors for organic photovoltaics: an emerging horizon. *Materials Horizons* **1**, 470-488 (2014).
135. J. D. Douglas *et al.*, Solution-Processed, Molecular Photovoltaics that Exploit Hole Transfer from Non-Fullerene, n-Type Materials. *Advanced Materials* **26**, 4313-4319 (2014).
136. W. Ni *et al.*, Fullerene-free small molecule organic solar cells with a high open circuit voltage of 1.15 V. *Chemical Communications* **52**, 465-468 (2016).
137. W. Ni, X. Wan, M. Li, Y. Wang, Y. Chen, A–D–A small molecules for solution-processed organic photovoltaic cells. *Chemical Communications* **51**, 4936-4950 (2015).
138. S. E. Shaheen *et al.*, 2.5% efficient organic plastic solar cells. *Applied Physics Letters* **78**, 841-843 (2001).
139. C. J. Brabec, S. E. Shaheen, C. Winder, N. S. Sariciftci, P. Denk, Effect of LiF/metal electrodes on the performance of plastic solar cells. *Applied Physics Letters* **80**, 1288-1290 (2002).
140. M. Reyes-Reyes, K. Kim, D. L. Carroll, High-efficiency photovoltaic devices based on annealed poly(3-hexylthiophene) and 1-(3-methoxycarbonyl)-propyl-1-phenyl-(6,6)C-61 blends. *Applied Physics Letters* **87**, 083506 (2005).
141. J. Y. Kim *et al.*, New Architecture for High-Efficiency Polymer Photovoltaic Cells Using Solution-Based Titanium Oxide as an Optical Spacer. *Advanced Materials* **18**, 572-576 (2006).

142. W. L. Ma, C. Y. Yang, X. Gong, K. Lee, A. J. Heeger, Thermally stable, efficient polymer solar cells with nanoscale control of the interpenetrating network morphology. *Advanced functional materials* **15**, 1617-1622 (2005).
143. K. Lee, H. Kim, Polymer photovoltaic cells based on conjugated polymer–fullerene composites. *Current Applied Physics* **4**, 323-326 (2004).
144. J. Hou, H.-Y. Chen, S. Zhang, G. Li, Y. Yang, Synthesis, Characterization, and Photovoltaic Properties of a Low Band Gap Polymer Based on Silole-Containing Polythiophenes and 2,1,3-Benzothiadiazole. *Journal of the American Chemical Society* **130**, 16144-16145 (2008).
145. D. H. Wang *et al.*, Transferable Graphene Oxide by Stamping Nanotechnology: Electron-Transport Layer for Efficient Bulk-Heterojunction Solar Cells. *Angewandte Chemie International Edition* **52**, 2874-2880 (2013).
146. T. Yang *et al.*, Inverted polymer solar cells with 8.4% efficiency by conjugated polyelectrolyte. *Energy & Environmental Science* **5**, 8208-8214 (2012).
147. A. Gadisa *et al.*, A New Donor–Acceptor–Donor Polyfluorene Copolymer with Balanced Electron and Hole Mobility. *Advanced functional materials* **17**, 3836-3842 (2007).
148. F. Zhang *et al.*, Influence of Solvent Mixing on the Morphology and Performance of Solar Cells Based on Polyfluorene Copolymer/Fullerene Blends. *Advanced functional materials* **16**, 667-674 (2006).
149. Q. Zheng, B. J. Jung, J. Sun, H. E. Katz, Ladder-Type Oligo-p-phenylene-Containing Copolymers with High Open-Circuit Voltages and Ambient Photovoltaic Activity. *Journal of the American Chemical Society* **132**, 5394-5404 (2010).
150. S. Loser *et al.*, A Naphthodithiophene-Diketopyrrolopyrrole Donor Molecule for Efficient Solution-Processed Solar Cells. *Journal of the American Chemical Society* **133**, 8142-8145 (2011).
151. B. Walker *et al.*, A Systematic Approach to Solvent Selection Based on Cohesive Energy Densities in a Molecular Bulk Heterojunction System. *Advanced Energy Materials* **1**, 221-229 (2011).
152. Y. Li, Q. Guo, Z. Li, J. Pei, W. Tian, Solution processable D–A small molecules for bulk-heterojunction solar cells. *Energy & Environmental Science* **3**, 1427-1436 (2010).
153. J. Roncali, Molecular Bulk Heterojunctions: An Emerging Approach to Organic Solar Cells. *Accounts of chemical research* **42**, 1719-1730 (2009).
154. D. H. Wang, A. K. K. Kyaw, V. Gupta, G. C. Bazan, A. J. Heeger, Enhanced Efficiency Parameters of Solution-Processable Small-Molecule Solar Cells Depending on ITO Sheet Resistance. *Advanced Energy Materials* **3**, 1161-1165 (2013).
155. J. Zhou *et al.*, Solution-Processed and High-Performance Organic Solar Cells Using Small Molecules with a Benzodithiophene Unit. *Journal of the American Chemical Society* **135**, 8484-8487 (2013).
156. B. Kan *et al.*, Solution-Processed Organic Solar Cells Based on Dialkylthiol-Substituted Benzodithiophene Unit with Efficiency near 10%. *Journal of the American Chemical Society* **136**, 15529-15532 (2014).
157. Y. He, Y. Li, Fullerene derivative acceptors for high performance polymer solar cells. *Physical chemistry chemical physics* **13**, 1970-1983 (2011).
158. G. Zhao, Y. He, Y. Li, 6.5% Efficiency of Polymer Solar Cells Based on poly(3-hexylthiophene) and Indene-C60 Bisadduct by Device Optimization. *Advanced Materials* **22**, 4355-4358 (2010).
159. A. L. Roes, E. A. Alsema, K. Blok, M. K. Patel, Ex-ante environmental and economic evaluation of polymer photovoltaics. *Progress in Photovoltaics: Research and Applications* **17**, 372-393 (2009).
160. J. Kalowekamo, E. Baker, Estimating the manufacturing cost of purely organic solar cells. *Solar Energy* **83**, 1224-1231 (2009).

161. T. D. Nielsen, C. Cruickshank, S. Foged, J. Thorsen, F. C. Krebs, Business, market and intellectual property analysis of polymer solar cells. *Solar Energy Materials and Solar Cells* **94**, 1553-1571 (2010).
162. A. Anctil, C. W. Babbitt, R. P. Raffaele, B. J. Landi, Material and Energy Intensity of Fullerene Production. *Environmental Science & Technology* **45**, 2353-2359 (2011).
163. L. Chen *et al.*, A non-fullerene acceptor with all "A" units realizing high open-circuit voltage solution-processed organic photovoltaics. *Journal of Materials Chemistry A* **2**, 2657-2662 (2014).
164. Y. Lin *et al.*, An Electron Acceptor Challenging Fullerenes for Efficient Polymer Solar Cells. *Advanced Materials* **27**, 1170-1174 (2015).
165. Y. Lin *et al.*, High-Performance Electron Acceptor with Thienyl Side Chains for Organic Photovoltaics. *Journal of the American Chemical Society* **138**, 4955-4961 (2016).
166. Y. Lin, P. Cheng, Y. Li, X. Zhan, A 3D star-shaped non-fullerene acceptor for solution-processed organic solar cells with a high open-circuit voltage of 1.18 V. *Chemical Communications* **48**, 4773-4775 (2012).
167. P. Cheng *et al.*, Binary additives synergistically boost the efficiency of all-polymer solar cells up to 3.45%. *Energy & Environmental Science* **7**, 1351-1356 (2014).
168. Y. Liu *et al.*, A Tetraphenylethylene Core-Based 3D Structure Small Molecular Acceptor Enabling Efficient Non-Fullerene Organic Solar Cells. *Advanced Materials* **27**, 1015-1020 (2015).
169. D. Mori, H. Benten, I. Okada, H. Ohkita, S. Ito, Highly efficient charge-carrier generation and collection in polymer/polymer blend solar cells with a power conversion efficiency of 5.7%. *Energy & Environmental Science* **7**, 2939-2943 (2014).
170. Y. Liang, L. Yu, A New Class of Semiconducting Polymers for Bulk Heterojunction Solar Cells with Exceptionally High Performance. *Accounts of chemical research* **43**, 1227-1236 (2010).
171. Y. Li, Molecular Design of Photovoltaic Materials for Polymer Solar Cells: Toward Suitable Electronic Energy Levels and Broad Absorption. *Accounts of chemical research* **45**, 723-733 (2012).
172. C. J. Brabec, M. Heeney, I. McCulloch, J. Nelson, Influence of blend microstructure on bulk heterojunction organic photovoltaic performance. *Chemical Society Reviews* **40**, 1185-1199 (2011).
173. F. Liu *et al.*, Characterization of the morphology of solution-processed bulk heterojunction organic photovoltaics. *Progress in Polymer Science* **38**, 1990-2052 (2013).
174. L.-M. Chen, Z. Xu, Z. Hong, Y. Yang, Interface investigation and engineering—achieving high performance polymer photovoltaic devices. *Journal of Materials Chemistry* **20**, 2575-2598 (2010).
175. H.-L. Yip, A. K.-Y. Jen, Recent advances in solution-processed interfacial materials for efficient and stable polymer solar cells. *Energy & Environmental Science* **5**, 5994-6011 (2012).
176. Z. He, H. Wu, Y. Cao, Recent Advances in Polymer Solar Cells: Realization of High Device Performance by Incorporating Water/Alcohol-Soluble Conjugated Polymers as Electrode Buffer Layer. *Advanced Materials* **26**, 1006-1024 (2014).
177. A. K. K. Kyaw *et al.*, Efficient Solution-Processed Small-Molecule Solar Cells with Inverted Structure. *Advanced Materials* **25**, 2397-2402 (2013).
178. X. Li *et al.*, Dual Plasmonic Nanostructures for High Performance Inverted Organic Solar Cells. *Advanced Materials* **24**, 3046-3052 (2012).
179. L. Dou *et al.*, 25th Anniversary Article: A Decade of Organic/Polymeric Photovoltaic Research. *Advanced Materials* **25**, 6642-6671 (2013).
180. C. Winder, N. S. Sariciftci, Low bandgap polymers for photon harvesting in bulk heterojunction solar cells. *Journal of Materials Chemistry* **14**, 1077-1086 (2004).
181. D. Alberico, M. E. Scott, M. Lautens, Aryl–Aryl Bond Formation by Transition-Metal-Catalyzed Direct Arylation. *Chemical reviews* **107**, 174-238 (2007).

182. L. G. Mercier, M. Leclerc, Direct (hetero) arylation: a new tool for polymer chemists. *Accounts of chemical research* **46**, 1597-1605 (2013).
183. F. Neese, an ab initio, density functional and semiempirical program package. *ORCA, version 2.9, Max Planck-Institute for Bioinorganic Chemistry: Mülheim a.d. Ruhr, Germany*, (2012).
184. K. Wolfram, M. Holthausen, A Chemist's Guide to Density Functional Theory. *New York*, 216 (2000).
185. C. G. Claessens, D. González-Rodríguez, T. Torres, Subphthalocyanines: singular nonplanar aromatic compounds synthesis, reactivity, and physical properties. *Chemical reviews* **102**, 835-854 (2002).
186. C. G. Claessens, D. González-Rodríguez, M. S. Rodríguez-Morgade, A. Medina, T. s. Torres, Subphthalocyanines, Subporphyrines, and Subporphyrins: Singular Nonplanar Aromatic Systems. *Chemical reviews* **114**, 2192-2277 (2013).
187. C. R.-S. J. Hachmann, K. Trepte, A. Gold-Parker, M.A. Blood-Forsythe, L.R. Seress, R. Olivares-Amaya, A. Aspuru-Guzik, , (the Harvard Clean Energy Project. <http://cleanenergy.molecularspace.org/>).
188. J. Hachmann *et al.*, Lead candidates for high-performance organic photovoltaics from high-throughput quantum chemistry—the Harvard Clean Energy Project. *Energy & Environmental Science* **7**, 698-704 (2014).
189. J. Hachmann *et al.*, The Harvard Clean Energy Project: Large-Scale Computational Screening and Design of Organic Photovoltaics on the World Community Grid. *The Journal of Physical Chemistry Letters* **2**, 2241-2251 (2011).
190. A. O. Aliprantis, J. W. Canary, Observation of Catalytic Intermediates in the Suzuki Reaction by Electrospray Mass Spectrometry. *Journal of the American Chemical Society* **116**, 6985-6986 (1994).
191. D. Clery, IBM offers free number crunching for humanitarian research projects. *Science* **308**, 773-773 (2005).
192. CEPDB, the Harvard Clean Energy Project Database. <https://cepdb.molecularspace.org/>.
193. W. Shockley, H. J. Queisser, Detailed Balance Limit of Efficiency of p-n Junction Solar Cells. *Journal of Applied Physics* **32**, 510-519 (1961).
194. Y.-T. Fu, C. Risko, J.-L. Brédas, Intermixing at the Pentacene-Fullerene Bilayer Interface: A Molecular Dynamics Study. *Advanced Materials* **25**, 878-882 (2013).
195. R. A. Cantrell, C. James, P. Clancy, Computationally Derived Rules for Persistence of C60 Nanowires on Recumbent Pentacene Bilayers. *Langmuir* **27**, 9944-9954 (2011).
196. R. Cantrell, P. Clancy, A computational study of surface diffusion of C60 on pentacene. *Surface Science* **602**, 3499-3505 (2008).
197. R. Cantrell, P. Clancy, A molecular dynamics study of the effect of pentacene polymorphs on C60 surface adsorption and diffusional properties and the tendency to form nanowires. *Molecular Simulation* **36**, 590-603 (2010).
198. P. K. Watkins, A. B. Walker, G. L. B. Verschoor, Dynamical Monte Carlo Modelling of Organic Solar Cells: The Dependence of Internal Quantum Efficiency on Morphology. *Nano Letters* **5**, 1814-1818 (2005).
199. N. Blouin *et al.*, Toward a Rational Design of Poly(2,7-Carbazole) Derivatives for Solar Cells. *Journal of the American Chemical Society* **130**, 732-742 (2008).
200. M. Morana *et al.*, Bipolar Charge Transport in PCPDTBT-PCBM Bulk-Heterojunctions for Photovoltaic Applications. *Advanced functional materials* **18**, 1757-1766 (2008).
201. C. Soci *et al.*, Photoconductivity of a Low-Bandgap Conjugated Polymer. *Advanced functional materials* **17**, 632-636 (2007).
202. W. Ma *et al.*, Organic Solar Cells: Influence of Processing Parameters and Molecular Weight on the Morphology and Properties of High-Performance PffBT4T-2OD: PC71BM Organic Solar Cells. *Advanced Energy Materials* **5**, (2015).

203. J. T. Bloking *et al.*, Solution-Processed Organic Solar Cells with Power Conversion Efficiencies of 2.5% using Benzothiadiazole/Imide-Based Acceptors. *Chemistry of Materials* **23**, 5484-5490 (2011).
204. C. H. Woo, T. W. Holcombe, D. A. Unruh, A. Sellinger, J. M. J. Fréchet, Phenyl vs Alkyl Polythiophene: A Solar Cell Comparison Using a Vinazene Derivative as Acceptor. *Chemistry of Materials* **22**, 1673-1679 (2010).
205. K.-H. Kim *et al.*, Influence of intermolecular interactions of electron donating small molecules on their molecular packing and performance in organic electronic devices. *Journal of Materials Chemistry A* **1**, 14538-14547 (2013).
206. C. Cui *et al.*, A D-A copolymer of dithienosilole and a new acceptor unit of naphtho[2,3-c]thiophene-4,9-dione for efficient polymer solar cells. *Chemical Communications* **47**, 11345-11347 (2011).
207. T.-Y. Chu *et al.*, Effects of the Molecular Weight and the Side-Chain Length on the Photovoltaic Performance of Dithienosilole/Thienopyrrolodione Copolymers. *Advanced functional materials* **22**, 2345-2351 (2012).
208. P. M. Beaujuge *et al.*, Tailoring Structure–Property Relationships in Dithienosilole–Benzothiadiazole Donor–Acceptor Copolymers. *Journal of the American Chemical Society* **131**, 7514-7515 (2009).
209. L. Liao *et al.*, Photovoltaic-Active Dithienosilole-Containing Polymers. *Macromolecules* **40**, 9406-9412 (2007).
210. L.-Y. Lin *et al.*, New A-A-D-A-A-Type Electron Donors for Small Molecule Organic Solar Cells. *Organic letters* **13**, 4962-4965 (2011).
211. J. Zhou *et al.*, A Planar Small Molecule with Dithienosilole Core for High Efficiency Solution-Processed Organic Photovoltaic Cells. *Chemistry of Materials* **23**, 4666-4668 (2011).
212. A. Meller, A. Ossko, Phthalocyaninartige Bor-Komplexe. *Monatshefte für Chemie/Chemical Monthly* **103**, 150-155 (1972).
213. T. Torres, From subphthalocyanines to subporphyrins. *Angewandte Chemie International Edition* **45**, 2834-2837 (2006).
214. K. M. Kadish, K. M. Smith, R. Guilard, Handbook of porphyrin science. *World Scientific: Singapore* **2012**, 1-25 (2010).
215. H. Kietai, The crystal and molecular structure of a new phthalocyaninelike boron complex. (1974).
216. H. Gommans *et al.*, Perfluorinated Subphthalocyanine as a New Acceptor Material in a Small-Molecule Bilayer Organic Solar Cell. *Advanced functional materials* **19**, 3435-3439 (2009).
217. H. Gommans *et al.*, On the role of bathocuproine in organic photovoltaic cells. *Advanced functional materials* **18**, 3686-3691 (2008).
218. H. Gommans *et al.*, Electro-Optical Study of Subphthalocyanine in a Bilayer Organic Solar Cell. *Advanced functional materials* **17**, 2653-2658 (2007).
219. C. E. Mauldin *et al.*, Axial Thiophene–Boron (subphthalocyanine) Dyads and Their Application in Organic Photovoltaics. *ACS Applied Materials & Interfaces* **2**, 2833-2838 (2010).
220. B. Verreet *et al.*, The characterization of chloroboron (III) subnaphthalocyanine thin films and their application as a donor material for organic solar cells. *Journal of Materials Chemistry* **19**, 5295-5297 (2009).
221. G. E. Morse, T. P. Bender, Boron Subphthalocyanines as Organic Electronic Materials. *ACS Applied Materials & Interfaces* **4**, 5055-5068 (2012).
222. L.-J. Pegg, S. Schumann, R. A. Hatton, Enhancing the open-circuit voltage of molecular photovoltaics using oxidized Au nanocrystals. *Acs Nano* **4**, 5671-5678 (2010).
223. R. Pandey, Y. Zou, R. J. Holmes, Efficient, bulk heterojunction organic photovoltaic cells based on boron subphthalocyanine chloride-C70. *Applied Physics Letters* **101**, 033308 (2012).
224. Y.-q. Zheng *et al.*, Highly efficient bulk heterojunction photovoltaic cells based on C70 and tetraphenylidibenzoperiflanthene. *Applied Physics Letters* **102**, 143304 (2013).

225. S.-W. Liu *et al.*, Absorbing visible light materials of subphthalocyanine and C70 for efficient planar-mixed organic photovoltaic devices. *Journal of The Electrochemical Society* **160**, G14-G18 (2013).
226. B. Verreet *et al.*, A 4% efficient organic solar cell using a fluorinated fused subphthalocyanine dimer as an electron acceptor. *Advanced Energy Materials* **1**, 565-568 (2011).
227. J. Yang, S. Schumann, R. A. Hatton, T. Jones, Copper hexadecafluorophthalocyanine (F₁₆ CuPc) as an electron accepting material in bilayer small molecule organic photovoltaic cells. *Organic Electronics* **11**, 1399-1402 (2010).
228. D. Klaus, R. Knecht, A. Dragässer, C. Keil, D. Schlettwein, (Photo-) conduction measurements during the growth of evaporated bulk heterojunctions of a subphthalocyanine donor and a perfluorinated phthalocyanine acceptor. *physica status solidi (a)* **206**, 2723-2730 (2009).
229. N. Beaumont *et al.*, Boron Subphthalocyanine Chloride as an Electron Acceptor for High-Voltage Fullerene-Free Organic Photovoltaics. *Advanced functional materials* **22**, 561-566 (2012).
230. H. Gommans, S. Schols, A. Kadashchuk, P. Heremans, S. Meskers, Exciton diffusion length and lifetime in subphthalocyanine films. *The Journal of Physical Chemistry C* **113**, 2974-2979 (2009).
231. B. Verreet *et al.*, Decreased Recombination Through the Use of a Non-Fullerene Acceptor in a 6.4% Efficient Organic Planar Heterojunction Solar Cell. *Advanced Energy Materials*, (2014).
232. D. González-Rodríguez *et al.*, Subphthalocyanines: Tuneable molecular scaffolds for intramolecular electron and energy transfer processes. *Journal of the American Chemical Society* **126**, 6301-6313 (2004).
233. D. D. Díaz *et al.*, Subphthalocyanines as narrow band red-light emitting materials. *Tetrahedron letters* **48**, 4657-4660 (2007).
234. G. E. Morse, M. G. Helander, J. F. Maka, Z.-H. Lu, T. P. Bender, Fluorinated phenoxy boron subphthalocyanines in organic light-emitting diodes. *ACS Applied Materials & Interfaces* **2**, 1934-1944 (2010).
235. Y.-H. Chen *et al.*, Enhancement in current efficiency in organic light-emitting diodes with incorporation of subphthalocyanine. *Applied Physics Letters* **95**, 133302 (2009).
236. M. G. Helander *et al.*, Pentafluorophenoxy Boron Subphthalocyanine As a Fluorescent Dopant Emitter in Organic Light Emitting Diodes. *ACS Applied Materials & Interfaces* **2**, 3147-3152 (2010).
237. T. Yasuda, T. Tsutsui, n-Channel Organic Field-Effect Transistors Based on Boron-Subphthalocyanine. *Molecular Crystals and Liquid Crystals* **462**, 3-9 (2006).
238. C. K. Renshaw, X. Xu, S. R. Forrest, A monolithically integrated organic photodetector and thin film transistor. *Organic Electronics* **11**, 175-178 (2010).
239. X. Tong, S. R. Forrest, An integrated organic passive pixel sensor. *Organic Electronics* **12**, 1822-1825 (2011).
240. M. Singh, A. Mahajan, R. Bedi, D. Aswal, Dielectric spectroscopic studies of boron subphthalocyanine chloride thin films. *Electronic Materials Letters* **9**, 101-106 (2013).
241. Y. Wang, D. Gu, F. Gan, Optical recording properties of a novel subphthalocyanine thin film. *physica status solidi (a)* **186**, 71-77 (2001).
242. Y. Wang, D. Gu, F. Gan, in *Optical Storage (ISOS 2002)*. (International Society for Optics and Photonics, 2003), pp. 15-19.
243. A. Natarajan *et al.* (Google Patents, 2012).
244. A. Natarajan *et al.* (Google Patents, 2013).
245. A. Natarajan *et al.* (Google Patents, 2013).
246. C. G. Claessens, T. Torres, Synthesis, separation, and characterization of the topoisomers of fused bicyclic subphthalocyanine dimers. *Angewandte Chemie International Edition* **41**, 2561-2565 (2002).

247. J. Guilleme, D. González-Rodríguez, T. Torres, Triflate-Subphthalocyanines: Versatile, Reactive Intermediates for Axial Functionalization at the Boron Atom. *Angewandte Chemie* **123**, 3568-3571 (2011).
248. D. González-Rodríguez, T. Torres, Peripheral Functionalization of Subphthalocyanines. *European Journal of Organic Chemistry* **2009**, 1871-1879 (2009).
249. D. González-Rodríguez *et al.*, Photoinduced charge-transfer states in subphthalocyanine-ferrocene dyads. *Journal of the American Chemical Society* **128**, 10680-10681 (2006).
250. G. E. Morse, T. P. Bender, Aluminum Chloride Activation of Chloro-Boronsubphthalocyanine: a Rapid and Flexible Method for Axial Functionalization with an Expanded Set of Nucleophiles. *Inorganic chemistry* **51**, 6460-6467 (2012).
251. G. E. Morse *et al.*, Experimentally Validated Model for the Prediction of the HOMO and LUMO Energy Levels of Boronsubphthalocyanines. *The Journal of Physical Chemistry C* **115**, 11709-11718 (2011).
252. D. González-Rodríguez *et al.*, Tuning Photoinduced Energy-and Electron-Transfer Events in Subphthalocyanine-Phthalocyanine Dyads. *Chemistry-A European Journal* **11**, 3881-3893 (2005).
253. J.-H. Kim, M. E. El-Khouly, Y. Araki, O. Ito, K.-Y. Kay, Photoinduced processes of subphthalocyanine-diazobenzene-fullerene triad as an efficient excited energy transfer system. *Chemistry Letters* **37**, 544-545 (2008).
254. I. Sánchez-Molina, C. Claessens, B. Grimm, D. Guldi, T. Torres, Trapping fullerenes with jellyfish-like subphthalocyanines. *Chemical Science* **4**, 1338-1344 (2013).
255. M. E. El-Khouly, D. K. Ju, K. Y. Kay, F. D'Souza, S. Fukuzumi, Supramolecular Tetrad of Subphthalocyanine-Triphenylamine-Zinc Porphyrin Coordinated to Fullerene as an "Antenna-Reaction-Center" Mimic: Formation of a Long-Lived Charge-Separated State in Nonpolar Solvent. *Chemistry-A European Journal* **16**, 6193-6202 (2010).
256. F. Camerel, G. Ulrich, P. Retailleau, R. Ziessel, Ethynyl-Boron Subphthalocyanines Displaying Efficient Cascade Energy Transfer and Large Stokes Shifts. *Angewandte Chemie International Edition* **47**, 8876-8880 (2008).
257. M. E. El-Khouly, J. B. Ryu, K.-Y. Kay, O. Ito, S. Fukuzumi, Long-Lived Charge Separation in a Dyad of Closely-Linked Subphthalocyanine-Zinc Porphyrin Bearing Multiple Triphenylamines. *The Journal of Physical Chemistry C* **113**, 15444-15453 (2009).
258. D. González-Rodríguez *et al.*, Screening Electronic Communication through ortho-, meta- and para-Substituted Linkers Separating Subphthalocyanines and C60. *Chemistry-A European Journal* **14**, 7670-7679 (2008).
259. D. González-Rodríguez, E. Carbonell, D. M. Guldi, T. Torres, Modulating Electronic Interactions between Closely Spaced Complementary π Surfaces with Different Outcomes: Regio- and Diastereomerically Pure Subphthalocyanine-C60 Tris Adducts. *Angewandte Chemie International Edition* **48**, 8032-8036 (2009).
260. D. González-Rodríguez *et al.*, Activating Multistep Charge-Transfer Processes in Fullerene-Subphthalocyanine-Ferrocene Molecular Hybrids as a Function of π - π Orbital Overlap. *Journal of the American Chemical Society* **132**, 16488-16500 (2010).
261. M. E. El-Khouly, S. H. Shim, Y. Araki, O. Ito, K.-Y. Kay, Effect of dual fullerenes on lifetimes of charge-separated states of subphthalocyanine-triphenylamine-fullerene molecular systems. *The Journal of Physical Chemistry B* **112**, 3910-3917 (2008).
262. M. E. El-Khouly, J.-H. Kim, J.-H. Kim, K.-Y. Kay, S. Fukuzumi, Subphthalocyanines as Light-Harvesting Electron Donor and Electron Acceptor in Artificial Photosynthetic Systems. *The Journal of Physical Chemistry C* **116**, 19709-19717 (2012).
263. C. Romero-Nieto *et al.*, Ultrafast Photoinduced Processes in Subphthalocyanine Electron Donor-Acceptor Conjugates Linked by a Single B-N Bond // . *Organic letters* **14**, 5656-5659 (2012).
264. C. Romero-Nieto *et al.*, Towards enhancing light harvesting—subphthalocyanines as electron acceptors. *Chemical Communications* **48**, 4953-4955 (2012).

265. C. R. Nieto *et al.*, Subphthalocyanine-polymethine cyanine conjugate: an all organic panchromatic light harvester that reveals charge transfer. *Journal of Materials Chemistry* **21**, 15914-15918 (2011).
266. R. Bauernschmitt, R. Ahlrichs, Treatment of electronic excitations within the adiabatic approximation of time dependent density functional theory. *Chemical Physics Letters* **256**, 454-464 (1996).
267. R. E. Stratmann, G. E. Scuseria, M. J. Frisch, An efficient implementation of time-dependent density-functional theory for the calculation of excitation energies of large molecules. *The Journal of Chemical Physics* **109**, 8218-8224 (1998).
268. M. E. Casida, C. Jamorski, K. C. Casida, D. R. Salahub, Molecular excitation energies to high-lying bound states from time-dependent density-functional response theory: Characterization and correction of the time-dependent local density approximation ionization threshold. *The Journal of Chemical Physics* **108**, 4439-4449 (1998).
269. S. Agrawal, P. Dev, N. J. English, K. R. Thampi, J. M. D. MacElroy, A TD-DFT study of the effects of structural variations on the photochemistry of polyene dyes. *Chemical Science* **3**, 416-424 (2012).
270. A. J. Cohen, P. Mori-Sánchez, W. Yang, Challenges for Density Functional Theory. *Chemical Reviews* **112**, 289-320 (2012).
271. C. B. Nielsen, A. J. P. White, I. McCulloch, Effect of Fluorination of 2,1,3-Benzothiadiazole. *The Journal of organic chemistry* **80**, 5045-5048 (2015).
272. R. L. Martin, Natural transition orbitals. *The Journal of Chemical Physics* **118**, 4775-4777 (2003).
273. S. Wong, H. Ma, A. K. Y. Jen, R. Barto, C. W. Frank, Highly Fluorinated Trifluorovinyl Aryl Ether Monomers and Perfluorocyclobutane Aromatic Ether Polymers for Optical Waveguide Applications. *Macromolecules* **36**, 8001-8007 (2003).
274. K. Reichenbacher, H. I. Suss, J. Hulliger, Fluorine in crystal engineering-"the little atom that could". *Chemical Society Reviews* **34**, 22-30 (2005).
275. M. Pagliaro, R. Ciriminna, New fluorinated functional materials. *Journal of Materials Chemistry* **15**, 4981-4991 (2005).
276. Y. Wang, S. R. Parkin, J. Gierschner, M. D. Watson, Highly Fluorinated Benzobisbenzothiophenes. *Organic letters* **10**, 3307-3310 (2008).
277. L. Yang, J. R. Tumbleston, H. Zhou, H. Ade, W. You, Disentangling the impact of side chains and fluorine substituents of conjugated donor polymers on the performance of photovoltaic blends. *Energy & Environmental Science* **6**, 316-326 (2013).
278. H. J. Son *et al.*, Synthesis of Fluorinated Polythienothiophene-co-benzodithiophenes and Effect of Fluorination on the Photovoltaic Properties. *Journal of the American Chemical Society* **133**, 1885-1894 (2011).
279. J. K. Stille, The palladium-catalyzed cross-coupling reactions of organotin reagents with organic electrophiles [new synthetic methods (58)]. *Angewandte Chemie, International Edition* **25**, 508-524 (1986).
280. N. Miyaura, A. Suzuki, Stereoselective synthesis of arylated (E)-alkenes by the reaction of alk-1-enylboranes with aryl halides in the presence of palladium catalyst. *Journal of the Chemical Society, Chemical Communications*, 866-867 (1979).
281. N. Miyaura, K. Yamada, A. Suzuki, A new stereospecific cross-coupling by the palladium-catalyzed reaction of 1-alkenylboranes with 1-alkenyl or 1-alkynyl halides. *Tetrahedron Letters* **20**, 3437-3440 (1979).
282. P. Berrouard *et al.*, Synthesis of 5-Alkyl [3, 4-c] thienopyrrole-4, 6-dione-Based Polymers by Direct Heteroarylation. *Angewandte Chemie* **124**, 2110-2113 (2012).
283. R. Grisorio *et al.*, Sustainability of Organic Dye-Sensitized Solar Cells: The Role of Chemical Synthesis. *ACS Sustainable Chemistry & Engineering* **3**, 770-777 (2015).
284. J. Wencel-Delord, F. Glorius, CH bond activation enables the rapid construction and late-stage diversification of functional molecules. *Nature Chemistry* **5**, 369-375 (2013).

285. K. Okamoto, J. Zhang, J. B. Housekeeper, S. R. Marder, C. K. Luscombe, C–H arylation reaction: atom efficient and greener syntheses of π -conjugated small molecules and macromolecules for organic electronic materials. *Macromolecules* **46**, 8059-8078 (2013).
286. A. Facchetti, L. Vaccaro, A. Marrocchi, Semiconducting polymers prepared by direct arylation polycondensation. *Angewandte Chemie, International Edition* **51**, 3520-3523 (2012).
287. S. Kowalski, S. Allard, K. Zilberberg, T. Riedl, U. Scherf, Direct arylation polycondensation as simplified alternative for the synthesis of conjugated (co) polymers. *Progress in Polymer Science* **38**, 1805-1814 (2013).
288. A. Ohta *et al.*, Palladium-catalyzed arylation of furan, thiophene, benzo [b] furan and benzo [b] thiophene. *Heterocycles* **31**, 1951-1958 (1990).
289. J. Roger, F. Požgan, H. Doucet, Ligand-less palladium-catalyzed direct 5-arylation of thiophenes at low catalyst loadings. *Green Chemistry* **11**, 425-432 (2009).
290. J. Roger, H. Doucet, Phosphine-free palladium-catalysed direct 5-arylation of imidazole derivatives at low catalyst loading. *Tetrahedron* **65**, 9772-9781 (2009).
291. J. J. Dong, J. Roger, F. Požgan, H. Doucet, Low catalyst loading ligand-free palladium-catalyzed direct arylation of furans: an economically and environmentally attractive access to 5-arylfurans. *Green Chemistry* **11**, 1832-1846 (2009).
292. J. Roger, H. Doucet, Regioselective C-2 or C-5 Direct Arylation of Pyrroles with Aryl Bromides using a Ligand-Free Palladium Catalyst. *Advanced Synthesis & Catalysis* **351**, 1977-1990 (2009).
293. J. Roger, F. Pozgan, H. Doucet, Ligand-free palladium-catalyzed direct arylation of thiazoles at low catalyst loadings. *The Journal of organic chemistry* **74**, 1179-1186 (2009).
294. Y. Bouazizi, K. Beydoun, A. Romdhane, H. Ben Jannet, H. Doucet, Palladium-catalysed direct arylations of heteroaromatics bearing dicyanovinyls at C2. *Tetrahedron letters* **53**, 6801-6805 (2012).
295. A. Takfaoui *et al.*, One pot Pd (OAc)₂-catalysed 2, 5-diarylation of imidazoles derivatives. *Tetrahedron* **70**, 8316-8323 (2014).
296. M. T. Reetz, G. Lohmer, Propylene carbonate stabilized nanostructured palladium clusters as catalysts in Heck reactions. *Chemical Communications*, 1921-1922 (1996).
297. M. T. Reetz, J. G. de Vries, Ligand-free Heck reactions using low Pd-loading. *Chemical Communications*, 1559-1563 (2004).
298. R. F. Heck, in *Organic Reactions*. (John Wiley & Sons, Inc., 2004).
299. Y. Fujinami, J. Kuwabara, W. Lu, H. Hayashi, T. Kanbara, Synthesis of thiophene-and bithiophene-based alternating copolymers via Pd-catalyzed direct C–H arylation. *ACS Macro Letters* **1**, 67-70 (2011).
300. S. Roquet *et al.*, Triphenylamine-thienylenevinylene hybrid systems with internal charge transfer as donor materials for heterojunction solar cells. *Journal of the American Chemical Society* **128**, 3459-3466 (2006).
301. Y. Lin, Z.-G. Zhang, H. Bai, Y. Li, X. Zhan, A star-shaped oligothiophene end-capped with alkyl cyanoacetate groups for solution-processed organic solar cells. *Chemical Communications* **48**, 9655-9657 (2012).
302. T. C. Parker *et al.*, Heteroannulated acceptors based on benzothiadiazole. *Materials Horizons* **2**, 22-36 (2015).
303. Y. Liu *et al.*, Spin-Coated Small Molecules for High Performance Solar Cells. *Advanced Energy Materials* **1**, 771-775 (2011).
304. G. Long *et al.*, Investigation of quinquethiophene derivatives with different end groups for high open circuit voltage solar cells. *Advanced Energy Materials* **3**, 639-646 (2013).
305. S. Shen *et al.*, Solution-processable organic molecule photovoltaic materials with bithienyl-benzodithiophene central unit and indenedione end groups. *Chemistry of Materials* **25**, 2274-2281 (2013).

306. G. He *et al.*, Efficient small molecule bulk heterojunction solar cells with high fill factors via introduction of π -stacking moieties as end group. *Journal of Materials Chemistry A* **1**, 1801-1809 (2013).
307. F. M. Pasker, S. M. Le Blanc, G. Schnakenburg, S. Höger, Thiophene-2-aryl-2 H-benzotriazole-thiophene Oligomers with Adjustable Electronic Properties. *Organic Letters* **13**, 2338-2341 (2011).
308. L. Marin, L. Lutsen, D. Vanderzande, W. Maes, Quinoxaline derivatives with broadened absorption patterns. *Organic & Biomolecular Chemistry* **11**, 5866-5876 (2013).
309. J. Zhang *et al.*, Controllable direct arylation: Fast route to symmetrical and unsymmetrical 4, 7-diaryl-5, 6-difluoro-2, 1, 3-benzothiadiazole derivatives for organic optoelectronic materials. *Journal of the American Chemical Society* **135**, 16376-16379 (2013).
310. F. Machui *et al.*, Cost analysis of roll-to-roll fabricated ITO free single and tandem organic solar modules based on data from manufacture. *Energy & Environmental Science* **7**, 2792-2802 (2014).
311. K. Van Aken, L. Strekowski, L. Patiny, EcoScale, a semi-quantitative tool to select an organic preparation based on economical and ecological parameters. *Beilstein Journal of Organic Chemistry* **2**, 3 (2006).
312. R. A. Sheldon, The E factor: fifteen years on. *Green Chemistry* **9**, 1273-1283 (2007).
313. Y. Geng *et al.*, Electronic tuning effects via [small pi]-linkers in tetrathiafulvalene-based dyes. *New Journal of Chemistry* **38**, 3269-3274 (2014).
314. J.-H. Huang *et al.*, Nanoscale Correlation between Exciton Dissociation and Carrier Transport in Silole-Containing Cyclopentadithiophene-Based Bulk Heterojunction Films. *The Journal of Physical Chemistry C* **115**, 2398-2405 (2011).
315. S. Kowalski, S. Allard, U. Scherf, Synthesis of Poly(4,4-dialkyl-cyclopenta[2,1-b:3,4-b']dithiophene-alt-2,1,3-benzothiadiazole) (PCPDTBT) in a Direct Arylation Scheme. *ACS Macro Letters* **1**, 465-468 (2012).
316. C. G. Claessens *et al.*, Highly Efficient Synthesis of Chloro-and Phenoxy-Substituted Subphthalocyanines. *European Journal of Organic Chemistry* **2003**, 2547-2551 (2003).
317. M. Geyer *et al.*, Subphthalocyanines: preparation, reactivity and physical properties. *Synthesis*, 1139-1151 (1996).
318. G. E. Morse, A. S. Paton, A. Lough, T. P. Bender, Chloro boron subphthalocyanine and its derivatives: dyes, pigments or somewhere in between? *Dalton Transactions* **39**, 3915-3922 (2010).
319. Ł. Łapok, C. G. Claessens, D. Wöhrle, T. Torres, Synthesis of water-soluble subphthalocyanines. *Tetrahedron letters* **50**, 2041-2044 (2009).
320. E. R. Brisson, A. S. Paton, G. E. Morse, T. P. Bender, Boron Subphthalocyanine Dyes: 3-Pentadecylphenol as a Solubilizing Molecular Fragment. *Industrial & Engineering Chemistry Research* **50**, 10910-10917 (2011).
321. D. González-Rodríguez *et al.*, Thermal stability of boron subphthalocyanines as a function of the axial and peripheral substitution. *Journal of Organometallic Chemistry* **694**, 1617-1622 (2009).
322. A. B. Tamayo, B. Walker, T.-Q. Nguyen*, A Low Band Gap, Solution Processable Oligothiophene with a Diketopyrrolopyrrole Core for Use in Organic Solar Cells. *The Journal of Physical Chemistry C* **112**, 11545-11551 (2008).
323. X. Yu *et al.*, High-Performance Field-Effect Transistors Based on Polystyrene-b-Poly(3-hexylthiophene) Diblock Copolymers. *Acs Nano* **5**, 3559-3567 (2011).
324. W. Ma *et al.*, Influence of Processing Parameters and Molecular Weight on the Morphology and Properties of High-Performance PffBT4T-2OD:PC71BM Organic Solar Cells. *Advanced Energy Materials* **5**, 1501400 (2015).
325. Z. Chen *et al.*, Low Band-Gap Conjugated Polymers with Strong Interchain Aggregation and Very High Hole Mobility Towards Highly Efficient Thick-Film Polymer Solar Cells. *Advanced Materials* **26**, 2586-2591 (2014).

326. H. Shang *et al.*, A Solution-Processable Star-Shaped Molecule for High-Performance Organic Solar Cells. *Advanced Materials* **23**, 1554-1557 (2011).
327. D. Hernandez Maldonado, Université de Toulouse, Université Toulouse III-Paul Sabatier, (2015).
328. Y. Zhou, T. Taima, T. Kuwabara, K. Takahashi, Efficient Small-Molecule Photovoltaic Cells Using a Crystalline Diindenoperylene Film as a Nanostructured Template. *Advanced Materials* **25**, 6069-6075 (2013).
329. C. M. Cardona, W. Li, A. E. Kaifer, D. Stockdale, G. C. Bazan, Electrochemical Considerations for Determining Absolute Frontier Orbital Energy Levels of Conjugated Polymers for Solar Cell Applications. *Advanced Materials* **23**, 2367-2371 (2011).
330. D. Haristoy *et al.*, Structure and photoconductive behaviour of a sanidic liquid crystal. *Liquid Crystals* **27**, 321-328 (2000).
331. I. Dierking, *Textures of liquid crystals*. (John Wiley & Sons, 2006).
332. F. Lincker *et al.*, Influence of polymorphism on charge transport properties in isomers of fluorenone-based liquid crystalline semiconductors. *Chemical Communications* **48**, 3209-3211 (2012).
333. S.-H. Liao, H.-J. Jhuo, Y.-S. Cheng, S.-A. Chen, Fullerene Derivative-Doped Zinc Oxide Nanofilm as the Cathode of Inverted Polymer Solar Cells with Low-Bandgap Polymer (PTB7-Th) for High Performance. *Advanced Materials* **25**, 4766-4771 (2013).
334. F. Weigend, R. Ahlrichs, Balanced basis sets of split valence, triple zeta valence and quadruple zeta valence quality for H to Rn: design and assessment of accuracy. *Physical Chemistry Chemical Physics* **7**, 3297-3305 (2005).
335. S. Grimme, J. Antony, S. Ehrlich, H. Krieg, A consistent and accurate ab initio parametrization of density functional dispersion correction (DFT-D) for the 94 elements H-Pu. *Journal of Chemical Physics* **132**, 154104 (2010).
336. S. Grimme, S. Ehrlich, L. Goerigk, Effect of the damping function in dispersion corrected density functional theory. *Journal of Computational Chemistry* **32**, 1456-1465 (2011).
337. A. D. Becke, Density-functional exchange-energy approximation with correct asymptotic behavior. *Physical Review A* **38**, 3098 (1988).
338. C. Lee, W. Yang, R. G. Parr, Development of the Colle-Salvetti correlation-energy formula into a functional of the electron density. *Physical Review B* **37**, 785 (1988).
339. A. Klamt, Conductor-like screening model for real solvents: a new approach to the quantitative calculation of solvation phenomena. *Journal of Physical Chemistry* **99**, 2224-2235 (1995).
340. A. Dreuw, M. Head-Gordon, Single-reference ab initio methods for the calculation of excited states of large molecules. *Chemical Reviews* **105**, 4009-4037 (2005).
341. H. Usta, G. Lu, A. Facchetti, T. J. Marks, Dithienosilole- and Dibenzosilole-Thiophene Copolymers as Semiconductors for Organic Thin-Film Transistors. *Journal of the American Chemical Society* **128**, 9034-9035 (2006).
342. <http://www.thenurj.com/a-self-assembled-organic/inorganic-nanostructure-for-photovoltaic-applications/>. (Julian Minuzzo; Samuel I. Stupp and David Herman 2013).
343. N. Miyaura, A. Suzuki, Palladium-Catalyzed Cross-Coupling Reactions of Organoboron Compounds. *Chemical reviews* **95**, 2457-2483 (1995).
344. L. Kurti, B. Czakó, *Strategic applications of named reactions in organic synthesis*. (Elsevier, 2005).
345. M. Moreno-Mañas, M. Pérez, R. Pleixats, Palladium-Catalyzed Suzuki-Type Self-Coupling of Arylboronic Acids. A Mechanistic Study. *The Journal of organic chemistry* **61**, 2346-2351 (1996).
346. P. Espinet, A. M. Echavarren, The Mechanisms of the Stille Reaction. *Angewandte Chemie International Edition* **43**, 4704-4734 (2004).
347. H. B. Stoner, J. M. Barnes, J. I. Duff, Studies on the Toxicity of Alkyl Tin Compounds. *British Journal of Pharmacology and Chemotherapy* **10**, 16-25 (1955).

348. R. Rossi, F. Bellina, M. Lessi, C. Manzini, Cross-Coupling of Heteroarenes by C-H Functionalization: Recent Progress towards Direct Arylation and Heteroarylation Reactions Involving Heteroarenes Containing One Heteroatom. *Advanced Synthesis & Catalysis* **356**, 17-117 (2014).
349. T. W. Lyons, M. S. Sanford, Palladium-Catalyzed Ligand-Directed C-H Functionalization Reactions. *Chemical reviews* **110**, 1147-1169 (2010).

Titre: Design, synthesis and characterization of new organic semi-conductors for photovoltaics

Résumé

Les cellules photovoltaïques organiques sont une technologie prometteuse pour répondre aux besoins futurs en énergie. Elles présentent de faibles coûts de production, peuvent être réalisées sur substrats flexibles et s'intègrent dans des dispositifs légers. Une voie d'amélioration du rendement de photoconversion est la conception de nouvelles molécules actives présentant des propriétés structurales optimisées.

Le présent travail s'inscrit dans cette dynamique: sur la base de calculs utilisant la théorie de la fonctionnelle de la densité, de nouveaux semiconducteurs organiques ont été conçus puis synthétisés. Pour cela, des techniques de synthèses les plus économiques et les moins polluantes possible ont été mises en œuvre. Ainsi, le couplage du benzothiadiazole avec le thiophène carboxaldéhyde par hétéroarylation directe sans additif ni ligand est utilisé avec succès pour la première fois selon des techniques de chimie verte. Cinq molécules sont ainsi isolées en seulement deux étapes. L'étude de leurs propriétés optiques et électroniques par différentes techniques spectroscopiques (UV/vis, fluorescence) et par électrochimie, de leurs propriétés thermiques, et de leur aptitude à s'auto-organiser ont permis de révéler leur aptitude prometteuse pour une utilisation en photovoltaïque organique.

Une série de molécules dérivées du fragment dithiénosilole (DTS) ont été également étudiées par calculs de DFT. Les résultats obtenus montrent que ces dérivés présentent des largeurs de bande interdite très faibles, ce qui constitue un atout pour leur utilisation en cellule photovoltaïque. Ces résultats ont par conséquent motivé leur synthèse. Enfin, un travail purement théorique a été réalisé sur des molécules dérivées des subphthalocyanines de bore. Les calculs effectués révèlent des propriétés électroniques originales pour ces nouveaux matériaux qui devraient mener à des performances intéressantes pour le photovoltaïque organique, ouvrant ainsi la voie vers des matériaux innovants et prometteurs.

Mots clés: Semi-conducteurs organiques; photovoltaïque organique; synthèse; caractérisation

Abstract

Organic solar cells appear as a promising technology to meet future energy requirements, owing to their low production costs, their great flexibility and their ability to be integrated into light devices. Currently, they exhibit modest performances in photoconversion, thus new active molecules with optimized structural properties need to be developed.

This work comes in that aim: on the basis of theoretical calculations with density functional theory, new organic semiconductors have been designed and synthesized. For this, the more economical and cleaner syntheses techniques have been employed. Thus, the coupling of the benzothiadiazole with thiophene carboxaldehyde via direct heteroarylation without additive nor ligand is performed with success for the first time. According to green chemistry techniques, five molecules are thus isolated in only two steps. The study of their optical and electronic properties by means of different spectroscopic techniques (UV/vis, fluorescence) and electrochemistry, of their thermal properties, and of their ability to self-organize have revealed their promising abilities for use in organic photovoltaics.

A series of small molecules based on dithienosilole (DTS) core have also been designed *via* DFT computations. The calculations show their considerable low bandgap. Their syntheses have been conducted. It anticipates their promising potential for organic photovoltaic applications. Finally, a purely theoretical work has been completed on molecules derived from boron subphthalocyanines. The calculations predict interesting electronic properties for these new materials that may lead to promising performances in organic photovoltaics, paving the way for innovative materials.

Keywords: Organic semiconductors; organic photovoltaics; synthesis; characterization